UNIVERSITAT POLITÈCNICA
DE CATALUNYA
BARCELONATECH

Bioresorbable Zn-based alloys for biomedical applications

Claudia García Mintegui

ADVERTIMENT La consulta d'aquesta tesi queda condicionada a l'acceptació de les següents condicions d'ús: La difusió d'aquesta tesi per mitjà del repositori institucional UPCommons (http://upcommons.upc.edu/tesis) i el repositori cooperatiu TDX (http://www.tdx.cat/) ha estat autoritzada pels titulars dels drets de propietat intel·lectual **únicament per a usos privats** emmarcats en activitats d'investigació i docència. No s'autoritza la seva reproducció amb finalitats de lucre ni la seva difusió i posada a disposició des d'un lloc aliè al servei UPCommons o TDX. No s'autoritza la presentació del seu contingut en una finestra o marc aliè a UPCommons (*framing*). Aquesta reserva de drets afecta tant al resum de presentació de la tesi com als seus continguts. En la utilització o cita de parts de la tesi és obligat indicar el nom de la persona autora.

ADVERTENCIA La consulta de esta tesis queda condicionada a la aceptación de las siguientes condiciones de uso: La difusión de esta tesis por medio del repositorio institucional UPCommons (http://upcommons.upc.edu/tesis) y el repositorio cooperativo TDR (http://www.tdx.cat/?locale-attribute=es) ha sido autorizada por los titulares de los derechos de propiedad intelectual **únicamente para usos privados enmarcados** en actividades de investigación y docencia. No se autoriza su reproducción con finalidades de lucro ni su difusión y puesta a disposición desde un sitio ajeno al servicio UPCommons No se autoriza la presentación de su contenido en una ventana o marco ajeno a UPCommons (*framing*). Esta reserva de derechos afecta tanto al resumen de presentación de la tesis como a sus contenidos. En la utilización o cita de partes de la tesis es obligado indicar el nombre de la persona autora.

WARNING On having consulted this thesis you're accepting the following use conditions: Spreading this thesis by the institutional repository UPCommons (http://upcommons.upc.edu/tesis) and the cooperative repository TDX (http://www.tdx.cat/?locale- attribute=en) has been authorized by the titular of the intellectual property rights **only for private uses** placed in investigation and teaching activities. Reproduction with lucrative aims is not authorized neither its spreading nor availability from a site foreign to the UPCommons service. Introducing its content in a window or frame foreign to the UPCommons service is not authorized (framing). These rights affect to the presentation summary of the thesis as well as to its contents. In the using or citation of parts of the thesis it's obliged to indicate the name of the author.

CLAUDIA GARCÍA MINTEGUI

Bioresorbable Zn-based alloys for biomedical applications

Doctoral programme in Materials Science and Engineering
Supervisors: Dr. Marta Pegueroles and Dr. José Luis Cortina

CLAUDIA GARCÍA MINTEGUI

Bioresorbable Zn-based alloys for biomedical applications

Doctoral programme in Materials Science and Engineering

Supervisors: Dr. Marta Pegueroles and Dr. José Luis Cortina

Department of Materials Science and Engineering
Department of Chemical Engineering
Universitat Politècnica de Catalunya – Barcelona Tech

Barcelona, 2022

UNIVERSITAT POLITÈCNICA
DE CATALUNYA
BARCELONATECH

BIOMATERIALS,
BIOMECHANICS &
TISSUE ENGINEERING

A todas las personas que habéis contribuido a que cuatro años de trabajo hayan acabado en forma de tesis doctoral.

A quienes celebrasteis mis alegrías y consolasteis mis penas. Vuestro apoyo ha sido tan fundamental como el resultado de los experimentos.

Index i
Abstract vi
Glossary ix

Introduction 5

- I. Bioresorbable implants 7
- II. Current state of the bioresorbable implants market 7
- III. Potential applications of bioresorbable metals 8
  - III.1. Bioresorbable cardiovascular stents 9
  - III.2. Bioresorbable antibacterial implants 11
    - III.2.1. Bioresorbable ureteral stents 12
    - III.2.2. Wound closure devices 13
  - III.3. General remarks on bioresorbable implants 14
- IV. Bioresorbable metals for biomedical applications 14
  - IV.1. Biodegradation mechanism 15
  - IV.2. Evaluation of bioresorbable metallic implants 17
  - IV.3. Iron (Fe) 18
  - IV.4. Magnesium (Mg) 19
  - IV.5. Zinc (Zn) 19
  - IV.6. Molybdenum (Mo) 20
  - IV.7. General remarks on bioresorbable metals 20
- V. Zn alloys 21
  - V.1. Zn-Mg alloy system 22
  - V.2. Zn-Cu alloy system 23
  - V.3. Zn-Ag alloy system 25
  - V.4. General remarks of zinc alloys 25
- VI. Techniques to control degradation and promote biointegration of Zn-based materials 26
  - VI.1. Protective coatings 26
  - VI.2. Surface functionalization 27
  - VI.3. Metal forming processing and post-processing 28
  - VI.4. General remarks on the modification of Zn-based alloys 30
- VII. References 30

Objectives 44

Part I. Characterization of Zn-based alloys..45

Chapter I. Characterization of Zn-Mg and Zn-Cu alloys for bioresorbable cardiovascular stents...47

I. Introduction.. ...54
II. Materials and methods...56
  II.1. Materials...56
  II.2. Microstructural characterization...56
  II.3. Mechanical characterization...57
  II.4. Corrosion evaluation...58
    II.4.1. Potentiodynamic polarization test...58
    II.4.2. Static immersion test..58
    II.4.3. Electrochemical impedance spectroscopy (EIS).......................................59
  II.5. Wettability..59
  II.6. Antibacterial activity...60
  II.7. Endothelial cell *in vitro* assays...60
  II.8. Statistical analysis...62
III. Results...62
  III.1. Microstructure..63
  III.2. Mechanical properties..63
  III.3. Corrosion behaviour...66
    III.3.1. Potentiodynamic polarization test...66
    III.3.2. Static immersion test..67
    III.3.3. Corrosion evolution by EIS..70
  III.4. Wettability..72
  III.5. Antibacterial activity..73
  III.6. Endothelial cell response..75
    III.6.1. Indirect contact cytotoxicity...75
    III.6.2. HAoEC viability by direct contact...75
IV. Discussion...78
V. Conclusions..83
VI. References...83
Supplementary Material...91

Chapter II. Characterization of Zn-Ag alloys for bioresorbable ureteral stents...............................92

I. Introduction...99
II. Materials and methods..100
  II.1. Materials... 100

II.2. Microstructural characterization 100
II.3. Mechanical characterization..101
II.4. Corrosion evaluation 101
II.4.1. Potentiodynamic polarization test 101
II.4.2. Static immersion tests...102
II.5. Antibacterial activity...102
II.5.1. Agar diffusion plate test..103
II.5.2. Bacterial indirect contact test...103
II.5.3. Bacterial direct contact test..103
II.6. Statistical analysis...104
III. Results 104
III.1. Microstructure..104
III.2. Mechanical characterization...105
III.3. Degradation evaluation..106
III.4. Antibacterial effect *via* ion diffusion 109
III.5. Antibacterial effect by contact...111
IV. Discussion...117
V. Conclusions..121
VI. References..121

Part II. Modification of Zn-based alloys...128

Chapter III. Implementation of dual-action coatings to control degradation and enhance endothelialisation of Zn alloys...130

I. Introduction...133
II. Materials and Methods...134
II.1. Sample preparation..134
II.1.1. ZnMg and ZnAg substrates...134
II.1.2. Polycaprolactone (PCL) coating..134
II.1.3. Solid-phase peptide synthesis...135
II.1.4. Surface functionalisation of the PCL spin-coated samples with peptides............136
II.2. Physico-chemical characterization of PCL coated and functionalized surfaces..........137
II.3. Corrosion evaluation..138
II.4. Endothelial cell adhesion...139
II.5. Statistical analysis...139
III. Results...140
III.1. Physicochemical characterization of PCL coating.......................................140

III.1.1. PCL coating thickness ……...140
III.1.2. Adhesion strength of the PCL coating..140
III.1.3. Wettability..141
III.1.4. XPS analysis...141
III.1.5. Surface characterization of RGD, REDV, and RGD-REDV biofunctionalized surfaces...143
III.2. Corrosion evaluation..143
III.2.1. Potentiodynamic polarization test...143
III.2.2. Electrochemical Impedance Spectroscopy ……...144
III.3. In vitro biocompatibility...146
IV. Discussion...148
V. Conclusions...151
VI. References..152

Chapter IV. Influence of ECAP process on mechanical, corrosion and bacterial properties of Zn-2Ag alloy..159

I. Introduction.. 162
II. Materials and Methods...163
II.1. Materials and ECAP processing...163
II.2. Microstructure characterization..164
II.3. Electron Backscattered Diffraction (EBSD) analysis 164
II.4. High-speed nanoindentation mapping..164
II.5. Mechanical characterization...165
II.6. Corrosion characterization..165
II.7. Bacterial adhesion...166
II.8. Statistical analysis...167
III. Results...167
III.1. Microstructure characterization..167
III.2. EBSD analysis...168
III.3. High-speed nanoindentation mapping...170
III.4. Mechanical characterization.. 171
III.5. Corrosion characterization...172
III.6. Bacterial response..175
IV. Discussion...176
V. Conclusions...179
VI. References..180

Concluding remarks..**186**

Conclusions...**188**

Future perspectives..**191**

Outcomes of the Thesis...**197**

Abstract

Biodegradable metals have emerged as promising materials to fabricate temporary biomedical devices to avoid the potential side effects of permanent implants. Among them, zinc (Zn) has increased interest due to its suitable degradation rate between iron (Fe) and magnesium (Mg) for biomedical applications. However, its low mechanical properties require alloying for mechanical reinforcement *via* solid precipitation hardening. Nevertheless, the formation of secondary phases induces galvanic corrosion and reduces biocompatibility. So far, the compromise among mechanical strength, corrosion rate, and biological activity of Zn alloys remains unknown.

This PhD Thesis aims to gain an increased understanding of biodegradable Zn-based alloys for biomedical applications, with an emphasis on establishing correlations between microstructure, mechanical properties, degradation behaviour, and *in vitro* biological response.

Chapter I aim is the characterization of Zn–xMg (x = 0.5, 1 wt. %) and Zn–xCu (x = 3, 5 wt.%) as potential material candidates for bioresorbable cardiovascular stents. Tensile tests confirmed that alloying with Mg or Cu increases yield strength (YS), ultimate tensile strength (UTS), and elongation at fracture. Nanoindentation tests confirmed mechanical reinforcement *via* solid precipitation of $Zn+Mg_2Zn_{11}$ and ε-$CuZn_5$ phases for Zn–Mg and Zn–Cu, respectively. Degradation tests in Hanks' solution indicated the formation of galvanic pairs between formed secondary phases and the Zn matrix. Zn–Cu presented antibacterial activity against *S. aureus* and *P. aeruginosa* but cytotoxicity to endothelial cells. All the studied alloys reported poor biocompatibility, attributed to locally released ions into solution and degrading surfaces. Thus, coating and functionalisation strategies are needed to be explored. Among all the samples, Zn-Mg alloys presented the best compromise among mechanical, corrosion, and biological properties.

Chapter II characterizes Zn–xAg (x = 2, 4 wt. %) alloys as potential material candidates for bioresorbable ureteral stents. Tensile tests evidenced the mechanical reinforcement of Zn-Ag alloys compared with pure Zn, where the higher volume fraction of $AgZn_3$ in the Zn-4Ag alloy led to reduced UTS, YS, and higher toughness than Zn-2Ag alloy. Moreover, the galvanic couple between $AgZn_3$ and Zn of Zn-4Ag alloy resulted in severe localized corrosion contraindicated for the proper implant performance. Furthermore, bacterial tests suggested that *S. aureus* and *E. coli* can infiltrate the corrosion pits hampering the antibacterial effect of Zn-4Ag alloy. In summary, Zn-2Ag presented the best degradation performance and optimal antibacterial effect.

Chapter III proposes a dual-action coating for Zn–0.5Mg and Zn–2Ag alloys to control degradation and enhance endothelialisation of cardiovascular stents. First, a polycaprolactone (PCL) coating was successfully implemented on the alloys via cold plasma polymerization of ε–caprolactone and subsequent PCL spin coating. Secondly, the PCL-coated alloys were functionalized with the linear RGD (Arg-Gly-Asp) and REDV (Arg-Glu-Asp-Val) peptides and the RGD-REDV platform, synthesized *via* solid solution and covalently immobilized via EDC/NHS chemistry. A homogeneous PCL coating of 800 nm with good adhesion strength provided adequate corrosion resistance to both alloys. Functionalised samples showed an increased number and spread of endothelial cells. Moreover, the increasing number of attached cells on samples functionalized with the RGD-REDV platform demonstrated the synergistic effect of RGD and REDV peptides.

Chapter IV explores the effect of equal channel angular pressing (ECAP) on the mechanical properties, corrosion behaviour, and bacterial response of Zn–2Ag alloy. To this end, two ECAP cycles (route Bc; R.T.) were performed on Zn–2Ag alloy. Ultrafine-grained structure and randomly distributed texture were obtained after ECAP, with no evident $AgZn_3$ breaking or distribution. Nanoindentation mapping indicated mechanical isotropy, and corrosion studies in brain heart infusion (BHI) media suggested a more uniform degradation after ECAP. The pressed sample presents exceptional antibacterial activity against *S. aureus*, attributed to the reduction of corrosion pits and distribution of Ag through the matrix. Overall, the ECAP process exhibited a potential technique for homogenizing the mechanical and corrosion properties of Zn–Ag alloys with excellent antibacterial properties.

In summary, this PhD Thesis contributes to increasing our knowledge of the relations between microstructure, mechanical properties, degradation rate, and biological response of studied Zn alloys. Moreover, it provides relevant clues to select the proper Zn-based formulation together with the coating and plastic deformation strategies to overcome the intrinsic galvanic corrosion of Zn alloys for different biomedical applications.

Glossary

A %	Elongation at break
Ac	Acetylated
ANOVA	Analysis of variance
ASTM	American Society for Testing and Materials
BHI	Brain heart infusion
BMP-2	Bone morphogenetic 2
BMS	Bare metal stent
BRS	Bioresorbable stent
BRS	Bioresorbable stent
CAD	Coronary artery disease
CF	5(6)-carboxyfluorescein
CFU	Colony forming unit
CPE	Constant phase element
CR	Corrosion rate
DAPI	4′,6-diamidino-2-phenylindole
DCM	Dichloromethane
DES	Drug-eluting stents
DMEM	Dulbecco's modified eagle medium
DMF	*N*,*N*-dimethylformamide
DRX	Dynamic recrystallization
EBSD	Electron backscattered diffraction
EC	Equivalent circuit
ECAP	Equal channel angular pressing
ECM	Extracellular matrix
E_{corr}	Corrosion potential
EDC	1-ethyl-3-(3-dimethylaminopropyl)carbodiimide
EDS	Energy-dispersive X-ray spectroscopy
EIS	Electrochemical impedance spectroscopy
EW	Equivalent weight
FIB/FESEM	Focused ion beam/field emission scanning electron microscope
HAoEC	Human aortic endothelial cell
HA	Hydroxyapatite
HE	Hot extrusion
HR	Hot rolling
HUVEC	Human umbilical vein endothelial cells
HV	Vickers hardness
i_{corr}	Current density
ICP-MS	Inductively coupled plasma mass spectroscopy
ICP-OES	Inductively coupled plasma optical emission spectroscopy
IPF	Inverse pole figure

ISO	International Standard Organization
ISR	Intra-stent restenosis
LD_{50}	Lethal median dose
LDH	Lactate dehydrogenase
LST	Late stent thrombosis
MIC	Minimum inhibitory concentration
MRSA	Methicillin-resistant *Staphylococcus aureus*
NHS	*N*-hydroxy-succinimide
OCP	Open circuit potencial
PBS	Phosphate buffered saline
PCI	Percutaneous coronary intervention
PDP	Potentiodynamic polarization
PEO	Plasma electrolytic oxidation
PFA	Paraformaldehyde
PGA	Poly(glycolic acid)
PI	Propidium iodide
PLA	Poly(lactic acid)
PLGA	Poly(lactic-co-glycolic acid)
PP	Plasma polymerization
R	Resistance
RDA	Recommended dietary allowance
ROS	Reactive oxygen species
RP-HPLC	Reversed-phase high-performance liquid chromatography
SC	Spin coating
SCA	Static contact angle
SCE	Saturated calomel electrode
SD	Standard deviation
SEM	Scanning electron microscopy
SMC	Smooth muscle cell
SOD	Superoxide dismutase
SPD	Severe plastic deformation
SSI	Surgical site infection
U-2 OS	Bone osteosarcoma epithelial cells
UFG	Ultrafine-grained
UTI	Urinary tract infection
UTS	Ultimate tensile strength
VEGF	Vascular endothelial growth factor
W	Warburg impedance
XPS	X-ray photoelectron spectroscopy
XRD	X-ray diffractometry
YS	Yield strength
β-TCP	β-tricalcium phosphate
ε-CL	ε-caprolactone
ρ	Density

AMINO ACIDS

Name	3 letter code	1 letter code
Arginine	Arg	R
Aspartic acid	Asp	D
Glutamic acid	Glu	E
Glycine	Gly	G
Serine	Ser	S
Tyrosine	Tyr	Y
Valine	Val	V

Outline of the Thesis

This PhD Thesis investigates the potential use of Zn-based materials for biomedical implants, focused on the compromise among mechanical performance, degradation behaviour, and biocompatibility. The applications considered are bioresorbable cardiovascular stents and antibacterial applications in implantology. To this end, the manuscript is divided into different sections, as indicated in **Fig. 1.**

The **Introduction** reviews the current status of bioresorbable metallic implants, including biomedical applications of biodegradable metals and microstructural and surface modifications. A thorough description of the corrosion mechanisms, the existing bioresorbable metals, and the techniques to control degradation and promote biointegration are included. Specifically, this section focuses on the prospect of Zn alloys as bioresorbable implants and the possible approaches to managing the galvanic corrosion problems of Zn-based alloys through surface coatings or metal forming processing. Finally, potential biomedical applications of biodegradable materials, such as cardiovascular and antibacterial applications (i.e., ureteral stents or wound closure devices), are presented.

The results and main findings of the Thesis are divided into two main domains: **Part I** explores different binary Zn alloys for stenting applications, and **Part II** proposes two strategies for overcoming the galvanic corrosion of Zn alloys.

Concerning Part I, **Chapter I** characterizes Zn-Mg and Zn-Cu alloys as potential candidates for bioresorbable cardiovascular stents. At the same time, **Chapter II** focuses on Zn-Ag alloys for bioresorbable ureteral stents. The results demonstrated the direct correlation between the percentage of alloying content in the alloy formulation and the final mechanical properties and galvanic corrosion mechanisms. Moreover, the resulting fast surface degradation avoids *in vitro* cell adhesion and increased bacterial attachment to the degradation products.

Therefore, Part II demonstrates different structural and surface strategies to overcome galvanic corrosion and control the degradation rate. Thus, **Chapter III** introduces a dual-action coating consisting of a PCL layer that protects the metal from early degradation and functionalization with RGD, REDV, and RGD-REDV platform peptides to promote endothelial adhesion. On the other hand, **Chapter IV** presents ECAP as a potential processing route to homogenize the mechanical and degradation properties of Zn-Ag alloys, meanwhile improving their bacterial activity.

The **Concluding remarks** summarize the principal results of each chapter and relate their conclusions to discuss future perspectives on the field. Finally, the **Outcomes of the Thesis** are included.

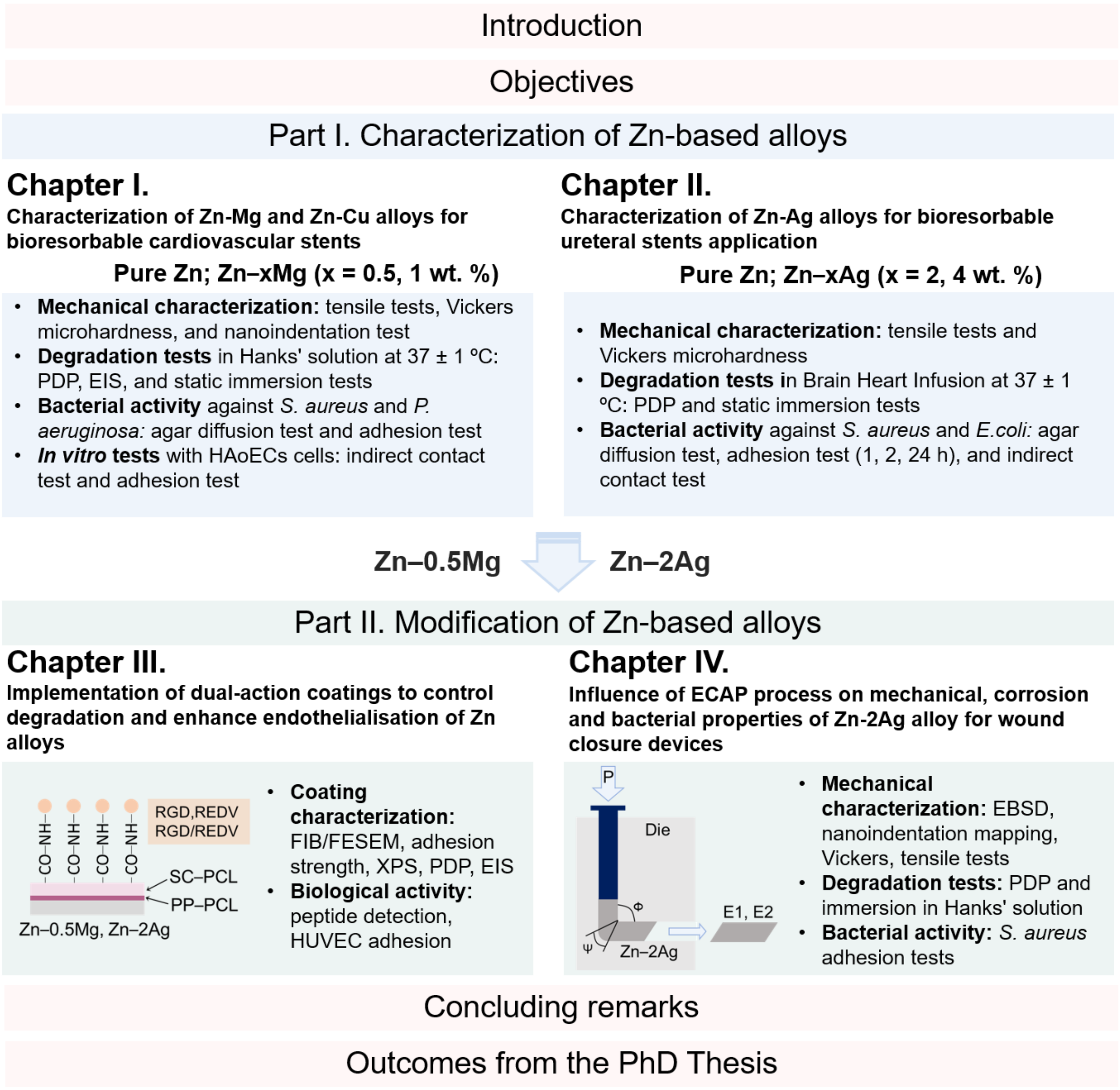

Introduction

Objectives

Part I. Characterization of Zn-based alloys

Chapter I.

Characterization of Zn-Mg and Zn-Cu alloys for bioresorbable cardiovascular stents

Pure Zn; Zn–xMg (x = 0.5, 1 wt. %)

- **Mechanical characterization:** tensile tests, Vickers microhardness, and nanoindentation test
- **Degradation tests** in Hanks' solution at 37 ± 1 °C: PDP, EIS, and static immersion tests
- **Bacterial activity** against *S. aureus* and *P. aeruginosa:* agar diffusion test and adhesion test
- ***In vitro* tests** with HAoECs cells: indirect contact test and adhesion test

Chapter II.

Characterization of Zn-Ag alloys for bioresorbable ureteral stents application

Pure Zn; Zn–xAg (x = 2, 4 wt. %)

- **Mechanical characterization:** tensile tests and Vickers microhardness
- **Degradation tests i**n Brain Heart Infusion at 37 ± 1 °C: PDP and static immersion tests
- **Bacterial activity** against *S. aureus* and *E.coli:* agar diffusion test, adhesion test (1, 2, 24 h), and indirect contact test

Zn–0.5Mg **Zn–2Ag**

Part II. Modification of Zn-based alloys

Chapter III.

Implementation of dual-action coatings to control degradation and enhance endothelialisation of Zn alloys

- **Coating characterization:** FIB/FESEM, adhesion strength, XPS, PDP, EIS
- **Biological activity:** peptide detection, HUVEC adhesion

Chapter IV.

Influence of ECAP process on mechanical, corrosion and bacterial properties of Zn-2Ag alloy for wound closure devices

- **Mechanical characterization:** EBSD, nanoindentation mapping, Vickers, tensile tests
- **Degradation tests:** PDP and immersion in Hanks' solution
- **Bacterial activity:** *S. aureus* adhesion tests

Concluding remarks

Outcomes from the PhD Thesis

Fig. 1. Scheme representation of the outline of the PhD Thesis.

Introduction

I. Bioresorbable implants

Significant advances in medicine, materials science, and engineering have enabled the possibility of developing and introducing biosynthetic materials into the human body. The global implant market exceeds €100.000 million, and it is expected to increase an 8.6 % by 2023 [1].

Implants have traditionally been subjected to strict requirements of non-reactiveness. However, this inertia condition has drawbacks in specific applications, i.e., removal of screws, pins, or sutures for bone fixation, late-stent thrombosis of cardiovascular stents, or implants for paediatric applications in which the inert implant cannot adapt to the patient growing [2]. In the 1980s, a new generation of bioresorbable implants arose to overcome the previous drawbacks. The idea was to have a non-permanent implant that degrades after the tissue healing and to take advantage of the interactions between the implanted material and the surrounding tissue in which the released material could stimulate tissue recovering [3]. **Table 1** summarizes the key differences between permanent and bioresorbable implants.

Table 1. Main characteristics of permanent and bioresorbable implants.

	Permanent implants	**Bioresorbable implants**
Mechanical properties	Stable over time	Degraded with time, and should match the tissue recovery process
Release of material	Unwanted, try to avoid	The released material should be accepted by the host locally and all over the body
Interaction with surroundings	Bioinert	Bioactive

The degradation condition of the bioresorbable materials changes the traditional understanding of implants. Wound healing is a dynamic process in which different stages occur until the complete recovery of the tissue. Therefore, the biological needs may vary over time. On the other hand, the properties of a bioresorbable material will fluctuate within its degradation. Thus, an ideal biodegradable implant should be able to fit all the necessities demanded by the surrounding tissue until its total remodelling and disappear after accomplishing its function.

II. Current state of the bioresorbable implants market

The global bioresorbable implants market is predicted to grow at a CAGR (compound annual growth rate) of 10.5 % from 2022 to 2030 [4]. This growth would happen due to the increasing demand for minimally invasive surgeries, the rising incidence of chronic diseases such as heart disease or stroke, and the technological advancements in bioresorbable implant investigations. Several ceramics, polymers, and metals work as bioresorbable materials in different biomedical applications. **Table 2** lists some examples of the bioresorbable materials now used in the biomedical market.

Table 2. Bioresorbable materials currently used in the biomedical market and their function in the intended biomedical application.

Bioresorbable material	**Biomedical application**
Hydroxyapatite (HA)	Fill small bone defects after bone tumor resection or after a bone loss in fresh fractures [5]
β-tricalcium phosphate (β-TCP)	Bone void fillers in orthopedic and dental applications [6]
Bio-glass	Filling bone defects alone or combined with autografts and allografts [7,8]
Poly(glycolic acid) (PGA)	Resorbable sutures (Dexon™, American Cyanamid Co), scaffolds in tissue engineering [9]
Poly(lactic acid) (PLA)	Suture materials (Vicryl™, Ethicon Inc), drug delivery systems [10]
Mg alloys	Resorbable stent (Magmaris™, Biotronik), bone screw (MAGNEZIX™, Syntelix), bone flaps [11].

The ceramic-based materials are mainly based on calcium phosphate derivates and they are successfully used in bone-related applications due to their ability to mimic the natural bone tissue [5–8]. The use of bioresorbable polymers such as poly(glycolic acid) (PGA), poly(lactic acid) (PLA), and their copolymers is limited to soft tissue and non-load-bearing applications due to their limited mechanical properties. However, their good biocompatibility and exceptional tuneability allow them to be used as wound closure devices, protecting coatings, or drug-delivery systems [9,12,13]. Finally, the current metallic bioresorbable implants are Mg-based and used in cardiovascular or orthopaedic applications due to their superior mechanical strength and ductility compared with their polymeric or ceramic counterparts [14].

III. Potential applications of bioresorbable metals

Bioresorbable metals would be indicated for load-bearing applications in which the bioresorbable ceramics or polymers are limited due to their fragility or insufficient mechanical strength, including cardiovascular or ureteral stents, screws for bone fixation, or metallic scaffolds for bone tissue regeneration [14–18].

III.1. Bioresorbable cardiovascular stents

According to the World Health Organization (WHO), the two principal leading causes of death in 2019 are ischaemic heart disease and stroke, associated with cardiovascular diseases and gathering 27 % of global deaths [19]. Atherosclerosis is the dominant cause of cardiovascular diseases. Atherosclerosis is an immunoinflammatory condition elicited by the deposition of lipids in the artery wall. This accumulation can lead to an atherosclerotic plaque reducing the blood flow within the vessel. The resulting narrowing of the artery is known as stenosis and might culminate in myocardial infarction and stroke [20].

The current treatment for atherosclerosis consists of an angioplasty followed by the insertion of a stent. **Fig. 1** summarizes the angioplasty intervention and the implantation of the stent. First, the stent is crimped onto a balloon-tipped catheter and driven through the artery until the obstructed area (**Fig. 1a**). Secondly, the balloon is inflated, and the atherosclerotic plaque gets compressed, restoring the natural blood flow (**Fig. 1b**). Finally, the catheter and the balloon are removed, and the expanded stent remains in the artery to prevent the vessel recoil (**Fig. 1c**).

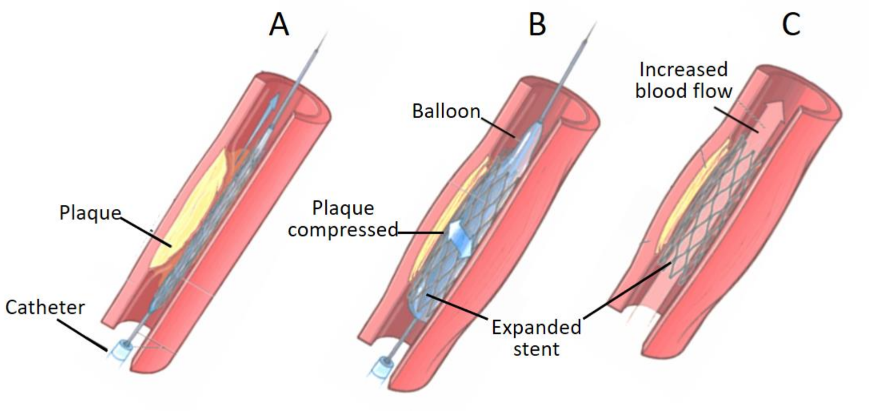

Fig. 1. Angioplasty with stent implantation. (A) Introduction of the balloon and the stent. (B) Inflation of the balloon, expansion of the stent, and compression of the atherosclerotic plaque. (C) The stent remains expanded after the removal of the balloon. Adapted from [21].

The first generation of bare metal stents (BMS) was made of SS, cobalt-chromium (CoCr) alloys, or nitinol and provided the required radial support to the artery. Nevertheless, the stent implantation is highly aggressive and damages the inner endothelial monolayer, stimulating the proliferation and migration of the smooth muscle cells (SMCs) to the lumen. Thus, six months after implantation, intra-stent restenosis (ISR) occurred in 20 – 30% of the cases. Antiproliferative drugs, such as *everolimus* or *paclitaxel*, were implemented in the drug-eluting stents (DES) to reduce ISR [22]. However, their non-specificity also inhibited the proliferation of endothelial cells (ECs), delaying the re-endothelialisation. A healthy endothelium inhibits stenosis and thrombosis; thus, without its recovery, the long-term exposure of the stent to the blood flow led to late stent thrombosis (LST), subjecting patients to antiplatelet therapies for several years after the intervention [23,24]. A new generation of bioresorbable stents (BRS) arose to overcome the long-term drawbacks of conventional inert stents.

BRS should be expandable, prevent vessel recoil, induce re-endothelialisation, and avoid thrombosis. A yield strength (YS) of 200 MPa is desirable for the stent crimping and expansion and would avoid vessel recoil [25]. Ultimate tensile strength (UTS) higher than 300 MPa and elongation at fracture of 15 – 18 % enhance the fatigue resistance and the stent fracture toughness [26].

As indicated in **Fig. 2**, an ideal BRS should maintain its mechanical integrity during the first six months after its implantation and degrade completely after one year. Therefore, the optimal degradation rate value is established as 0.020 mm/yr [25].

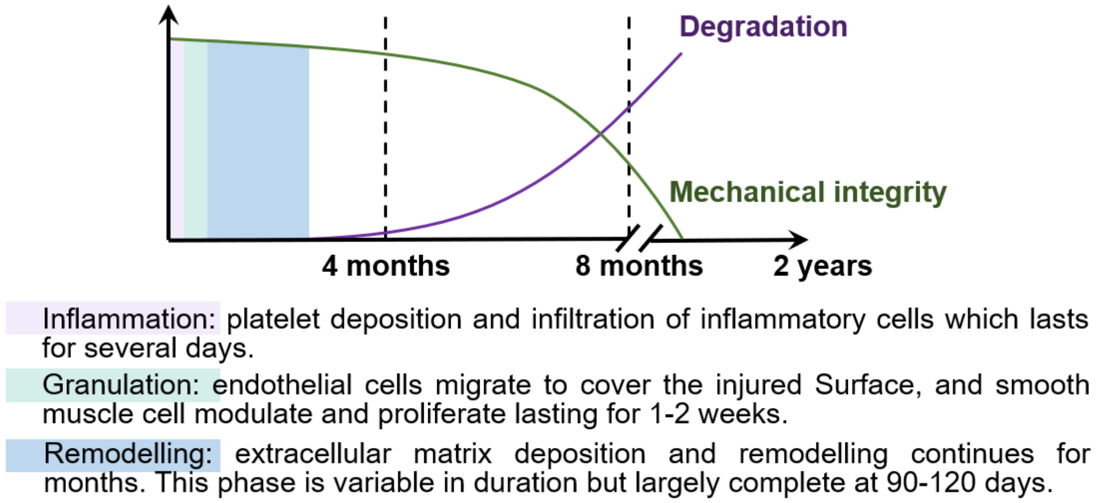

Inflammation: platelet deposition and infiltration of inflammatory cells which lasts for several days.

Granulation: endothelial cells migrate to cover the injured Surface, and smooth muscle cell modulate and proliferate lasting for 1-2 weeks.

Remodelling: extracellular matrix deposition and remodelling continues for months. This phase is variable in duration but largely complete at 90-120 days.

Fig. 2. Expected variation on the mechanical integrity and degradation of an ideal BRS through the vascular healing process. Adapted from [3].

Commercial biodegradable polymeric stents based on a poly(l-lactic acid) (PLLA) scaffold, such as Absorb® stent (Abbott Vascular), received CE approval. Nevertheless, the insufficient mechanical strength of PLLA (UTS: 60-70 MPa; elongation: 2-6 %) requires twice the strut thickness than current metallic stents [2]. Having thicker struts can result in more flow disturbance, potentially increasing the incidence of acute thrombotic events. Moreover, the lack of radiopacity complicates angioplasty [27]. Biotronik launched the AMS stent, which consisted of a Mg-based scaffold. Following generations of Biotronik stents, DREAMS and DREAMS-2G (Magmaris®) include polymeric coatings and antiproliferative drugs [28]. Mg is reported to have three times higher radial strength than PLLA hence allowing the Magmaris® stent to have thinner struts than the Absorb® [29], reducing the risk of late thrombotic events [28].

III.2. Bioresorbable antibacterial implants

In the last years, the scientific community has been communicating the severe complications of the misuse or abuse of antibiotics. The overuse of antibiotics caused 4.95 million deaths in 2019 [30]. The six leading pathogens with 1.27 million deaths were: *Escherichia coli (E. coli), Staphylococcus aureus (S. aureus), K pneumoniae, S pneumoniae, Acinetobacter baumannii*, and *Pseudomonas aeruginosa (P. aeruginosa)*, by order of the number of deaths [30].

Surgical site infections (SSI) are the most common infections worldwide among hospitalized patients, occurring in 2 – 20 % of the surgeries [31]. SSIs are handled with antibiotics and surgical interventions depending on the underlying pathology. Despite their biocompatibility, the widespread use of biomaterials as implants is threatened by the risk of associated infections and the drug resistance developed by bacteria [30]. **Fig. 3** illustrates the general steps of the bacterial infection of an implant. The window of opportunity for fighting the infection is previous to the biofilm formation. Therefore, the ideal implant should exert its antibacterial effect at the first stages of bacterial adhesion.

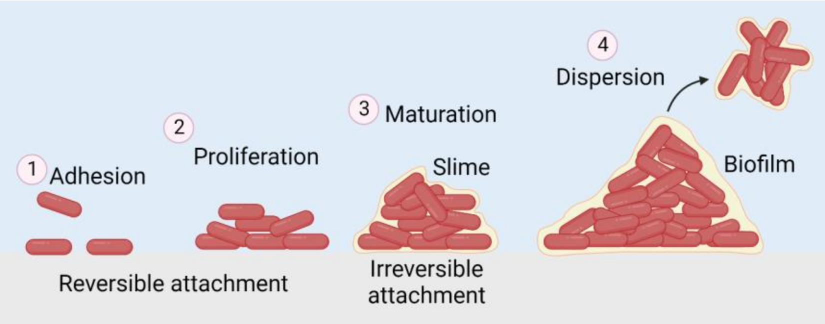

Fig. 3. Schematic representation of the bacterial colonization of an implant starting from individual bacterial adhesion across expansion towards the formation and maturation of biofilm. Adapted from [32].

Fig. 4 shows the different antibacterial strategies currently used in implantology to fight bacterial colonization [33]. Biodegradable metals form a natural passivation layer when immersed in a physiological media [34]. The dynamism of their surface is thought to avoid bacterial adhesion by providing a non-stable surface to which bacteria could barely attach [35]. Besides, the oxidation and reduction reactions involved in the degradation release metallic ions into the medium [36].

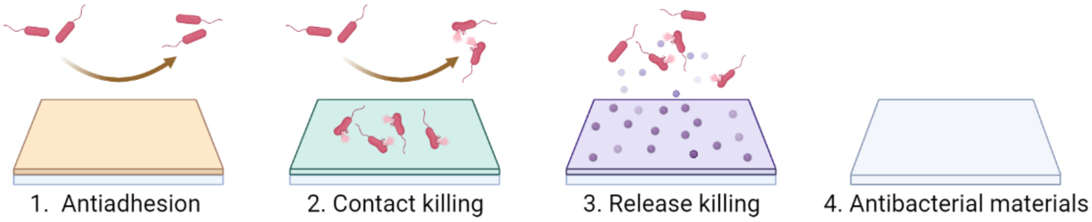

Fig. 4. Schematic illustration of the antibacterial strategies of biomaterials. 1. Antiadhesive surfaces use different topographies and coatings to avoid bacterial adhesion. 2. Adhered bacteria are killed when entering in contact with the biomaterial surface (e.g. biofunctionalization of surfaces, photoinduced coatings). 3. The biomaterial is loaded with antibacterial agents as ions or drugs. 4. The intrinsic composition of the material provides the implant with antibacterial properties. Adapted from [33].

It has been demonstrated that metallic ions can exert an antibacterial effect by disrupting bacterial membranes and affecting their essential functions [37,38]. Moreover, these antibacterial agents introduced as alloying elements in the biomaterial would confer intrinsic antibacterial properties to the implant [39]. Therefore, bioresorbable metallic implants might exert an efficient antibacterial effect based on contact killing, release killing, and acting as intrinsic antibacterial materials.

Bioresorbable metals would be potential candidates for ureteral stents or wound closure devices by combining superior mechanical properties, continuous degradation, and antibacterial potential.

III.2.1. Bioresorbable ureteral stents

Ureteral stents are implanted to restore the natural urine flow after total or partial obstruction of the urinary system. As indicated in **Fig. 5a**, the stent starts at the kidney and drains the urine into the bladder [40]. As in cardiovascular stents, the stent should provide adequate radial strength to reopen the ureter [41]. Besides, the formability of the initial material should be high enough to manufacture the double J shape (**Fig. 5b**), designed to avoid the migration of the stent [42]. Other common complications are urinary tract infections (UTIs), encrustations, or stone formation [35], gathering 80 % of the patients. Encrustations occur due to the accumulation of mineral deposits onto the stent surface, which might further lead to stone formation [43]. Besides, the irregularities of the surface after the salty precipitation can be used as anchor points by bacteria, increasing the risk of infections [44]. Bioresorbable ureteral stents would diminish minerals precipitation, bacterial colonization and stone formation.

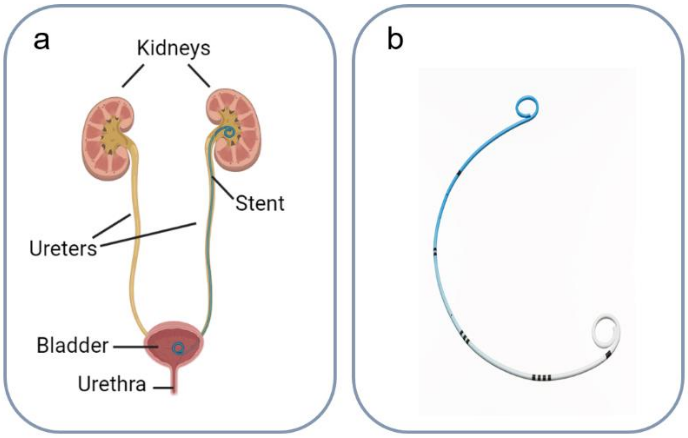

Fig. 5. (a) Schematic representation of the stent colocation in the urinary system. (b) Double J shape of Polaris^{TM} Ultra (Boston Scientific, USA).

Polymeric stents are made from polyurethane or derivates, as the Bardex^{TM} (BD, USA) or the Polaris^{TM} Ultra (Boston Scientific, USA), due to their flexibility and easy handling. However, they failure, in the 58 % of the cases, is due to their low mechanical strength [35]. Their metallic counterparts are based on nitinol (Memokath® 051, PNN© medical) or CoCr (Resonance®, Cook® Medical). Both polymeric and metallic stents present encrustation and bacterial risks. Thus, bioresorbable metals with antibacterial properties may be an appropriate alternative.

III.2.2. Wound closure devices

Wound closure devices are designed to approximate the wound edges until healing. The selected device should distribute the strain along the injury for proper tissue recovery, where excessive tension might lead to inflammation and necrosis [45]. **Table 3** classifies the current bioresorbable and inert materials used for staples and sutures.

Table 3. Current bioresorbable and inert materials used for wound closure devices [49].

Wound closure device	**Device material**	
	Bioresorbable	**Inert**
Staples	Copolymer of PLA and PGA	Ti, SS
Sutures	• Natural: catgut, collagen • Synthetic: PGA, polyglactin, polydioxanone, polytrimethylene carbonate, poliglecaprone, poly-4-hydroxybutyrate	• Natural: silk, cotton, SS • Synthetic: nylon, Dacron, polyester, polypropylene, polybutester, polyethylene

Polymeric materials are widely used in wound closure devices due to their intrinsic elasticity and biocompatibility [46] but they are contraindicated for load-bearing applications such as gastrointestinal anastomosis, due to their lower strength [47]. In this regard, inert staples made from Titanium (Ti) or stainless steel (SS) provide higher tension, but must be removed after the wound closure [48]. Bioresorbable and inert sutures are polymer-based and need multifilament and braided structures to reach the minimum tension to fulfil the suture requirements [13,50]. These complex configurations are prone to bacterial infection due to the easier bacterial adhesion on larger surfaces and the ability of bacteria to infiltrate the filaments' interstices which leukocytes cannot access [51]. For this reason, current polymeric sutures such as Dexon® (Covidien) and Vicryl® (Ethicon, Inc.) are usually loaded with antibiotics such as triclosan or gentamicin [52].

Here, the superior mechanical strength of bioresorbable metals would allow designing less-complex structures, diminishing the risks of bacterial colonization [47].

III.3. General remarks on bioresorbable implants

There are several biomedical applications in which the implant is unnecessary after tissue healing, and its further presence triggers serious complications such as late-stent thrombosis, encrustations, or bacterial infections. In this regard, bioresorbable metals for stents or wound closure devices may open a new opportunity to overcome the shortcomings associated with inert implants. However, their biodegradation must be carefully considered since it might compromise biocompatibility.

IV. Bioresorbable metals for biomedical applications

The biodegradable metals considered for biomedical applications, are iron (Fe), magnesium (Mg), zinc (Zn), and molybdenum (Mo), in order of emergence.

Zheng et al [3] postulated that the definition of a biodegradable metal can be given as follows: '*Biodegradable metals are metals expected to corrode gradually in vivo, with an appropriate host response elicited by released corrosion products, then dissolve completely upon fulfilling the mission to assist with tissue healing with no implant residues. Therefore, the major component of biodegradable metals should be essential metallic elements that can be metabolized by the human body, and demonstrate appropriate degradation rates and modes in the human body'*.

In other words, an ideal biodegradable metal perfectly fulfils three main aspects: (1) enhanced mechanical properties, (2) adequate degradation rate, and (3) excellent biocompatibility (**Fig. 6**). Thus, the implant should (1) provide the needed support for the tissue recovering; (2)

completely degrade after the total wound healing; and (3) the material along with the degradation products should be metabolized or excreted by the human body. The specific criteria for the mechanical properties, the degradation behaviour, or the biological response depend on the final purpose of the material. Regardless of the application, an optimal compromise among the three properties must be accomplished.

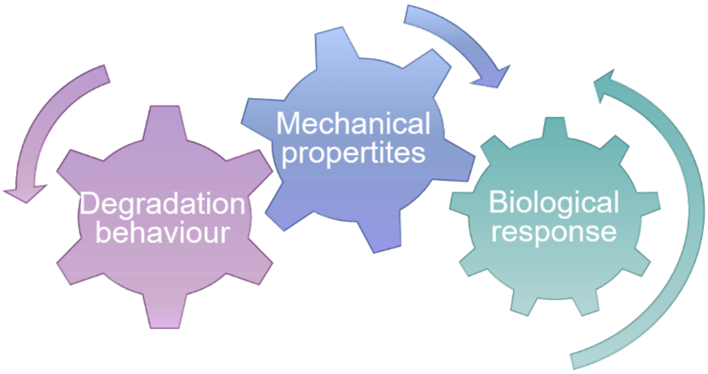

Fig. 6. Scheme of the main three aspects a bioresorbable implant must accomplish.

IV.1. Biodegradation mechanism

Metal biodegradation occurs through reactions in which the corrosion or oxidation of the metal (anodic reaction) reduces the water or oxygen from the physiological solution (cathodic reaction). Equations 1-4 summarize the main corrosion reactions expected for a model metal, M (s) [3]:

$M\ (s) \rightarrow M^{n+} + ne^{-}$ (anodic reaction) (1)

$2H_2O\ (l) + 2e^{-} \rightarrow H_2\ (g) + 2OH^{-}$ (cathodic reaction) (2)

$2H_2O\ (l) + O_2(g) + 4e^{-} \rightarrow 4OH^{-}$ (cathodic reaction) (3)

$M^{n+} + nOH^{-} \rightarrow M(OH)_n\ (s)$ (by-product formation) (4)

The anodic reaction corresponding to the oxidation of Fe, Mg, and Zn is described in Eq. 1. The specific reduction potentials for the previous metals are: $E^o\ (Fe^{2+}/Fe) = -0.41$ V, $E^o\ (Mg^{2+}/Mg) = -2.38$ V, and $E^o\ (Zn^{2+}/Zn) = -0.76$ V. The reduction potential for H_2O (l) and O_2 (g) reduction are 0.00 V and 1.23 V, respectively. According to thermodynamics, the produced electrons reduce the dissolved oxygen to OH^{-} (Eq. 3 for Fe and Zn); or the water to H_2 (g) (Eq. 2 for Mg). Both cathodic reactions are associated to the produced hydroxyl ions favouring the increase of the pH and the precipitation of the corresponding metallic hydroxides (Eq. 4).

This simplified description is far from the conditions expected in physiological fluids, where the presence of inorganic and organic ions and molecules will affect the previously described reactions. The typical composition of such media indicates the presence of inorganic anions such as HCO_3^-, Cl^-, HPO_4^{2-}; cationic species like Ca^{2+}, K^+, and Na^+; organic molecules including glucose, free fatty acids, amino acids and other compounds such as ammonia or urea. The interaction with the inorganic anions is expected to be relevant due to their complexing properties resulting with oxidized forms of the metal and then, participating in the formation of the mineral phases such as metal carbonates, chlorides, or phosphates, which may precipitate due to the local alkalinisation of the media.

The degradation of the metals occurs through the continuous formation and breaking of a corrosion layer. **Fig. 7** illustrates the degradation process of biodegradable metal in a physiological environment.

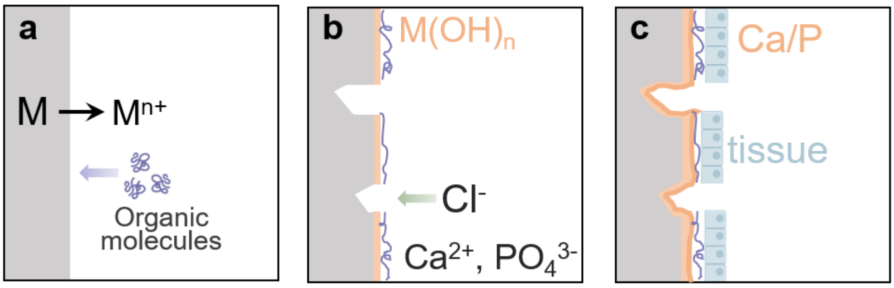

Fig. 7. Schematic diagram of the biodegradation at the metal-medium interface. (a) Dissolution of the metal and adsorption of organic molecules onto the metallic surface. (b) Formation of a passivation layer by the precipitation of salts. Breaking of the layer by the chloride anions. (c) Repassivation of the surface and deposition of Ca/P mineral phases. Adapted from [3].

Immediately after contacting the medium, the metal is oxidized, and the organic molecules from the media adsorb onto the metallic surface (**Fig. 7a**). Afterwards, the metal hydroxides, carbonates, phosphates, or chlorides precipitate over the metallic surface, passivating the metal. Subsequently, the aggressive chloride anions breakdown the passivation layer leading to pitting corrosion (**Fig. 7b**). As the degradation proceeds, Ca/P based mineral phases (e.g., hydroxyapatite, apatite, calcium phosphate) could be deposited onto the surface due to the localized alkalization and the saturation of calcium and phosphate in the body fluid (**Fig. 7c**). Cells might also adhere to the surface and proliferate to form tissues adjacent to the corrosion layer. Besides, irregular particles could detach from the surface into surrounding media [3].

IV.2. Evaluation of bioresorbable metallic implants

Cytotoxicity of biomedical devices is evaluated following Part 5 and Part 12 of ISO 10993 [53,54]. This evaluation must strictly adapt to the standard in which the conditioned medium is analysed after 72 h of immersion with the testing biomaterial [53,54]. In this regard, inert metals may present a slight ion release during the test, and it is compulsory to ensure the biosafety of the possible toxic ions. Likewise, it is required to control the cytotoxicity of inert materials loaded with metallic ions or nanoparticles. On the other hand, bioresorbable polymers such as PLA or PGA degrade by hydrolysis in a maximum period of 2 years [55]. Resulting acidification and autocatalysis accelerate degradation, which is negligible at the first stages of immersion [56]. Thus, polymers preserve their stability at short immersion periods as in the accorded for cytotoxic evaluation, without free polymeric chains released into the surrounding media.

As explained in Section IV.1, bioresorbable metals immediately react with the physiological media forming a passivation layer and releasing ions and by-products to the surroundings. Moreover, the direct influence of the selected solution on their degradation has been reported numerous times [57–59]. For instance, simulated body fluid (SBF) seems to be the adequate medium for *in vitro* biodegradation of Mg [60,61], and the presence of proteins in SBF, such as albumin, significantly affects corrosion [62]. On the other hand, the biocompatibility of bioresorbable metallic implants has been demonstrated. Several *in vivo* tests on Mg-based implants have confirmed their biocompatibility and biosafety [63–66]. *In vivo* studies on Zn-based materials have also been reported showing no tissue inflammation and proper integration of the tested implants [67,68]. However, the current ISO 10993 standard for evaluating *in vitro* cytotoxicity was designed without allowance of released ions from the implant through the body, as is the case with biodegradable metals. Therefore, the bioresorbable metals are subjected to high-quality standards of non-reactiveness that do not suit them, producing huge discrepancies between the *in vitro* and the *in vivo* performance of the implants.

Wang *et al.* suggested modifying the current ISO standards since the *in vitro* results do not correlate with *in vivo* outcomes for biodegradable metals [69]. The inconsistencies between *in vivo* and *in vitro* performance demonstrate the need for further understanding to obtain physiological relevant results from *in vitro* measurements [70]. In this regard, Working Group 13 within ISO TC 150 is designing new standards for bioresorbable metals. Meanwhile, the characterization of biodegradable metals must follow conventional standards used for inert materials until the specific regulations are approved.

Apart from biocompatibility, mechanical strength and corrosion rate are usually evaluated as follows. The mechanical properties of the bioresorbable metals are assessed by tensile tests (ASTM E8/E8M [71]) and Vickers hardness measurements. The corrosion rate is calculated from potentiodynamic polarization (PDP) tests (ASTM G5-14 [72]) and static immersion tests (ASTM G31-72 [73]) in physiological conditions. **Table 4** reviews the values obtained for the UTS, YS, elongation at fracture, elastic modulus, and corrosion rate of current bioresorbable metallic materials for biomedical applications.

Table 4. Key properties of potential bioresorbable metals for biomedical applications [3,74,75].

Tested property	Fe alloys	Mg alloys	Zn alloys	Mo
UTS (MPa)	200 – 1550	86 – 550	150 – 386	620 – 868
YS (MPa)	150 – 1100	20 – 247	<150 – 296	515 – 673
Elongation (%)	0.5 – 48	2 – 30	1 – 20.5	35
Elastic modulus (GPa)	54 – 210	41 – 45	94 – 110	324
Corrosion rate (mm/year)	0.001 – 1.86	<0.23 – 10	0.02 – 0.1	0.006 – 0.013

The following sections critically review the state of the art of mechanical, corrosion, and biological properties of bioresorbable metals.

IV.3. Iron (Fe)

As a constituent of haemoglobin, myoglobin, and enzymes, Fe is an essential trace element for the human body. The recommended dietary allowance (RDA) is approximately 20 mg/day for adults (gender-specific). Fe plays a fundamental role in haemoglobin synthesis, oxidation-reduction reactions, and cellular proliferation. The excessive accumulation of Fe ions induces organ dysfunction by producing reactive oxygen species (ROS) [76].

Fe was selected as a potential biodegradable material for stents due to its suitable mechanical properties, close to those of SS 316L. Armco® launched the first Fe stent (Fe > 99.8%) in 2011 and implanted it in descending aorta of New Zealand white rabbits. The stent successfully maintained its integrity without significant changes in its mechanical properties during the first six months, but its overall degradation was too slow. Alloying, thermodynamic treatment, or microstructure modification are the principal strategies to accelerate the degradation rate of Fe [26]. Other *in vivo* approaches also evidenced the heterogeneous degradation behaviour of Fe and the presence of pitting at its surface. Moreover, the corrosion products accumulated over nine months and were retained in the arterial wall as voluminous flakes that threatened their integrity [77]. In the end, no Fe-based biodegradable implant has received any CE mark or FDA approval.

IV.4. Magnesium (Mg)

As a coenzyme, Mg participates in more than 300 enzymatic reactions. The RDA for Mg is about 500 mg/day [27]. The elastic modulus is closer to the natural bone, reducing stress shielding [17]. Its degradation promotes osteosynthesis and osseointegration [78]. MAGNEZIX® (Syntellix AG, Germany) implant is a Mg-based screw that received CE approval. Besides, its high UTS and YS values reach the criteria to be used as cardiovascular stents (**Table 4**). Magmaris® stent (BIOTRONIK, Germany) received CE approval and has passed clinical trials [79]. It consists of a Mg-based scaffold with a PLA coating loaded with *everolimus*. However, its early degradation reduces the radial strength of the stent after a short period of implantation. and results in the total dissolution of the implant in the third month of implantation. Besides, the release of hydrogen gas resulted from its degradation may cause cytotoxicity and implant rejection [80]. Therefore, the control of its degradation together with its mechanical properties with time is under extensive research. Different alloying strategies and surface treatments have been tested to slow down its degradation rate and reduce hydrogen production [81–84].

IV.5. Zinc (Zn)

Zn is an essential trace element in the human body. It interacts with more than 300 enzymes and proteins. The RDA for Zn is 11 mg/day for men and 8 mg/day for women. Lower Zn intake is recommended for infants (2-3 mg/day) and children (5-9 mg/day), and the lethal median dose (LD_{50}) is 27 mg/day [85].

In 2011, Vojtech *et al*. suggested Zn as a potential bioresorbable material for bone fixation with a suitable degradation rate between Fe and Mg [86]. Afterward, Bowen *et al.* [87] performed the first *in vivo* assay, in which pure Zn wires were implanted in the abdominal aorta of Sprague-Dawley rats for 1.5, 3, 4.5, and 6 months. Zn wires remained mechanically stable for four months, and homogeneously degraded after. The compact corrosion layer of ZnO(s), $ZnCO_3$(s) and Ca/P were similar to the observed for Mg, with no tissue necrosis or repulsion adjacent to the implant. Yang *et al.* [88] implanted pure Zn stents in the rabbit abdominal aorta up to 12 months. The presence of neointimal coverage in the first month after implantation indicated rapid endothelialization. No neointimal hyperplasia or platelet adhesion was reported throughout the experiment. Drelich *et al.* [89] implanted Zn wires in the murine artery for 20 months, observing no thrombotic events or obstructions. It was reported the presence of a thick corrosion layer and encapsulation of the implants, which may be beneficial to the biointegration of the stents.

Nevertheless, the lower mechanical properties of Zn require strengthening strategies to accomplish the requirements of the final biomedical application. Different fabrication methods and thermomechanical treatments have been investigated to enhance the mechanical performance of Zn alloys [90]. A review of the alloying elements introduced for Zn strengthening is provided in Section V.

IV.6. Molybdenum (Mo)

In 2020, Redlich *et al.* [75] presented Mo as a novel biodegradable metal with superior strength and good formability. The reported corrosion rates are 0.006 – 0.013 mm/year between Fe and Zn (**Table 4**). Later, they reported good *in vitro* performance when testing with ECs and SMCs without cell apoptosis or tissue necrosis. Moreover, no activation of thrombocytes was reported indicating a low thrombogenicity [91]. Thus, the first results are promising but further investigation is needed to support Mo as a candidate for biomedical applications.

IV.7. General remarks on bioresorbable metals

Bioresorbable metals react when entering into contact with a physiological medium, releasing ions, degradation by-products, and quickly changing the local pH. Thus, their degradation usually does not accomplish the strict non-reactiveness standards currently mandatory for medical devices. Nevertheless, the scientific community is making outstanding efforts to design new standards and to demonstrate their biosafety. In this regard, Mg is the leading metal, with Mg-based implants passing clinical trials. Even though Fe perfectly accomplishes the mechanical requirements for implants, its degradation might be inadequate for biomedical applications. In the last years, Zn and its alloys have been attracting increasing interest due to their suitable corrosion rate, and Mo has been presented as a potential candidate for bioresorbable implants.

V. Zn alloys

Bioresorbable implants should have adequate degradation behaviour, biocompatibility, and mechanical performance. Despite fulfilling the degradation and biocompatibility criteria, the mechanical properties of pure Zn are insufficient for biomedical applications. Alloying Zn is a good strategy for mechanical reinforcement *via* solid solution hardening or precipitation hardening [90]. Nevertheless, alloying can also have detrimental effects on its biocompatibility. Therefore, body essential elements or body essential trace elements must be selected as the first option. Other elements that are not essential to the body must be carefully included in the composition, limiting the alloying to low concentrations to ensure the biosafety of the implant. **Table 5** lists some Zn alloying elements and their general effect on the mechanical and corrosion properties.

Table 5. Summary of the effect of the most common alloying elements on the mechanical and corrosion properties of Zn. [3,85,92,93].

Element	Blood serum level (mg/L)	Effect on Zn
ESSENTIAL ELEMENT		
Mg	17.7-25.8	↑ mechanical properties; ↑ corrosion rate [94]
Ca	36.8-39.8	↑ mechanical properties; ↑ corrosion rate [94]
Fe	5000-17600	↑ corrosion rate by galvanic corrosion mechanism [95]
ESSENTIAL TRACE ELEMENT		
Zn	0.8-1.14	-
Cu	4.51-8.32	↑ mechanical properties; ↑ corrosion rate [96,97]
Mn	<0.0008	↑ susceptibility of galvanic micro-cell corrosion [98]
OTHER ELEMENTS		
Sr	0.17 mg (total concentration)	↑ mechanical properties; ↑corrosion rate [94]
Li	0.002-0.004	↑ UTS, ↓ ductility; ↓ corrosion rate [99]
Al	0.0021-0.0048	↑ mechanical properties; ↑ corrosion rates [100]

As it is logical, the main effort of strengthening Zn has been performed by alloying it with Fe or Mg due to its biodegradability. The Zn-Mg alloys have been widely considered for cardiovascular and orthopaedic applications, whereas Zn-Fe alloys are degraded by extensive galvanic corrosion [101]. Since they are assumed to stimulate bone regeneration, calcium (Ca) and strontium (Sr) have been considered alloying elements for orthopaedics [102]. Lithium (Li) and aluminium (Al) enhance the mechanical properties of Zn, but their potential toxicity limits the alloying to low-weight percent alloys [99,100].

V.1. Zn-Mg alloy system

According to the Zn-Mg phase diagram in **Fig. 8,** the solid solubility of Mg in Zn is around 0.15 wt.% at the eutectic temperature (364 ºC). Thus, a low concentration of Mg alloying produces the precipitation of the Zn+Mg_2Zn_{11} secondary phase along the grain boundaries of the primary α-Zn grains [103]. The Zn+Mg_2Zn_{11} provides a hardening effect through dispersion strengthening [104]. However, the eutectic phase decreases the Zn ductility and then, it is suggested to work in Zn-Mg alloys with a content under 1.2 wt.% of Mg [105].

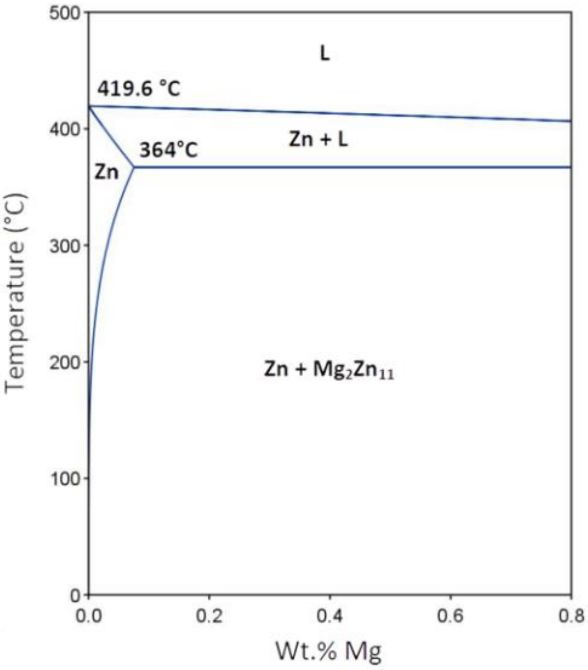

Fig. 8. Zn-Mg equilibrium phase diagram [106].

Mostaed *et al.* [107] evaluated Zn-xMg (x = 0.15, 0.5, 1 wt.%) for cardiovascular stents. As indicated in **Table 6**, Zn-Mg alloys exhibited enhanced YS and UTS compared with the unalloyed Zn, reducing elongation at fracture values. Besides, the corrosion potential and the current density changed from –0.99 mV and 8.98 $\mu A/cm^2$ of pure Zn to –1.05 mV and 11.32 $\mu A/cm^2$of Zn-1Mg alloy, suggesting that higher Mg content led to a lower corrosion resistance.

Kubasek *et al.* [109] characterized Zn-xMg alloys (x = 0.8, 1.6 wt.% Mg) for bone fixation, obtaining similar results where the increase of UTS and YS occurred in parallel with a decrease in elongation. Moreover, both studies reported higher corrosion rate values for Zn-Mg alloys compared with the unalloyed Zn, attributed to the formation of galvanic pairs between the Zn matrix and the Zn+Mg_2Zn_{11} eutectic phase and the consequent activation of galvanic corrosion mechanisms in the sample.

Table 6. Mechanical properties of Zn-Mg [107], Zn-Cu [97], and Zn-Ag [108] alloys.

Sample	YS (MPa)	UTS (MPa)	Elongation (%)
Zn-Mg system			
Zn	51 ± 3.8	111 ± 4.5	60 ± 5.9
Zn-0.15Mg	114 ± 7.7	250 ± 9.2	22 ± 4.0
Zn-0.5	159 ± 8.5	297 ± 6.5	13 ± 0.9
Zn-1Mg	180 ± 7.3	340 ± 15.6	6 ± 1.1
Zn-Cu system			
Zn	45 ± 3.5	61 ± 3.7	3.8 ± 0.8
Zn-1Cu	148.7 ± 0.5	186.3 ± 0.5	21.0 ± 4.4
Zn-2Cu	199.7 ± 4.2	240.0 ± 1.4	46.8 ± 1.4
Zn-3Cu	213.7 ± 1.2	257.0 ± 0.8	47.2 ± 1.0
Zn-4Cu	227.0 ± 5.0	270.7 ± 0.5	50.6 ± 2.8
Zn-Ag system			
Zn	55	111	63
Zn-2.5Ag	147	203	35
Zn-5Ag	208	250	37
Zn-7Ag	236	287	32

Finally, the maximum safe Zn^{2+} concentration for non-toxicity of bone osteosarcoma epithelial cells (U-2 OS) and L929 fibroblast cells was 120 µM and 80 µM, respectively [109]. Therefore, the ideal alloying wt.% of Mg would enhance mechanical strength while preserving adequate ductility and controlling corrosion rate to avoid abrupt Zn^{2+} release.

V.2. Zn-Cu alloy system

Copper (Cu) is an essential trace element that stimulates angiogenesis and endothelialisation [110–112]. Moreover, the antibacterial activity of Cu^{2+} cation might reduce the risk of infection during and after a surgical infection [113,114]. Thus far, only a few studies about Zn-Cu as a bioresorbable biomaterial have been published.

Tang *et al.* [97] investigated Zn-xCu (x = 1, 2, 3, and 4 wt. %) for cardiovascular applications. The mechanical reinforcement by Cu alloying was lower than the provided by Mg with the same alloy content. Nevertheless, increased values of UTS and YS were also reported for all the Zn-Cu compositions (**Table 6**). Furthermore, the increasing Cu alloying led to exceptional elongation at fracture values.

The Zn-Cu phase diagram in **Fig. 9** shows a peritectic reaction of Zn + L → ε-$CuZn_5$ at 425 ºC when the concentration of Cu is higher than 1.53 wt. %. The ε-$CuZn_5$ phase has the same hexagonal close pack (hcp) structure as Zn, associated with compatible deformation, which would explain the excellent elongation obtained after alloying.

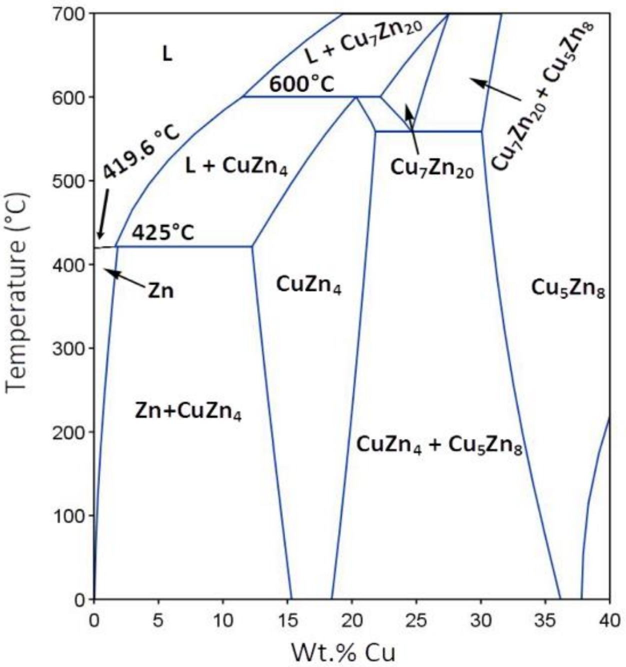

Fig. 9. Zn-Cu equilibrium phase diagram [106].

The calculated corrosion rate after 480 h of immersion in SBF was 22.1 ± 4.7 µm/year for the pure Zn, and 33.0 ± 0.1 µm/year for Zn-Cu alloys [97], suggesting that the presence of Cu contributed to the formation of galvanic pairs with the Zn matrix.

Moreover, the Zn-Cu alloys did not show cytotoxicity to ECs, and the compositions above 2 wt.% Cu exhibited antibacterial activity against *S. aureus.* Qu *et al.* [38] reported the antibacterial activity of Zn-2Cu alloy against MRSA by downregulating the expression of genes related to adhesion, colonization, biofilm formation, and secretion of virulence factors.

Zhou *et al.* [115] implanted a Zn-xCu (x = 0.8 wt.% Cu) stent into porcine coronary arteries for up to two years, demonstrating adequate radial strength during the remodelling and no thrombosis, necrosis, or inflammation at any stage. After 24 months, 28 ± 13 % of the stent remained.

V.3. Zn-Ag alloy system

Silver (Ag) has been introduced in biomaterials as Ag nanoparticles, Ag oxides, or Ag ions due to its excellent antibacterial activity and acceptable biocompatibility [116,117]. Moreover, its high solubility into Zn matrix allows a broad range of Ag concentrations for the alloying without extensive precipitation of Ag-rich phases.

At 431 ºC, a peritectic reaction between a primary solid phase (β-$AgZn_3$) and a liquid phase forms the η-Zn solid phase (Fig. 10). Within its solubility limit (around 2.5 wt.% of Ag), the ε-$AgZn_3$ phase precipitates, where the higher Ag content leads to higher $AgZn_3$ area [106].

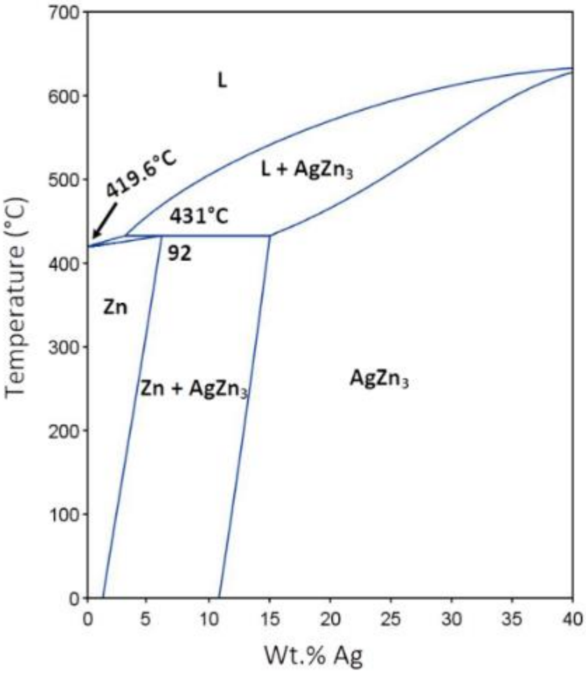

Fig. 10. Zn-Ag equilibrium phase diagram [106].

Sikora-Jasinska *et al.* [108] evaluated Zn-xAg (x = 2.5, 5.0, and 7.0 wt. % Ag) for bioresorbable implants. The characterization showed effective mechanical strengthening by grain refinement and precipitation hardening, where YS and UTS increased with the increasing Ag content (**Table 6**). Moreover, Ag alloying provided better fracture at elongation than Mg, with no significant differences with increasing Ag content. Good formability would avoid recrystallization and grain growth through manufacturing, accelerating processes in milder conditions. Finally, the higher volume fraction of the ε-$AgZn_3$ phase led to more powerful galvanic mechanisms.

Li *et al.* [118] revealed that the released Zn^{2+} ion determined the cytotoxicity of the Zn-4Ag alloy. Thus, the control of its degradation might be fundamental. Moreover, the antibacterial effect against *S. gordonii* bacteria was demonstrated.

V.4. General remarks on Zn-based alloys

Alloying is an effective strategy to reinforce Zn by precipitation hardening. However, the new phases form galvanic pairs with the Zn matrix might accelerate degradation *via* galvanic corrosion mechanisms. Although promising results have been reported, galvanic corrosion must be controlled since its further development could produce material cracking and implant failure. Moreover, the accelerated degradation increases the local Zn^{2+} release, which might lead to local cytotoxicity. Thus, current investigations are focused on controlling alloys corrosion to mimic the natural degradation mechanisms of Zn.

VI. Techniques to control degradation and promote biointegration of Zn-based materials

Different surface treatments have been studied to control the Zn alloys degradation rate and to enhance their biocompatibility (**Fig. 11**). Protective coatings are a solution to delay the degradation until the tissue remodelling finishes and the mechanical integrity is no longer needed. Tissue healing can be also promoted by the immobilization of cell-adhesive molecules onto the surfaces [119]. On the other hand, plastic deformation techniques could break and distribute secondary phases through the Zn matrix, avoiding galvanic corrosion and ameliorating biocompatibility of the alloys. [120].

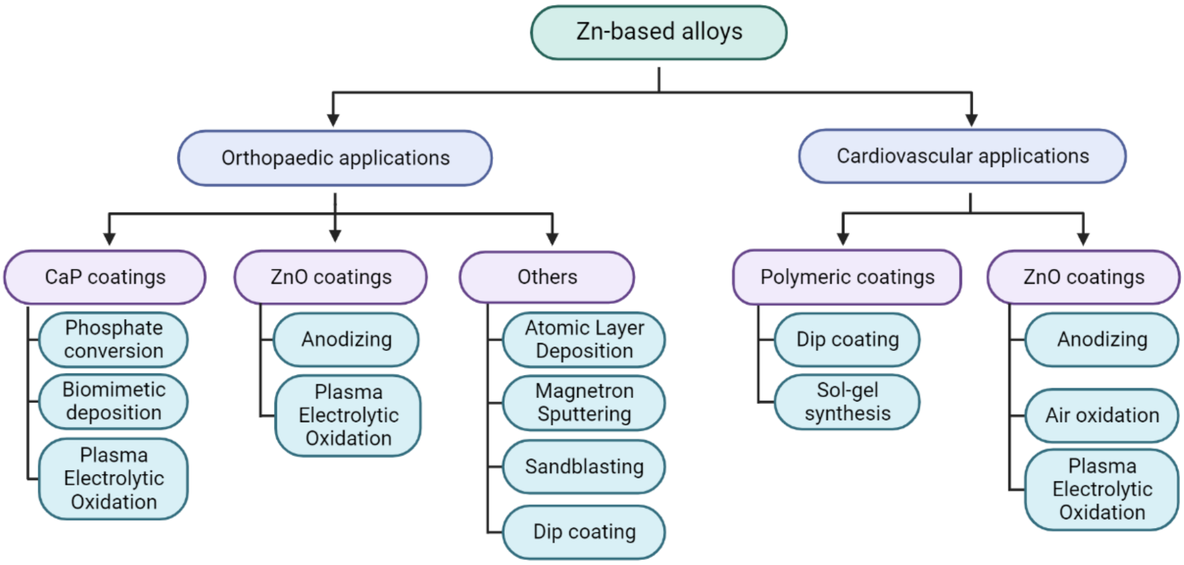

Fig. 11. Scheme of different surface modification methods that can be applied to biodegradable Zn-based alloys to ameliorate biological and corrosion properties for orthopaedic and cardiovascular applications. Adapted from on [121].

VI.1. Protective coatings

Coatings are intended to be an effective physical barrier that protects the underlying metal from the external environment. Protective coatings must have high adhesion, adequate mechanical resistance, flexibility towards substrate deformation, and cannot be susceptible to surface imperfections [81].

Anodizing is a traditional electrolytic process in which a thick and stable oxide layer is formed onto the surface to protect the metal. Anodized coatings delay the early degradation of metals [80]. When it is used in very high voltages, the process is generally known as Plasma Electrolytic Oxidation (PEO) which provides more uniform surface films [122]. Several layers can be obtained by varying parameters such as temperature, electrolyte concentration, current density, and applied voltage. However, the surrounding media may infiltrate the oxide porous layers being counterproductive to corrosion resistance. Therefore, additional coating layers and sealing strategies may be needed for adequate corrosion protection [83]. Drelich *et al.* [123] reported significantly different *in vivo* corrosion behaviour of Zn depending on the structure and thickness of the oxide layer obtained by oxidation, anodization, and electropolishing. The study determined that the corrosion protection is not only related to the layer thickness but also to its uniformity, where defects and porous should be avoided.

Polymeric coatings are attractive for biomedical applications due to their biocompatibility and tunability. The number and thickness of the coating layers would depend on the intended application [81]. Thicker coatings provide higher corrosion protection; however, excessive thickness would decrease the interfacial adhesion and lead to coating delamination in the presence of shear stresses [124]. A successful polymeric coating must adhere to the surface and withstand the usual movements of the implant. Polymeric coatings stand out due to their capacity to be chemically, physically, and mechanically customized for a specific application. Thus, polymeric coatings can combine corrosion protection with improved lubricity, antimicrobial activity, blood compatibility, or drug delivery. PLA, PGA, and polycaprolactone (PCL) are used in several biomedical applications such as soft tissue engineering, drug delivery, or wound closure devices [9,12,125]. They have been reported to provide proper corrosion resistance to Mg-based subtracts [126,127]. Their biodegradability condition is adequate for bioresorbable metallic implants. In fact, a PLA derivate is used in Magmaris® stent (BIOTRONIK, Germany), combining corrosion protection and drug eluting capacities.

VI.2. Surface functionalization

Accelerating the biointegration of the implants might have beneficial effects since the recovered tissue could act as a natural protective layer. For instance, early re-endothelialisation after stent implantation would protect the stent from corrosion or platelet adhesion [128].

Synthetic biomaterials currently used in implantology, including bioresorbable metals, are bioinert. Providing biomaterials with bioactive molecules mimicking the extracellular matrix

(ECM) microenvironment would initiate a determined biological response. Consequently, the surface functionalization with molecules such as proteins [129,130] or growth factors [131] confers the implant with cellular cues to provoke desired cellular responses without modifying the bulk material. Nevertheless, their fast degradability, pH sensitivity, and the high costs associated with their production entail some limitations. Synthetic peptides that include specific regions of ECM proteins have been explored due to their higher stability and tuneability [132,133]. One of the most common peptides used is the RGD (Arg-Gly-Asp) sequence, identified in the ten-type III domain of fibronectin [134], and recognized by $\alpha_5\beta_1$ integrin accelerating cell adhesion. Other cell adhesive peptides enhance the adhesion of specific cells. REDV (Arg-Glu-Asp-Val) motif is located in the Cs5 fibronectin domain and it is recognized by the $\alpha_4\beta_1$ integrin specifically promoting EC adhesion [135]. Other peptides stimulate stem cell differentiation, such as bone morphogenetic 2 (BMP-2) or vascular endothelial growth factor (VEGF) peptides, used in osteogenesis or vasculogenesis, respectively [136–138].

VI.3. Metal forming processing and post-processing

Conventional metal-forming processes such as extrusion, drawing, rolling, and forging have been explored on Zn-based alloys for mechanical reinforcement [90]. These techniques break the as-cast microstructure and activate dislocation slip and twinning. The consequent microstructural refinement also affects the corrosion behaviour of the Zn-based alloys. **Table 7** lists some examples of the mechanical properties and corrosion rates of different Zn-based alloys after conventional metal-forming processes.

Table 7. Mechanical properties and corrosion rate of Zn-Mg [139], Zn-Cu [140], and Zn-Cu-Ti [141] alloys as-cast and after hot extrusion (HE) and hot rolling (HR) processing.

Zn alloy	YS (MPa)	UTS (MPa)	E (%)	CR (mm/yr)
Zn-1Mg, Cast	130 ± 10	180 ± 21	2 ± 0.2	0.28
Zn-1Mg, HE	210 ± 15	265 ± 16	9 ± 1	0.12
Zn-1Cu, Cast	26	33	3.9	0.16
Zn-1Cu, HE	236	291	38.9	0.06
Zn-2Cu, Cast	50	60	3.4	0.13
Zn-2Cu, HE	275	328	48.8	0.13
Zn-1Cu-0.1Ti, Cast	86 ± 3	92 ± 4	1.4 ± 0.8	0.029
Zn-1Cu-0.1Ti, HR	175 ± 4	206 ± 6	39 ± 1.4	0.034

Kabir *et al.* [120] reviewed the different forming processing applied to Zn-based alloys and concluded that extrusion-based techniques provided the most effective mechanical reinforcement and corrosion resistance. The decreasing volume fraction of the secondary phases after extrusion reduced the cathode-to-anode fraction in the alloys, hampering galvanic corrosion mechanisms and homogenising degradation.

After the initial processing technique to obtain metallic bars, post-processing may improve mechanical properties and control degradation. Severe plastic deformation (SPD) techniques introduce extremely high strain during the deformation to produce bulk ultrafine-grained (UFG) structures. The obtained microstructure refinement remarkably modifies mechanical strength and corrosion resistance. There is no extensive investigation of the SPD techniques on Zn-based alloys. Nevertheless, equal angular channel pressing (ECAP) on different alloys have been reported. Bednarczyk *et al.* [142] studied the ECAP effects on the microstructure and mechanical properties of Zn, Zn-Cu, Zn-Ag, and Zn-Mg alloys. All materials after the ECAP process presented equiaxial grains produced by continuous dynamic recrystallization (DRX) (**Fig. 12**).

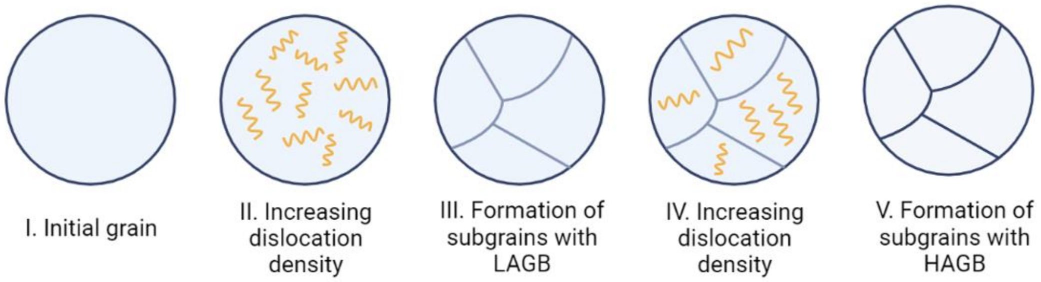

Fig. 12. Scheme of the dynamic recrystallization process. I. Zn grain at the as-cast microstructure. II. The dislocation density inside the Zn grain increases with the strain. III. Dislocations assemble and form sub-grains with low angle grain boundary (LAGB). IV. The dislocation density inside sub-grains increases with the strain. V. The misorientation of the grains increases creating a high angle grain boundary (HAGB). Adapted from [143].

Wang *et al.* [144] investigated the microstructural, mechanical, and corrosion evolution of Zn-Mg (0.033 wt. % Mg) after 4, 8, and 12 ECAP cycles. The microstructural refinement and mechanical reinforcement were observed after 4 and 8 ECAP cycles. However, extensive grain refinement after 12 cycles led to an accumulation of dislocations that diminished the ductility. Likewise, the corrosion resistance obtained after 4 and 8 cycles disappeared after 12 cycles. The increasing Gibb’s free energy associated with the grain boundaries can accelerate corrosion in UFG structures where the grain boundary concentration is higher. Alateyah *et al.* [145] also reported improved corrosion behaviour of ZA31 (Mg-3Zn-1Al) after ECAP, where the deformation improved pitting corrosion resistance. Thus, ECAP processing after conventional metal forming of bars could be a strategy to enhance mechanical properties and control corrosion of Zn alloys for biomedical applications.

VI.4. General remarks on the modification of Zn-based alloys

Different approaches can be used to tune the degradation of bioresorbable Zn-based alloys. Surface modifications based on oxide or polymeric layers may protect the alloys from surface degradation. Moreover, peptide functionalization promotes cell adhesion and subsequent tissue healing, where the recovered tissue may act as a natural corrosion barrier. On the other hand, deformation routes such as ECAP processing can be a solution to reduce galvanic corrosion and control the degradation of Zn alloys for biomedical applications.

VII. References

[1] A. Sumayli, Recent trends on bioimplant materials: A review, in: Mater Today Proc, Elsevier Ltd, 2021: pp. 2726–2731. https://doi.org/10.1016/j.matpr.2021.02.395.

[2] Y. Sotomi, Y. Onuma, C. Collet, E. Tenekecioglu, R. Virmani, N.S. Kleiman, P.W. Serruys, Bioresorbable scaffold: The emerging reality and future directions, Circ Res. 120 (2017) 1341–1352. https://doi.org/10.1161/CIRCRESAHA.117.310275.

[3] Y.F. Zheng, X.N. Gu, F. Witte, Biodegradable metals, Materials Science and Engineering R. 77 (2014) 1–34. https://doi.org/10.1007/978-1-4614-3942-4_5.

[4] Dataintelo, Global Bioresorbable Implants Market by Type (Metals, Polymers), By Application (Stents, Orthopedics, Others) And By Region (North America, Latin America, Europe, Asia Pacific and Middle East & Africa), Forecast From 2022 To 2030, 2022.

[5] P. Habibovic, J.E. Barralet, Bioinorganics and biomaterials: Bone repair, Acta Biomater. 7 (2011) 3013–3026. https://doi.org/10.1016/j.actbio.2011.03.027.

[6] W. Wang, K.W.K. Yeung, Bone grafts and biomaterials substitutes for bone defect repair: A review, Bioact Mater. 2 (2017) 224–247. https://doi.org/10.1016/j.bioactmat.2017.05.007.

[7] L.L. Hench, R.J. Splinter, W.C. Allen, T.K. Greenlee, Bonding mechanisms at the interface of ceramic prosthetic materials, J Biomed Mater Res. 5 (1971) 117–141. https://doi.org/10.1002/jbm.820050611.

[8] L.L. Hench, The story of Bioglass®, J Mater Sci Mater Med. 17 (2006) 967–978. https://doi.org/10.1007/s10856-006-0432-z.

[9] B. Dhandayuthapani, Y. Yoshida, T. Maekawa, D.S. Kumar, Polymeric scaffolds in tissue engineering application: A review, Int J Polym Sci. 2011 (2011). https://doi.org/10.1155/2011/290602.

[10] M.L. Hans, A.M. Lowman, Biodegradable nanoparticles for drug delivery and targeting, Curr Opin Solid State Mater Sci. 6 (2002) 319–327. https://doi.org/10.1016/S1359-0286(02)00117-1.

[11] D. Zhao, F. Witte, F. Lu, J. Wang, J. Li, L. Qin, Current status on clinical applications of magnesium-based orthopaedic implants: A review from clinical translational perspective, Biomaterials. 112 (2017) 287–302. https://doi.org/10.1016/j.biomaterials.2016.10.017.

[12] R. Song, M. Murphy, C. Li, K. Ting, C. Soo, Z. Zheng, Current development of biodegradable polymeric materials for biomedical applications, Drug Des Devel Ther. 12 (2018) 3117–3145. https://doi.org/10.2147/DDDT.S165440.

[13] M. Costa Da Silva, H.N. da Silva, S.A. Holanda, A.R.O. Silva, M.V.L. Fook, Biodegradable polymeric wires: monofilament and multifilament, Materials Research Innovations. 24 (2020) 166–170. https://doi.org/10.1080/14328917.2019.1622256.

[14] S. Chatterjee, M. Saxena, D. Padmanabhan, M. Jayachandra, H.J. Pandya, Futuristic medical implants using bioresorbable materials and devices, Biosens Bioelectron. 142 (2019). https://doi.org/10.1016/j.bios.2019.111489.

[15] A.A. Oliver, M. Sikora-Jasinska, A.G. Demir, R.J. Guillory, Recent advances and directions in the development of bioresorbable metallic cardiovascular stents: Insights from recent human and in vivo studies, Acta Biomater. 127 (2021) 1–23. https://doi.org/10.1016/j.actbio.2021.03.058.

[16] H. Ryu, M.H. Seo, J.A. Rogers, Bioresorbable Metals for Biomedical Applications: From Mechanical Components to Electronic Devices, Adv Healthc Mater. 10 (2021). https://doi.org/10.1002/adhm.202002236.

[17] V. Herber, B. Okutan, G. Antonoglou, N.G. Sommer, M. Payer, Bioresorbable magnesium-based alloys as novel biomaterials in oral bone regeneration: General review and clinical perspectives, J Clin Med. 10 (2021). https://doi.org/10.3390/jcm10091842.

[18] D. Xia, F. Yang, Y. Zheng, Y. Liu, Y. Zhou, Research status of biodegradable metals designed for oral and maxillofacial applications: a review, Bioact Mater. (2021) 4186–4208.

[19] World Health Organization, The top 10 causes of death, (n.d.). https://www.who.int/news-room/fact-sheets/detail/the-top-10-causes-of-death (accessed November 14, 2022).

[20] H. Ait-Oufella, B.L. Salomon, S. Potteaux, A.K.L. Robertson, P. Gourdy, J. Zoll, R. Merval, B. Esposito, J.L. Cohen, S. Fisson, R.A. Flavell, G.K. Hansson, D. Klatzmann, A. Tedgui, Z. Mallat, Natural regulatory T cells control the development of atherosclerosis in mice, Nat Med. 12 (2006) 178–180. https://doi.org/10.1038/nm1343.

[21] I. Neamtu, A.P. Chiriac, A. Diaconu, L.E. Nita, V. Balan, M.T. Nistor, Current Concepts on Cardiovascular Stent Devices, 2014. https://doi.org/10.2174/1389557514666140530093620.

[22] G.W. Stone, A. Rizvi, W. Newman, K. Mastali, J.C. Wang, R. Caputo, J. Doostzadeh, S. Cao, C.A. Simonton, K. Sudhir, A.J. Lansky, D.E. Cutlip, D.J. Kereiakes, N. York, A. Vascular, S. Clara, Everolimus-Eluting versus Paclitaxel-Eluting Stents in Coronary Artery Disease, 2010.

[23] S. Borhani, S. Hassanajili, S.H. Ahmadi Tafti, S. Rabbani, Cardiovascular stents: overview, evolution, and next generation, Prog Biomater. 7 (2018) 175–205. https://doi.org/10.1007/s40204-018-0097-y.

[24] I. Cockerill, C.W. See, M.L. Young, Y. Wang, D. Zhu, Designing Better Cardiovascular Stent Materials: A Learning Curve, Adv Funct Mater. 31 (2021). https://doi.org/10.1002/adfm.202005361.

[25] P.K. Bowen, E.R. Shearier, S. Zhao, R.J. Guillory, F. Zhao, J. Goldman, J.W. Drelich, Biodegradable Metals for Cardiovascular Stents: from Clinical Concerns to Recent Zn-Alloys, Adv Healthc Mater. 5 (2016) 1121–1140. https://doi.org/10.1002/adhm.201501019.

[26] M. Moravej, D. Mantovani, Biodegradable metals for cardiovascular stent application: Interests and new opportunities, Int J Mol Sci. 12 (2011) 4250–4270. https://doi.org/10.3390/ijms12074250.

[27] J.M. Seitz, M. Durisin, J. Goldman, J.W. Drelich, Recent Advances in Biodegradable Metals for Medical Sutures: A Critical Review, Adv Healthc Mater. 4 (2015) 1915–1936. https://doi.org/10.1002/adhm.201500189.

[28] H.S. Han, S. Loffredo, I. Jun, J. Edwards, Y.C. Kim, H.K. Seok, F. Witte, D. Mantovani, S. Glyn-Jones, Current status and outlook on the clinical translation of biodegradable metals, Materials Today. 23 (2019) 57–71. https://doi.org/10.1016/j.mattod.2018.05.018.

[29] J.G. Wall, H. Podbielska, M. Wawrzyńska, Functionalised Cardiovascular Stents, 2017. https://doi.org/10.1016/c2014-0-04186-x.

[30] C.J. Murray, K.S. Ikuta, F. Sharara, L. Swetschinski, G. Robles Aguilar, A. Gray, C. Han, C. Bisignano, P. Rao, E. Wool, S.C. Johnson, A.J. Browne, M.G. Chipeta, F. Fell, S. Hackett, G. Haines-Woodhouse, B.H. Kashef Hamadani, E.A.P. Kumaran, B. McManigal, R. Agarwal, S. Akech, S. Albertson, J. Amuasi, J. Andrews, A. Aravkin, E. Ashley, F. Bailey, S. Baker, B. Basnyat, A. Bekker, R. Bender, A. Bethou, J. Bielicki, S. Boonkasidecha, J. Bukosia, C. Carvalheiro, C. Castañeda-Orjuela, V. Chansamouth, S. Chaurasia, S. Chiurchiù, F. Chowdhury, A.J. Cook, B. Cooper, T.R. Cressey, E. Criollo-Mora, M. Cunningham, S. Darboe, N.P.J. Day, M. de Luca, K. Dokova, A. Dramowski, S.J. Dunachie, T. Eckmanns, D. Eibach, A. Emami, N. Feasey, N. Fisher-Pearson, K. Forrest, D. Garrett, P. Gastmeier, A.Z. Giref, R.C. Greer, V. Gupta, S. Haller, A. Haselbeck, S.I. Hay, M. Holm, S. Hopkins, K.C. Iregbu, J. Jacobs, D. Jarovsky, F. Javanmardi, M. Khorana, N. Kissoon, E. Kobeissi, T. Kostyanev, F. Krapp, R. Krumkamp, A. Kumar, H.H. Kyu, C. Lim, D. Limmathurotsakul, M.J. Loftus, M. Lunn, J. Ma, N. Mturi, T. Munera-Huertas, P. Musicha, M.M. Mussi-Pinhata, T. Nakamura, R. Nanavati, S. Nangia, P. Newton, C. Ngoun, A. Novotney, D. Nwakanma, C.W. Obiero, A. Olivas-Martinez, P. Olliaro, E. Ooko, E. Ortiz-Brizuela, A.Y. Peleg, C. Perrone, N. Plakkal, A. Ponce-de-Leon, M. Raad, T. Ramdin, A. Riddell, T. Roberts,

J.V. Robotham, A. Roca, K.E. Rudd, N. Russell, J. Schnall, J.A.G. Scott, M. Shivamallappa, J. Sifuentes-Osornio, N. Steenkeste, A.J. Stewardson, T. Stoeva, N. Tasak, A. Thaiprakong, G. Thwaites, C. Turner, P. Turner, H.R. van Doorn, S. Velaphi, A. Vongpradith, H. Vu, T. Walsh, S. Waner, T. Wangrangsimakul, T. Wozniak, P. Zheng, B. Sartorius, A.D. Lopez, A. Stergachis, C. Moore, C. Dolecek, M. Naghavi, Global burden of bacterial antimicrobial resistance in 2019: a systematic analysis, The Lancet. 399 (2022) 629–655. https://doi.org/10.1016/S0140-6736(21)02724-0.

[31] B. Allegranzi, B. Nejad, W. Graafmans, A. Phd, L. Donaldson, D. Pittet, B. Allegranzi, S.B. Nejad, C. Combescure, W. Graafmans, H. Attar, L. Donaldson, D. Pittet, Articles Burden of endemic health-care-associated infection in developing countries: systematic review and meta-analysis, Lancet. 377 (2011) 228–269. https://doi.org/10.1016/S0140.

[32] J. Gallo, M. Holinka, C.S. Moucha, Antibacterial surface treatment for orthopaedic implants, Int J Mol Sci. 15 (2014) 13849–13880. https://doi.org/10.3390/ijms150813849.

[33] Z. Chen, Z. Wang, W. Qiu, F. Fang, Overview of Antibacterial Strategies of Dental Implant Materials for the Prevention of Peri-Implantitis, Bioconjug Chem. 32 (2021) 627–638. https://doi.org/10.1021/acs.bioconjchem.1c00129.

[34] H. Dong, F. Lin, A.R. Boccaccini, S. Virtanen, Corrosion behavior of biodegradable metals in two different simulated physiological solutions: Comparison of Mg, Zn and Fe, Corros Sci. 182 (2021). https://doi.org/10.1016/j.corsci.2021.109278.

[35] A.A. Barros, C. Oliveira, E. Lima, A.R.C. Duarte, K. Healy, R.L. Reis, 7.41 Ureteral stents technology: Biodegradable and drug-eluting perspective, in: Comprehensive Biomaterials II, Elsevier, 2017: pp. 793–812. https://doi.org/10.1016/B978-0-12-803581-8.10189-4.

[36] A.M. Emelyanenko, V. v. Kaminsky, I.S. Pytskii, K.A. Emelyanenko, A.G. Domantovsky, E. v. Chulkova, A.A. Shiryaev, A. v. Aleshkin, L.B. Boinovich, Antimicrobial activity and degradation of superhydrophobic magnesium substrates in bacterial media, Metals (Basel). 11 (2021). https://doi.org/10.3390/met11071100.

[37] Z. Lin, X. Sun, H. Yang, The Role of Antibacterial Metallic Elements in Simultaneously Improving the Corrosion Resistance and Antibacterial Activity of Magnesium Alloys, Mater Des. 198 (2021). https://doi.org/10.1016/j.matdes.2020.109350.

[38] X. Qu, H. Yang, B. Jia, Z. Yu, Y. Zheng, K. Dai, Biodegradable Zn–Cu alloys show antibacterial activity against MRSA bone infection by inhibiting pathogen adhesion and biofilm formation, Acta Biomater. 117 (2020) 400–417. https://doi.org/10.1016/j.actbio.2020.09.041.

[39] J. Jiao, S. Zhang, X. Qu, B. Yue, Recent Advances in Research on Antibacterial Metals and Alloys as Implant Materials, Front Cell Infect Microbiol. 11 (2021). https://doi.org/10.3389/fcimb.2021.693939.

[40] D. Lange, S. Bidnur, N. Hoag, B.H. Chew, Ureteral stent-associated complications-where we are and where we are going, Nat Rev Urol. 12 (2015) 17–25. https://doi.org/10.1038/nrurol.2014.340.

[41] A. de Grazia, B.K. Somani, F. Soria, D. Carugo, A. Mosayyebi, Latest advancements in ureteral stent technology, Transl Androl Urol. 8 (2019) S436–S441. https://doi.org/10.21037/tau.2019.08.16.

[42] Y. Ahallal, A. Khallouk, M. Jamal, E. Fassi, H. Farih, Risk Factor Analysis and Management of Ureteral Double-J Stent Complications, Rev Urol. 12 (2010) 147–151. https://doi.org/10.3909/riu0447.

[43] N. Venkatesan, S. Shroff, K. Jeyachandran, M. Doble, Effect of uropathogens on in vitro encrustation of polyurethane double J ureteral stents, Urol Res. 39 (2011) 29–37. https://doi.org/10.1007/s00240-010-0280-7.

[44] N. Altunal, A. Willke, O. Hamzaoğlu, Ureteral stent infections: a prospective study, Brazilian Journal of Infectious Diseases. 21 (2017) 361–364. https://doi.org/10.1016/j.bjid.2016.12.004.

[45] D. L. Dunn, Wound Closure Manual, 2005.

[46] B. Joseph, A. George, S. Gopi, N. Kalarikkal, S. Thomas, Polymer sutures for simultaneous wound healing and drug delivery – A review, Int J Pharm. 524 (2017) 454–466. https://doi.org/10.1016/j.ijpharm.2017.03.041.

[47] H. Guo, J. Hu, Z. Shen, D. Du, Y. Zheng, J. Peng, In vitro and in vivo studies of biodegradable Zn-Li-Mn alloy staples designed for gastrointestinal anastomosis, Acta Biomater. 121 (2021) 713–723. https://doi.org/10.1016/j.actbio.2020.12.017.

[48] S. Ghosh, N. More, G. Kapusetti, Surgical staples: Current state-of-the-art and future prospective, Med Nov Technol Devices. (2022) 100166. https://doi.org/10.1016/j.medntd.2022.100166.

[49] J.J.D. Venezuela, S. Johnston, M.S. Dargusch, The Prospects for Biodegradable Zinc in Wound Closure Applications, Adv Healthc Mater. 8 (2019) 1–15. https://doi.org/10.1002/adhm.201900408.

[50] M. Byrne, A. Aly, The surgical suture, Aesthet Surg J. 39 (2019) S67–S72. https://doi.org/10.1093/asj/sjz036.

[51] L. Xu, Y. Liu, W. Zhou, D. Yu, Electrospun Medical Sutures for Wound Healing: A Review, Polymers (Basel). 14 (2022). https://doi.org/10.3390/polym14091637.

[52] D.J. Hess, M.J. Henry-Stanley, C.L. Wells, Gentamicin promotes staphylococcus aureus biofilms on silk suture, Journal of Surgical Research. 170 (2011) 302–308. https://doi.org/10.1016/j.jss.2011.06.011.

[53] ISO 10993-5:2009. Biological evaluation of medical devices — Part 5: Tests for in vitro cytotoxicity, International Organization for Standardization. (2009).

[54] ISO 10993-12: 2012(E). Biological Evaluation of Medical Devices–Part 12: Sample Preparation and Reference Materials, International Organization for Standardization. (2012).

[55] A.C. Vieira, J.C. Vieira, R.M. Guedes, A.T. Marques, Degradation and viscoelastic properties of PLA-PCL, PGA-PCL, PDO and PGA fibres, in: Materials Science Forum, Trans Tech Publications Ltd, 2010: pp. 825–832. https://doi.org/10.4028/www.scientific.net/MSF.636-637.825.

[56] W. Jiang, Q. Tian, T. Vuong, M. Shashaty, C. Gopez, T. Sanders, H. Liu, Comparison Study on Four Biodegradable Polymer Coatings for Controlling Magnesium Degradation and Human Endothelial Cell Adhesion and Spreading, ACS Biomater Sci Eng. 3 (2017) 936–950. https://doi.org/10.1021/acsbiomaterials.7b00215.

[57] K. Törne, M. Larsson, A. Norlin, J. Weissenrieder, Degradation of zinc in saline solutions, plasma, and whole blood, J Biomed Mater Res B Appl Biomater. 104 (2016) 1141–1151. https://doi.org/10.1002/jbm.b.33458.

[58] K.B. Törne, Zn – Mg and Zn – Ag degradation mechanism under biologically relevant conditions, Surf Innov. (2017) 1–12.

[59] K. Beaussant Törne, A. Örnberg, J. Weissenrieder, Characterization of the protective layer formed on zinc in whole blood, Electrochim Acta. 258 (2017) 1476–1483. https://doi.org/10.1016/j.electacta.2017.12.018.

[60] E. Mena-Morcillo, L. Veleva, Degradation of AZ31 and AZ91 magnesium alloys in different physiological media: Effect of surface layer stability on electrochemical behaviour, Journal of Magnesium and Alloys. 8 (2020) 667–675. https://doi.org/10.1016/j.jma.2020.02.014.

[61] M. Kieke, F. Feyerabend, J. Lemaitre, P. Behrens, R. Willumeit-Römer, Degradation rates and products of pure magnesium exposed to different aqueous media under physiological conditions, BioNanoMaterials. 17 (2016) 131–143. https://doi.org/10.1515/bnm-2015-0020.

[62] M. Sikora-Jasinska, J. Goldman, E. Mostaed, J.W. Drelich, Albumins inhibit the corrosion of absorbable Zn alloys at initial stages of degradation, Surf Innov. 8 (2020) 234–249. https://doi.org/10.1680/jsuin.19.00063.

[63] C. Chen, J. Chen, W. Wu, Y. Shi, L. Jin, L. Petrini, L. Shen, G. Yuan, W. Ding, J. Ge, E.R. Edelman, F. Migliavacca, In vivo and in vitro evaluation of a biodegradable magnesium vascular stent designed by shape optimization strategy, Biomaterials. 221 (2019). https://doi.org/10.1016/j.biomaterials.2019.119414.

[64] D. Tie, H. Liu, R. Guan, P. Holt-Torres, Y. Liu, Y. Wang, N. Hort, In vivo assessment of biodegradable magnesium alloy ureteral stents in a pig model, Acta Biomater. 116 (2020) 415–425. https://doi.org/10.1016/j.actbio.2020.09.023.

[65] H.S. Han, I. Jun, H.K. Seok, K.S. Lee, K. Lee, F. Witte, D. Mantovani, Y.C. Kim, S. Glyn-Jones, J.R. Edwards, Biodegradable Magnesium Alloys Promote Angio-Osteogenesis to Enhance Bone Repair, Advanced Science. 7 (2020). https://doi.org/10.1002/advs.202000800.

[66] H.S. Han, S. Loffredo, I. Jun, J. Edwards, Y.C. Kim, H.K. Seok, F. Witte, D. Mantovani, S. Glyn-Jones, Current status and outlook on the clinical translation of biodegradable

metals, Materials Today. 23 (2019) 57–71. https://doi.org/10.1016/j.mattod.2018.05.018.

[67] H. Yang, X. Qu, W. Lin, C. Wang, D. Zhu, K. Dai, Y. Zheng, In vitro and in vivo studies on zinc-hydroxyapatite composites as novel biodegradable metal matrix composite for orthopedic applications, Acta Biomater. 71 (2018) 200–214. https://doi.org/10.1016/j.actbio.2018.03.007.

[68] A. Kafri, S. Ovadia, G. Yosafovich-Doitch, E. Aghion, In vivo performances of pure Zn and Zn–Fe alloy as biodegradable implants, J Mater Sci Mater Med. 29 (2018). https://doi.org/10.1007/s10856-018-6096-7.

[69] J. Wang, F. Witte, T. Xi, Y. Zheng, K. Yang, Y. Yang, D. Zhao, J. Meng, Y. Li, W. Li, K. Chan, L. Qin, Recommendation for modifying current cytotoxicity testing standards for biodegradable magnesium-based materials., Acta Biomater. 21 (2015) 237–49. https://doi.org/10.1016/j.actbio.2015.04.011.

[70] K.B. Törne, Investigation of corrosion properties of metals for degradable implant applications, 2017.

[71] ASTM Committee on Mechanical Testing, ASTM E8/E8M-13a. Standard Test Methods for Tension Testing of Metallic Materials, Annual Book of ASTM Standards. ASTM Stds. (2013) 1–28. https://doi.org/10.1520/E0008.

[72] ASTM G5-14. Standard Reference Test Method for Making Potentiodynamic Anodic Polarization Measurements, Annual Book of ASTM Standards. (2014). https://doi.org/10.1520/G0005-14.2.

[73] ASTM G31-72, 2004. Standard Practice for Laboratory Immersion Corrosion Testing of Metals, Annual Book of ASTM Standards. (2004). https://doi.org/10.1520/G0031-72R04.2.

[74] M. Sikora-Jasinska, L.M. Morath, M.P. Kwesiga, M.E. Plank, A.L. Nelson, A.A. Oliver, M.L. Bocks, R.J. Guillory, J. Goldman, In-vivo evaluation of molybdenum as bioabsorbable stent candidate, Bioact Mater. 14 (2022) 262–271. https://doi.org/10.1016/j.bioactmat.2021.11.005.

[75] C. Redlich, P. Quadbeck, M. Thieme, B. Kieback, Molybdenum – A biodegradable implant material for structural applications?, Acta Biomater. 104 (2020) 241–251. https://doi.org/10.1016/j.actbio.2019.12.031.

[76] Y. Kohgo, K. Ikuta, T. Ohtake, Y. Torimoto, J. Kato, Body iron metabolism and pathophysiology of iron overload, Int J Hematol. 88 (2008) 7–15. https://doi.org/10.1007/s12185-008-0120-5.

[77] D. Pierson, J. Edick, A. Tauscher, E. Pokorney, P. Bowen, J. Gelbaugh, J. Stinson, H. Getty, C.H. Lee, J. Drelich, J. Goldman, A simplified in vivo approach for evaluating the bioabsorbable behavior of candidate stent materials, J Biomed Mater Res B Appl Biomater. 100 B (2012) 58–67. https://doi.org/10.1002/jbm.b.31922.

[78] Y.K. Kim, K.B. Lee, S.Y. Kim, Y.S. Jang, J.H. Kim, M.H. Lee, Improvement of osteogenesis by a uniform PCL coating on a magnesium screw for biodegradable applications, Sci Rep. 8 (2018) 1–11. https://doi.org/10.1038/s41598-018-31359-9.

[79] R. Erbel, C. Di Mario, J. Bartunek, J. Bonnier, B. de Bruyne, F.R. Eberli, P. Erne, M. Haude, B. Heublein, M. Horrigan, C. Ilsley, D. Böse, J. Koolen, T.F. Lüscher, N. Weissman, R. Waksman, Temporary scaffolding of coronary arteries with bioabsorbable magnesium stents: a prospective, non-randomised multicentre trial, Lancet. 369 (2007) 1869–1875. https://doi.org/10.1016/S0140-6736(07)60853-8.

[80] G. Song, Control of biodegradation of biocompatable magnesium alloys, Corros Sci. 49 (2007) 1696–1701. https://doi.org/10.1016/j.corsci.2007.01.001.

[81] L.M. Calado, M.F. Montemor, Corrosion protection of magnesium alloys by functional coatings, 2018. https://doi.org/10.1007/978-3-319-32101-1_151.

[82] R.G. Hu, S. Zhang, J.F. Bu, C.J. Lin, G.L. Song, Recent progress in corrosion protection of magnesium alloys by organic coatings, Prog Org Coat. 73 (2012) 129–141. https://doi.org/10.1016/j.porgcoat.2011.10.011.

[83] C. Blawert, W. Dietzel, E. Ghali, G. Song, Anodizing treatments for magnesium alloys and their effect on corrosion resistance in various environments, Adv Eng Mater. 8 (2006) 511–533. https://doi.org/10.1002/adem.200500257.

[84] E. Mostaed, M. Hashempour, A. Fabrizi, D. Dellasega, M. Bestetti, F. Bonollo, M. Vedani, Microstructure, texture evolution, mechanical properties and corrosion behavior of ECAP processed ZK60 magnesium alloy for biodegradable applications, J Mech Behav Biomed Mater. 37 (2014) 307–322. https://doi.org/10.1016/j.jmbbm.2014.05.024.

[85] G. Katarivas Levy, J. Goldman, E. Aghion, The Prospects of Zinc as a Structural Material for Biodegradable Implants—A Review Paper, Metals (Basel). 7 (2017) 402. https://doi.org/10.3390/met7100402.

[86] D. Vojtěch, J. Kubásek, J. Šerák, P. Novák, Mechanical and corrosion properties of newly developed biodegradable Zn-based alloys for bone fixation, Acta Biomater. 7 (2011) 3515–3522. https://doi.org/10.1016/j.actbio.2011.05.008.

[87] P.K. Bowen, J.W. Drelich, J. Goldman, Zinc exhibits ideal physiological corrosion behavior for bioabsorbable stents, Advanced Materials. 25 (2013) 2577–2582. https://doi.org/10.1002/adma.201300226.

[88] H. Yang, C. Wang, C. Liu, H. Chen, Y. Wu, J. Han, Z. Jia, W. Lin, D. Zhang, W. Li, W. Yuan, H. Guo, H. Li, G. Yang, D. Kong, D. Zhu, K. Takashima, L. Ruan, J. Nie, X. Li, Y. Zheng, Evolution of the degradation mechanism of pure zinc stent in the one-year study of rabbit abdominal aorta model, Biomaterials. 145 (2017) 92–105. https://doi.org/10.1016/j.biomaterials.2017.08.022.

[89] A.J. Drelich, S. Zhao, R.J. Guillory, J.W. Drelich, J. Goldman, Long-term surveillance of zinc implant in murine artery: Surprisingly steady biocorrosion rate, Acta Biomater. 58 (2017) 539–549. https://doi.org/10.1016/j.actbio.2017.05.045.

[90] J. Venezuela, M.S. Dargusch, The influence of alloying and fabrication techniques on the mechanical properties, biodegradability and biocompatibility of zinc: A comprehensive review, Acta Biomater. 87 (2019) 1–40. https://doi.org/10.1016/j.actbio.2019.01.035.

[91] C. Redlich, A. Schauer, J. Scheibler, G. Poehle, P. Barthel, A. Maennel, V. Adams, T. Weissgaerber, A. Linke, P. Quadbeck, In vitro degradation behavior and biocompatibility of bioresorbable molybdenum, Metals (Basel). 11 (2021). https://doi.org/10.3390/met11050761.

[92] F. Witte, N. Hort, C. Vogt, S. Cohen, K.U. Kainer, R. Willumeit, F. Feyerabend, Degradable biomaterials based on magnesium corrosion, Curr Opin Solid State Mater Sci. 12 (2008) 63–72. https://doi.org/10.1016/j.cossms.2009.04.001.

[93] X.N. Gu, Y.F. Zheng, A review on magnesium alloys as biodegradable materials, Front Mater Sci China. 4 (2010) 111–115. https://doi.org/10.1007/s11706-010-0024-1.

[94] H.F. Li, X.H. Xie, Y.F. Zheng, Y. Cong, F.Y. Zhou, K.J. Qiu, X. Wang, S.H. Chen, L. Huang, L. Tian, L. Qin, Development of biodegradable Zn-1X binary alloys with nutrient alloying elements Mg, Ca and Sr, Sci Rep. 5 (2015). https://doi.org/10.1038/srep10719.

[95] M. Luo, W. Shen, Y. Wang, M.G. Allen, In vitro degradation og biodegradable metal zn and Zn/Fe-couples and their application as conductors in biodegradable sensors, Transducers. (2015).

[96] J. Niu, Z. Tang, H. Huang, J. Pei, H. Zhang, G. Yuan, W. Ding, Research on a Zn-Cu alloy as a biodegradable material for potential vascular stents application, Materials Science and Engineering: C. 69 (2016) 407–413. https://doi.org/10.1016/j.msec.2016.06.082.

[97] Z. Tang, J. Niu, H. Huang, H. Zhang, J. Pei, J. Ou, G. Yuan, Potential biodegradable Zn-Cu binary alloys developed for cardiovascular implant applications, J Mech Behav Biomed Mater. 72 (2017) 182–191. https://doi.org/10.1016/j.jmbbm.2017.05.013.

[98] X. Liu, J. Sun, F. Zhou, Y. Yang, R. Chang, K. Qiu, Z. Pu, L. Li, Y. Zheng, Micro-alloying with Mn in Zn-Mg alloy for future biodegradable metals application, Mater Des. 94 (2016) 95–104. https://doi.org/10.1016/j.matdes.2015.12.128.

[99] S. Zhao, J.-M. Seitz, R. Eifler, H.J. Maier, R.J. Guillory, E.J. Earley, A. Drelich, J. Goldman, J.W. Drelich, Zn-Li alloy after extrusion and drawing: Structural, mechanical characterization, and biodegradation in abdominal aorta of rat, Materials Science and Engineering: C. 76 (2017) 301–312. https://doi.org/10.1016/j.msec.2017.02.167.

[100] P.K. Bowen, J.-M. Seitz, R.J. Guillory, J.P. Braykovich, S. Zhao, J. Goldman, J.W. Drelich, Evaluation of wrought Zn-Al alloys (1, 3, and 5 wt % Al) through mechanical and in vivo testing for stent applications, J Biomed Mater Res B Appl Biomater. 106 (2017) 245–258. https://doi.org/10.1002/jbm.b.33850.

[101] M. Luo, W. Shen, Y. Wang, M.G. Allen, In vitro degradation of biodegradable metal Zn and Zn/Fe-couples and their application as conductors in biodegradable sensors, 2015 Transducers - 2015 18th International Conference on Solid-State Sensors, Actuators and

Microsystems, TRANSDUCERS 2015. (2015) 1370–1373. https://doi.org/10.1109/TRANSDUCERS.2015.7181187.

[102] H. Li, H. Yang, Y. Zheng, F. Zhou, K. Qiu, X. Wang, Design and characterizations of novel biodegradable ternary Zn-based alloys with IIA nutrient alloying elements Mg, Ca and Sr, Mater Des. 83 (2015) 95–102. https://doi.org/10.1016/j.matdes.2015.05.089.

[103] Z. Tang, H. Huang, J. Niu, L. Zhang, H. Zhang, J. Pei, J. Tan, G. Yuan, Design and characterizations of novel biodegradable Zn-Cu-Mg alloys for potential biodegradable implants, Mater Des. 117 (2017) 84–94. https://doi.org/10.1016/j.matdes.2016.12.075.

[104] C. Yao, Z. Wang, S.L. Tay, T. Zhu, W. Gao, Effects of Mg on microstructure and corrosion properties of Zn-Mg alloy, J Alloys Compd. 602 (2014) 101–107. https://doi.org/10.1016/j.jallcom.2014.03.025.

[105] C. Shen, X. Liu, B. Fan, P. Lan, F. Zhou, X. Li, H. Wang, X. Xiao, L. Li, S. Zhao, Z. Guo, Z. Pu, Y. Zheng, Mechanical properties,: In vitro degradation behavior, hemocompatibility and cytotoxicity evaluation of Zn-1.2Mg alloy for biodegradable implants, RSC Adv. 6 (2016) 86410–86419. https://doi.org/10.1039/c6ra14300h.

[106] E. Mostaed, M. Sikora-Jasinska, J.W. Drelich, M. Vedani, Zinc-based alloys for degradable vascular stent applications, Acta Biomater. 71 (2018) 1–23. https://doi.org/10.1016/j.actbio.2018.03.005.

[107] E. Mostaed, M. Sikora-Jasinska, A. Mostaed, S. Loffredo, A.G. Demir, B. Previtali, D. Mantovani, R. Beanland, M. Vedani, Novel Zn-based alloys for biodegradable stent applications: Design, development and in vitro degradation, J Mech Behav Biomed Mater. 60 (2016) 581–602. https://doi.org/10.1016/j.jmbbm.2016.03.018.

[108] M. Sikora-Jasinska, E. Mostaed, A. Mostaed, R. Beanland, D. Mantovani, M. Vedani, Fabrication, mechanical properties and in vitro degradation behavior of newly developed Zn-Ag alloys for degradable implant applications, Materials Science and Engineering C. 77 (2017) 1170–1181. https://doi.org/10.1016/j.msec.2017.04.023.

[109] J. Kubásek, D. Vojtěch, E. Jablonská, I. Pospíšilová, J. Lipov, T. Ruml, Structure, mechanical characteristics and in vitro degradation, cytotoxicity, genotoxicity and mutagenicity of novel biodegradable Zn–Mg alloys, Materials Science and Engineering: C. 58 (2016) 24–35. https://doi.org/10.1016/j.msec.2015.08.015.

[110] E.D. Harris, A Requirement for Copper in Angiogenesis, Nutriton Reviews. 62 (2004) 60–64. https://doi.org/10.1301/nr.2004.feb.60.

[111] L. Finney, S. Vogt, T. Fukai, D. Glesne, Copper and angiogenesis: Unravelling a relationship key to cancer progression, Clin Exp Pharmacol Physiol. 36 (2009) 88–94. https://doi.org/10.1111/j.1440-1681.2008.04969.x.

[112] C. Giacomelli, M.L. Trincavelli, C. Satriano, Ö. Hansson, D. la Mendola, E. Rizzarelli, C. Martini, Copper (II) ions modulate Angiogenin activity in human endothelial cells, International Journal of Biochemistry and Cell Biology. 60 (2015) 185–196. https://doi.org/10.1016/j.biocel.2015.01.005.

[113] A. Cabrero, S. Fernandez, F. Mirada, J. Garcia, EFFECTS OF COPPER AND ZINC ON THE ACTIVATED SLUDGE BACTERIA GROWTH KINETICS, n.d.

[114] B. Bagchi, S. Kar, S.K. Dey, S. Bhandary, D. Roy, T.K. Mukhopadhyay, S. Das, P. Nandy, In situ synthesis and antibacterial activity of copper nanoparticle loaded natural montmorillonite clay based on contact inhibition and ion release, Colloids Surf B Biointerfaces. 108 (2013) 358–365. https://doi.org/10.1016/j.colsurfb.2013.03.019.

[115] C. Zhou, H.F. Li, Y.X. Yin, Z.Z. Shi, T. Li, X.Y. Feng, J.W. Zhang, C.X. Song, X.S. Cui, K.L. Xu, Y.W. Zhao, W.B. Hou, S.T. Lu, G. Liu, M.Q. Li, J. ying Ma, E. Toft, A.A. Volinsky, M. Wan, X. jun Yao, C. bin Wang, K. Yao, S. kun Xu, H. Lu, S.F. Chang, J.B. Ge, L.N. Wang, H.J. Zhang, Long-term in vivo study of biodegradable Zn-Cu stent: A 2-year implantation evaluation in porcine coronary artery, Acta Biomater. 97 (2019) 657–670. https://doi.org/10.1016/j.actbio.2019.08.012.

[116] A.B.G. Lansdown, A pharmacological and toxicological profile of silver as an antimicrobial agent in medical devices, Adv Pharmacol Sci. 2010 (2010). https://doi.org/10.1155/2010/910686.

[117] A.B.G. Lansdown, Silver I: its antibacterial properties and mechanism of action, J Wound Care. 11 (2002).

[118] P. Li, C. Schille, E. Schweizer, U.E. Klotz, J. Geis-Gerstorfer, L. Scheideler, F. Rupp, C. Legner, A. Heiss, Mechanical Characteristics, In Vitro Degradation, Cytotoxicity, and Antibacterial Evaluation of Zn-4.0Ag Alloy as a Biodegradable Material, Int J Mol Sci. 19 (2018) 755. https://doi.org/10.3390/ijms19030755.

[119] M.I. Castellanos, C. Mas-Moruno, A. Grau, X. Serra-Picamal, X. Trepat, F. Albericio, M. Joner, F.J. Gil, M.P. Ginebra, J.M. Manero, M. Pegueroles, Functionalization of CoCr surfaces with cell adhesive peptides to promote HUVECs adhesion and proliferation, Appl Surf Sci. 393 (2017) 82–92. https://doi.org/10.1016/j.apsusc.2016.09.107.

[120] H. Kabir, K. Munir, C. Wen, Y. Li, Recent research and progress of biodegradable zinc alloys and composites for biomedical applications: Biomechanical and biocorrosion perspectives, Bioact Mater. 6 (2021) 836–879. https://doi.org/10.1016/j.bioactmat.2020.09.013.

[121] W. Yuan, D. Xia, S. Wu, Y. Zheng, Z. Guan, J. v. Rau, A review on current research status of the surface modification of Zn-based biodegradable metals, Bioact Mater. 7 (2022) 192–216. https://doi.org/10.1016/j.bioactmat.2021.05.018.

[122] J.Y. Yu, S.D. Choi, J.I. Yu, J.G. Yun, H. Ko, Y.J. Jung, The characteristic study of plasma electrolytic oxidation in AZ31B magnesium alloy, Journal of Electrical Engineering and Technology. 10 (2015) 1747–1752. https://doi.org/10.5370/JEET.2015.10.4.1747.

[123] A.J. Drelich, P.K. Bowen, L. LaLonde, J. Goldman, J.W. Drelich, Importance of oxide film in endovascular biodegradable zinc stents, Surf Innov. 4 (2016) 133–140. https://doi.org/10.1680/jsuin.16.00014.

[124] R.B. Heimann, Osseoconductive and corrosion-inhibiting plasma-sprayed calcium phosphate coatings for metallic medical implants, Metals (Basel). 7 (2017). https://doi.org/10.3390/met7110468.

[125] E. Malikmammadov, T.E. Tanir, A. Kiziltay, V. Hasirci, N. Hasirci, PCL and PCL-based materials in biomedical applications, J Biomater Sci Polym Ed. 29 (2018) 863–893. https://doi.org/10.1080/09205063.2017.1394711.

[126] B.M. Wilke, L. Zhang, Electrochemical Investigations of Polycaprolactone-Coated AZ31 Mg Alloy in Earle’s Balance Salt Solution and Conventional Simulated Body Fluid, Jom. 68 (2016) 1701–1710. https://doi.org/10.1007/s11837-016-1869-2.

[127] J. Degner, F. Singer, L. Cordero, A.R. Boccaccini, S. Virtanen, Electrochemical investigations of magnesium in DMEM with biodegradable polycaprolactone coating as corrosion barrier, Appl Surf Sci. 282 (2013) 264–270. https://doi.org/10.1016/j.apsusc.2013.05.115.

[128] T. Inoue, K. Croce, T. Morooka, M. Sakuma, K. Node, D.I. Simon, Vascular inflammation and repair: Implications for re-endothelialization, restenosis, and stent thrombosis, JACC Cardiovasc Interv. 4 (2011) 1057–1066. https://doi.org/10.1016/j.jcin.2011.05.025.

[129] X. Liu, J.M. Holzwarth, P.X. Ma, Functionalized Synthetic Biodegradable Polymer Scaffolds for Tissue Engineering, Macromol Biosci. 12 (2012) 911–919. https://doi.org/10.1002/mabi.201100466.

[130] Q. Shi, X. Chen, T. Lu, X. Jing, The immobilization of proteins on biodegradable polymer fibers via click chemistry, Biomaterials. 29 (2008) 1118–1126. https://doi.org/10.1016/j.biomaterials.2007.11.008.

[131] G. Sun, Y.I. Shen, S. Kusuma, K. Fox-Talbot, C.J. Steenbergen, S. Gerecht, Functional neovascularization of biodegradable dextran hydrogels with multiple angiogenic growth factors, Biomaterials. 32 (2011) 95–106. https://doi.org/10.1016/j.biomaterials.2010.08.091.

[132] N. Falcone, T. Shao, N.M.O. Andoy, R. Rashid, R.M.A. Sullan, X. Sun, H.B. Kraatz, Multi-component peptide hydrogels-a systematic study incorporating biomolecules for the exploration of diverse, tuneable biomaterials, Biomater Sci. 8 (2020) 5601–5614. https://doi.org/10.1039/d0bm01104e.

[133] K. Firipis, M. Boyd-Moss, B. Long, C. Dekiwadia, W. Hoskin, E. Pirogova, D.R. Nisbet, R.M.I. Kapsa, A.F. Quigley, R.J. Williams, Tuneable hybrid hydrogels via complementary self-assembly of a bioactive peptide with a robust polysaccharide, ACS Biomater Sci Eng. 7 (2021) 3340–3350. https://doi.org/10.1021/acsbiomaterials.1c00675.

[134] K. Ishihara, K. Mitera, Y. Inoue, K. Fukazawa, Effects of molecular interactions at various polymer brush surfaces on fibronectin adsorption induced cell adhesion, Colloids Surf B Biointerfaces. 194 (2020). https://doi.org/10.1016/j.colsurfb.2020.111205.

[135] M.I. Castellanos, C. Mas-Moruno, A. Grau, X. Serra-Picamal, X. Trepat, F. Albericio, M. Joner, F.J. Gil, M.P. Ginebra, J.M. Manero, M. Pegueroles, Functionalization of CoCr surfaces with cell adhesive peptides to promote HUVECs adhesion and proliferation, Appl Surf Sci. 393 (2017) 82–92. https://doi.org/10.1016/j.apsusc.2016.09.107.

[136] E. Lee, J.Y. Ko, J. Kim, J.W. Park, S. Lee, G. il Im, Osteogenesis and angiogenesis are simultaneously enhanced in BMP2-/VEGF-transfected adipose stem cells through activation of the YAP/TAZ signaling pathway, Biomater Sci. 7 (2019) 4588–4602. https://doi.org/10.1039/c9bm01037h.

[137] B. Divband, M. Aghazadeh, Z.H. Al-qaim, M. Samiei, F.H. Hussein, A. Shaabani, S. Shahi, R. Sedghi, Bioactive chitosan biguanidine-based injectable hydrogels as a novel BMP-2 and VEGF carrier for osteogenesis of dental pulp stem cells, Carbohydr Polym. 273 (2021). https://doi.org/10.1016/j.carbpol.2021.118589.

[138] Z. Wang, J. Sun, Y. Li, C. Chen, Y. Xu, X. Zang, L. Li, K. Meng, Experimental study of the synergistic effect and network regulation mechanisms of an applied combination of BMP-2, VEGF, and TGF-β1 on osteogenic differentiation, J Cell Biochem. 121 (2020) 2394–2405. https://doi.org/10.1002/jcb.29462.

[139] H. Gong, K. Wang, R. Strich, J.G. Zhou, In vitro biodegradation behavior, mechanical properties, and cytotoxicity of biodegradable Zn-Mg alloy, J Biomed Mater Res B Appl Biomater. 103 (2015) 1632–1640. https://doi.org/10.1002/jbm.b.33341.

[140] P. Li, W. Zhang, J. Dai, A.B. Xepapadeas, E. Schweizer, D. Alexander, L. Scheideler, C. Zhou, H. Zhang, G. Wan, J. Geis-Gerstorfer, Investigation of zinc-copper alloys as potential materials for craniomaxillofacial osteosynthesis implants, Materials Science and Engineering C. 103 (2019) 109826. https://doi.org/10.1016/j.msec.2019.109826.

[141] J. Lin, X. Tong, Z. Shi, D. Zhang, L. Zhang, K. Wang, A. Wei, L. Jin, J. Lin, Y. Li, C. Wen, A biodegradable Zn-1Cu-0.1Ti alloy with antibacterial properties for orthopedic applications, Acta Biomater. 106 (2020) 410–427. https://doi.org/10.1016/j.actbio.2020.02.017.

[142] W. Bednarczyk, M. Wątroba, J. Kawałko, P. Bała, Can zinc alloys be strengthened by grain refinement? A critical evaluation of the processing of low-alloyed binary zinc alloys using ECAP, Materials Science and Engineering A. 748 (2019) 357–366. https://doi.org/10.1016/j.msea.2019.01.117.

[143] M. Azarbarmas, S.S. Mirjavadi, A. Ghasemi, A.M. Hamouda, A combined method to model dynamic recrystallization based on cellular automaton and a phenomenological (CAP) approach, Metals (Basel). 8 (2018). https://doi.org/10.3390/met8110923.

[144] X. Wang, Y. Ma, B. Meng, M. Wan, Effect of equal-channel angular pressing on microstructural evolution, mechanical property and biodegradability of an ultrafine-grained zinc alloy, Materials Science and Engineering A. 824 (2021). https://doi.org/10.1016/j.msea.2021.141857.

[145] A.I. Alateyah, T.A. Aljohani, M.O. Alawad, H.A. El-Hafez, A.N. Almutairi, E.S. Alharbi, R. Alhamada, B.W. El-Garaihy, W.H. El-Garaihy, Improved corrosion

behavior of AZ31 alloy through ECAP processing, Metals (Basel). 11 (2021) 1–19. https://doi.org/10.3390/met11020363.

Objectives

Bioresorbable metals may overcome the limitations of current inert metallic implants, such as late-stent thrombosis or surgical site infections, and biodegradable polymeric implants, such as low mechanical properties. Despite adequate biocompatibility and optimal degradation behaviour of Zn, its limited mechanical strength requires alloying elements for mechanical reinforcement *via* precipitation hardening. Controlling the galvanic corrosion of Zn-based alloys is essential to reduce local toxicity and bacterial infection and ensure the needed mechanical support. In this regard, protective coatings and cell adhesive biomolecules immobilization present a paramount potential for tissue integration after device implantation. On the other hand, severe plastic deformation techniques homogenize corrosion and thus, could inhibit bacterial infiltration and further infections.

Thus, the main aim of the present PhD Thesis is **to develop novel bioresorbable Zn-based materials combining mechanical reinforcement, suitable degradation behaviour, and proper biological response for stent and antibacterial applications.** A first characterization of binary Zn-based systems (Zn-Mg, Zn-Cu and Zn-Ag) will be thoroughly performed to detect the material needs according to the final application. Secondly, dual-action coatings or severe deformation techniques will be investigated to tune the degradation behaviour and biological response of the alloys.

To achieve this main goal, the following specific objectives will be addressed:

Objective I. To understand the influence of secondary phases on the mechanical properties, corrosion behaviour, and biological response of Zn–based alloys. Chapter I will collect the fundamental characterization of Zn–xMg (x = 0.5, 1 wt. %) and Zn–xCu (x = 3, 5 wt.%) mainly focused on cardiovascular stents application. The study compiles the effects of secondary phases with different chemical compositions and volume fractions onto corrosion behaviour, following the next aims:

- To characterize the microstructure of the different secondary phases and determination of the relation between the volume fraction and the wt. % content of the studied Zn–based alloy.
- To understand the influence of secondary phases in the mechanical performance of the studied Zn-alloy at the nano-, micro-, and macro-scales.
- To investigate the effect of galvanic pairs on the overall degradation of the alloys due to corrosion processes in inorganic Hanks’ solution.

- To evaluate the biocompatibility of the alloys in human aortic endothelial cells and the antibacterial activity against *S. aureus* and *P. aeruginosa*.

Objective II. To investigate the relation between antibacterial performance and degradation mechanisms of Zn–Ag alloys for ureteral stents. From the fundamental understanding of Chapter I, Chapter II will analyse the correlation among secondary phases, galvanic corrosion, degradation, and antibacterial activity of Zn–xAg (x = 2, 4 wt.%) alloys. To this end, the study will gather the following aims:

- To study the microstructure of the alloys and discuss the mechanical reinforcement of Zn when alloyed with Ag element.
- Analysis of the degradation behaviour of the Zn and Zn–Ag alloys in bacterial media (brain heard infusion media). Investigation of the antibacterial mechanisms of the Zn–Ag alloys against *S. aureus* and *E. coli*. Discussion on the effects of bacterial and galvanic degradation on the antibacterial activity effectiveness.

Objective III. To implement dual-action coatings gathering corrosion protection and endothelialisation of Zn–based alloys. From the information collected in Chapters I and II, Zn–0.5Mg and Zn–2Ag were coated and functionalized with cell adhesive biomolecules for cardiovascular applications. Thus, the following tasks will be accomplished in Chapter III:

- Implementation of a biodegradable PCL coating layer with adequate interfacial adhesion and corrosion protection.
- Synthesis of linear RGD and REDV peptides and RGD-REDV peptide platform and their successful immobilization on the PCL coated surfaces.
- Investigation of the biomolecules influence on human umbilical vein endothelial cells adhesion and the synergistic effect of RGD and REDV peptides when combined in the RGD-REDV platform.

Objective IV. To explore severe plastic deformation techniques for microstructural refinement of Zn–2Ag alloy as a candidate for wound closure applications. Chapter IV will deal with the implications galvanic corrosion mechanisms previously discussed in Chapters I and II. Thus, the following aims will be addressed:

- Processing of Zn–2Ag by equal channel angular pressing and analysis of the secondary phases distribution, grain refinement, and resulting texture.

- Evaluation of the mechanical properties at nano-, micro- and macro-scale. Study the degradation evaluation in inorganic Hanks’ solution before and after deformation.
- To determine the effect of severe plastic deformation and grain refinement on the antibacterial activity against *S. aureus*.

Part I.

Characterization of Zn-based alloys

Chapter I.

Characterization of Zn-Mg and Zn-Cu alloys for bioresorbable cardiovascular stents

Results published in Bioactive Materials. 2021, 6, 4430–4446.
DOI: 10.1016/j.bioactmat.2021.04.015

Chapter I. Characterization of Zn-Mg and Zn-Cu alloys for bioresorbable cardiovascular stents

Objective

To evaluate Zn-xMg (x = 0.5, 1 wt.%) and Zn-xCu (x = 3, 5 wt.%) alloys for bioresorbable cardiovascular stents, and understanding the effect of eutectic and peritectic phases precipitation on the mechanical, corrosion, and biological response of Zn.

Graphical abstract

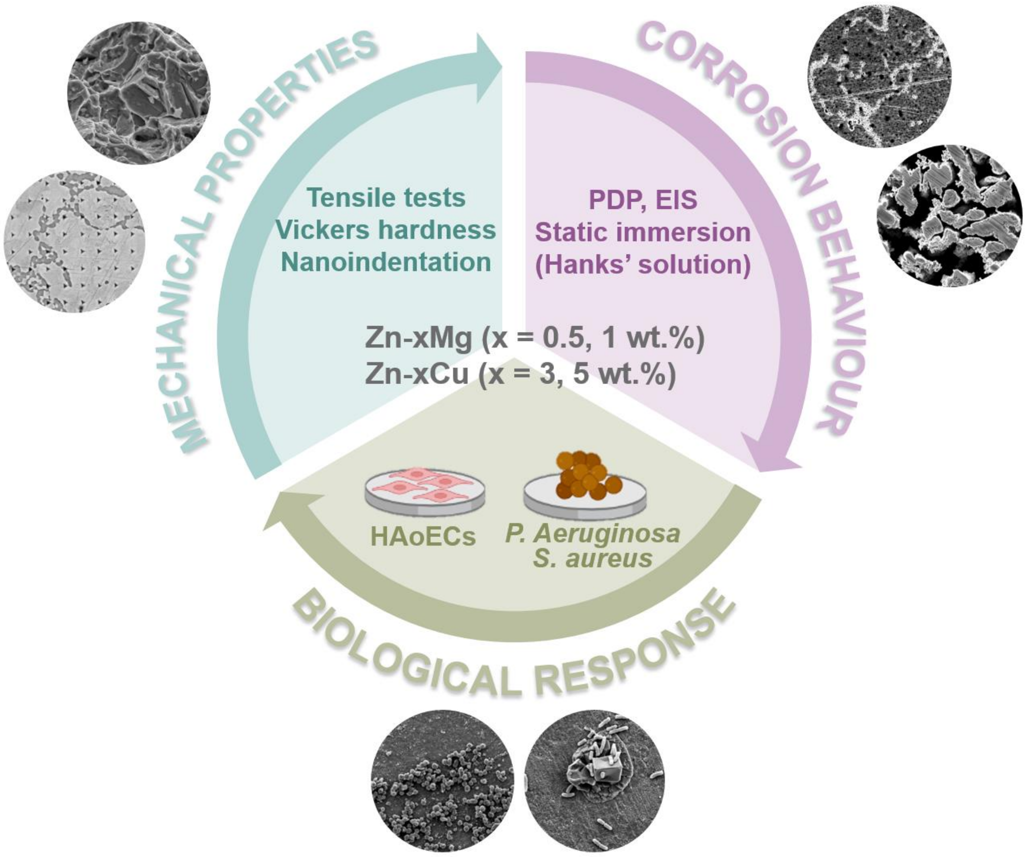

Main results

This chapter confirms that the precipitation of $Zn+Mg_2Zn_{11}$ or ε-$CuZn_5$ phases in the Zn matrix refines the Zn microstructure and enhances YS and UTS. Moreover, Zn-Mg alloys present more homogeneous corrosion than Zn-Cu alloys, where extensive galvanic corrosion is observed. Zn-Cu alloys exhibit an antibacterial effect against *S. aureus* and *P. aeruginosa*. However, all the alloys show poor biocompatibility, attributed to the local ion release and the corrosion by-products. In conclusion, Zn-Mg alloys presented more adequate properties than Zn-Cu alloys for cardiovascular stents.

I. Introduction

Coronary artery disease (CAD) is the leading cause of death worldwide and it is characterized by the progressive occlusion of the artery blood flow due to the formation of a plaque. Percutaneous coronary intervention (PCI) with stent placement has become the most popular treatment for atherosclerosis, with around three million stents being implanted worldwide each year [1]. A new generation of bioresorbable stents (BRS) has emerged to overcome the side effects of conventional stents by assisting the arterial healing and dissolving with no implant residues [3].

During the last two decades, bioresorbable materials have been widely investigated for their use in both cardiovascular and orthopedic applications [4–6]. The degradability and resorbability of the materials within the body after implantation simplifies many surgical interventions. The mechanical properties of an ideal stent should be close to those of stainless steel 316L and its total degradation should be fulfilled after one year of the implantation [7]. Bioresorbable polymers predominantly undergo hydrolytic or enzymatic degradation, releasing biocompatible products [8]. Nevertheless, their limited mechanical strength requires thicker struts to match the structural strength of current metallic stents, disrupting laminar blood flow, and potentially increasing the incidence of acute thrombotic events [4]. Mg- and Fe-based bioresorbable metals have received much attention in the past years due to their inherent mechanical properties, which make them more attractive stent material candidates than their polymeric counterparts [3,9]. Unfortunately, Mg shows a relatively high degradation rate and release of hydrogen gas which can induce cytotoxicity and can create gas bubbles at the adjacent areas to the implant promoting the separation of the surrounding tissue [10,11]. Fe corrodes at a slow degradation rate for stenting applications and accumulates corrosion products at the artery wall [5,12]. The development and characterization of Zn and its alloys as bioresorbable metals is an ongoing research and rigorous studies must be performed in order to determine and control their biocompatibility, degradation rate, and optimal mechanical properties. In fact, the risks associated with BRS restrain the growth of the market. Problems are related to limited mechanical material characteristics or unsuitable corrosion characteristics [14]. Thus, a thoroughly understanding of the mechanical properties at the nanoscale of the different alloys phases and the oxidation by-products and species with the biological fluids is needed.

Biocompatibility of Zn alloys and its corrosion products is crucial for stenting applications. Differences in the *in vitro* response depend on the studied alloy, selected cell line and cell culture medium, and the obtained products of corrosion. Zn alloys bacterial response is of interest since stent infection is a rare complication with high mortality (32 %), in which the *S. aureus* and the *P. aeruginosa* bacteria are responsible for over 80 % of the cases [19].

The mechanical properties of Zn are not optimal and thus, different strategies (e.g. alloying, thermal treatments and plastic deformation) have been evaluated. Katarivas Levy *et al*. [20] reviewed a numerous list of Zn-based formulations along with the reported mechanical properties and corrosion rates, and suggested essential elements Mg, Ca, Cu, Mn, and Sr as alloying elements for biomedical zinc alloys. Indeed, ternary alloys as Zn-Mg-Ca [21] or Zn-Mg-Cu [22,23] have been evaluated as promising compositions for biodegradable implants. Yang *et al*. [24] performed an extensive evaluation of binary Zn alloys for bioresorbable bone implants. Among all tested conditions, Zn-Li and Zn-Mg alloys showed noteworthy improvements in terms of strength, uniform degradation behavior, and biocompatibility [25,26].

However, the ductility significantly declined with respect to pure Zn, while Zn-Cu alloys have elongation values above 30 %, which successfully accomplishes the criteria for cardiovascular stents applications [27]. Moreover, Cu is well-known for its antibacterial properties [1,28–30] and it is reported to stimulate endothelial cell migration and angiogenesis [31–33]. Alloying with peritectic-forming elements such as copper (Cu) or eutectic-forming elements such as Mg, refines the microstructure of pure Zn and enhances its mechanical properties [34,35]. The importance of controlling topography, chemistry, and mechanical properties at micro and nanoscale is fundamental for obtaining the desired cellular response [28]. However, no studies have been devoted to evaluate the mechanical behavior of Zn-Mg and Zn-Cu alloys different phases at the nanoscale depth range.

This chapter aims to gain a better understanding of the addition of the peritectic and eutectic phases at the Zn matrix and their effect on the corrosion and nanoscale mechanical properties of Zn-Mg and Zn-Cu alloys. To that end, a thoroughly nanoindentation characterization and corrosion evaluation of Zn-based alloys was studied by potentiodynamic polarization (PDP) and electrochemical impedance spectroscopy (EIS) in Hanks' solution. The ion release of the alloys was evaluated through an immersion test by analyzing the released Zn^{2+}, Mg^{2+}, and Cu^{2+} cations. Finally, it has been evaluated the biological response with human aortic endothelial cells (HAoECs), the bacterial activity via agar diffusion tests and the bacterial adhesion with both *S. aureus* and *P. aeruginosa* of Zn-based alloys.

II. Materials and Methods

II.1. Materials

Pure Zn (99.9 % purity), Zn-xMg (x = 0.5 and 1 wt.%) and Zn-xCu (x = 3 and 5 wt.%) alloys were provided by Goodfellow, UK, in rods of 10 mm diameter. The as-received condition of Zn was extruded, and Zn-Mg and Zn-Cu bars were extruded and cold rolled. The chemical compositions of the zinc alloys as determined by inductively coupled plasma optical emission spectroscopy (ICP-OES) are presented in **Table 1.**

Table 1. Chemical composition (wt.%) of Zn-Mg and Zn-Cu alloys determined by ICP-OES.

Sample	Zn	Mg	Cu	Pb	S	Others
Pure Zn	99.939	-	-	0.030	-	<0.02*
Zn-0.5Mg	99.393	0.464	-	0.099	-	<0.01**
Zn-1Mg	98.498	0.904	-	0.113	-	<0.01**
Zn-3Cu	97.144	-	2.708	0.094	0.032	<0.01***
Zn-5Cu	95.385	-	4.482	0.084	0.011	<0.01***

*: As, Cd, Sn, Fe; **: Ag, Al, As, Cu, S, Se, Si; ***: Ag, Al, As, Fe, Sb, Se, Si

II.2. Microstructural characterization

Metallographic samples for the microstructural characterization were prepared from cross-sections and longitudinal samples using standard metallographic procedures followed by etching. The rods were cut into 2.5 mm thick discs, abraded with silicon carbide grinding papers (P800, P1200, P2500 and P4000 from Neuertek S.A., Spain). The ground samples were polished using 0.05 µm silica suspension (Buehler, Germany) while lubricated with ethanol (≥96% (v/v) Sigma-Aldrich, USA) until achieving smooth surfaces. A previous step of polishing using 6 µm diamond suspension (ATM, Germany) was required for Zn-Cu alloys. All polished samples were ultrasonically cleaned in absolute ethanol (Sigma-Aldrich, USA) and acetone (Sigma-Aldrich, USA) for 5 min. Pure Zn and Zn-Cu alloys were etched by a solution of 200 g/L CrO_3 (Sigma-Aldrich, USA) and 15g/L Na_2SO_4 (Sigma-Aldrich, USA), and rinsed of 200 g/L CrO_3. Zn-Mg alloys were etched by a solution of 4.2 g picric acid (Sigma-Aldrich, USA), 10 mL acetic acid (Sigma-Aldrich, USA), 70 mL absolute ethanol, and 10 mL of deionized water, and rinsed in absolute ethanol. Microstructure was observed by scanning electron microscopy

(SEM) equipped with X-ray energy-dispersive spectrometry (EDS) (JSM-7001F, JEOL, Japan). X-ray diffractometer (XRD) (D8 ADVANCE Twin, Bruker, USA) using CuKα was operated was operated at 40 kV and 100 mA to identify the phase composition of samples with scanning range from 20° to 90° at a scan rate of 2° min^{-1} and step size of 0.02°. The volume fraction percentage of secondary phase area was calculated using ImageJ software (National Institutes of Health, MD).

II.3. Mechanical characterization

Mechanical properties of the different Zn alloys were evaluated through tensile testing, Vickers micro-hardness, and nanoindentation. The tensile tests were carried out on a universal material test loading machine (Bionix 858 uniaxial, MTS Systems) according to ASTM E8-04 standard [36]. Tensile dog-bone samples (30 mm gage length, 6 mm diameter and 6 mm radius of fillet) were cut from the rolled rods with long axis parallel to the extrusion direction. The tensile tests were carried out at room temperature and at strain rate of 1 mm/min. Fracture surfaces after tensile tests were observed with SEM. Surface micro-hardness, H_v, was measured using a Vickers micro-hardness tester (Durascan G5, Emcotest) with a load of 100 g and dwelling time of 10 s. Mean hardness was averaged from 5 measurements.

Nanoindentations were performed on a MTS Nanoindenter XP equipped with a continuous stiffness measurement (CSM) using a Berkovich diamond tip with its area function determined against fused silica standard. Matrixes of 10 by 10 indentations were done with constant strain rate of 0.05 s^{-1} and a maximum penetration depth of 200 nm. The distance between consecutive indentations was set to 5 μm in order to avoid the interaction of the plastic deformation field between indentations. Results were analyzed with the Oliver and Pharr method [37], usually applied for metallic samples and sharp indenters. This approach minimizes the plastic effects providing a more accurate calculation of the elastic properties of the material [38,39]. Nanoindentation mapping was performed by KLA iMicro nanoindenter (KLA, USA). High-speed nanoindentations performed one complete indentation cycle per second. Matrixes of 60 by 60 indentations were done at constant load up to 2 mN. A constant distance around 5 μm was held between each imprint in order to avoid any overlapping effect. Results were analyzed by InView software (KLA, USA). Prior to nanoindentation studies, the metallic discs were abraded up to 4000 grit and polished with silica.

II.4. Corrosion evaluation

The corrosion behavior of Zn and Zn alloys was studied by potentiodynamic polarization (PDP) test [40], static immersion test [41], and electrochemical impedance spectroscopy (EIS). The solution used for all corrosion tests was Hanks' solution (H4891, Sigma-Aldrich, USA) supplemented with $NaHCO_3$ (Sigma-Aldrich, USA) and $CaCl_2 \cdot 2H_2O$ (Sigma-Aldrich, USA) to simulate the ionic composition of blood plasma but without Mg^{2+} to avoid interfering with the ICP-MS measurements. The chemical composition of the solution is listed in **Table S1.** The volume of the solution was 20 mL for all tests. The metallic discs were abraded up to 4000 grit and ultrasonically cleaned with absolute ethanol and acetone. The area of the samples exposed to the solution was 0.79 cm^2 in all cases. For this purpose, Lacomit varnish (Agar Scientific, UK) was used for electrochemically isolate the non-exposed areas.

II.4.1. Potentiodynamic polarization test

Electrochemical analysis was performed in Hanks' modified solution at 37 ± 1 ºC and pH 7.4 using a PARSTAT 2273 potentiostat (Princeton Applied Research, USA). Saturated calomel electrode (SCE) and platinum electrode were used as the reference electrode and counter electrode, respectively. After 30 min of stabilization of the open circuit potential (OCP), polarization curves were obtained by scanning from -1.4 to -0.6 V potential against the OCP at a scan rate of 0.16 mV/s, according to ASTM G5-14 [40]. The corrosion current density (i_{corr}) and the corrosion potential (E_{corr}) were determined by extrapolating the cathodic Tafel line with Origin 2020 software (OriginLab, USA). The corrosion rate (CR) (μm/year) was calculated from the corrosion current density using Eq. 1 [42]:

$$CR = 3.27 \cdot 10^{-3} \frac{i_{corr} EW}{\rho} \tag{1}$$

where i_{corr} is the corrosion current density (μA/cm^2), EW is the equivalent metal weight and ρ is the metal density. According to ASTM G102-89 [42], the EW and ρ used for calculation were 32.68, 32.42, 32.15, 33.70, 34.41, and 7.14, 7.11, 7.09, 7.19, 7.23 g/cm^3 for Zn, Zn-0.5Mg, Zn-1Mg, Zn-3Cu, and Zn-5Cu, respectively.

II.4.2. Static immersion test

Static immersion test was performed according to ASTM G31-72 [41]. Samples were first weighted and then totally immersed during 10 days in 20 mL of Hanks' modified solution under non-aerated controlled conditions (T = 37 ± 1 ºC, pH 7.4 ± 0.1). The whole solution was renewed every 48 h. Aliquots of the solution collected at 1, 3, 7, and 10 days of immersion time were filtered with 0.2 μm filter and the released concentration of Zn^{2+}, Mg^{2+}, and Cu^{2+} was determined by using Inductively Coupled Plasma Mass Spectroscopy (ICP-MS) **(**7800 ICP-MS**,** Agilent Technologies). The redox potential (E) and the pH were monitored during the immersion test with Hanna HI 5521 multiparameter (Hanna Instruments, Italy). After 10 days of immersion, the corrosion products accumulated onto the sample surface were ultrasonically removed with a solution of 200g/L CrO_3 at 70 ºC according to ISO 8407 [43]. Degraded samples were then weighted to calculate the CR through weight loss according to Eq. (2) [41]:

$$CR = (8.76 \cdot 10^4 \times W)/(A \times T \times D) \qquad (2)$$

where W is the weight loss (g) after the removal of the corrosion products, A is the sample surface area exposed to the solution (cm^2), T is the immersion time (h), and D is the metal density (g/cm^{-3}).

Surface morphology and chemical composition of the Zn alloys before and after the removal of corrosion products were examined by SEM, EDS, and confocal Raman microscopy (inVia^{TM} Qontor® confocal Raman microscope, Renishaw Inc.).

II.4.3. Electrochemical impedance spectroscopy (EIS)

EIS experiments were carried out in Hanks' solution at 37 ºC and pH 7.4 for 7 days. A conventional three-electrode electrochemical cell as described in II.4.1 was used with an exposed area of the working electrode of 0.8 cm^2. The EIS data were recorded at OCP applying AC amplitude of 10 µA·rms from 10^5 Hz down to 10^{-2} Hz. ZSimpWin v3.21 software, Princeton Applied Research was used to treat the raw data.

II.5. Wettability

Static contact angles (SCA) measurements on Zn and Zn alloys surfaces were performed using a Contact Angle System OCA15 plus (Dataphysics, Germany) with the sessile drop method. Prior to measurements, metallic discs were ground up to P4000 grit and ultrasonically cleaned with absolute ethanol. All measurements were done at room temperature with 3 µL ultrapure milli-Q water drop. SCA were calculated at 5, 10, 15, 20, 25, and 30 seconds after drop deposition using a Laplace-Young fitting with SCA20 software (Dataphysics, Germany). Prior to wettability measurements, the metallic discs were abraded up to 4000 grit and ultrasonically cleaned with absolute ethanol and acetone.

II.6. Antibacterial activity

Staphylococcus aureus (*S. aureus,* CCUG 15915, Culture Collection University of Göteborg (CCUG), Göteborg, Sweden) and *Pseudomonas aeruginosa* (*P. aeruginosa,* CECT 110, Colección Española de Cultivos Tipo (CECT), Valencia, Spain) were used as Gram positive and Gram negative bacteria model to determine the antibacterial properties of Zn and the Zn alloys samples *in vitro*. Bacteria in frozen stock were aerobically cultured in a brain heart infusion (BHI, Scharlab, Spain) medium at 37 ± 1 ºC overnight. Afterwards bacteria were diluted in BHI medium to achieve a final optical density of 0.2 at 600 nm, corresponding to 10^8 colony forming units (CFU) per milliliter.

The inhibition effect on *S. aureus* and P. aeruginosa of Zn and Zn alloys was measured by the agar diffusion plate test. Agar plates were prepared by mixing the culture medium with 7.5g of agar (Agar bacteriological, Scharlab, Spain). Sterilized agar plates were inoculated with 100 µL of the bacteria suspension at 10^8CFU/mL. Based on CLSI M07-A9 [44], the samples were sterilized by immersion in ethanol 96% (v/v) for 30 min, washed with PBS, put in contact with the plates with spread bacteria and incubated at 37 ± 1 ºC for 24 h. The antibacterial activity is related to the size of inhibition zone (H), which can be calculated as describes Eq. 3 [44]:

$$H = (D - d)/2 \tag{3}$$

Where *H* is the inhibition zone in mm, D is the total diameter of specimen and inhibition zone in mm, d is the diameter of specimen in mm. The ideal antibacterial effect occurs when $H \geq 1$. When H = 0 and few bacteria are observed, the antibacterial effect is limited; when H = 0 and many bacteria observed, there is no antibacterial effect. The image analysis was performed using ImageJ software (National Institutes of Health, MD).

Moreover, the adhesion test was performed by adding 20 µL of the bacteria suspension at 10^8CFU/mL to each sample and incubating at 37 ± 1 ºC for 2h. After incubation, samples were rinsed in PBS three times to remove the non-adhered bacteria. The adhered bacteria were fixed with 500 µL of 2.5% glutaraldehyde in PBS at 5 ± 1 ºC for 30 minutes. Samples were then dehydrated sequentially in a series of ethanol water mixtures (50%, 70%, 90%, 96%, and 100%) for 10 min each. The morphology and number of the adhered bacteria were analyzed by SEM.

II.7. Endothelial cell *in vitro* assays

Human aortic endothelial cells (HAoEC, 304-05a Cell Applications®) were cultured under standard conditions (humidified atmosphere, 5% CO_2 at 37 ± 1ºC) in Growth

Medium ready to use (211-500, Cell applications®) in Nunc tissue culture flasks (Termo Fisher Scientific) and passaged when reached 60–70% confluency. Cell isolation from culture flasks was made by 1 mL-trypsinization (Trypsin/EDTA, Sigma-Aldrich) at room temperature for 5 min followed by cell rinsing and resuspension in Growth Medium. Cells were used for experiments at passage 8-12. Cell viability was determined using cytotoxicity detection kit^{PLUS} lactate dehydrogenase (LDH, Roche®) assay, a microplate reader and calculated as a ratio to the positive control group. Each material was assessed by triplicate.

Cytotoxicity assays were performed according to ISO 10993-5/12 [45,46]. Indirect cell viability of HAoEC was measured after 24 h incubation in supernatant at various dilutions. Prior to cell experiments, the discs were sterilized by immersion for 20 minutes in ethanol followed by three baths with phosphate buffered saline (PBS, Sigma-Aldrich, USA) solution. The supernatants were prepared by immersion of discs (surface finish: polished with 4000 grit emery paper) in Growth Medium ready to use under standard conditions for 3 days at a surface-to-volute ratio of 3 cm^2/mL [46]. Aliquots of supernatants were prepared at 1, 1:1, 1:10, 1:100 and 1:1000 volume-to-volume ratio. Prior to the addition of supernatants, cells were incubated for 24 h in fresh Growth Medium on 96-well plate at a cell density of 10.000 cells/well to allow attachment. After that, the medium was replaced by the diluted supernatants. Cell viability was determined using cytotoxicity detection kit^{PLUS} LDH assay. The optical density was measured at the wavelength of 492 nm using a microplate reader (Synergy HTX, Biotek) and calculated as a ratio to the positive control group.

HAoEC adhesion/proliferation tests were performed for 1 day, 3 days and 7 days (500 µl with 3×10^4 cells/sample). Cell were seeded onto the alloys polished surfaces previously sterilized as described-above and cultured under standard conditions. Experiments were performed by triplicate for viability measurements by LDH assay as described above and additional samples were run for microscopical observation. For this purpose, cells were fixed with 4% paraformaldehyde (PFA, Sigma-Aldrich, USA) for 30 min followed by three baths with phosphate buffered saline (PBS) solution to remove residual PFA and dehydrated through an ascending series of 50%, 70%, 95% and 100% ethanol for SEM observation. For confocal laser scanning microscopy characterization (Carl ZEISS LSM 800) of viable/dead cells, a double staining Kit (Sigma-Aldrich) of Calcein-AM and Propidium Iodide (PI, Sigma-Aldrich, USA) was used.

II.8. Statistical Analysis

The experimental data collected in this study were reported as mean ± standard deviation (SD). Unless previous specified, all physicochemical characterization and cell culture experiments were performed with $n = 3$ samples for each specimen group for each assay used in this study. A normality test (Shapiro-Wilk test) was performed to determine if data-set were modeled by a normal distribution. An equality of variances test (ANOVA) was used to determine statistically significant differences when data were normally distributed. A non-parametric test (Kruskal-Wallis test) was used for non-normally distributed data (p-value < 0.05 for all tests). Statistical analysis was performed using Minitab Statistical Software (Minitab Inc., USA).

III. Results

III.1. Microstructure

Fig. 1 shows SEM images of the microstructure of metallic discs in the cross-section (left) and longitudinal section (right), the detected phases, and their volume fraction. The microstructure of the longitudinal section confirmed the preferential grain orientation due to cold rolling manufacturing for Zn-based alloys (**Fig. 1d, f, h, j**). Pure Zn microstructure consisted of heterogeneous grains of Zn, ranging from 200 μm up to 1 mm at the cross-section, with partial recrystallization [47]. On the other hand, the microstructure of Zn-Mg alloys consisted of Zn matrix and eutectic mixture of Zn+Mg_2Zn_{11} formed along the grain boundaries of $\alpha-$Zn (**Fig. 1c-f**). Image analysis confirmed an increase of the volume fraction for the eutectic mixture from 10 % to 19 %, for Zn-0.5Mg and Zn-1Mg alloys respectively, with increasing content of alloying element (**Fig. S1a-d**). Zn-Cu alloys presented a dual-phase microstructure of Zn and the dendritic ε-$CuZn_5$ phase (**Fig. 1g-j**). **Fig. 1h-i** showed elongated ε-dendrites and η-Zn grains following the rolling direction. The volume fraction of intermetallic ε-phase significantly increased with the higher percentage of Cu content in the alloy, 7% for Zn-3Cu alloy and 25% for Zn-5Cu alloy (**Fig. S1e-f**). XRD results confirmed the phases composition of studied samples are in **Fig. S2.**

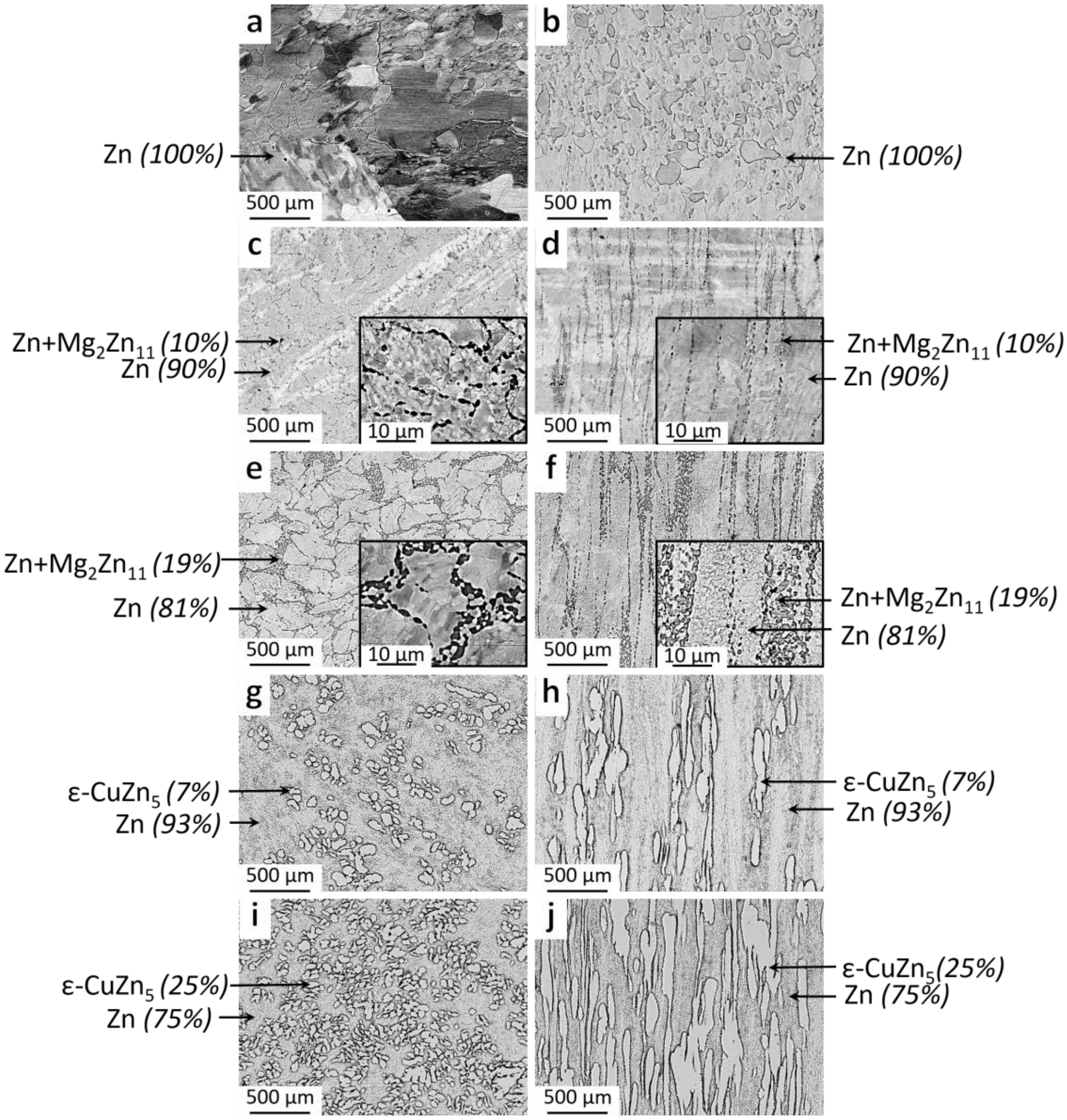

Fig. 1. Microstructure of the cross-section (left) and longitudinal (right) of: extruded Zn (a, b), and cold rolled Zn-0.5Mg (c, d), Zn-1Mg (e, f), Zn-3Cu (g, h), and Zn-5Cu (I, j) alloys.

III.2. Mechanical properties

Tensile mechanical properties and Vickers hardness results are shown in **Fig. 2** with UTS, YS, elongation at break and Vickers hardness (HV) parameters. Pure Zn showed low values of YS (30 ± 6 MPa), UTS (97 ± 7 MPa), and fracture elongation (8 ± 2 %) for this application. As expected, the increasing Mg concentration significantly enhanced the YS up to 192 ± 13 and 222 ± 6 MPa for Zn-0.5Mg and Zn-1Mg, respectively. The UTS values also increased to 219 ± 7 MPa for Zn-0.5Mg, and 260 ± 8 MPa for Zn-1Mg alloy. However, the elongation at break reached 28 ± 6% for Zn-0.5Mg but dramatically decreased down to 11 ± 1% for Zn-1Mg alloy.

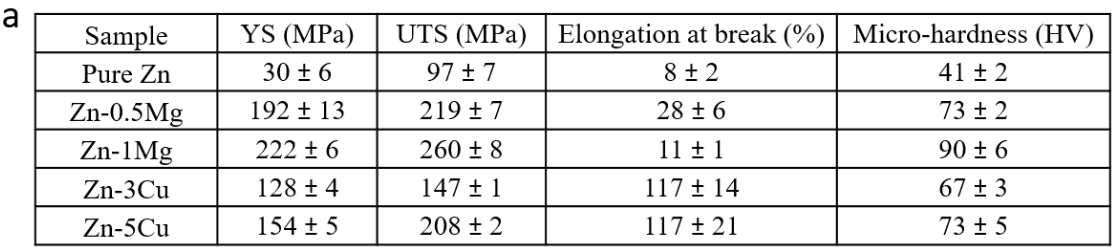

a

Sample	YS (MPa)	UTS (MPa)	Elongation at break (%)	Micro-hardness (HV)
Pure Zn	30 ± 6	97 ± 7	8 ± 2	41 ± 2
Zn-0.5Mg	192 ± 13	219 ± 7	28 ± 6	73 ± 2
Zn-1Mg	222 ± 6	260 ± 8	11 ± 1	90 ± 6
Zn-3Cu	128 ± 4	147 ± 1	117 ± 14	67 ± 3
Zn-5Cu	154 ± 5	208 ± 2	117 ± 21	73 ± 5

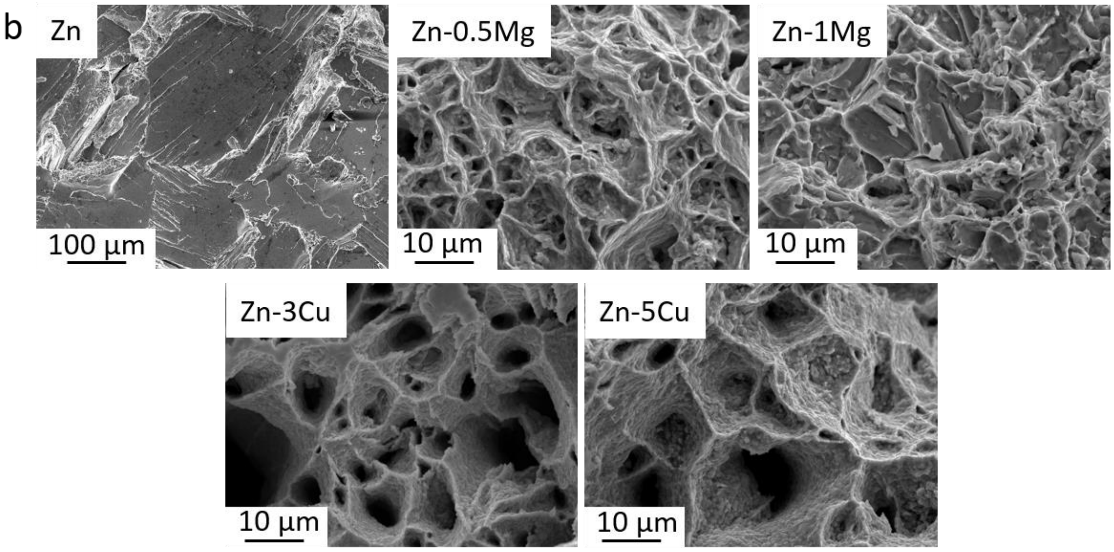

Fig. 2. Tensile test of Zn-Mg and Zn-Cu alloys: a) mechanical parameters obtained after tensile and micro-hardness testing. $^{a, b,}$ symbols join groups with non-statistically significant differences. b) SEM morphology of the tensile fracture surface.

The tensile mechanical properties of Zn-Cu alloys were improved compared to pure Zn. Both YS and UTS parameters were 128 ± 4 and 147 ± 1 MPa for Zn-3Cu alloy, and 154 ± 5 and 208 ± 2 MPa, for Zn-5Cu alloy, respectively. As observed, elongation at fracture consistently increased up to 117 % for Zn-Cu alloys. No statistical differences in fracture elongation were observed between Zn-3Cu and Zn-5Cu alloys. Vickers micro-hardness of pure Zn resulted of 41 ± 2 HV while Zn-Mg alloys showed higher values up to 90 ± 6 HV for Zn-1Mg alloy (**Fig. 2a**). This trend is attributed to the increasing volume fraction of the hard Zn+Mg_2Zn_{11} eutectic phase. For Zn-Cu alloys, the hardness was also enhanced up to 73 ± 5 HV for Zn-5Cu alloys, correlated with the larger the volume fraction of ε-$CuZn_5$ intermetallic phase.

The morphology of the fracture surfaces after tensile testing tests is shown in **Fig. 2b**. The fracture surface of pure Zn presented fully trans-granular morphology, indicating a brittle fracture without plastic deformation, in accordance to its low fracture elongation (8 ± 2 %). Zn-0.5Mg alloy exhibited dimple-fracture features, which is consistent with the enhanced elongation at fracture (28 ± 6 %) compared to pure Zn. The number of plastic dimples decreased with the increasing in Zn-1Mg alloy, and the predominance of cleavage planes confirmed the macroscopic fragility and lower elongation at fracture (11 ± 1 %). Zn-Cu alloys fracture surface exhibited a ductile fracture behavior, coherent with the larger elongation at break value of around 117 %. The magnitude of the ridges suggested more refined microstructure of Zn-Cu alloys when compared to Zn, and larger grain size than Zn-Mg alloys.

As shown in **Fig. 3**, nanoindentations on Zn matrix and secondary phases (eutectic Zn+Mg_2Zn_{11} for Zn-Mg alloys, and peritectic ε-$CuZn_5$ for Zn-Cu alloys) provided the hardness and elastic modulus (E) of each specific phase (**Table 2**). The Zn matrix showed hardness of 1.11 ± 0.08 GPa for pure Zn. Statistically higher values for Zn-0.5Mg, and Zn-1Mg alloys (1.18 ± 0.15, and 1.19 ± 0.12 GPa, respectively), and statistically lower values for Zn-3Cu (0.82 ± 0.13 GPa) and Zn-5Cu (0.84 ± 0.15 GPa) were reported. E values ranged from 71 up to 89 GPa but no statistical differences were found between studied surfaces.

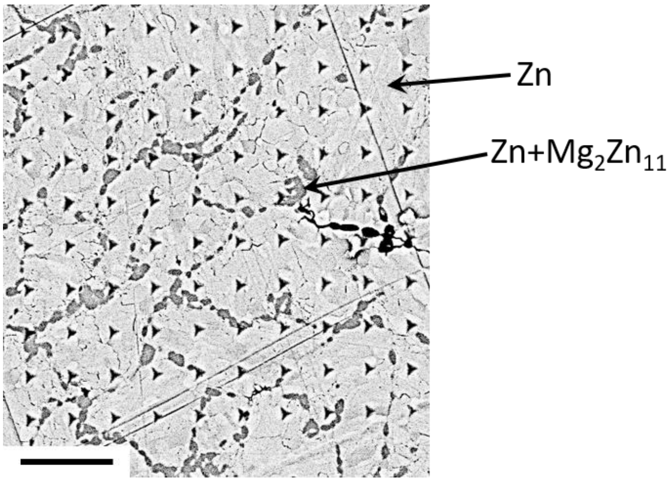

Fig. 3. SEM image of nanoindented Zn-0.5Mg alloy with the matrix of 10 by 10 nanoindentations and the phases composition. Scale bar: 10 μm.

Table 2. Elastic modulus and hardness of the zinc matrix and the secondary phases of the tested samples.

Surface	**Zn matrix**		**Secondary phase***	
	Hardness (GPa)	**E (GPa)**	**Hardness (GPa)**	**E (GPa)**
Pure Zn	1.11 ± 0.08^a	89 ± 5	n.d.	n.d.
Zn-0.5Mg	1.18 ± 0.15^b	80 ± 12	2.50 ± 0.64^a	98 ± 2^a
Zn-1Mg	1.19 ± 0.12^b	71 ± 21	2.65 ± 0.46^a	100 ± 11^a
Zn-3Cu	0.82 ± 0.13^c	75 ± 5	1.85 ± 0.33^b	104 ± 5^b
Zn-5Cu	0.84 ± 0.15^c	80 ± 9	1.84 ± 0.43^b	106 ± 4^b

* Zn+Mg_2Zn_{11} for the Zn-Mg alloys, and ε-$CuZn_5$ for the Zn-Cu alloys, n.d. not determined. $^{a, b, c}$ symbols join groups with non-statistically significant differences.

High-speed nanoindentation test provided values of Zn matrix hardness of 0.89 ± 0.272, 1.104 ± 0.216, and 1.112 ± 0.329 GPa for pure Zn, Zn-1Mg, and Zn-3Cu, respectively. The reported hardness of the ε-$CuZn_5$ secondary phase was 2.008 ± 0.328 GPa, and higher hardness was obtained for Zn+Mg_2Zn_{11} (2.684 ± 0.457 GPa). Hardness histograms and maps compiled from the high-speed nanoindentation test are shown in **Fig. S3**. The E values of Zn matrix were 69.73 ± 11.88, 72.47 ± 9.41, and 75.36 ± 17.32 GPa for Zn, Zn-1Mg, and Zn-3Cu, respectively. The E of secondary phases was 95.70 ± 9.15 GPa, for Zn+Mg_2Zn_{11}, and 109.92 ± 11.26 GPa for $CuZn_5$.

III.3. Corrosion behavior

III.3.1. Potentiodynamic polarization test

The corrosion resistance of the alloys was first evaluated by potentiodynamic measurements in modified Hanks' solution at 37 ± 1 °C. Prior, OCP curves measured upon stabilization are presented in **Fig. S4**. The most representative polarization curves for pure Zn and Zn alloys are shown in **Fig. 4**. The behavior of the cathodic region was similar for all materials, whereas some differences were observed in the anodic region as a function of the alloy composition. In all cases, a net anodic potential was observed at approximately -1.1 V (see E_{corr} in **Table 3**).

Three regions are observed in the anodic branch: first, an activation region around the E_{corr}; followed by a passive region where potential shifts towards to more positive values with low variation of current density; and finally, a third region where it is detected a change in the anodic-current slope around –0.9 V. In the case of Zn-3Cu and Zn-5Cu, the passive region is not as pronounced as in the case of Zn, Zn-0.5Mg and Zn-1Mg. The passive region for Zn-5Cu is much smaller than that of the other materials, with an evident breakdown of the passive corrosion layer at about –1.0 V. The constant increasing of the current density for Zn-3Cu and Zn-5Cu above E_{corr}, suggest that the passive layer formed on these alloys is less protective than the layer formed on Zn and the Zn-Mg alloys. Moreover, Zn-Mg alloys displayed higher anodic current density than Zn-Cu alloys and pure Zn (see i_{corr} in **Table 3**). The calculated CR from potentiodynamic curves was around 0.03 mm/year for all samples (see CR from PDP test in **Table 3**).

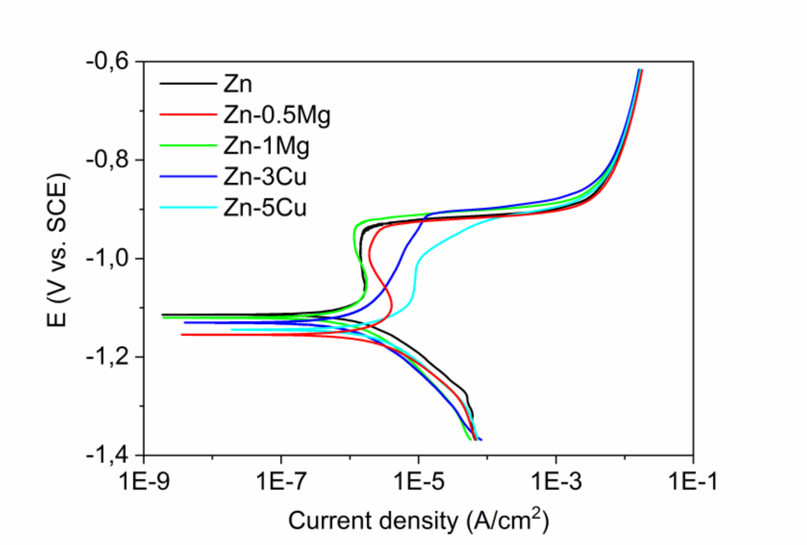

Fig. 4. Potentiodynamic polarization curves of Zn, Zn-0.5Mg, Zn-1Mg, Zn-3Cu, and Zn-5Cu in Hanks' solution at 37 ± 1 ºC.

Table 3. Corrosion parameters obtained from PDP test (E_{corr}, i_{corr}, and CR), and calculated CR by weight loss after 10 days of immersion in Hanks' solution at 37 ± 1 ºC and pH 7.4.

Surface	**Corrosion parameters from PDP test**			**CR, immersion test (mm/year)**
	E_{corr} (V)	**i_{corr} (µA·cm^{-2})**	**CR (mm/year)**	
Pure Zn	-1.1237 ± 0.0171	2.10 ± 0.05	0.031 ± 0.001	0.132 ± 0.046
Zn-0.5Mg	-1.1289 ± 0.0348	2.34 ± 0.29	0.035 ± 0.004	0.115 ± 0.004
Zn-1Mg	-1.1298 ± 0.0202	2.45 ± 0.65	0.036 ± 0.010	0.105 ± 0.017
Zn-3Cu	-1.1479 ± 0.0215	2.02 ± 0.56	0.031 ± 0.009	0.094 ± 0.005
Zn-5Cu	-1.1293 ± 0.0234	2.21 ± 0.51	0.034 ± 0.008	0.103 ± 0.009

III.3.2. Static immersion test

CR was calculated from degraded samples after 10 days of immersion into modified Hank's solution and subsequent removing of corrosion products, obtaining a value of approximately 0.1 mm/year for all samples (see CR, immersion test in **Table 3**). **Fig. 5a** shows the curves of Zn^{2+} release after 1, 3, 7, and 10 days of immersion in Hanks' solution. The released Zn^{2+} reached a maximum between 100 – 150 µg/dL at day 1, and decreased towards a minimum below 8.0 µg/dL at day 10 for all samples. For Zn-Mg alloys, the Mg^{2+} concentration detected was below 10 µg/dL. The detection limit for ICP-MS is 0.01 µg/dL, and Cu^{2+} cations were not detected in any case. Indicating that Cu^{2+} concentration in inorganic Hanks' solution was lower than 0.01 µg/dL.

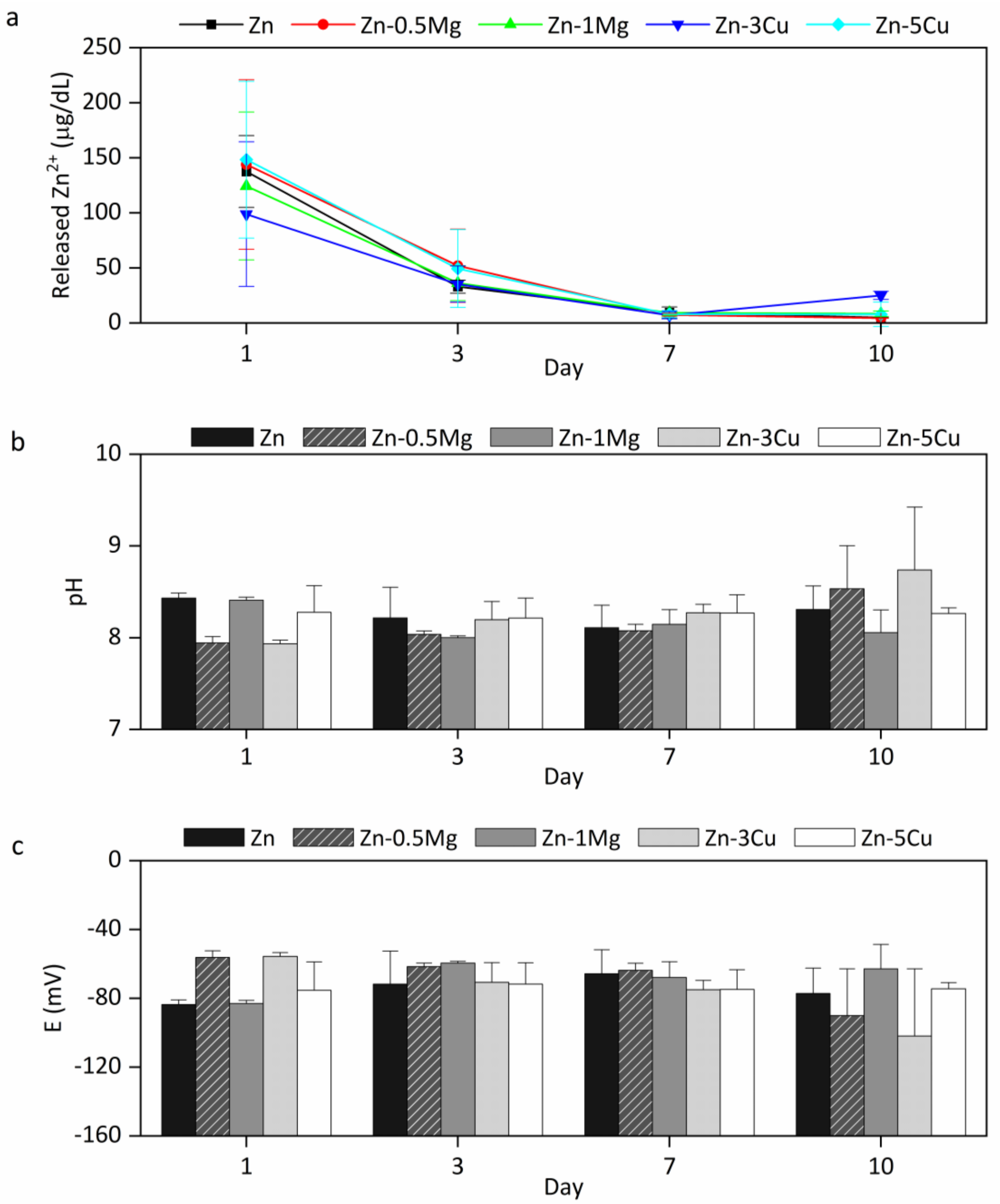

Fig. 5. Immersion evaluation of studied Zn and Zn-based surfaces after 1, 3, 7, and 10 days in Hanks' solution at 37ºC: (a) Values of released Zn^{2+} expressed as (µg/dL), (b) pH, and (c) redox potential.

Fig. 5b showed a pH increase from 7.4 ± 0.1 of Hanks' solution during the immersion test confirming the corrosion of all studied samples. Finally, negative values of redox potentials were maintained during the degradation of all samples, maintaining the redox homeostasis for a normal physiological steady state (**Fig. 5c**) [48]. SEM images of the corroded samples before and after the removal of the corrosion products are presented in **Fig. 6**.

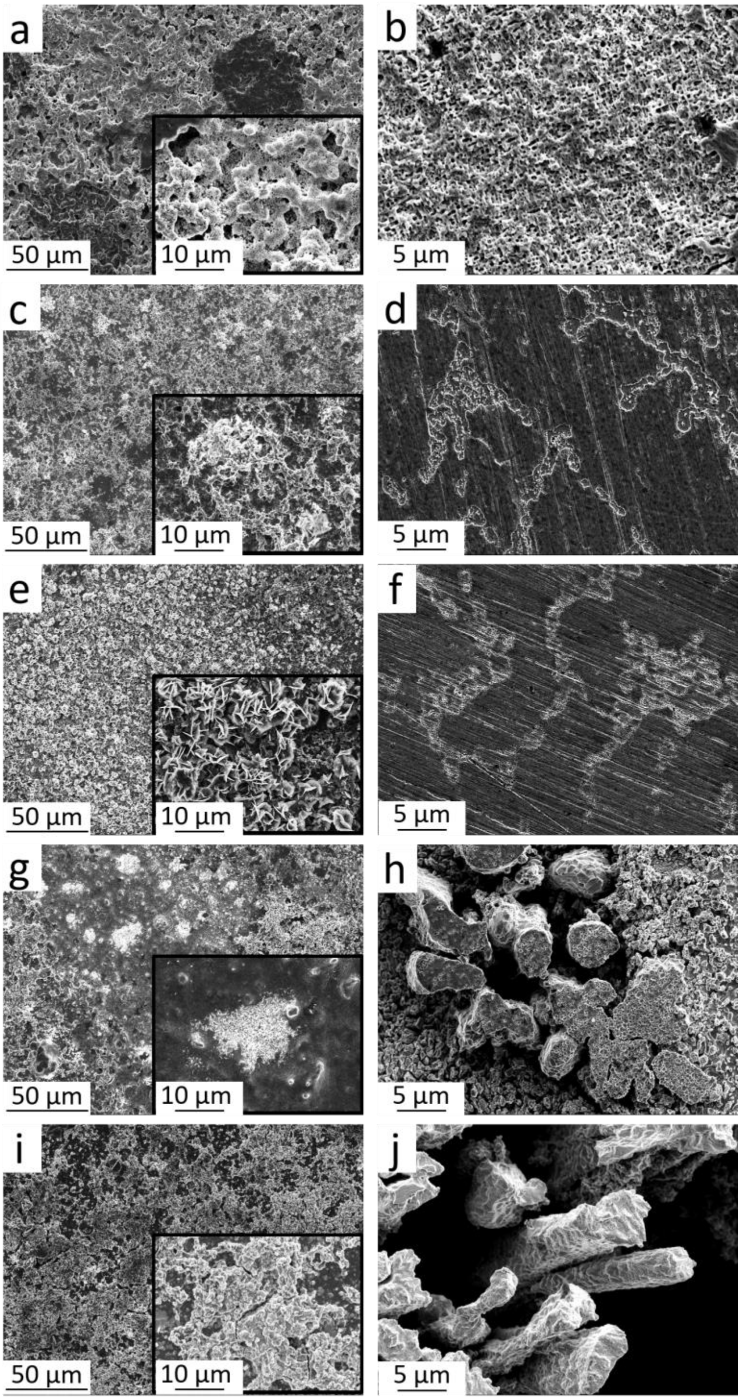

Fig. 6. SEM images of the corroded samples after 10 days of immersion in Hanks' solution at 37℃, before (left column) and after (right column) the removal of the corrosion products: Zn (a, b), Zn-0.5Mg (c, d), Zn-1Mg (e, f), Zn-3Cu (g, h), and Zn-5Cu (i, j).

SEM images of corroded surfaces showed similar rounded-features for pure Zn (**Fig. 6a**) and Zn-5Cu (**Fig. 6i**). The Zn-0.5Mg alloy combined these rounded-shapes with crystals with morphology typical of hydroxyapatites (**Fig. 6c**), which formed a uniform corrosion layer in the case of the Zn-1Mg alloy (**Fig. 6e**). EDS confirmed the presence of Ca, O and P. The corrosion products of Zn-3Cu alloy were clustered in specific areas suggesting localized corrosion (**Fig. 6g**). EDS analysis confirmed the presence of Zn, Ca, C, O, P, and Cl in the corroded surfaces of the samples. Mg and Cu were detected at the surface of corroded Zn-Mg alloys and Zn-Cu alloys, respectively. Raman spectra of the corroded mineral surfaces (**Fig. S5**) confirmed the presence of complex Zn mineral phases (*simonkolleite* ($Zn_5(OH)_8Cl_2{\cdot}H_2O$), *hydrozincite* ($Zn_5(CO_3)_2(OH)_6$) and s*korpionite* ($Ca_3Zn_2(PO_4)_2CO_3(OH)_2{\cdot}H_2O$)), and hydroxyapatite (**Fig. S5**).

After removal of the corrosion products, a uniform corroded surface of pure Zn was revealed (**Fig. 6b**). On the other hand, micro-galvanic activity between Zn matrix and the secondary phases for the alloys confirmed galvanic corrosion mechanisms. SEM images of the corroded surfaces of Zn-Mg alloys (**Fig. 6d, f**) indicated faster degradation of Zn+Mg_2Zn_{11} eutectic than Zn matrix over all surfaces. On the contrary, Zn-Cu alloys showed areas nearly impassive and others with localized corrosion in which the degradation of Zn matrix is preferred over the ε-$CuZn_5$ phase (**Fig. 6h, j**). The powerful galvanic cell Zn/ε-$CuZn_5$ led to noticeable galvanic corrosion in Zn-5Cu alloy (**Fig. 6j**). The release of Zn^{2+} reached a maximum after 24 h of immersion and decreased to a minimum after 10 days. At every time point, the total Zn^{2+} concentration in solution is within the range of regular blood zinc level (60 – 240 ug/dL) [49,50]. Although similar CR values were obtained from weight difference, different corrosion mechanisms were evidenced. Uniform degradation behavior was evidenced for pure Zn. However, the presence of secondary phases forms galvanic pairs with Zn matrix that resulted in galvanic corrosion. The degradation of both Zn+Mg_2Zn_{11} eutectic and ε-$CuZn_5$ peritectic has been observed. Faster degradation of Zn+Mg_2Zn_{11} than Zn matrix was observed all over the surface of Zn-Mg alloys, whereas Zn-Cu alloys showed points of localized corrosion in which the ε-CuZn5 peritectic remained impassive and Zn matrix considerably degraded. This behavior is coherent with the polarization curves that showed less protective passive film for Zn-Cu alloys than those for Zn-Mg alloys (**Fig. 4**).

III.3.3. Corrosion evolution by EIS

The corrosion behavior of Zn and the four Zn alloys was determined by EIS measurements at open circuit potential. The most representative Nyquist plots of all materials and the equivalent circuits (ECs) are depicted in **Fig. 7**. The corrosion degradation behavior was based on the formation and breakdown of the corrosion products layer as previously reported [51–53].

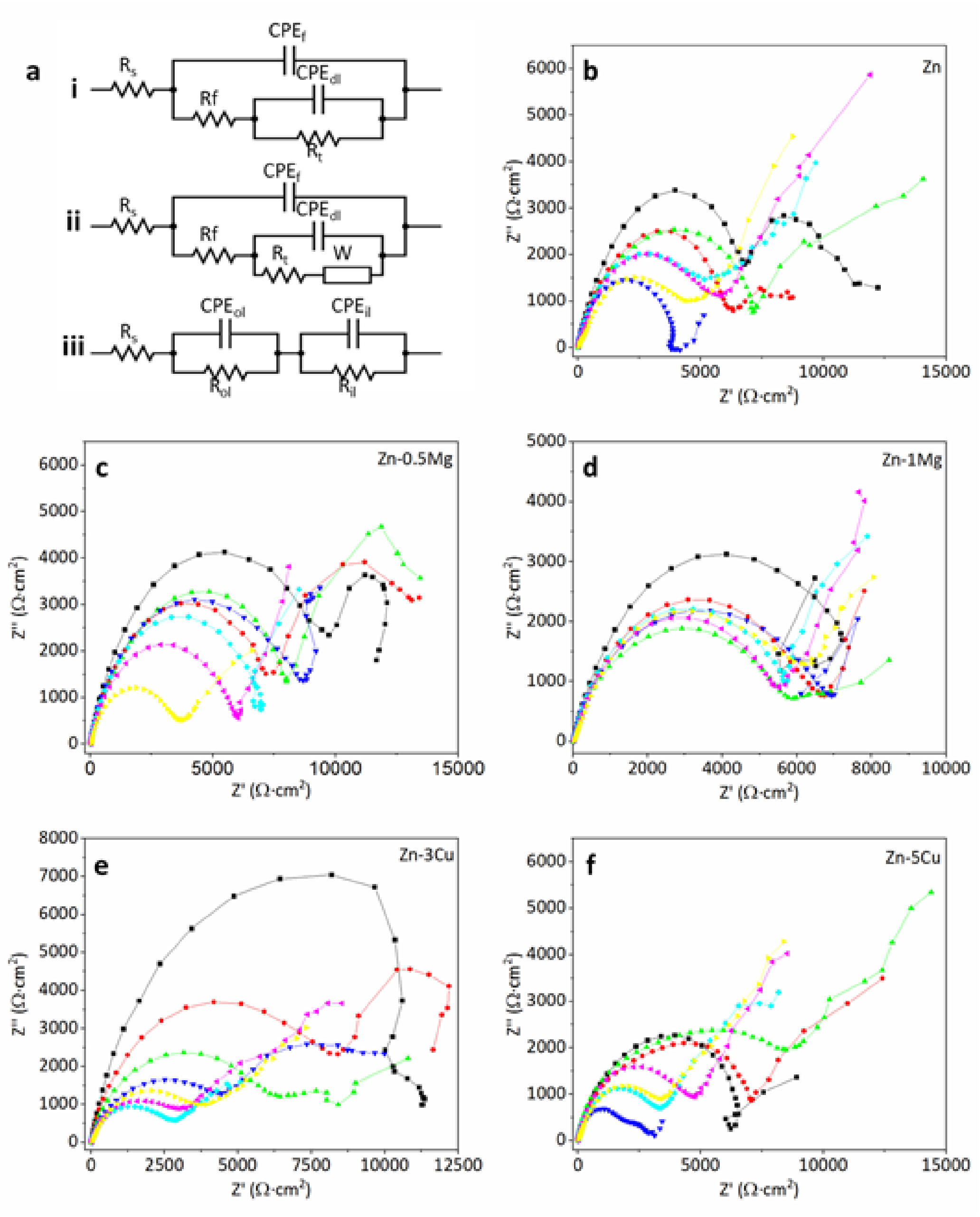

Fig. 7. Electrochemical impedance spectroscopy (EIS) evaluation in Hanks' solution of Zn and Zn-based alloys: (a) Equivalent circuits of (i) passivation layer, (ii) porous layer, and (iii) bi-layer model. EIS Nyquist plots: (b) Zn, (c) Zn-0.5Mg, (d) Zn-1Mg, (e) Zn-3Cu, and (f) Zn-5Cu. Time after immersion: ●*-2h,* ●*-4h,* ▲*-8h,* ▼*-26h,* ◆*-2d,* ◀*-3d, and* ▶*-7d.*

The Nyquist plots for pure Zn (**Fig. 7b**) and Zn-0.5Mg alloy (**Fig. 7c**) evidenced dynamic corrosion mechanisms where initially a corrosion layer was formed, followed by its rupture at later stages. Two capacitive loops appeared for pure Zn at 2 h after immersion. The high frequency capacitive loop could be assigned to charge transfer resistance, and the mid-frequency capacitive loop could be attributed to the electrolyte resistance inside the corrosion film pores. The EC used for the fitting the experimental data is presented in **Fig. 7a,ii**. The circuit consists of the following elements: R_s (solution resistance), R_{ct}

(charge transfer resistance), CPE_{dl} (double layer capacitance), R_f (resistance of the solution inside the pores of the corrosion film), and Warburg component (W) which represents diffusion controlled processes through the corrosion layer [54]. The impedance modulus (|Z|) of pure Zn at 2 h was 3389 $\Omega\cdot cm^2$ and decreased down to 2501 $\Omega\cdot cm^2$ at 4 h, indicating the progression of the corrosion processes. The evolution of |Z| suggested that the corrosion layer appeared between 4 and 8 h. After 8 h of immersion, the mid-frequency loop transformed and better fitted to an EC without W component (**Fig. 7a,i**), suggesting a densification of the corrosion film. The local breakdown of this film was recorded after 26 h. The increase of |Z| up to 2018 $\Omega\cdot cm^2$ at 2 days could be assigned to the thickening of a corrosion film, whose barrier properties were deteriorated after 7 days of immersion leading to lower corrosion resistance (|Z| = 1516 $\Omega\cdot cm^2$).

Fig. 7c shows the Nyquist plots of Zn-0.5Mg alloy. A corrosion layer appeared after 4 h of immersion (fitted to **Fig. 7a,i**). At 8 h of immersion the Nyquist plots fitted to the EC shown in **Fig. 7a,iii**, which is modeled by an inner layer (R_{il}, CPE_{il}) and an outer layer (R_{ol}, CPE_{ol}) [51]. Here, the inner layer and the outer layer corresponded to the oxide film initially formed and the later deposited hydroxyapatite crystals shown in **Fig. 6c**, respectively. The |Z| of Zn-0.5Mg decreased from 2138 $\Omega\cdot cm^2$ at 3d to 1213 $\Omega\cdot cm^2$ at 7 d, suggesting the deterioration of the corrosion layer (fitted to **Fig. 7ii**).

In the case of Zn-1Mg, the |Z| decreased from 2 h to 8 h (**Fig. 7d**). After 8 h, the increase of |Z| suggested a corrosion layer formation. Beyond 2 days, minor fluctuations of |Z|, which was 2100 $\Omega\cdot cm^2$, were observed; this indicated a more stable corrosion products film compared to those formed on Zn and Zn-0.5Mg. EC used for the fitting was **Fig. 7ii**.

The impedance of Zn-3Cu (**Fig. 7e**) continuously decreased from 2 h to 2 days. After this period, |Z| slightly raised and stabilized about 1300 $\Omega\cdot cm^2$. In the case of Zn-5Cu (**Fig. 7f**), it showed a rather stable behavior at early immersion (2 h – 8 h) after which |Z| had a sharp drop between 8 and 26 h (both Zn-Cu alloys fitted to **Fig. 7a,ii**). After 26 h, impedance of Zn-5Cu slightly increased and continued with minor fluctuations over the remaining of the immersion. The curves fitted to the EC in **Fig. 7d**. In general, both Zn-Cu alloys showed lower corrosion resistance than the Zn-Mg alloys in Hanks' solution under the here studied conditions.

III.4. Wettability

Fig. S6 illustrates the wettability of studied Zn and Zn-based alloys with deionized water. For all studied surfaces, the contact angle slightly decreased with increasing deposition time, but no statistically significant differences were observed after 30 s. The contact angle of pure Zn at 5 s after the deposition of the droplet was 91.70 ± 1.03°**.** The Zn-Cu alloys were more hydrophobic (92.71 ± 0.70º for Zn-3Cu; and 97.32 ± 3.61º for Zn-5Cu), while the Zn-Mg alloys showed a more hydrophilic behavior compared to Zn (87.19 ± 0.60º for Zn-0.5Mg; and 85.73 ± 1.65º for Zn-1Mg). The wettability behavior of Zn-Mg and Zn-Cu alloys may be attributed to changes in the surface chemistry. Chemically heterogeneous surfaces (as multiphase alloys) count with multiple states individually associated with a local minimum in the Gibbs energy [55]. Here, samples series with higher fraction of $Zn+Mg_2Zn_{11}$ are more hydrophilic, whereas series with higher ε-$CuZn_5$ shown a more hydrophobic behavior.

III.5. Antibacterial activity

Agar diffusion test showed no inhibition zone for *S. aureus* cultured on pure Zn, Zn-0.5Mg, and Zn-1Mg, indicating no antibacterial effect. On the opposite, both Zn-Cu alloys manifested inhibition zone of 1 mm size (1 ± 0.07 mm for Zn-3Cu, and 0.88 ± 0.03 mm for Zn-5Cu). Moreover, no inhibition zone was observed for *P. aeruginosa* bacteria for any studied surface.

Fig. 8 shows the SEM images of the morphology of adhered *S. aureus* and *P. aeruginosa* after 2 h of culturing on the investigated samples. No morphology changes were observed in the *S. aureus* after 2 h in contact with the samples. However, the number of adhered bacteria on Zn-Mg alloys increased compared to pure Zn (**Fig. 8a, c, e**). On the other hand, there was much less *S. aureus* adhesion on the Zn-Cu alloys (**Fig. 8g, i**), especially the Zn-5Cu alloy, which showed an anti-adhesion performance against the *S. aureus*. Moreover, localized evidences of degradation of the Zn-5Cu surface were observed (**Fig. 8i**). The adhesion studies with *P. aeruginosa* showed that morphology remained intact after the culturing. Similar bacteria adhesion is observed for pure Zn, Zn-0.5Mg, and Zn-1Mg alloys (**Fig. 8b, d, f**, respectively). The number of bacteria adhered on the Zn-Cu alloys surfaces were lower in comparison to pure Zn (**Fig. 8h, j**). Additionally, it was observed surface morphology changes of Zn and Zn-Mg alloys after incubation with *P. aeruginosa*. SEM images showed that *P. aeruginosa* adhesion was higher onto degraded areas of Zn and Zn-Mg alloys compared to smoother parts (**Fig. 8b, d, f)**. No adhered bacteria were found onto non-degraded Zn-5Cu surface (**Fig. 8j).**

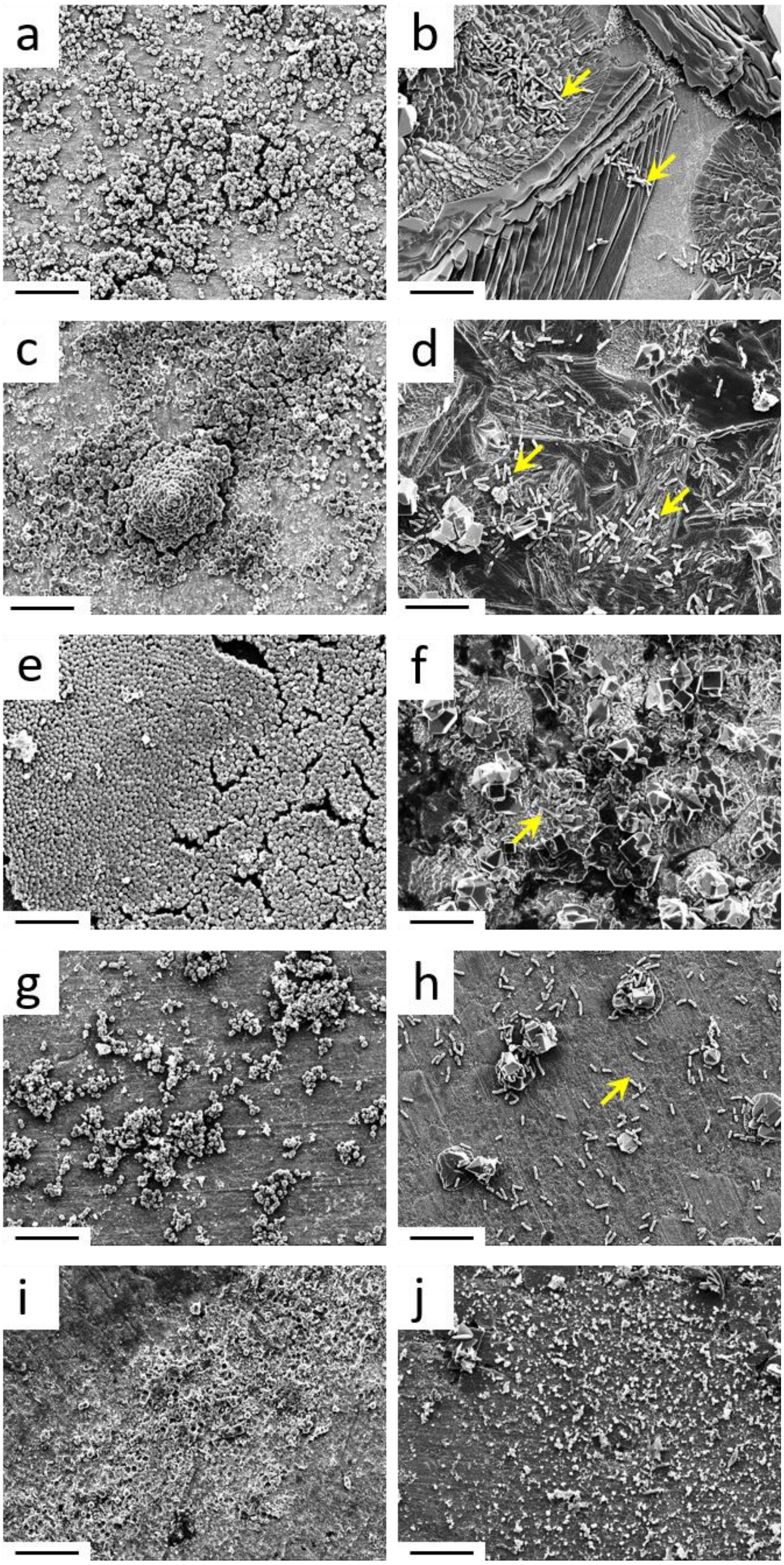

Fig. 8. SEM images of bacterial morphology for both *S. aureus* (left) and *P. aeruginosa* (right) after culturing for 2 h on pure Zn (a, b), Zn-0.5Mg (c, d), Zn-1Mg (e, f), Zn-3Cu (g, h), and Zn-5Cu (i, j). Scale bar: 20 µm. Yellow arrows indicate *P. aeruginosa* bacteria.

III.6. Endothelial cell response

III.6.1. Indirect contact cytotoxicity

Fig. 9 shows the results from cytotoxicity assays by indirect contact of HAoEC with metal extracts obtained from incubating alloys discs for 3 days in Growth Medium. Viability results suggested that Zn and the here studied alloys are cytotoxic to HAoEC. According to the ISO 10993-5 [45], a cell viability reduction larger than 30% is considered as cytotoxic. Since we measure viability as a ratio to the positive control group, a value below 70% indicates cytotoxicity. This was the case of cells cultured in undiluted and 50% diluted extracts. For diluted extracts below 1:10 v/v, there was not an evident cytotoxic effect, particularly in the case of Zn-Mg alloys. Among the alloys with Cu content, the results suggested cytotoxicity of Zn-5Cu.

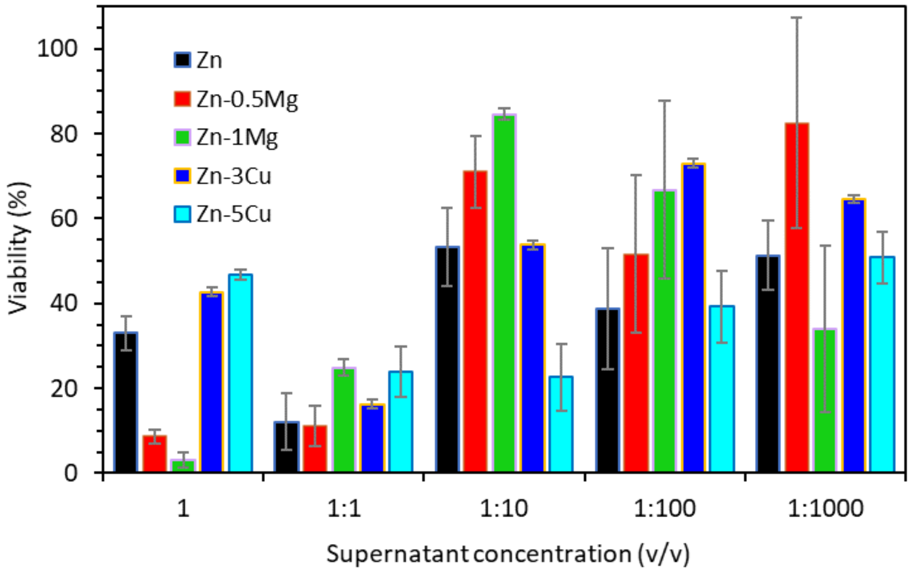

Fig. 9. Indirect HAoEC viability after 24 h of culture in supernatants prepared by immersion of the alloys in Growth Medium for 3 days. Aliquots of supernatants at decreased concentrations were added to adhered cells.

III.6.2. HAoEC viability by direct contact

HAoEC adhesion/proliferation of the cells were evaluated at day 1, day 3 and day 7. **Fig. 10** summarizes the results for all alloys including pure Zn. In general, all materials showed poor cell adhesion with viability values below 30 % after day 1. After 3 and 7 days, there was a prominent decrease in HAoEC population particularly on Zn-Cu alloys.

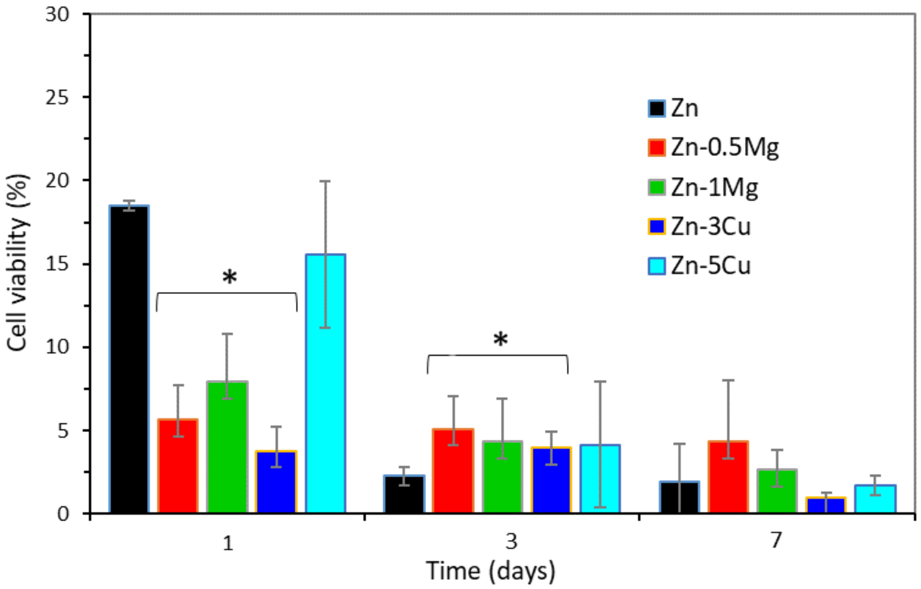

Fig. 10. Cell viability of HAoEC seeded on the alloys measured by LDH test. (*) Statistically significant differences in comparison to Zn control group, $P < 0.05$.

To further investigate cytotoxicity effects, cell morphologies in direct contact with the alloys were observed with SEM at day 1, day 3 and day 7, and cell distribution was determined at day 7 by confocal microscopy. Representative images of HAoEC morphologies on the different materials are depicted in **Fig. 11**. Cells exhibited spread morphology on Zn (**Fig. 11a-c**) and Zn-0.5Mg (**Fig. 11e-g**) throughout the immersion period. This morphology was an indication of good cell adhesion to the surface; however, cell population showed to be low as observed from live/dead confocal images of both Zn (**Fig. 11d**) and Zn-0.5Mg (**Fig. 11h**). This was in accordance to cell viability results in **Fig. 10.** In the case of Zn-1Mg and Zn-Cu alloys (**Fig. 11i, m, q**), HAoEC tended to gather in bundles. In the case of healthy cells, such bundles might be an indication of local cell proliferation. However, it is probably not the current case. Anchorage dependent cells attach to each other to survive when they are not able to attach to the underlying surface.

Formation of localized corrosion products was observed for Zn-1Mg (**Fig. 11j-k**) and both Zn-Cu (**Fig. 11n-o, r-s**) alloys at day 3 and day 7, respectively, in contrast to a rather smooth corrosion layer observed at day 1 for all materials. In general, cell viability results (**Fig. 10**) agreed with cell morphology observations with SEM and dead/live confocal microscopy images. HAoEC adhesion and proliferation on the here studied Zn alloys and conditions, is negligible.

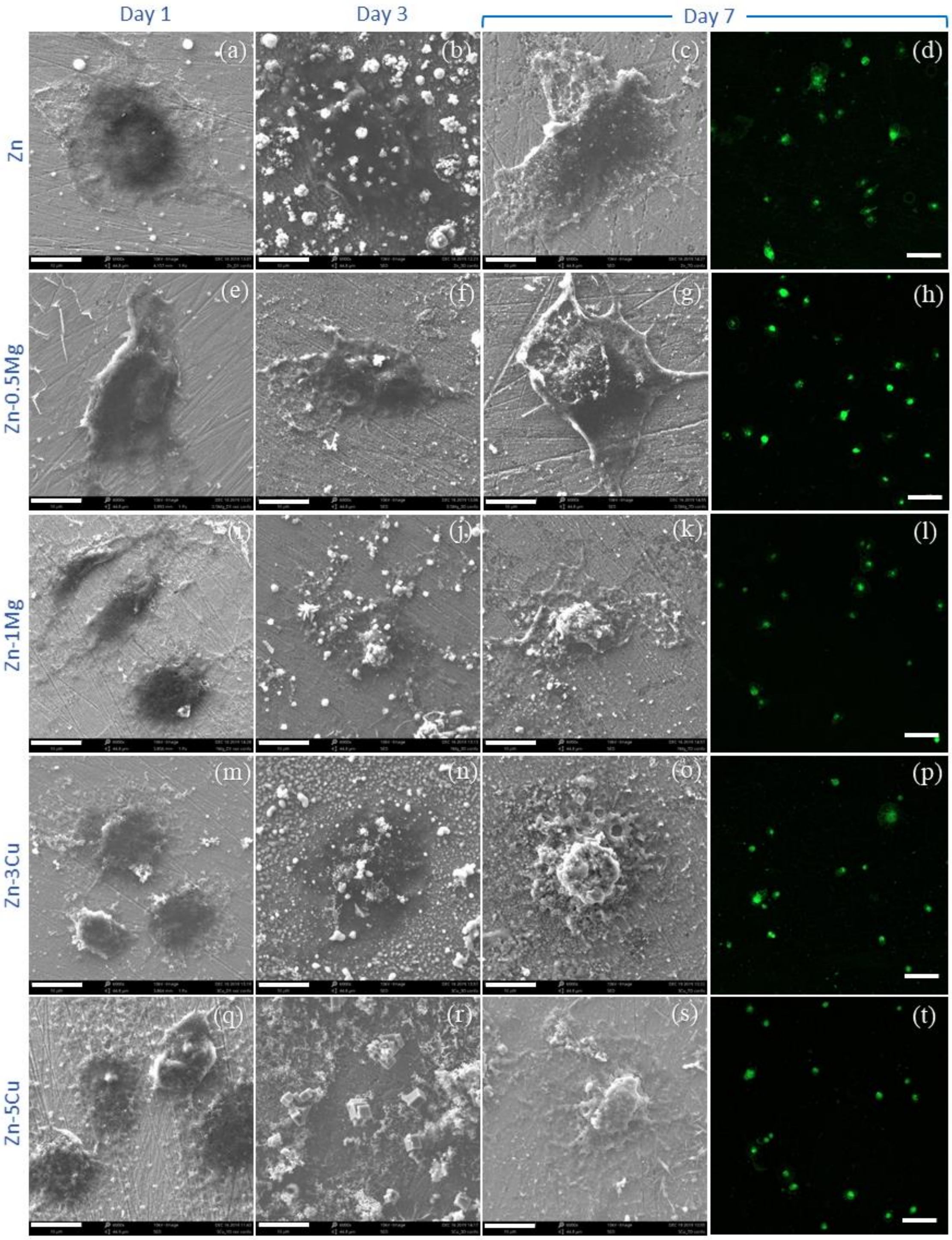

Fig. 11. SEM (scale bar 10 µm) and confocal (scale bar 100 µm) images of HAoEC morphology and distribution after 1 day (left hand column), 3 days (2nd column) and 7 days (right hand 2 columns) of culturing on Zn (a) – (d), Zn-0.5Mg (e) – (h), Zn-1Mg (i) – (l), Zn-3Cu (m) – (p), and Zn-5Cu (q) – (t).

IV. Discussion

Among bioresorbable metals, Zn and its alloys are becoming popular as part of the next generation of temporary implant materials that potentially prevent complications related to the use of permanent metals. From the mechanical point of view, Zn alloys have shown to have potential for cardiovascular stents. The requirements for cardiovascular stents include suitable stiffness that provide radial support to help restore the blood flow [56,57]; avoiding cracking during crimping and reinflation in order to prevent early loss of mechanical integrity; fatigue resistance to endure the stretching during cyclic heart contractions; and durability to avoid fracture that may lead to in-stent thrombosis [58].

The degradation rate, degradation products and biocompatibility are also key properties. Ideally, the degradation rate of a bioresorbable vascular stent should be about 20 μm/year to prevent excessive accumulation of degradation products that can cause long-term symptoms [59]. Unalloyed Zn has an appropriate degradation rate for cardiovascular stents application in comparison to Mg- and Fe-based alloys. Moreover, it is also an essential element for healthy bones, muscles and liver. However, the mechanical properties are lower compared to metallic materials used for commercial BMSs. The addition of alloying elements such as Mg and Cu has been reported to effectively refine the microstructure of Zn [34]. Moreover, extrusion process may modify the texture of alloyed Zn showing grain texture which also may influence the mechanical properties [60].

As expected, the microstructure of Zn-Mg alloys consisted of a primary α-Zn dendritic grains along with a Zn+Mg_2Zn_{11} eutectic, mainly located at grain boundaries (**Fig. 1c-f**) [61]. The reason is that Zn-Mg phase diagram shows a maximum of Mg solubility in Zn of 0.1 wt.% at 364 ºC [62], consistent with the results reported by Li [63], Prosek [64] and Yao [65]. **Fig. 1e** shows the eutectic phase surrounding the grains of 30 µm size, suggesting a refinement of the microstructure by alloying. The microstructure of the longitudinal sections showed Zn grains and the eutectic phase elongated to the rolling direction (**Fig. 1d,f)**. Zn-Cu phase diagram indicates a peritectic reaction where a Cu content between 2.7 and 22 wt. % results in the formation of a two-phase alloy consisting of a primary ε-$CuZn_5$ dendrites and Zn matrix [62,66,67].

The addition of Mg as an alloying element enhanced the mechanical properties of pure Zn. In fact, among the tested materials, Zn-1Mg the highest YS and UTS (**Fig. 2**). The limited elongation of Zn-1Mg alloy is due to the interconnected network of Zn+Mg_2Zn_{11} eutectic phase (**Fig. 1e**), which facilitates the growth of fracture cracks before the onset of plastic strain [18]. The statistically higher plasticity of Zn-0.5Mg is due to the absence of a continuous network (**Fig. 1c**). On the other hand, Zn-Cu alloys showed a larger elongation compared to Zn and Zn-Mg alloys. Superplastic behavior (>400% fracture elongation) has been previously reported for Zn-Cu alloys with Cu content below 1 wt.%, with preferential sliding at Zn/ε-$CuZn_5$ interphase rather than at Zn/Zn grain boundaries [68,69]. The obtained lower values can be attributed to the grain size and to the non-homogeneous distribution of ε-$CuZn_5$ intermetallic phase. The higher volume fraction of the secondary phases in both Zn-Mg and Zn-Cu alloys increased the final mechanical properties, as confirmed by nanoindentation results. The extremely low solubility of Mg in the Zn matrix (0.1 wt.%) [62] was enough to increase the hardness of Zn matrix. Similarly, the Cu dissolved into Zn matrix (2.75 wt.%) [62] reduces its hardness. As seen in **Table 2**, the secondary phases manifested statistically larger hardness in comparison to Zn matrix, 2.6 GPa for Zn+Mg_2Zn_{11} and 1.82 GPa for ε-$CuZn_5$, confirming that the presence of secondary phases enhances the macroscopic mechanical properties of Zn (**Fig. 2a**).

The anodic and catodic reactions involved in the corrosion mechanism of bioresorbable Zn-based alloys are summarized in Eqs 4-8. The released electrons from the oxidation of the metal (Eq. 4) are involved in cathodic processes as the reduction of protons from water molecules (Eq. 5) or the reduction of $O_2(g)$ (Eq. 6). Both cathodic reactions produce hydroxide ions increasing the pH of the solution and that could promote the formation of zinc hydroxides ($Zn(OH)_2(s)$) (Eq. 7) or zinc oxide ($ZnO(s)$) (Eq. 8).

$$Zn(s) \rightarrow Zn^{2+}(aq) + 2e^- \text{ (anodic reaction)} \quad (4)$$

$$2H_2O + 2e^- \rightarrow H_2(g) + 2OH^-(aq) \text{ (cathodic reaction)} \quad (5)$$

$$2H_2O + O_2(g) + 4e^- \rightarrow 4OH^-(aq) \text{ (cathodic reaction)} \quad (6)$$

$$Zn^{2+} + 2OH^- \rightarrow Zn(OH)_2(s) \text{ (by-product formation)} \quad (7)$$

$$Zn^{2+} + H_2O \rightarrow ZnO(s) + 2H^+ \text{ (by-product formation)} \quad (8)$$

This is a simplified model where it has not been considered the influence of other major species present in Hanks' solution, chloride, bicarbonate and phosphate ions. These ions are potentially responsible for the formation of chloride, carbonate and phosphate minerals as it is described in Eqs. 9-11.

$$Zn^{2+} + 2Cl^- \rightarrow ZnCl_2(s) \text{ (by-product formation)} \quad (9)$$

$$Zn^{2+} + HCO_3^- \rightarrow ZnCO_3(s) + 2H^+ \text{ (by-product formation)} \quad (10)$$

$$3Zn^{2+} + 2HPO_4^{-2} \rightarrow Zn_3PO_4(s) + 2H^+ \text{ (by-product formation)} \quad (11)$$

Oxidation-reduction reactions involve electron exchanges that require optimal balance for proper cell function. Enzymes as superoxide dismutase (SOD) and catalase act as redox buffers modulating different cellular processes. Redox homeostasis is governed by the presence of these antioxidants that absorb and buffer reductants and oxidants [48,70]. Under optimal cellular conditions, SOD and catalase are maintained in a highly reduced state ($E < 0$ V) and buffer the reactive oxygen species (ROS). A redox misbalance could transform the superoxide anion ($O_2^{\cdot-}$) to hydrogen peroxide (H_2O_2) (E, $O_2^{\cdot-}/H_2O_2 = +0.94$ V). The subsequent reduction of H_2O_2 produces the hydroxyl radical ($OH^{\cdot-}$) (E, $H_2O_2/OH^{\cdot-} = +0.54$ V), an extremely reactive electron and hydrogen acceptor whose reduction potentially comprises unselective oxidation of cellular components as the lipids present in the lipidic bilayers, aminoacids, or DNA [71]. Indeed, oxidative stress have been demonstrated to be related to atherosclerosis [72]. The degradation of studied Zn and Zn alloys occurred at negative redox potentials without subjecting cells to oxidative stress.

Pourbaix diagrams for Zn-Mg and Zn-Cu alloys in Hanks' modified solution at 37 ºC were calculated using HSC 5.1 Software (**Fig. S7**). At the measured pH and E values, the expected species for Zn^{2+} are $ZnCO_3$/ZnO (**Fig. S7a**); for Mg^{2+}: Mg^{2+}/MgO (**Fig. S7b**), and for Cu^{2+}: Cu/Cu_2O (**Fig. S7c**) According to Pourbaix diagrams of **Fig. S7c**, it is not expected any oxidized form of Cu as Cu^{2+} which is in agreement with the non-detection of Cu^{2+}, values were below the detection limit (<0.01 µg/dL). On the contrary, **Fig. S7a,** suggested to expect very low concentrations of Zn^{2+} in these conditions. However, it should be pointed out that Pourbaix diagrams provide a thermodynamic prediction and it should be added the integration of the kinetics of the different processes (Eqs. 4-10) describing the degradation mechanism of Zn and Zn alloys.

Regarding the corrosion degradation properties, the corrosion products layer formed on both Zn-Mg alloys demonstrated to be more protective to Zn than the corrosion layers of Zn-Cu alloys. Zn-1Mg showed the better performance in terms of corrosion layer stability and protection in Hanks' solution under the studied conditions. Some studies have reported that this is due to the presence of magnesium hydroxyl carbonate ($Mg(OH)(HCO_3)(s)$) that improve the corrosion resistance of Zn-based alloys as it is electrochemically inert in aqueous solutions [62]. Zn-1Mg alloy also showed the highest current density among the tested materials. The larger amount of fine intermetallic Zn+Mg_2Zn_{11} in the microstructure, results in a higher number of galvanic couples, which may explain the higher current density value. Immersion test stated that the total released

Zn^{2+} concentration is within the levels of Zn^{2+} in blood (60 – 240 µg/dL) [49,50]. Another challenge associated to cardiovascular stents is the platelet adhesion and thereby blood clotting. An strategy for the inhibition of the coagulation cascade is the control of the wettability, which could inhibit the adsorption of specific proteins and, thereby, promote hemocompatibility [73,74]. Moreover, the higher hydrophobicity is directly related to a better corrosion resistance [73,74]. Therefore, the values obtained suggested that Cu addition to Zn matrix increases the corrosion resistance of Zn. The hydrophilicity of Zn-1Mg alloy suggested a lower corrosion resistance of Zn, which is in accordance with the highest current density value reported in PDP studies (**Table 3**) and the galvanic couples homogeneously distributed (**Fig. 6d,f**).

Bacterial activity is related to the kinetics of degradation as well as the nature of the degradation products. Cu ions is an antibacterial agent and the the minimum inhibitory concentration (MIC) needed is 100 mg/L [75]. According to the results of the immersion test, the detected concentration of Cu^{2+} was below 0.01 mg/L. However, it must be pointed out the different conditions established for both experiments: immersion test comprises the total immersion of the materials into inorganic Hanks' solution; whereas in the agar diffusion test the samples are deposited onto the agar plate with BHI. Hence, it is hypothesized that Cu^{2+} dissolved into the Zn matrix in Zn-Cu alloys may diffuse with the degradation of the material at this primary stage, leading to an antibacterial effect for *S. aureus* controlled by diffusion mechanisms [76]. Cu^{2+} cations are often introduced to render antimicrobial properties to inert materials. Different antibacterial mechanisms based on Cu^{2+} diffusion have been reported. Cu^{2+} cations can interact with microbial membrane and alter their structure and permeability, or they can prevent microbial replication via interaction with microbial nucleic acids [1,28–30]. *Pseudomonas* have been used as metal resistant strains capable of bioaccumulation of multiple metals as zinc or copper and their dissolution [77]. Bacterial SEM images suggested that *P. aeruginosa* stimulates the degradation of Zn and Zn-Mg alloys under studied conditions modifying the chemical composition of the surface and its morphology. Moreover, the results showed a preferential adhesion of *P. aeruginosa* bacteria onto the degraded and rougher areas compared to non-degrades and smoother ones. Thus, controlling the degradation products and consequent roughness of BRS is also critical for avoiding bacterial infection [78].

Zn and its alloys indicated a deficient *in vitro* biocompatibility, however *in vivo* studies have shown positive results [16,17,20]. Shearier *et al.* [17] discussed two reasons for this: (i) the formation of a confluent protein layer over the material surface, that occurs *in vivo,* avoids the cells to be in direct contact with the implant surface; and (ii) the blood flow might help to alleviate the local concentration of cytotoxic ions or degradation products that may be harmful for cells. The absence of these conditions *in vitro* might lead to local high Zn^{2+} ions concentration that promotes cell dead [17]. This hypothesis is in accordance with the viability results in **Fig. 10**. The longer the incubation time of the cells in direct contact with the metallic surfaces, the lower the viability values were observed. Besides the exposure to local high Zn^{2+} ion concentration, cells are also exposed to degradation products that might also be cytotoxic. The nature and morphology of these corrosions' products certainly impacted cell viability and, as shown in **Fig. 10**, cells are in direct contact with these degradation products. HAoEC rounded shape surrounded by either corrosion products, is characteristic of weak cell adhesion. Once upon immersion, Zn degradation starts with oxidation processes releasing Zn^{2+} cations to the aqueous solution. Li *et al.* [79] reported that there is an apparent lethal dose depending on the cell type. Human aortic endothelial cells showed to be more resilient to the presence of Zn^{2+} in comparison to human aortic smooth muscle cells and human dermal fibroblasts [79]. Previous studies [62,80] have also reported a toxic effect for undiluted extracts in standard ISO 10993-5/12 test. Moreover, significant differences of cytotoxicity results among different studies have been also reported. It is important to remark that the ISO standards 10993-5/12 were originally developed for biocompatibility evaluation of inert materials. Due to their traditional use and simplicity of implementation, these standards were rapidly adopted for screening biocompatibility of bioresorbable materials. However, cytotoxicity is affected by degradation products released from the materials and sensitive to different extraction vehicles [79]. According to Li *et al.*, cytotoxicity results are directly affected by three main factors: alloy nature, cell line used and the extraction condition [79]. As stated by Li *et al.* [79], the medium and conditions of extraction influence the outcome of standardized *in vitro* cytotoxicity tests. In the same way, Wang *et al.* [81] recommend a minimal of 6 times to maximum 10 times dilution extracts since *in vitro* data should match in vivo data for cytotoxicity tests. However, still for HAoEC type Zn alloys inhibitory effect on cell viability confirms the need of functionalize Zn alloys surface intended for biomedical applications.

In general, Zn-based materials showed high potential to be used as BRS. As proven, their mechanical properties and degradation rate can be adjusted by alloying with Mg and Cu. However, cell adhesion and proliferation still need significant improvement. Therefore, future work should be focused on the functionalization of these alloys in order to achieve the desired *in vitro* and *in vivo* biocompatibility.

V. Conclusions

In this study, mechanical, corrosion and biocompatible properties of Zn, Zn-0.5Mg, Zn-1Mg, Zn-3Cu, and Zn-5Cu alloys were thoroughly characterized in order to select an adequate material for stenting applications. Tensile mechanical testing and Vickers assays confirmed that alloying with Mg or Cu alloying significantly increased YS and UTS of Zn. This is due to the formation of hard Zn+Mg_2Zn_{11} and ε-$CuZn_5$ secondary phases on Zn-Mg and Zn-Cu alloys, respectively, as determined by nanoindentation tests. Nanoindentation test determined the hardness and elastic modulus of the matrix and the secondary phases of the studied alloys. Fractured surfaces images were in accordance to tensile tests results showing the differences in grain size among the tested materials. Potentiodynamic results indicated that the corrosion layer of Zn-Mg is more protective than the formed onto Zn-Cu alloys., also confirmed by the Nyquist spectra from EIS measurements. Impedance and polarization results showed that the corrosion mechanisms consisted of galvanic corrosion followed by the formation of an inner corrosion layer plus local precipitation of compounds rich in Ca, C, O, P, and Cl. Static immersion assay in Hanks' modified solution indicated Zn^{2+} released values within normal blood levels, Mg^{2+} release was 10 µg/dL and Cu^{2+} was not detected by ICP-MS. The formation of these compounds and the Zn^{2+} release compromises the adhesion and proliferation of HAoECs in tested conditions. Cytotoxicity assays suggested that such products are cytotoxic to HAoECs. *S. aureus* showed to be more resilient to Zn-Mg alloys, different from this strain on Zn-Cu alloys evidenced by diffusion and adhesion tests. *In vitro* tests proved the need of functionalizing Zn-Mg and Zn-Cu alloys for the intended application. Among the tested materials, Zn-Mg alloys showed the best compromise in mechanical and degradation properties for cardiovascular stents.

VI. References

[1] H.M.M. van Beusekom, P.W. Serruys, Drug-Eluting Stent Endothelium. Presence or Dysfunction, JACC Cardiovasc. Interv. 3 (2010) 76–77. https://doi.org/10.1016/j.jcin.2009.10.016.

[2] P. Ramadugu, K. Latha Alikatte, A Review on Biodegradable and Bioabsorbable

Stents for Coronary Artery Disease, J. Bioequiv. Availab. 08 (2016) 64–67. https://doi.org/10.4172/jbb.1000269.

[3] Y.F. Zheng, X.N. Gu, F. Witte, Biodegradable metals, Mater. Sci. Eng. R. 77 (2014) 1–34. https://doi.org/10.1007/978-1-4614-3942-4_5.

[4] Y. Sotomi, Y. Onuma, C. Collet, E. Tenekecioglu, R. Virmani, N.S. Kleiman, P.W. Serruys, Bioresorbable scaffold: The emerging reality and future directions, Circ. Res. 120 (2017) 1341–1352. https://doi.org/10.1161/CIRCRESAHA.117.310275.

[5] M. Prakasam, J. Locs, K. Salma-Ancane, D. Loca, A. Largeteau, L. Berzina-Cimdina, Biodegradable Materials and Metallic Implants—A Review, J. Funct. Biomater. 8 (2017) 44. https://doi.org/10.3390/jfb8040044.

[6] H.S. Han, S. Loffredo, I. Jun, J. Edwards, Y.C. Kim, H.K. Seok, F. Witte, D. Mantovani, S. Glyn-Jones, Current status and outlook on the clinical translation of biodegradable metals, Mater. Today. 23 (2019) 57–71. https://doi.org/10.1016/j.mattod.2018.05.018.

[7] M. Moravej, D. Mantovani, Biodegradable metals for cardiovascular stent application: Interests and new opportunities, Int. J. Mol. Sci. 12 (2011) 4250–4270. https://doi.org/10.3390/ijms12074250.

[8] R. Song, M. Murphy, C. Li, K. Ting, C. Soo, Z. Zheng, Current development of biodegradable polymeric materials for biomedical applications, Drug Des. Devel. Ther. 12 (2018) 3117–3145. https://doi.org/10.2147/DDDT.S165440.

[9] A. Purnama, H. Hermawan, D. Mantovani, Biodegradable Metal Stents: A Focused Review on Materials and Clinical Studies, J. Biomater. Tissue Eng. 4 (2015) 868–874. https://doi.org/10.1166/jbt.2014.1263.

[10] D. Zhao, F. Witte, F. Lu, J. Wang, J. Li, L. Qin, Current status on clinical applications of magnesium-based orthopaedic implants: A review from clinical translational perspective, Biomaterials. 112 (2017) 287–302. https://doi.org/10.1016/j.biomaterials.2016.10.017.

[11] P.C. Banerjee, S. Al-Saadi, L. Choudhary, S.E. Harandi, R. Singh, Magnesium implants: Prospects and challenges, Materials (Basel). 12 (2019) 1–21. https://doi.org/10.3390/ma12010136.

[12] D. Pierson, J. Edick, A. Tauscher, E. Pokorney, P. Bowen, J. Gelbaugh, J. Stinson, H. Getty, C.H. Lee, J. Drelich, J. Goldman, A simplified in vivo approach for evaluating the bioabsorbable behavior of candidate stent materials, J. Biomed. Mater. Res. - Part B Appl. Biomater. 100 B (2012) 58–67. https://doi.org/10.1002/jbm.b.31922.

[13] D. Vojtěch, J. Kubásek, J. Šerák, P. Novák, Mechanical and corrosion properties of newly developed biodegradable Zn-based alloys for bone fixation, Acta Biomater. 7 (2011) 3515–3522. https://doi.org/10.1016/j.actbio.2011.05.008.

[14] M.I. Rahim, S. Ullah, P.P. Mueller, Advances and challenges of biodegradable implant materials with a focus on magnesium-alloys and bacterial infections, Metals (Basel). 8 (2018). https://doi.org/10.3390/met8070532.

[15] C. Li, C. Guo, V. Fitzpatrick, A. Ibrahim, M.J. Zwierstra, P. Hanna, A. Lechtig, A. Nazarian, S.J. Lin, D.L. Kaplan, Design of biodegradable, implantable devices towards clinical translation, Nat. Rev. Mater. 5 (2020) 61–81. https://doi.org/10.1038/s41578-019-0150-z.

[16] P.K. Bowen, J.W. Drelich, J. Goldman, Zinc exhibits ideal physiological corrosion behavior for bioabsorbable stents, Adv. Mater. 25 (2013) 2577–2582. https://doi.org/10.1002/adma.201300226.

[17] E.R. Shearier, P.K. Bowen, W. He, A. Drelich, J. Drelich, J. Goldman, F. Zhao, In Vitro Cytotoxicity, Adhesion, and Proliferation of Human Vascular Cells Exposed to Zinc, ACS Biomater. Sci. Eng. (2016). https://doi.org/10.1021/acsbiomaterials.6b00035.

[18] J. Kubásek, D. Vojtěch, E. Jablonská, I. Pospíšilová, J. Lipov, T. Ruml, Structure, mechanical characteristics and in vitro degradation, cytotoxicity, genotoxicity and mutagenicity of novel biodegradable Zn–Mg alloys, Mater. Sci. Eng. C. 58 (2016) 24–35. https://doi.org/10.1016/j.msec.2015.08.015.

[19] W.M.P.F. Bosman, B.L.S. Borger Van Der Burg, H.M. Schuttevaer, S. Thoma, P.P. Hedeman Joosten, Infections of intravascular bare metal stents: A case report and review of literature, Eur. J. Vasc. Endovasc. Surg. 47 (2014) 87–99. https://doi.org/10.1016/j.ejvs.2013.10.006.

[20] G. Katarivas Levy, J. Goldman, E. Aghion, The Prospects of Zinc as a Structural Material for Biodegradable Implants—A Review Paper, Metals (Basel). 7 (2017) 402. https://doi.org/10.3390/met7100402.

[21] G. Katarivas Levy, A. Leon, A. Kafri, Y. Ventura, J.W. Drelich, J. Goldman, R. Vago, E. Aghion, Evaluation of biodegradable Zn-1%Mg and Zn-1%Mg-0.5%Ca alloys for biomedical applications, J. Mater. Sci. Mater. Med. 28 (2017) 1–11. https://doi.org/10.1007/s10856-017-5973-9.

[22] Z. Tang, H. Huang, J. Niu, L. Zhang, H. Zhang, J. Pei, J. Tan, G. Yuan, Design and characterizations of novel biodegradable Zn-Cu-Mg alloys for potential biodegradable implants, Mater. Des. 117 (2017) 84–94. https://doi.org/10.1016/j.matdes.2016.12.075.

[23] D. Persaud-Sharma, N. Budiansky, In Vitro Degradation Behavior of Ternary Mg-Zn-Se and Mg-Zn-Cu Alloys as Biomaterials, 193 (2011) 118–125. https://doi.org/10.1016/j.jneumeth.2010.08.011.Autogenic.

[24] B. Jia, Z. Zhang, X. Qu, W. Lin, Alloying design of biodegradable zinc as promising bone implants for load-bearing applications, Nat. Commun. (2020) 1–16. https://doi.org/10.1038/s41467-019-14153-7.

[25] Y. Zhang, Y. Yan, X. Xu, Y. Lu, L. Chen, D. Li, Y. Dai, Y. Kang, K. Yu, Investigation on the microstructure, mechanical properties, in vitro degradation behavior and biocompatibility of newly developed Zn-0.8%Li-(Mg, Ag) alloys for guided bone regeneration, Mater. Sci. Eng. C. 99 (2019) 1021–1034. https://doi.org/10.1016/j.msec.2019.01.120.

[26] C. Xiao, L. Wang, Y. Ren, S. Sun, E. Zhang, C. Yan, Q. Liu, X. Sun, F. Shou, J.

Duan, H. Wang, G. Qin, Indirectly extruded biodegradable Zn-0.05wt%Mg alloy with improved strength and ductility: In vitro and in vivo studies, J. Mater. Sci. Technol. 34 (2018) 1618–1627. https://doi.org/10.1016/j.jmst.2018.01.006.

[27] H. Yang, B. Jia, Z. Zhang, X. Qu, G. Li, W. Lin, D. Zhu, K. Dai, Y. Zheng, Alloying design of biodegradable zinc as promising bone implants for load-bearing applications, Nat. Commun. 11 (2020) 1–16. https://doi.org/10.1038/s41467-019-14153-7.

[28] A.W. Feinberg, W.R. Wilkerson, C.A. Seegert, A.L. Gibson, L. Hoipkemeier-Wilson, A.B. Brennan, Systematic variation of microtopography, surface chemistry and elastic modulus and the state dependent effect on endothelial cell alignment, J. Biomed. Mater. Res. - Part A. 86 (2008) 522–534. https://doi.org/10.1002/jbm.a.31626.

[29] J.A. Ormiston, M.W.I. Webster, Trial Data and the Real World, (2015) 1–4. https://doi.org/10.4244/EIJY15M02.

[30] H. Pourabolghasem, M. Ghorbanpour, R. Shayegh, Antibacterial activity of copper-doped montmorillonite nanocomposites prepared by alkaline ion exchange method, J. Phys. Sci. 27 (2016) 1–12. https://doi.org/10.21315/jps2016.27.2.1.

[31] E.D. Harris, A Requirement for Copper in Angiogenesis, Nutr. Rev. 62 (2004) 60–64. https://doi.org/10.1301/nr.2004.feb.60.

[32] C. Giacomelli, M.L. Trincavelli, C. Satriano, Ö. Hansson, D. La Mendola, E. Rizzarelli, C. Martini, Copper (II) ions modulate Angiogenin activity in human endothelial cells, Int. J. Biochem. Cell Biol. 60 (2015) 185–196. https://doi.org/10.1016/j.biocel.2015.01.005.

[33] L. Finney, S. Vogt, T. Fukai, D. Glesne, Copper and angiogenesis: Unravelling a relationship key to cancer progression, Clin. Exp. Pharmacol. Physiol. 36 (2009) 88–94. https://doi.org/10.1111/j.1440-1681.2008.04969.x.

[34] Z. Liu, F. Wang, D. Qiu, J.A. Taylor, M. Zhang, The effect of solute elements on the grain refinement of cast Zn, Metall. Mater. Trans. A Phys. Metall. Mater. Sci. 44 (2013) 4025–4030. https://doi.org/10.1007/s11661-013-1861-1.

[35] W. Bednarczyk, M. Wątroba, J. Kawałko, P. Bała, Can zinc alloys be strengthened by grain refinement? A critical evaluation of the processing of low-alloyed binary zinc alloys using ECAP, Mater. Sci. Eng. A. 748 (2019) 357–366. https://doi.org/10.1016/j.msea.2019.01.117.

[36] ASTM E8/E8M-13a. Standard Test Methods for Tension Testing of Metallic Materials, Annu. B. ASTM Stand. (2013). https://doi.org/10.1520/E0008.

[37] W.C. Oliver, G.M. Pharr, An improved technique for determining hardness and elastic modulus using load and displacement sensing indentation experiments, 7 (1992).

[38] L. Qian, H. Zhao, Nanoindentation of soft biological materials, Micromachines. 9 (2018). https://doi.org/10.3390/mi9120654.

[39] A.K. Gartzke, S. Julmi, C. Klose, S. Besdo, A.C. Waselau, A. Meyer-Lindenberg,

H.J. Maier, P. Wriggers, Investigation of degraded bone substitutes made of magnesium alloy using scanning electron microscope and nanoindentation, J. Mech. Behav. Biomed. Mater. 109 (2020) 103825. https://doi.org/10.1016/j.jmbbm.2020.103825.

[40] ASTM G5-14. Standard Reference Test Method for Making Potentiodynamic Anodic Polarization Measurements, Annu. B. ASTM Stand. (2014). https://doi.org/10.1520/G0005-14.2.

[41] ASTM G31-72, 2004. Standard Practice for Laboratory Immersion Corrosion Testing of Metals, Annu. B. ASTM Stand. (2004). https://doi.org/10.1520/G0031-72R04.2.

[42] ASTM G102-89, 2015. Standard Practice for Calculation of Corrosion Rates and Related Information from Electrochemical Measurements, Annu. B. ASTM Stand. (2015) 1-. https://doi.org/10.1520/G0102-89R15E01.2.

[43] ISO 8407:2009. Corrosion of metals and alloys — Removal of corrosion products from corrosion test specimens, Int. Organ. Stand. (2009).

[44] CLSI M07-A9, 2012. Methods for Dilution Antimicrobial Susceptibility Tests for Bacteria That Grow Aerobically, Clin. Lab. Stand. Inst. (2012).

[45] ISO 10993-5:2009. Biological evaluation of medical devices — Part 5: Tests for in vitro cytotoxicity, Int. Organ. Stand. (2009).

[46] ISO 10993-12: 2012(E). Biological Evaluation of Medical Devices–Part 12: Sample Preparation and Reference Materials, Int. Organ. Stand. (2012).

[47] S. Liu, D. Kent, H. Zhan, N. Doan, M. Dargusch, G. Wang, Dynamic recrystallization of pure zinc during high strain-rate compression at ambient temperature, Mater. Sci. Eng. A. 784 (2020) 139325. https://doi.org/10.1016/j.msea.2020.139325.

[48] F. Ursini, M. Maiorino, H.J. Forman, Redox homeostasis: The Golden Mean of healthy living, Redox Biol. 8 (2016) 205–215. https://doi.org/10.1016/j.redox.2016.01.010.

[49] W. Hussain, A. Mumtaz, F. Yasmeen, S.Q. Khan, T. Butt, Reference range of zinc in adult population (20-29 years) of Lahore, Pakistan, Pakistan J. Med. Sci. 30 (2014) 545–548. https://doi.org/10.12669/pjms.303.4027.

[50] J. Arnaud, M. Touvier, P. Galan, M. Andriollo-Sanchez, D. Ruffieux, A.M. Roussel, S. Hercberg, A. Favier, Determinants of serum zinc concentrations in a population of French middle-age subjects (SU.VI.MAX cohort), Eur. J. Clin. Nutr. 64 (2010) 1057–1064. https://doi.org/10.1038/ejcn.2010.118.

[51] K. Törne, M. Larsson, A. Norlin, J. Weissenrieder, Degradation of zinc in saline solutions, plasma, and whole blood, J. Biomed. Mater. Res. - Part B Appl. Biomater. 104 (2016) 1141–1151. https://doi.org/10.1002/jbm.b.33458.

[52] P. Li, W. Zhang, J. Dai, A.B. Xepapadeas, E. Schweizer, D. Alexander, L. Scheideler, C. Zhou, H. Zhang, G. Wan, J. Geis-Gerstorfer, Investigation of zinc-copper alloys as potential materials for craniomaxillofacial osteosynthesis

implants, Mater. Sci. Eng. C. 103 (2019) 109826. https://doi.org/10.1016/j.msec.2019.109826.

[53] M.M. Alves, T. Prošek, C.F. Santos, M.F. Montemor, Evolution of the: In vitro degradation of Zn-Mg alloys under simulated physiological conditions, RSC Adv. 7 (2017) 28224–28233. https://doi.org/10.1039/c6ra28542b.

[54] M.B. Kannan, C. Moore, S. Saptarshi, S. Somasundaram, M. Rahuma, A.L. Lopata, Biocompatibility and biodegradation studies of a commercial zinc alloy for temporary mini-implant applications, Sci. Rep. 7 (2017) 1–11. https://doi.org/10.1038/s41598-017-15873-w.

[55] A. Marmur, Measures of wettability of solid surfaces, Eur. Phys. J. Spec. Top. 197 (2011) 193–198. https://doi.org/10.1140/epjst/e2011-01457-4.

[56] F. Witte, K. Yang, J. Wang, D. Zhao, W. Li, Y. Li, T. Xi, J. Meng, L. Qin, Y. Zheng, K. Chan, Y. Yang, Recommendation for modifying current cytotoxicity testing standards for biodegradable magnesium-based materials, Acta Biomater. 21 (2015) 237–249. https://doi.org/10.1016/j.actbio.2015.04.011.

[57] H. Yang, F. Zhang, J. Qian, J. Chen, J. Ge, Restenosis in Magmaris Stents Due to Significant Collapse, JACC Cardiovasc. Interv. 11 (2018) e77–e78. https://doi.org/10.1016/j.jcin.2018.02.040.

[58] K. Yamaji, Y. Ueki, G. Souteyrand, J. Daemen, J. Wiebe, H. Nef, T. Adriaenssens, J.P. Loh, B. Lattuca, J.J. Wykrzykowska, J. Gomez-Lara, L. Timmers, P. Motreff, P. Hoppmann, M. Abdel-Wahab, R.A. Byrne, F. Meincke, N. Boeder, B. Honton, C.J. O'Sullivan, A. Ielasi, N. Delarche, G. Christ, J.K.T. Lee, M. Lee, N. Amabile, A. Karagiannis, S. Windecker, L. Räber, Mechanisms of Very Late Bioresorbable Scaffold Thrombosis: The INVEST Registry, J. Am. Coll. Cardiol. 70 (2017) 2330–2344. https://doi.org/10.1016/j.jacc.2017.09.014.

[59] J. Wang, Y. Zhou, Z. Yang, S. Zhu, L. Wang, S. Guan, Processing and properties of magnesium alloy micro-tubes for biodegradable vascular stents, Mater. Sci. Eng. C. 90 (2018) 504–513. https://doi.org/10.1016/j.msec.2018.05.005.

[60] Y. Yang, Y. Cheng, S. Peng, L. Xu, C. He, F. Qi, M. Zhao, C. Shuai, Microstructure evolution and texture tailoring of reduced graphene oxide reinforced Zn scaffold, Bioact. Mater. 6 (2021) 1230–1241. https://doi.org/10.1016/j.bioactmat.2020.10.017.

[61] H. Jin, S. Zhao, R. Guillory, P.K. Bowen, Z. Yin, A. Griebel, J. Schaffer, E.J. Earley, J. Goldman, J.W. Drelich, Novel high-strength, low-alloys Zn-Mg (< 0.1 wt% Mg) and their arterial biodegradation, Mater. Sci. Eng. C. 84 (2018) 67–79. https://doi.org/10.1016/j.msec.2017.11.021.

[62] E. Mostaed, M. Sikora-Jasinska, J.W. Drelich, M. Vedani, Zinc-based alloys for degradable vascular stent applications, Acta Biomater. 71 (2018) 1–23. https://doi.org/10.1016/j.actbio.2018.03.005.

[63] B. Li, A. Dong, G. Zhu, S. Chu, H. Qian, C. Hu, B. Sun, J. Wang, Investigation of the corrosion behaviors of continuously hot-dip galvanizing Zn-Mg coating, Surf. Coatings Technol. 206 (2012) 3989–3999.

https://doi.org/10.1016/j.surfcoat.2012.03.079.

[64] T. Prosek, A. Nazarov, U. Bexell, D. Thierry, J. Serak, Corrosion mechanism of model zinc-magnesium alloys in atmospheric conditions, Corros. Sci. 50 (2008) 2216–2231. https://doi.org/10.1016/j.corsci.2008.06.008.

[65] C. Yao, Z. Wang, S.L. Tay, T. Zhu, W. Gao, Effects of Mg on microstructure and corrosion properties of Zn-Mg alloy, J. Alloys Compd. 602 (2014) 101–107. https://doi.org/10.1016/j.jallcom.2014.03.025.

[66] J. Niu, Z. Tang, H. Huang, J. Pei, H. Zhang, G. Yuan, W. Ding, Research on a Zn-Cu alloy as a biodegradable material for potential vascular stents application, Mater. Sci. Eng. C. 69 (2016) 407–413. https://doi.org/10.1016/j.msec.2016.06.082.

[67] Z. Tang, J. Niu, H. Huang, H. Zhang, J. Pei, J. Ou, G. Yuan, Potential biodegradable Zn-Cu binary alloys developed for cardiovascular implant applications, J. Mech. Behav. Biomed. Mater. 72 (2017) 182–191. https://doi.org/10.1016/j.jmbbm.2017.05.013.

[68] E. Mostaed, M.S. Ardakani, M. Sikora-Jasinska, J.W. Drelich, Precipitation induced room temperature superplasticity in Zn-Cu alloys, Mater. Lett. 244 (2019) 203–206. https://doi.org/10.1016/j.matlet.2019.02.084.

[69] W. Bednarczyk, J. Kawałko, M. Wątroba, P. Bała, Achieving room temperature superplasticity in the Zn-0.5Cu alloy processed via equal channel angular pressing, Mater. Sci. Eng. A. 723 (2018) 126–133. https://doi.org/10.1016/j.msea.2018.03.052.

[70] N. V. Margaritelis, V. Paschalis, A.A. Theodorou, A. Kyparos, M.G. Nikolaidis, Redox basis of exercise physiology, Redox Biol. 35 (2020) 101499. https://doi.org/10.1016/j.redox.2020.101499.

[71] C.H. Foyer, G. Noctor, Redox homeostasis and antioxidant signaling: A metabolic interface between stress perception and physiological responses, Plant Cell. 17 (2005) 1866–1875. https://doi.org/10.1105/tpc.105.033589.

[72] F. Bonomini, S. Tengattini, A. Fabiano, R. Rezzani, Atherosclerosis and oxidative stress, Japanese J. Geriatr. 45 (2008) 287–290. https://doi.org/10.3143/geriatrics.45.287.

[73] S. Rahimipour, E. Salahinejad, E. Sharifi, H. Nosrati, L. Tayebi, Structure, wettability, corrosion and biocompatibility of nitinol treated by alkaline hydrothermal and hydrophobic functionalization for cardiovascular applications, Appl. Surf. Sci. 506 (2020) 144657. https://doi.org/10.1016/j.apsusc.2019.144657.

[74] J. Vishnu, M. Calin, S. Pilz, A. Gebert, B. Kaczmarek, M. Michalska-Sionkowska, V. Hoffmann, G. Manivasagam, Superhydrophilic nanostructured surfaces of beta Ti[sbnd]29Nb alloy for cardiovascular stent applications, Surf. Coatings Technol. 396 (2020). https://doi.org/10.1016/j.surfcoat.2020.125965.

[75] A. Reyes-Jara, N. Cordero, J. Aguirre, M. Troncoso, G. Figueroa, Antibacterial effect of copper on microorganisms isolated from bovine mastitis, Front. Microbiol. 7 (2016) 1–10. https://doi.org/10.3389/fmicb.2016.00626.

[76] C.H. Hu, Z.R. Xu, M.S. Xia, Antibacterial effect of Cu2+-exchanged montmorillonite on Aeromonas hydrophila and discussion on its mechanism, Vet. Microbiol. 109 (2005) 83–88. https://doi.org/10.1016/j.vetmic.2005.04.021.

[77] A. Chester, R. Srivastava, G. Awasthi, J. Prakash, A Review on Bioremediation of Heavy Metals in Contaminated Water, IOSR J. Environ. Sci. Toxicol. Food Technol. 8 (2014) 44–50. https://doi.org/10.9790/2402-08714450.

[78] M. Bertuola, A. Miñán, C.A. Grillo, M.C. Cortizo, M.A. Fernández Lorenzo de Mele, Corrosion protection of AZ31 alloy and constrained bacterial adhesion mediated by a polymeric coating obtained from a phytocompound, Colloids Surfaces B Biointerfaces. 172 (2018) 187–196. https://doi.org/10.1016/j.colsurfb.2018.08.025.

[79] P. Li, C. Schille, E. Schweizer, E. Kimmerle-Müller, F. Rupp, A. Heiss, C. Legner, U.E. Klotz, J. Geis-Gerstorfer, L. Scheideler, Selection of extraction medium influences cytotoxicity of zinc and its alloys, Acta Biomater. 98 (2019) 235–245. https://doi.org/10.1016/j.actbio.2019.03.013.

[80] P.K. Bowen, E.R. Shearier, S. Zhao, R.J. Guillory, F. Zhao, J. Goldman, J.W. Drelich, Biodegradable Metals for Cardiovascular Stents: from Clinical Concerns to Recent Zn-Alloys, Adv. Healthc. Mater. 5 (2016) 1121–1140. https://doi.org/10.1002/adhm.201501019.

[81] J. Wang, F. Witte, T. Xi, Y. Zheng, K. Yang, Y. Yang, D. Zhao, J. Meng, Y. Li, W. Li, K. Chan, L. Qin, Recommendation for modifying current cytotoxicity testing standards for biodegradable magnesium-based materials., Acta Biomater. 21 (2015) 237–49. https://doi.org/10.1016/j.actbio.2015.04.011.

Supplementary Material

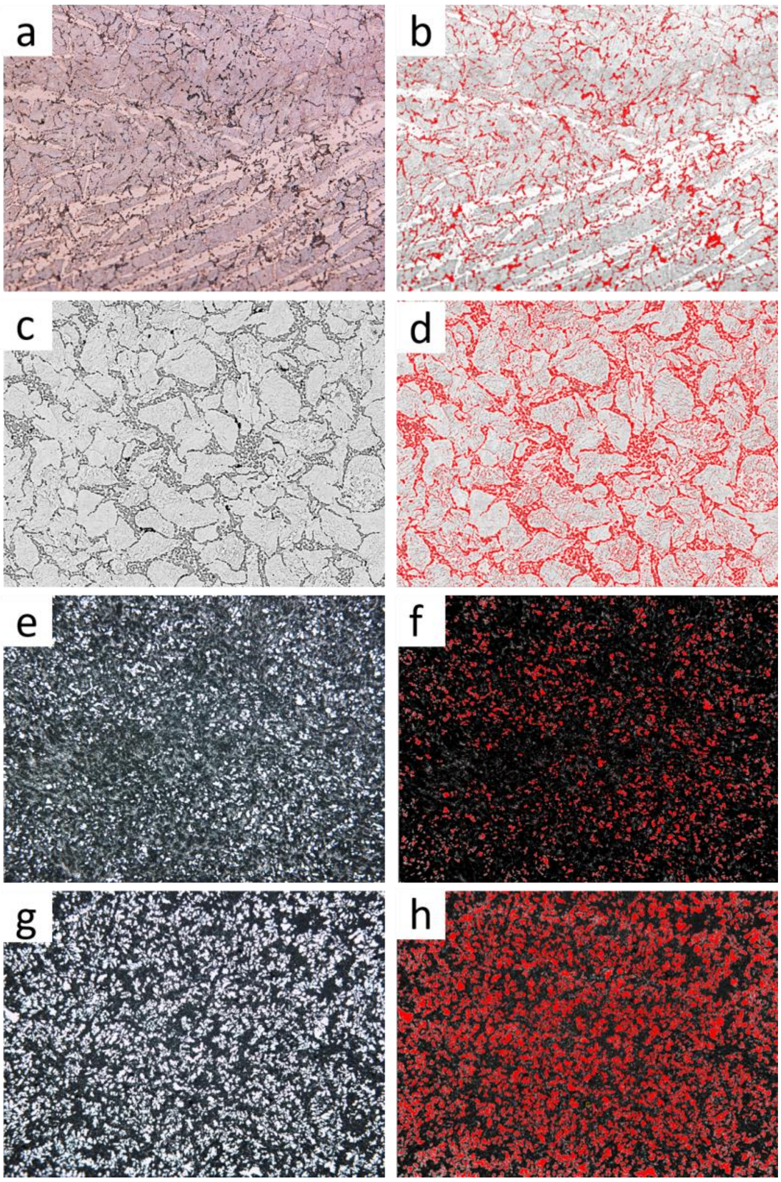

Fig. S1. Image analysis by ImageJ software (right column) of the metallographic microstructures (left column) of: Zn-0.5Mg (a,b); Zn-1Mg (c, d), Zn-3Cu (e, f), and Zn-5Cu (g, h). Areas colored in red indicate the volume fraction of secondary phases.

Table S1. Chemical composition of Hanks' modified solution.

Component	**Concentration (g/L)**
KCl	0,4
KH_2PO_4	0,06
NaCl	8
Na_2HPO_4	0,04788
$NaHCO_3$	0,35
$CaCl_2 \cdot 2H_2O$	0,185

a

Phases	Lattice parameters a (nm)	b (nm)	c (nm)	Person symbol	Space group
Zn	0.26649	0.26649	0.49468	hp2	$P6_3/mmc$
Mg_2Zn_{11}	0.85520	0.85520	0.85520	cP39	$Pm\bar{3}$
$CuZn_5$	0.27418	0.27418	0.42939	hp2	$P6_3/mmc$

b

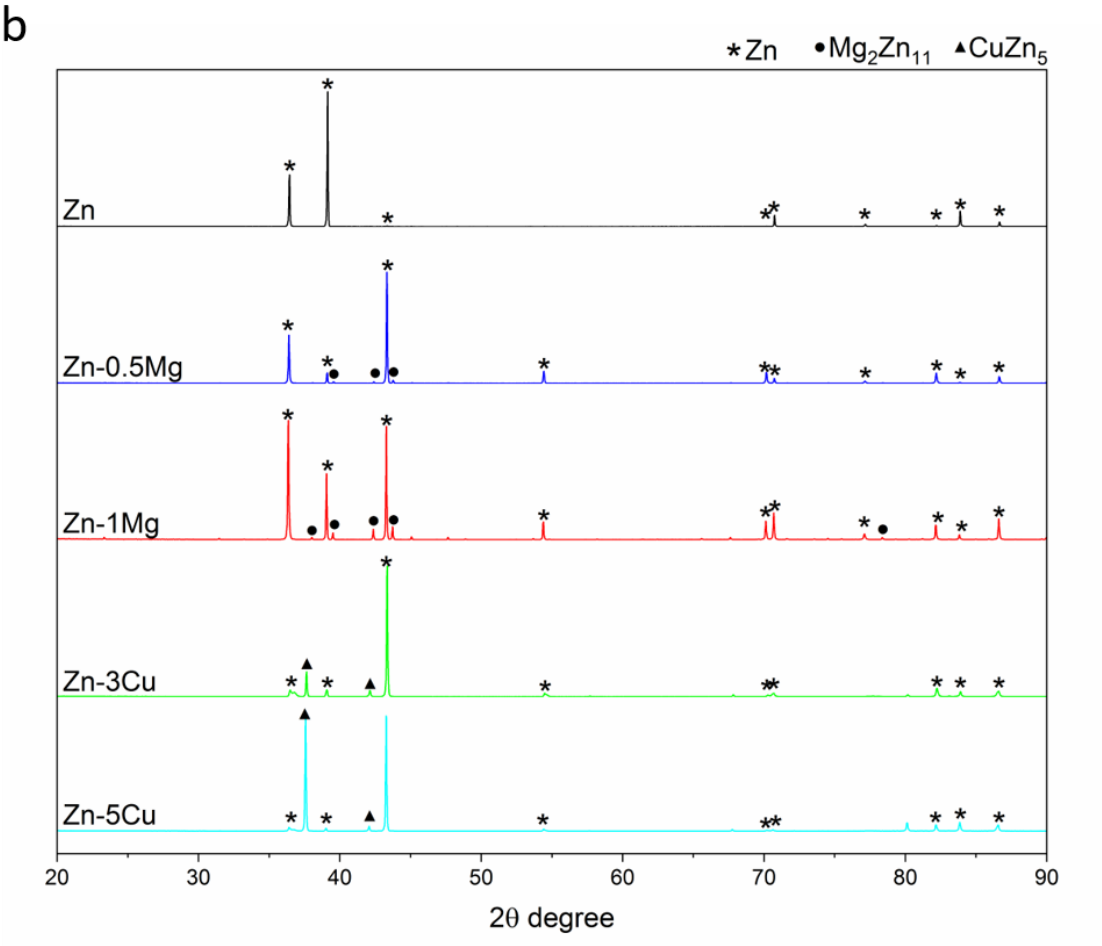

Fig. S2. X-Ray diffraction of the pure Zn and Zn alloys: (a) Crystallographic data of Zn, Mg_2Zn_{11}, and $CuZn_5$ phases. (b) XRD spectra of the tested samples.

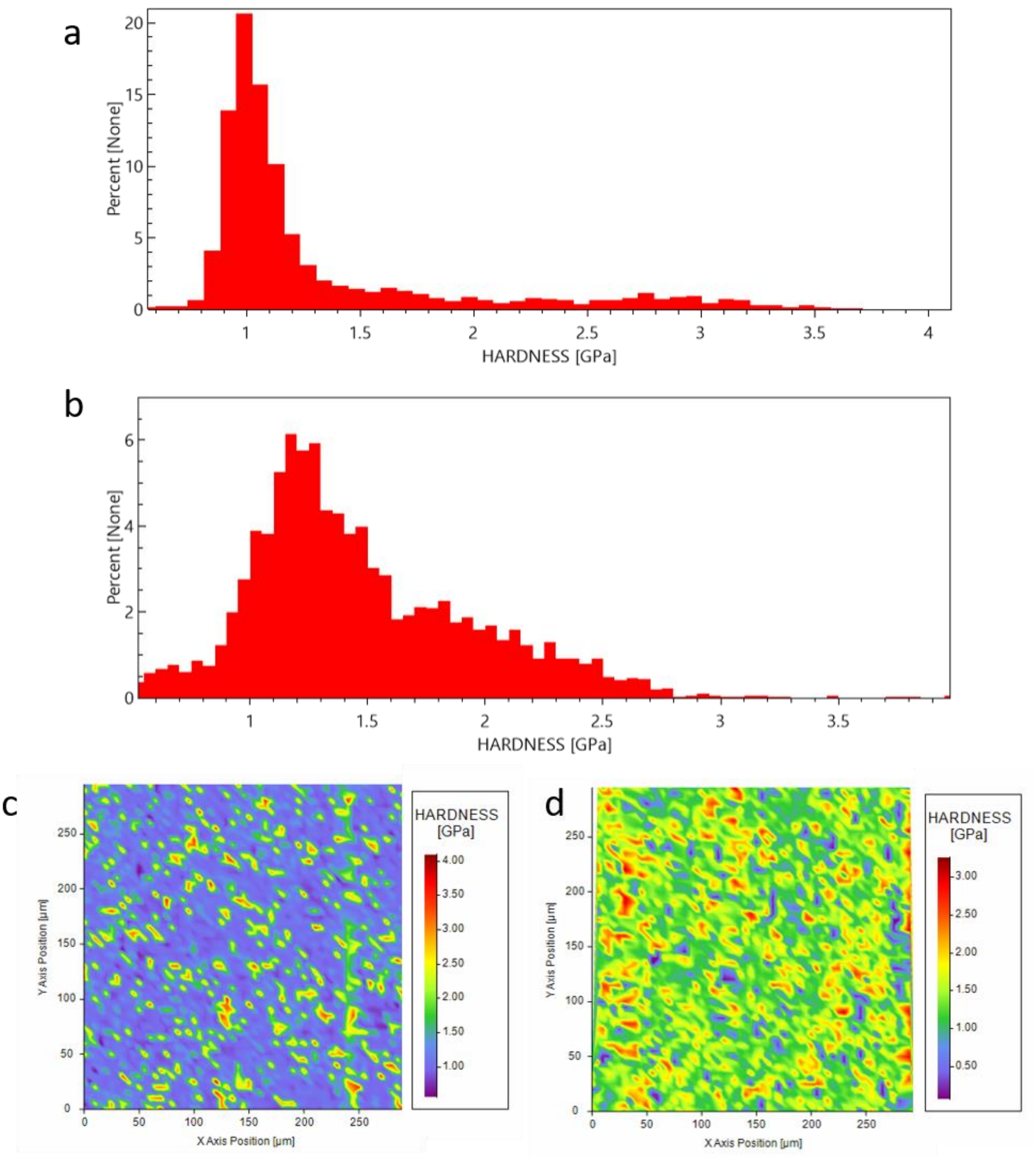

Fig. S3. High-speed nanoindentation results. Hardness histograms of (a) Zn-1Mg, and (b) Zn-3Cu alloy. Hardness maps compiled from the nanoindentation matrixes of (a) Zn-1Mg, and (b) Zn-3Cu alloy.

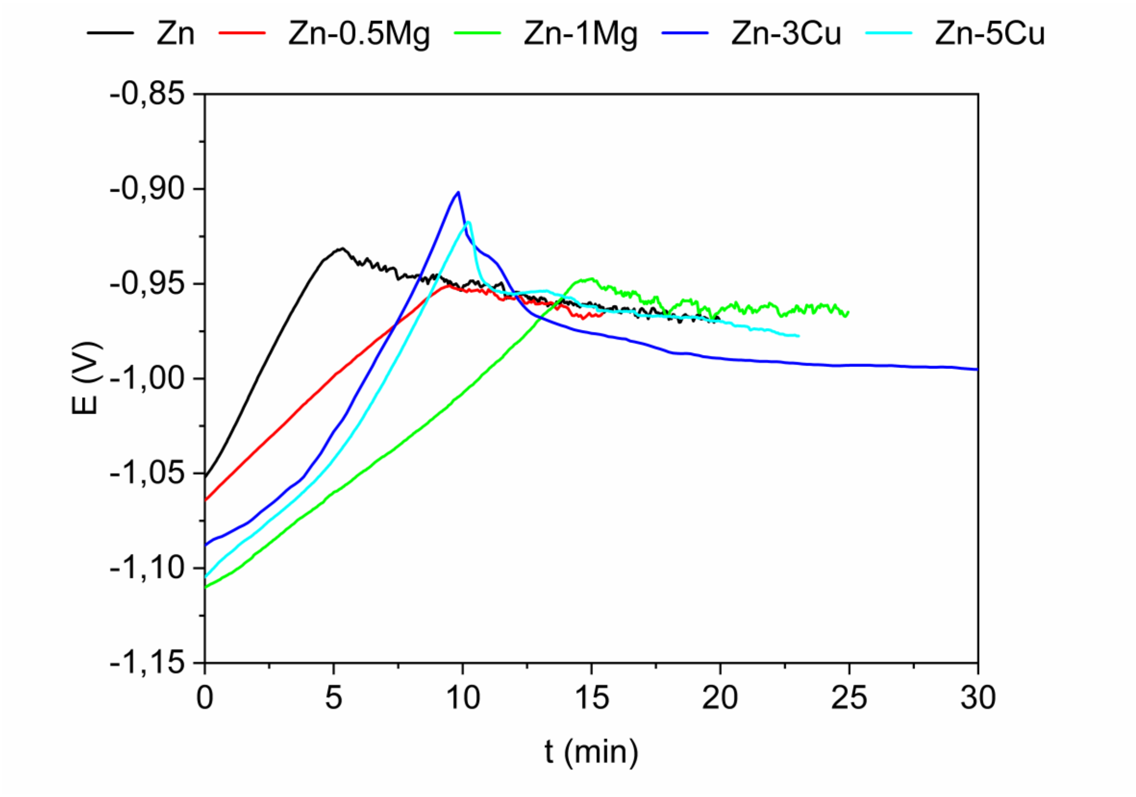

Fig. S4. OCP curves of Zn, Zn-Mg and Zn-Cu studied alloys.

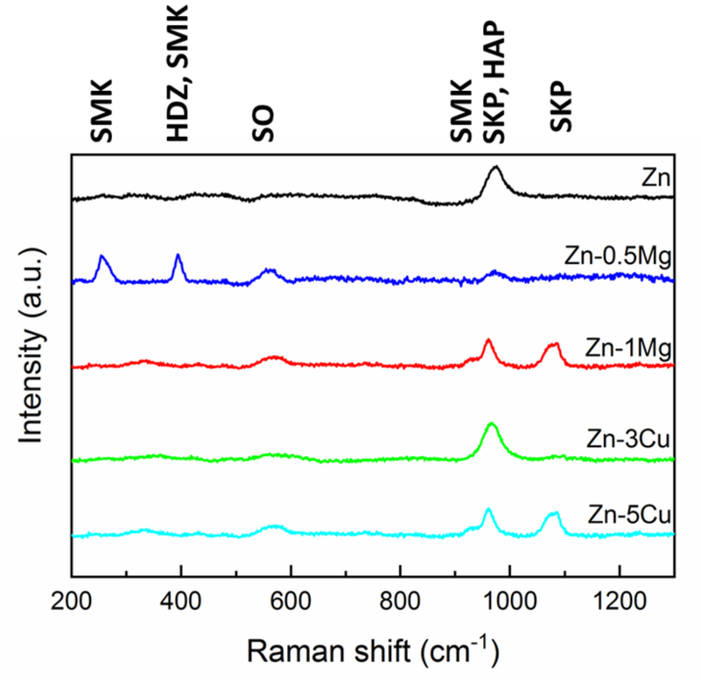

Fig. S5. Raman spectra of corroded samples after 10 days of immersion in Hanks' solution at 37 ± 1 ºC. **SMK** simonkolleite $Zn_5(OH)_8Cl_2 \cdot H_2O$; **HDZ** hydrozincite $Zn_5(CO_3)_2(OH)_6$; **HAP** hydroxiapatite; **SKP** skorpionite $Ca_3Zn_2(PO_4)_2CO_3(OH)_2 \cdot H_2O$; **SO** surface optical phonon vibrations [53].

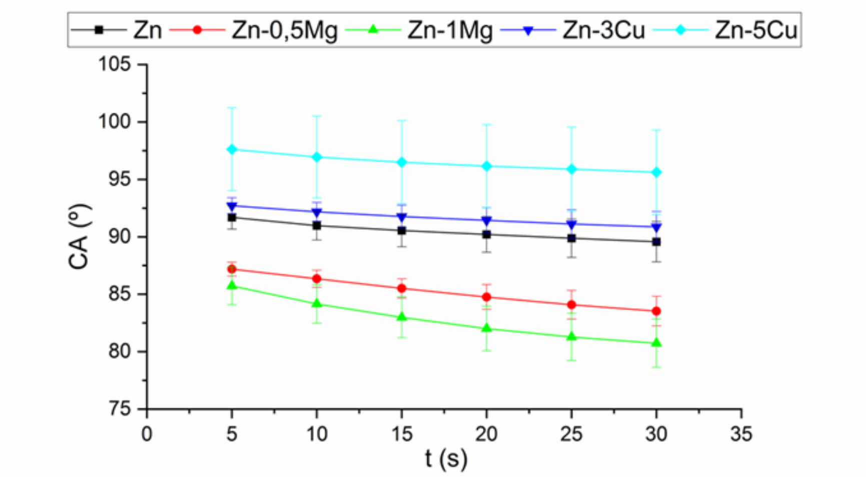

Contact angle (°)					
Time (s)	Pure Zn	Zn-0.5Mg	Zn-1Mg	Zn-3Cu	Zn-5Cu
5	91.70 ± 1.03	87.19 ± 0.60	85.73 ± 1.65	92.71 ± 0.70	97.62 ± 3.61
10	90.97 ± 1.25	86.34 ± 0.75	84.15 ± 1.68	92.18 ± 0.81	96.95 ± 3.57
15	90.55 ± 1.42	85.51 ± 0.85	82.99 ± 1.79	91.76 ± 0.99	96.50 ± 3.62
20	90.20 ± 1.56	84.76 ± 1.08	82.01 ± 1.94	91.43 ± 1.11	96.15 ± 3.62
25	89.87 ± 1.67	84.08 ± 1.25	81.28 ± 2.06	91.12 ± 1.25	95.89 ± 3.66
30	89.57 ± 1.76	83.53 ± 1.30	80.73 ± 2.10	90.86 ± 1.33	95.62 ± 3.69

Fig. S6. Water contact angle measurements on the Zn and Zn-alloys surfaces at 5, 10, 15, 20, 25, and 30 seconds after 3 µl drop deposition.

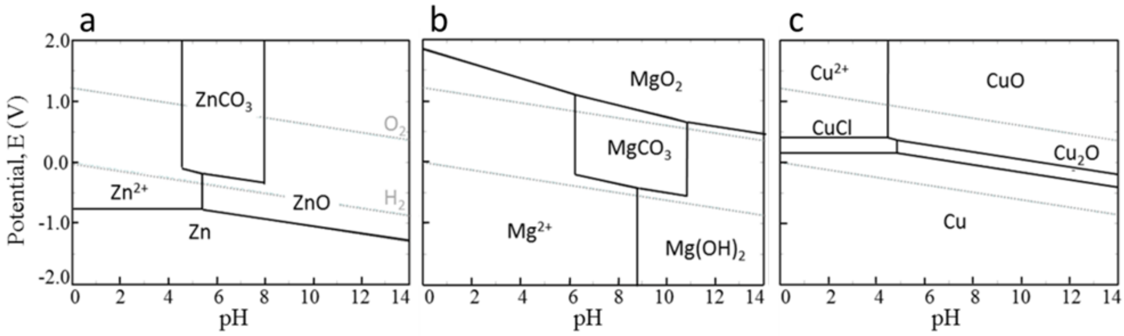

Fig. S7. Pourbaix diagrams of binary Zn-X alloys, where X = {Mg, Cu} and Zn > 95%. The medium simulated is Hanks' solution, at 37ºC and arterial pressure (Calculated using HSC 5.1 Software).

Chapter II.

Characterization of Zn-Ag alloys for bioresorbable ureteral stents

Chapter II. Characterization of Zn-Ag alloys for bioresorbable ureteral stents

Objective

To evaluate Zn-xAg (x = 2, 4 wt.%) as possible candidates for bioresorbable ureteral stents. The study aims to elucidate the antibacterial mechanisms of the alloys and the correlation between the degradation and the bacterial activity against *S. aureus* and *E. coli* strains.

Graphical abstract

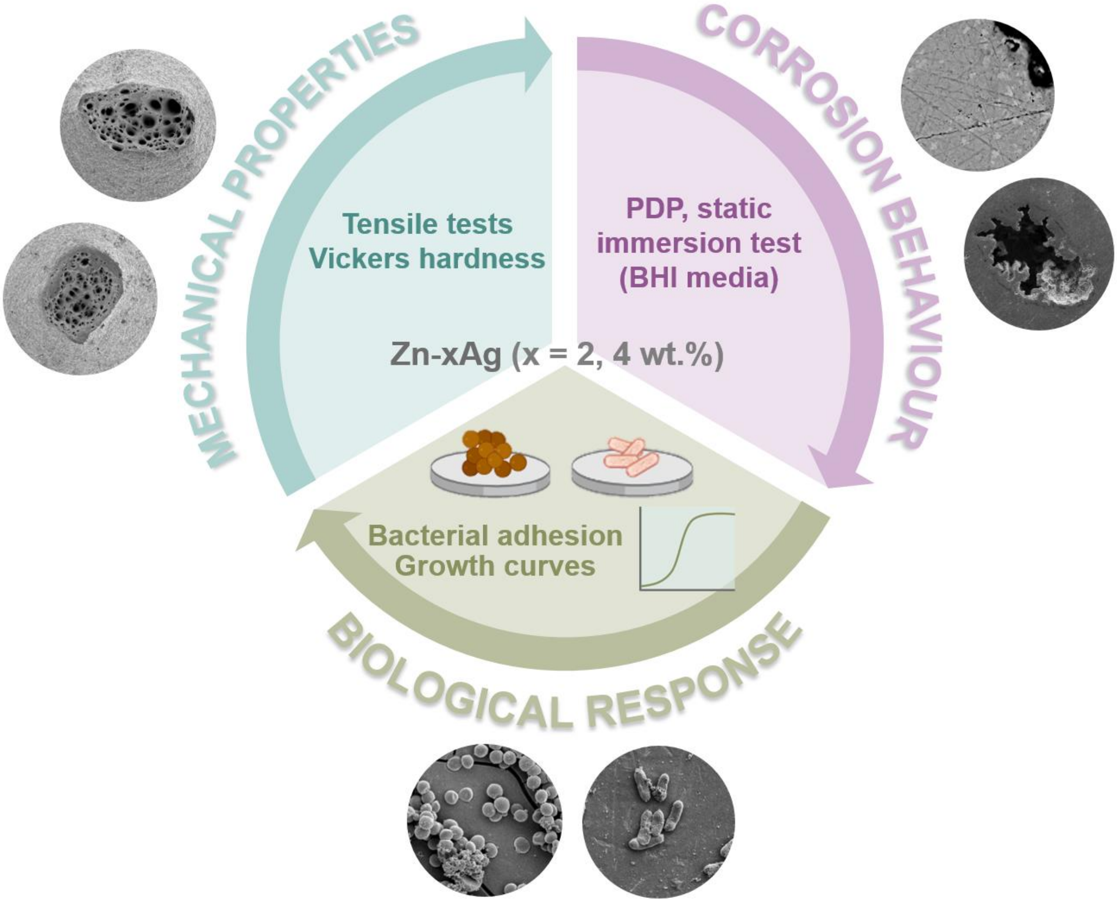

Main results

This chapter demonstrates that AgZn$_3$ precipitation enhances YS, UTS, and fracture elongation on Zn, but no real benefits in mechanical reinforcement are obtained with increasing AgZn$_3$ volume fraction. Moreover, increasing AgZn$_3$ leads to aggressive galvanic corrosion, where *S. aureus* and *E. coli* could penetrate the corrosion pits in Zn-4Ag alloy. The bacterial studies suggested that the antibacterial effect exerted by Zn-Ag alloys follows contact and not diffusion mechanisms. Overall, the Zn-2Ag alloy showed the better compromise among mechanical, degradation, and antibacterial performance.

I. Introduction

The ureteral stent is a flexible tube curled at both ends and placed into the ureter to relieve the obstruction and provide urine drainage [1]. It is implanted through a guide wire under cystoscopy, After the wire removal, the stent adopts the double J shape [2]. The continuous precipitation of salts on its surface can be used as anchor points by bacteria that further produce biofilm [4]. Previous studies showed that biofilm could form within 24 h after implantation and thus, the infections can occur at short indwelling times of two weeks [5,6]. Thus, an ideal ureteral stent should provide enough mechanical support for urine drainage; while avoiding migration, encrustations, bacterial infections and, finally, degrade after the required time.

Current biodegradable ureteral stents are based on poly(glycolic acid) (PGA), poly(lactic acid) (PLA), and poly(lactic-co-glycolic acid) (PLGA) [1]. Such polymeric structures are flexible and easily handled; however, the low resistance to loading forces sometimes requires an inert metallic scaffold [7,8]. Zn has been alloyed with a wide array of elements for mechanical reinforcement for load-bearing applications [18,19]. In addition, alloying elements might confer other properties such as superplasticity [20] or bacterial activity [21,22]. In this regard, silver (Ag) is reported to mechanically reinforce the Zn by precipitation hardening while providing exceptional elongation at fracture due to the activation of the pyramidal <c+a> slip systems of Zn [23]. Accurate material formability is fundamental for the double J shape of ureteral stents [1]. Moreover, Ag has been incorporated into several biomaterials and nanocomposites to provide antibacterial activity [24]. The advantage of these devices relies on the continuous and controlled release of Ag^+ ions [25]. The Ag^+ cation is reported to cause changes in the bacterial RNA, DNA, and mitochondrial respiration [26], and it can destroy the bacterial membrane causing bacterial death [27].

UTIs are generally attributed to the *Escherichia coli (E. coli)* family, which are adapted to colonize the urinary tract, and they are becoming increasingly resistant to antibiotics [28]. On the other hand, *Staphylococcus aureus (S. aureus)* is the most common bacteria causing infections after surgical interventions and it has also developed medicine resistance [29]. Therefore, alternative approaches to actual antibiotics need to be developed.

In this regard, the antibacterial activity of metallic cations such as Zn^{2+}, Cu^{2+}, and Ag^+ has been previously reported [30,31]. Biodegradation of the metals occurs through their corrosion processes, where metallic ions are released into the cellular environment [32]. Antimicrobial performance of Mg-based materials has been related to the release of Mg^{2+} ions, and the alkalinisation of the surrounding media during its degradation [33]. However, a pH increase in the ureteral system would accelerate the deposition of low solubility mineral deposits, which favours stone formation [34]. Recently, Qu *et al.* [35,36] reported the antibacterial effect of Zn-Cu and Zn-Ag alloys by inhibiting the expression of bacterial genes related to adhesion, colonization, and biofilm formation of *S. aureus, S. epidermidis,* and their methicillin-resistant counterparts. Likewise, the degradation of Zn-based materials releases antibacterial Zn^{2+} ions into the media affecting bacterial metabolism. The released ionic concentration should be above the corresponding minimum inhibitory concentration (MIC) to exert an efficacious antibacterial effect [37]. However, the rapid degradation of the metal may lead to mechanical failure of the implant or the excessive deposition of low solubility minerals onto its surface [38,39]. Moreover, the induced rugosity after the mineral precipitation could be used as bacterial anchorage points. Furthermore, degrading surfaces of bioresorbable metals are supposed to reduce bacterial infection by inhibiting bacterial attachment [3]. However, the antibacterial mechanisms of biodegradable metals, as well as the effect that degradation has on bacterial performance has not been unravelled.

This work aims to evaluate pure Zn and Zn-xAg (x = 2, 4 wt. %) alloys as possible material candidates for ureteral stents. Moreover, this study tends to provide more insights into the mechanisms of the bacterial activity of bioresorbable metals by relating their degradation with their exerted antibacterial effect.

II. Materials and methods

II.1. Materials

Metallic bars of pure Zn (99.9 % purity) and Zn-xAg (x = 2, 4 wt.%) of 10 mm diameter were provided by GoodFellow (UK). The as-received condition of the pure Zn bars was extruded, whereas the Zn-Ag bars were extruded and cold rolled.

II.2. Microstructural characterization

Microstructure was characterized both parallel and perpendicular sections to the extrusion direction. To this end, the bars were cut into disks of 2.5 mm thickness and abraded with silicon carbide papers down to P4000 (Neurtek S.A., Spain). Final polishing was achieved using a 50 nm silica suspension (Buehler, Germany) and ultrasonically cleaned in absolute ethanol (Sigma-Aldrich, USA) for 5 minutes. The samples were then etched with a solution containing 0.5 g of oxalic acid (Sigma-Aldrich, USA), 2.5 mL acetic acid (Sigma-Aldrich, USA), and 25 mL of absolute ethanol. The microstructure was observed by scanning electron microscopy

(SEM) equipped with X-ray energy-dispersive spectrometry (EDS) (JSM-70001F, JEOL, Japan). The volume fraction determination of the phases was performed using ImageJ software (National Institutes of Health, MD). The phase composition of the samples was characterized by X-ray diffractometry (XRD, D8 ADVANCE Twin, Bruker, USA) using CuKα at 40 kV and 100 mA with a scanning range from 20 ° to 90 °, the scan rate of 2 ^{o}min^{-1} and step size of 0.02°.

II.3. Mechanical characterization

The mechanical properties were evaluated through tensile tests (ASTM E8-04 [40]) and Vickers microhardness. Tensile dog-bone samples with 30 mm gage length, 6 mm diameter, and 6 mm radius of filled were machined from the rods with the long axis parallel to the extrusion direction. The tensile tests were carried out on a universal material test loading machine (AllroundLine Z020, Zwick/Roell, Germany) at room temperature and at 1 mm/min strain rate. Vickers microhardness, H_v, was measured using a microhardness tester (DuraScan G5, Emco-Test) with 100 g of load and 10 s of dwelling time. The H_v was calculated from 5 measurements.

II.4. Corrosion evaluation

The degradation evaluation was carried out by potentiodynamic polarization (PDP) and static immersion tests at 37 ± 1 ºC in a brain heart infusion (BHI) (Scharlab, Spain) used for bacterial culture. The composition of the BHI media is listed in **Table 1.**

Table 1. Composition of the brain heart infusion media (BHI) (Scharlab, Spain).

Compound	Concentration (g/L)
Enzymatic digest of animal tissues, and brain-heart extract	27.5
Dextrose	2.0
Disodium hydrogen phosphate	2.5
Sodium chloride	5.0

II.4.1. Potentiodynamic polarization test

PDP tests were performed according to ASTM G5-14 [41] using a PARSTAT 2273 potentiostat (Princeton Applied Research, USA) in a standard three-electrode set up, with the sample as the working electrode, a saturated calomel electrode (SCE) as the reference electrode, and platinum as the counter electrode. Before the PDP test, the samples were immersed in the BHI medium for 60 minutes to measure the open circuit potential (OCP). The polarization curves were scanned from -1.4 V to -0.6 V against OCP at a scan rate of 2 mV/s. The corrosion potential

(E_{corr}) and the current density (i_{corr}) were determined from the curves using the PowerSuite software (Princeton Applied Research, USA), and the corrosion rate (CR, μm/year) was calculated using Eq. 1 [42]:

$$CR = 3.27 \cdot 10^{-3} \frac{i_{corr} EW}{\rho} \quad (1)$$

where the i_{corr} is the current density (μA/cm^2), the EW is the equivalent metal weight (g/mol), and the ρ is the metal density (g/cm^3).

II.4.2. Static immersion tests

For the static immersion test, the samples were first weighted and then immersed for 10 days in BHI with a solution under standard conditions (humidified atmosphere, 5% CO_2 at 37 ±1 ºC) with a volume to surface area of 0.20 mL/mm^2 at 37 ± 1 ºC, following the ASTM G31-72 standard [43]. Before the immersion, the samples were sterilized by immersion in absolute ethanol for 15 minutes. The whole solution was renewed each 48 h. At 2 h, 1 d, 2 d, 3 d, 7 d, and 10 d, aliquots of the solution were collected and filtered with a 0.2 μm filter. The released Zn^{2+} and Ag^+ were analysed by Inductively coupled plasma mass spectrometry (7800 ICP-MS, Agilent Technologies). On the other hand, the aliquots were used as conditioned media in the indirect contact test (Section II.5.2). The pH was monitored through all the experiment. After 10 days of immersion, the corrosion products were removed at 70 ºC with a 200 g/L solution of CrO_3 [44], and the degraded samples were weighted for the CR (mm/year) calculation by mass loss using Eq. 2 [43]:

$$CR = (8.76 \cdot 10^4 \times W)/(A \times T \times \rho) \quad (2)$$

where the W is the weight loss (g), the A is the area of the sample exposed to solution (cm^2), T is the immersion time (h), and ρ is the metal density (g/cm^3).

The surface of the samples was observed by SEM and EDS, before and after, the removal of the corrosion products.

II.5. Antibacterial activity

Staphylococcus aureus (*S. aureus*, CCUG 15915, Culture Collection University of Göteborg (CCUG), Göteborg, Sweden) and *Escherichia coli* (*E. coli*, CECT 101, Colección Española de Cultivos Tipo (CECT), Valencia, Spain) were selected as Gram-positive and Gram-negative bacteria, respectively. All the bacteria suspensions used in the bacterial assays were prepared as follows: frozen bacteria were aerobically cultured in BHI medium at 37 ± 1 ºC overnight.

Then, the suspensions were diluted in BHI medium down to a final concentration of approximately 10^8 colony forming units (CFU) per millilitre, corresponding to an optical density of 0.2 at 600 nm. The agar plates were prepared by mixing the BHI medium with 7.5 g agar (Agar bacteriological, Scharlab, Spain). Previously to the tests, the samples were sterilized by immersion in absolute ethanol for 20 minutes and subsequently rinsed three times using a phosphate buffer solution (PBS, Sigma Aldrich, USA) into the sterile hood.

II.5.1. Agar diffusion plate test

The agar diffusion plate test was performed according to the standard CLSI M07-A9 [45]. First, 100 μL of the bacteria solution were placed onto agar plates. Then, the sterilized samples were placed on the agar plates and incubated at 37 ± 1 ºC overnight. According to the standard, the MIC corresponds to the lowest concentration of antimicrobial agent that completely inhibits bacterial growth. Thus, no zone of inhibition indicates no antibacterial effect.

II.5.2. Bacterial indirect contact test

The extracts for the indirect contact test were collected during the static immersion test (Section II.4.2) and put in contact with bacteria. Therefore, aliquots of 100 μL from 6, 24, 48, and 72 h after immersion were collected and mixed with 100 μL of the bacteria suspension diluted 1:10 in a 96-well culture plate. The plate was placed into a multimode microplate reader (Synergy™ HTX, BioTek, USA) during 16 h, and the absorbance was measured every 15 minutes. The negative control (C-) was composed of 200 μL of Hanks' solution and BHI (50:50). The positive control (C+) was prepared by mixing 100 μL of Hanks' solution with 100 μL of the bacteria suspension diluted 1:10 in BHI.

II.5.3. Bacterial direct contact test

Zn, Zn-2Ag and Zn-4Ag discs were inoculated with 20 µL of bacteria suspension and incubated for 1 h, 2 h, and 24 h at 37 ± 1 ºC. Afterwards, the discs were rinsed twice with PBS to remove the non-adhered bacteria.

The bacteria viability was evaluated by fixing the attached bacteria with 500 μL of 2.5 % glutaraldehyde in PBS at 5 ± 1 ºC for 30 min and staining with the LIVE/DEAD™ *Bac*Light™ bacterial viability Kit (Molecular Probes, USA). The green fluorophore (SYTO 9) stained the DNA of all the bacteria, whereas the red fluorophore (propidium iodide, PI) stained only the bacteria with a damaged membrane. The kit was prepared by diluting the SYTO9 and PI (1.67

mM) in PBS to a final concentration of 3 μm/mL. The stained bacteria were observed by fluorescent microscopy (Nikon E600, Tokyo, Spain).

Furthermore, the adhered bacteria were detached from the surfaces for their quantification. For this purpose, samples were immersed into 1 mL of PBS and subjected to 1-minute ultrasounds. The resulting solution containing the previously attached bacteria was serially diluted (1:100, 1:1000, and 1:10000) and incubated onto agar plates overnight. Afterward, the formed CFUs were counted for quantification following ASTM D5465-93 [46].

The surfaces after the adhesion test were observed by SEM. Bacteria were fixed by 500 μL of 2.5 % glutaraldehyde in PBS at 5 ± 1 ºC for 30 min and dehydrated by 10 minutes of immersion in an ethanol-water mixtures series (of 50%, 70%, 85%, 90%, and 100% ethanol). Then, the bacteria and the corrosion products were removed at 70 ºC with a 200 g/L solution of CrO_3 [44].

II.6. Statistical analysis

The results of this work were reported as the mean values ± the standard deviation. Three replicates (n = 3) were tested in the experiments. The Shapiro-Wilk test was used to determine if the data were normally distributed. The normally distributed data were then subjected to an equality of variances test (ANOVA). A non-parametric test (Kruskal-Wallis test) was used for the non-normally distributed data. The software used for the analysis was Minitab Statistical Software (Minitab Inc. USA).

III. Results

III.1. Microstructure

Fig. 1 shows the microstructure of the samples, and **Fig. 2** includes the XRD results. The microstructure of Zn consisted of large Zn grains with heterogeneous grain size distribution (**Fig. 1a, d**). SEM images and EDS analysis confirmed the presence of a Zn matrix (darker areas) and an Ag-rich phase (brighter areas) in both Zn-Ag alloys (**Fig. 1b-c, e-f**). According to the XRD results, the Zn-Ag alloys comprised a Zn matrix and a secondary $AgZn_3$ phase. The calculated volume fraction of the $AgZn_3$ phase increased from 3 % for the Zn-2Ag alloy to 14 % for the Zn-4Ag alloy. Finally, the microstructure of the longitudinal sections showed preferential grain orientation and phase elongation to the extrusion direction for the cold-rolled Zn-Ag alloys (**Fig. 1e, f**).

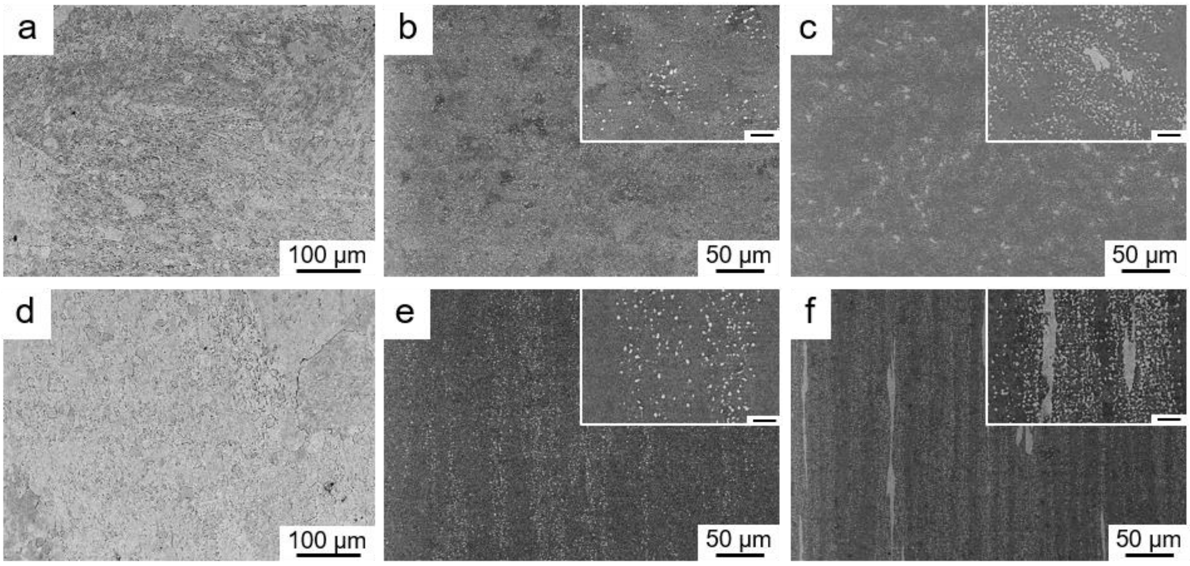

Fig. 1. SEM images of the microstructure of the transversal (top) and longitudinal (bottom) sections of Zn (a, d), Zn-2Ag (b, e), and Zn-4Ag (c, f). Scale bar of the zoomed regions: 10 µm.

	Lattice parameters				
Phase	**a (nm)**	**b (nm)**	**c (nm)**	**Pearson symbol**	**Space group**
Zn	2.6649	2.6649	4.9470	hP2	$P6_3/mmc$
$AgZn_3$	2.8227	2.8227	4.4274	hP2	$P6_3/mmc$

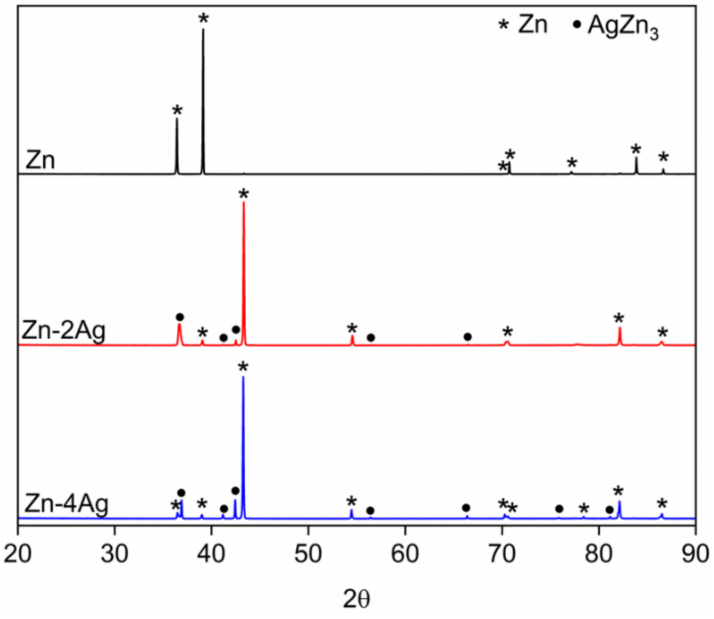

Fig. 2. XRD results: table with crystallographic data of the Zn and $AgZn_3$ phases and XRD spectra of pure Zn, Zn-2Ag, and Zn-4Ag samples.

III.2. Mechanical characterization

As expected, the UTS and $YS_{0.002}$ of the Zn-Ag alloys were significantly higher than those obtained for pure Zn (**Table 2**). Similar tendency could be observed from Vickers measurements, where the H_v increased from pure Zn to Zn-2Ag alloy, and mildly decreased from Zn-2Ag to Zn-4Ag alloy. Moreover, the elongation at fracture values arose from 8 ± 2 % for pure Zn to 244 ± 30 % for Zn-4Ag alloy. The SEM fractographs of the samples after the tensile test showed dimple-featured fractures in accordance with the high ductility of Zn-Ag alloys (**Fig. 3**). The Zn-2Ag alloy exhibited dimples with areas ranging 3 – 200 μm^2, and the Zn-4Ag showed reduced areas from 1 to 50 μm^2.

Table 2. Mechanical characterization results: ultimate tensile strength (UTS), yield strength at 0.2 % of elongation (YS0.002), and elongation at fracture calculated from tensile tests; and microhardness obtained from Vickers measurements. ^{a,b,c} symbols join groups with non-statistically significant differences.

Sample	**UTS (MPa)**	**$YS_{0.002}$ (MPa)**	**Elongation (%)**	**Micro-hardness (HV)**
Zn	97 ± 7^a	30 ± 6^a	8 ± 2^a	37.1 ± 0.6^a
Zn-2Ag	125 ± 1^b	100 ± 7^b	197 ± 19^b	49.3 ± 0.9^b
Zn-4Ag	113 ± 1^b	92 ± 2^b	244 ± 30^c	46.5 ± 0.2^c

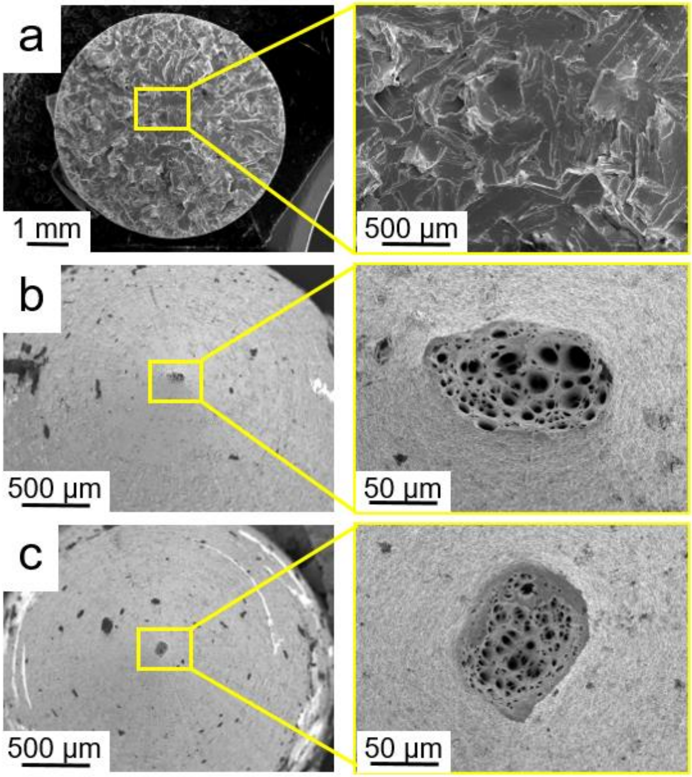

Fig. 3. SEM fractography images of (a) Zn, (b) Zn-2Ag, and (c) Zn-4Ag samples after tensile tests.

III.3. Degradation evaluation

Table 3 shows the corrosion parameters (E, i, and CR-PDP) obtained from the PDP tests. The Zn-Ag alloys exhibited decreased current density and hence a lower corrosion rate (CR, PDP) than pure Zn, where the Zn-2Ag alloy was the most corrosion resistant of the series.

Table 3. Current density (i), corrosion potential (E), and corrosion rate (CR-PDP) calculated from PDP tests; and the resulting corrosion rate determined from immersion test (CR-mass loss).

Sample	E (V)	i (μA/cm^2)	CR-PDP (mm/yr)	CR- mass loss (mm/yr)
Zn	-1.166 ± 0.013	3.13 ± 0.85	0.047 ± 0.013	0.080 ± 0.056
Zn-2Ag	-1.176 ± 0.013	2.00 ± 0.42	0.030 ± 0.006	0.034 ± 0.043
Zn-4Ag	-1.171 ± 0.001	2.59 ± 1.13	0.038 ± 0.0167	0.098 ± 0.082

The Zn-2Ag alloy presented a noticeable decrease in CR after the immersion test (**Table 3**) compared with pure Zn, while the Zn-4Ag alloy exhibited the highest CR of the series. **Fig. 4** shows the SEM images of the surfaces of the samples before and after removal of the corrosion products after 10 days of immersion in BHI solution at 37 ± 1 ºC. After the immersion, the surfaces were covered by a layer of corrosion products (**Fig. 4a, c, e**). The EDS analysis indicated the presence of Zn, C, O, and P. Ag was detected for the Zn-Ag alloys. After removal of the corrosion layer, the Zn and Zn-2Ag samples presented overall uniform surfaces (**Fig. 4b, d,** respectively), whereas the Zn-4Ag alloy exhibited several corrosion pits all over its surface (**Fig. 4f**).

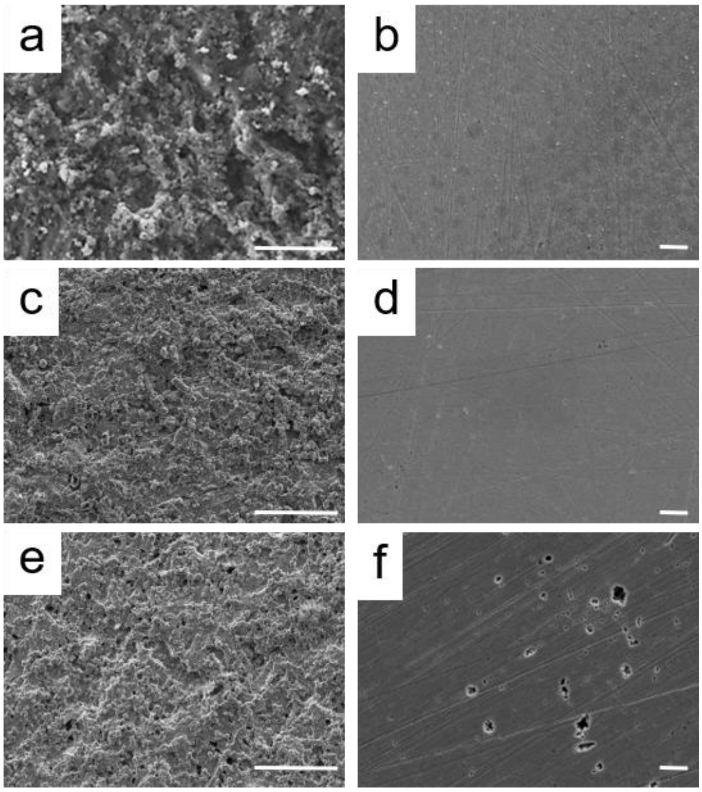

Fig. 4. SEM images of the general surfaces of the (a) Zn, (b) Zn-2Ag, and (c) Zn-4Ag samples before (left column) and after (right column) removal of the corrosion products after 10 days of immersion in BHI at 37 ± 1 ºC. Scale bar: 10 μm.

Fig. 5 shows the SEM images and the EDS analysis of the initial degradation points of the samples after immersion in BHI and with the removal of the corrosion products. Pure Zn exhibited an extensive homogeneous degradation, with no localized corrosion (**Fig. 5a**). However, the degradation of the Zn-Ag alloys began in specific areas where the $AgZn_3$ phase and the Zn matrix were perfectly distinguished (**Fig. 5b, c**). Spectra 1 and 3 in **Fig. 5b** indicated the presence of the Ag-rich phase, in contrast to the darker areas (Spectrum 2) of studied Zn-2Ag. A similar composition was found in the corrosion pit of the Zn-4Ag alloy (Spectrum 4 in **Fig. 5c**), where the Ag content was higher than in the non-degraded surface (Spectrum 5). Moreover, Spectra 1 and 4 presented a significant percentage of Cl.

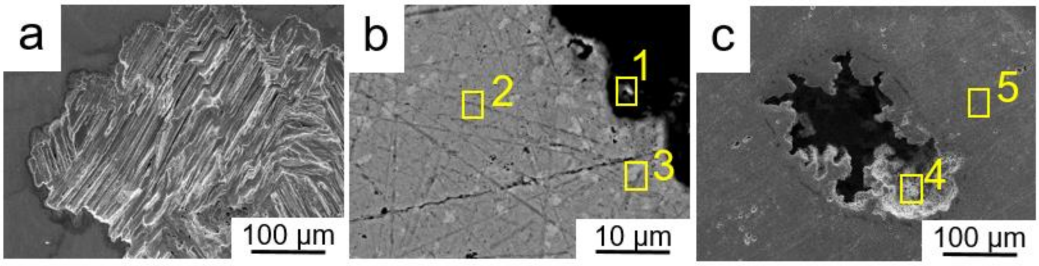

Spectrum	C	O	Cl	Zn	Ag
1	21.54	1.84	0.39	68.83	7.41
2	9.67	2.11	N.D.	86.76	1.45
3	13.62	N.D.	N.D.	77.00	9.38
4	9.22	2.66	0.30	75.73	12.09
5	8.31	2.39	N.D.	81.13	8.18

Fig. 5. SEM images and EDS analysis (wt. %) of the initial degradation points of (a) Zn, (b) Zn-2Ag, and (c) Zn-4Ag after the removal of the corrosion products after 10 days of immersion in BHI at 37 ± 1 ºC. N.D.: not detected.

As can be observed from **Fig. 6a**, the measured pH value of all the samples during the immersion assay was lower than the initial pH value of 7.4 ± 0.2 of the BHI medium. **Fig. 6b** shows the curves of Zn^{2+} released on days 1, 2, 3, and 10 of immersion. The initial values of released Zn^{2+} at 2 h of immersion were 154.0 ± 6.1 µg/dL, 136.1 ± 24.4 µg/dL, and 142.9 ± 26.8 µg/dL for Zn, Zn-2Ag, and Zn-4Ag, respectively. The concentration of Ag^{+} at 2 h was below the limit of detection of the ICP-MS instrument (< 0.07 µg/dL).

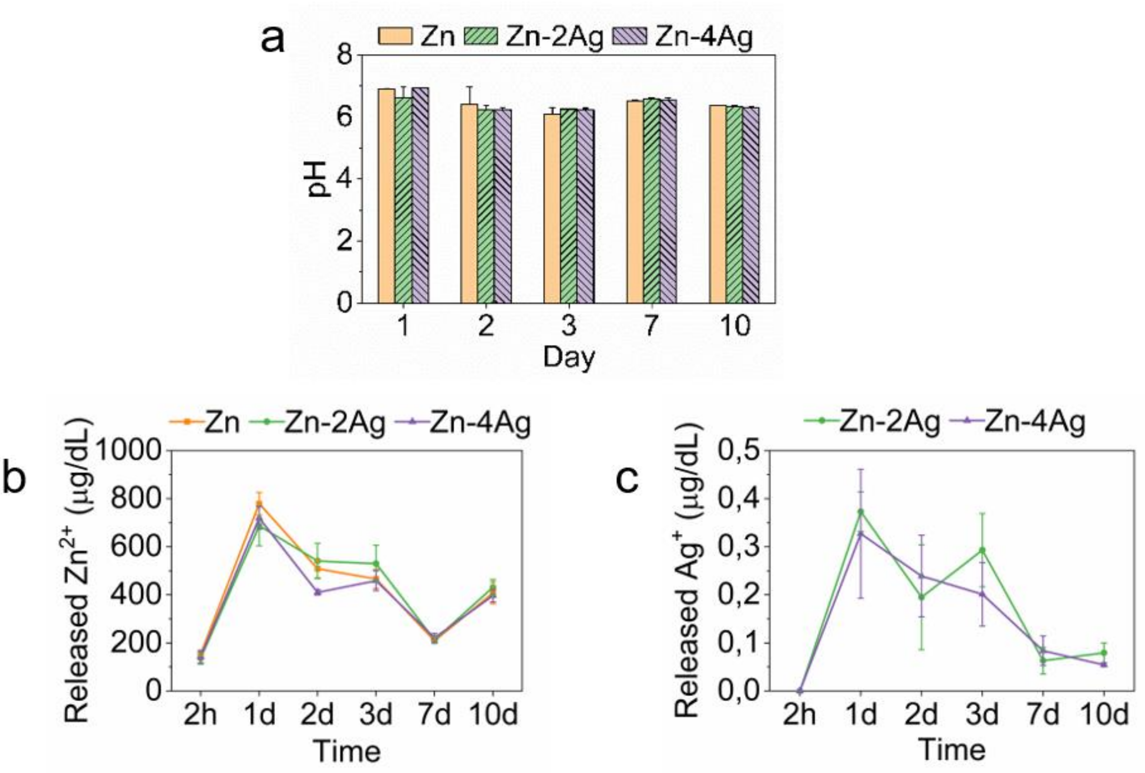

Fig. 6. Immersion test results at days 1, 2, 3, and 10 after immersion of the samples in BHI medium at 37 ± 1 ºC: (a) measured pH values; and ICP-MS analysis of the released (b) Zn^{2+}, and (c) Ag^{+} ions.

After 1 day, the Zn^{2+} concentration of all the samples rose to ≈ 700 μg/dL and continuously decreased to ≈ 200 μg/dL on day 7. On day 10 of immersion, the curve sharply increased up to ≈ 400 μg/dL in all the cases. On the other hand, the release profile of Ag^{+} for the Zn-Ag alloys also showed a decrease with the immersion day, with an initial maximum concentration of 0.37 ± 0.05 μg/dL for Zn-2Ag, and 0.33 ± 0.13 μg/dL for Zn-4Ag. Finally, the released Ag^{+} arose a plateau after 7 days of immersion.

III.4. Antibacterial effect *via* ion diffusion

Agar diffusion test showed no inhibition zone for pure Zn, Zn-2Ag and Zn-4Ag when cultured with *S. aureus* and *E. coli*, suggesting no antibacterial activity by ion diffusion for any strain. **Fig. 7** shows the *S. aureus* and *E. coli* growth curves cultured with the extracts collected from the immersion test. As it can be observed from the curves, there was no inhibition of the bacterial growth for any of the conditions, confirming that the samples did not present an effective antibacterial activity against *S. aureus* or *E. coli* by ion diffusion mechanisms.

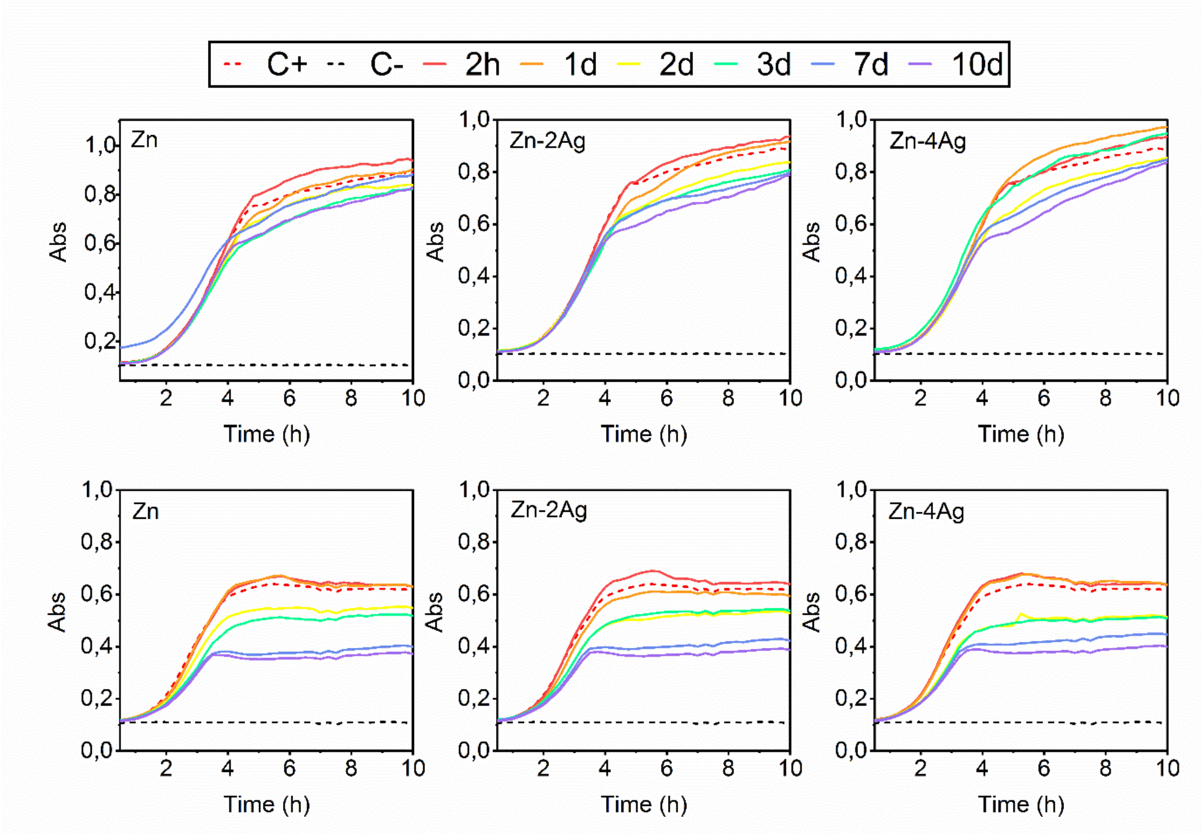

Fig. 7. Bacterial growth curves of *S. aureus* and *E. coli* cultured in the extracts from 2 h, 1 d, 2 d, 3 d, 7d, and 10 d, collected from the immersion test. C+ and C- represent the positive and the negative controls, respectively.

Table 4 lists the calculated lag time from the growth curves of *S. aureus* cultured in the extracts put in contact with the Zn, Zn-2Ag, and Zn-4Ag. No statistical differences with the control were detected in the lag time of *S. aureus* cultured with the extracts after 2 h and 1 d of immersion, in accordance with the absence of the inhibition zone in the agar test. The conditioned media from Zn-2Ag immersion did not produce significant changes on the bacterial lag time through all the immersion tests. In contrast, lower lag times were found in *S. aureus* growth when cultured with the 2 d, 3 d, 7 d, and 10 d extracts of pure Zn and Zn-4Ag samples.

Table 4. Lag time of *S. aureus* cultured with extracts of the immersion test. Lag time of positive control: 2.26 ± 0.01 h. ^{a,b} indexes join groups with no statistical differences.

Sample	2 h	1d	2 d	3 d	7 d	10 d
Zn	2.27 ± 0.06	2.22 ± 0.01	2.10 ± 0.12^{a}	2.08 ± 0.12^{a}	2.15 ± 0.02^{a}	2.09 ± 0.10^{a}
Zn-2Ag	2.17 ± 0.01	2.16 ± 0.27	2.18 ± 0.18	2.08 ± 0.12	2.09 ± 0.15	2.18 ± 0.07
Zn-4Ag	2.23 ± 0.03	2.25 ± 0.07	2.03 ± 0.04^{b}	2.16 ± 0.06^{a}	2.12 ± 0.06^{a}	1.99 ± 0.02^{b}

The calculated lag time values of *E. coli* cultured in the conditioned media are presented in **Table 5.** Longer lag times were found *E. coli* cultured in the conditioned media of Zn, until day 3 of immersion, and Zn-2Ag, after first day of immersion. The conditioned media Zn-4Ag alloy only affected the lag time on the third day.

Table 5. Lag time of E. coli cultured with extracts of the immersion test. Lag time of positive control: 1.65 ± 0.02 h. [a] index joins groups with no statistical differences.

Sample	2 h	1d	2 d	3 d	7 d	10 d
Zn	1.79 ± 0.05 [a]	1.79 ± 0.02 [a]	1.77 ± 0.05 [a]	1.85 ± 0.02 [a]	1.60 ± 0.04	1.71 ± 0.04
Zn-2Ag	1.73 ± 0.03	1.79 ± 0.09 [a]	1.86 ± 0.02 [a]	1.84 ± 0.12 [a]	1.88 ± 0.01 [a]	1.84 ± 0.05 [a]
Zn-4Ag	1.73 ± 0.03	1.74 ± 0.05	1.75 ± 0.08	1.82 ± 0.10 [a]	1.72 ± 0.05	1.63 ± 0.05

III.5. Antibacterial effect by contact

Fig. 8 shows the live-dead staining of *S. aureus* and *E. coli* after the bacterial adhesion tests. The corresponding CFU quantification is depicted in **Fig. 9.** An increase in bacterial adhesion was observed from 1 h to 2 h for both strains at every condition.

As can be observed from **Fig. 8a-i,** the adhered *S. aureus* to the surfaces decreased with the Ag content of the alloy, the quantification results confirmed this trend (**Fig. 9a**). After 24 h of incubation, a sharp decrease in *S. aureus* attachment was observed for Zn-2Ag surface compared with pure Zn, and <10 CFU/mL were counted for Zn-4Ag alloy (**Fig. 8g-i**).

A similar tendency was observed for *E. coli* at the first hour of adhesion (**Fig. 8j-l** and **Fig. 9 b**), in which the Zn-4Ag alloy exhibited the best antibacterial performance. However, no clear tendency regarding the Ag content was observed after 2 h (**Fig. 8m-o**), where the Zn-2Ag presented the lowest CFU value. Finally, no alive bacteria were found on the surfaces after 24 h of adhesion, independently of the studied surface (**Fig. 8p-r**). The yellow arrows indicate the presence of corrosion by-products that reacted with the staining.

The morphology of the attached bacteria and the surface changes after the tests were observed by SEM. **Fig. 10** shows the SEM images of the surfaces after 1 h of *S. aureus* and *E. coli* adhesion. The *S. aureus* found on the Zn surface appeared as a coccus with smooth round-shape morphology and a diameter of about 300 nm (**Fig. 10a**). The low CFU values reported for Zn-2Ag and Zn-4Ag difficulted the SEM observation of *S. aureus* attached to the surfaces (**Fig. 10b** and **c**, respectively). The *E. coli* found on all the surfaces showed typical bacteria morphology of rod shape with a size of about 1.5 μm (**Fig. 10d-f**). Furthermore, no degradation was observed in the samples.

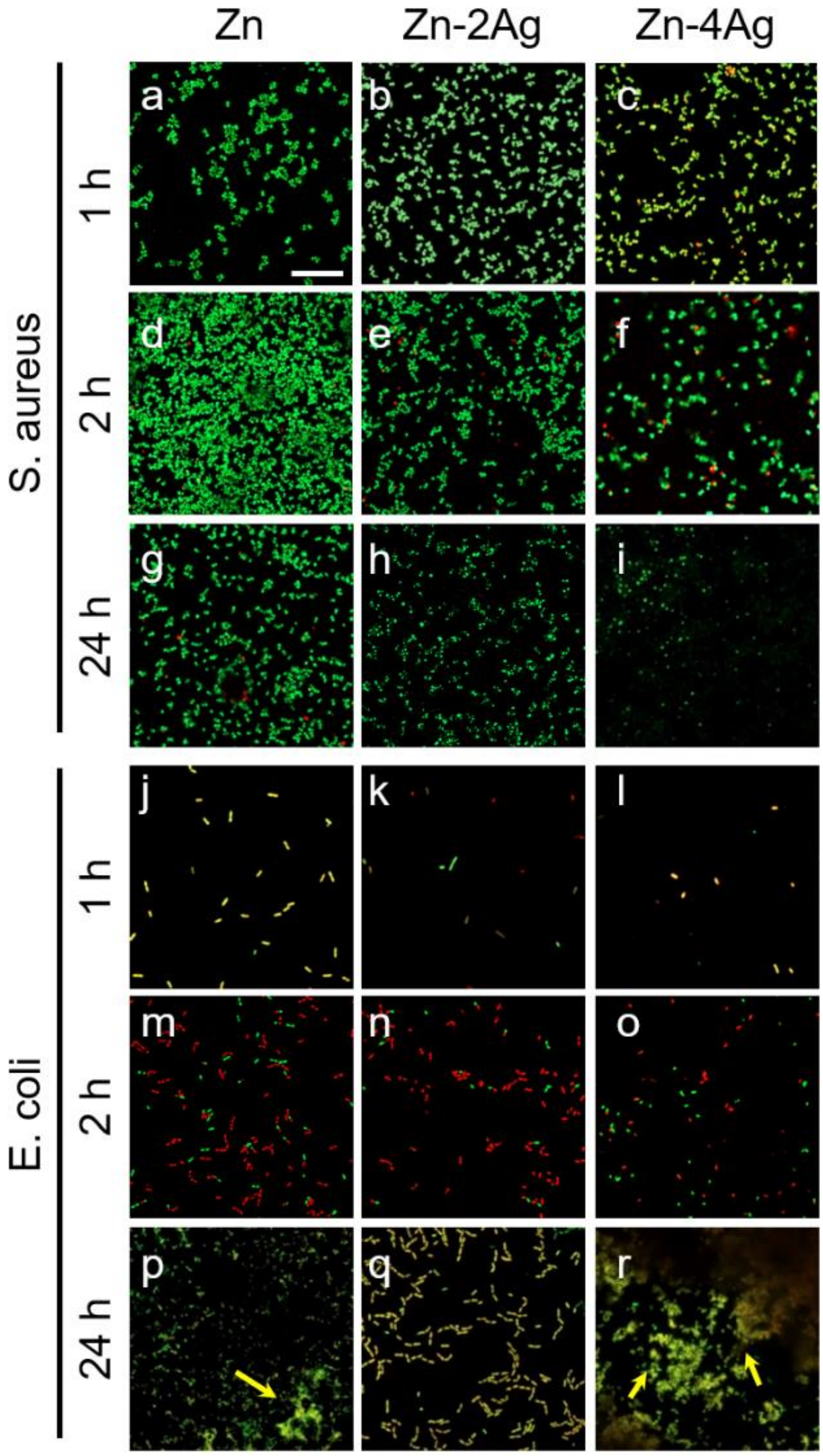

Fig. 8. Live-dead staining of *S. aureus* and *E. coli* cultured on pure Zn, Zn-2Ag, and Zn-4Ag alloys during 1, 2, and 24 h of incubation. Yellow arrows indicate the presence of stained corrosion products.

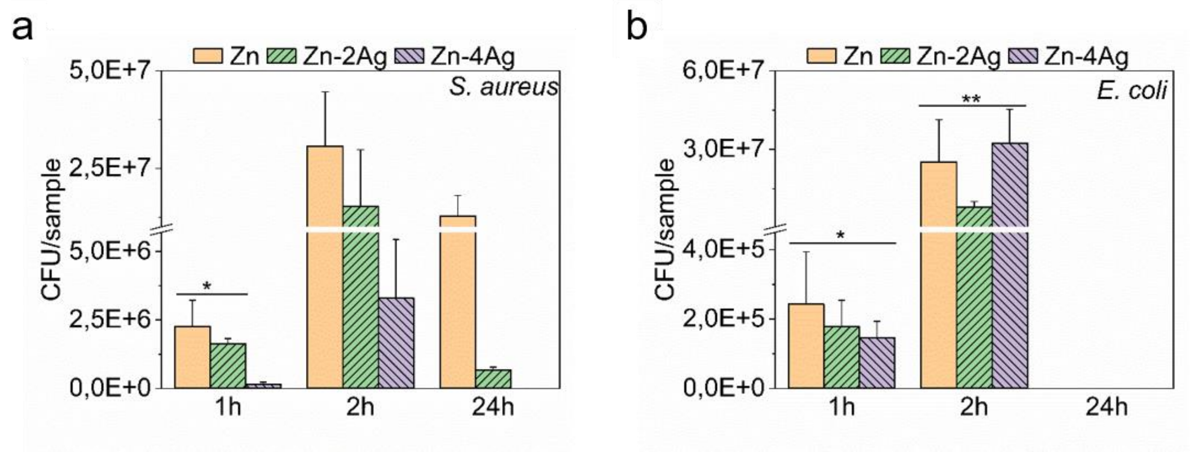

Fig. 9. Quantification of (a) *S. aureus* and (b) *E. coli* strains after 1, 2, and 24 h of incubation onto the Zn, Zn-2Ag, and Zn-4Ag surfaces. *, ** join groups with no statistical differences.

Fig. 11 shows the SEM images of the surfaces after 2 h of *S. aureus* adhesion. Higher bacterial adhesion along with biofilm formation was observed on the Zn surface (**Fig. 11a**). The lysed *S. aureus* on the Zn-2Ag surface indicated the death of bacteria posterior to the attachment (**Fig. 11c**). At this point, a few signs of bacterial degradation were found on Zn surface after the removal of the bacteria (**Fig. 11b**). The Zn-2Ag alloy showed no degradation signs but organic rests from the *S. aureus* adhesion (**Fig. 11d**). Finally, Zn-4Ag presented a smooth surface with no bacterial remnants (**Fig. 11f**).

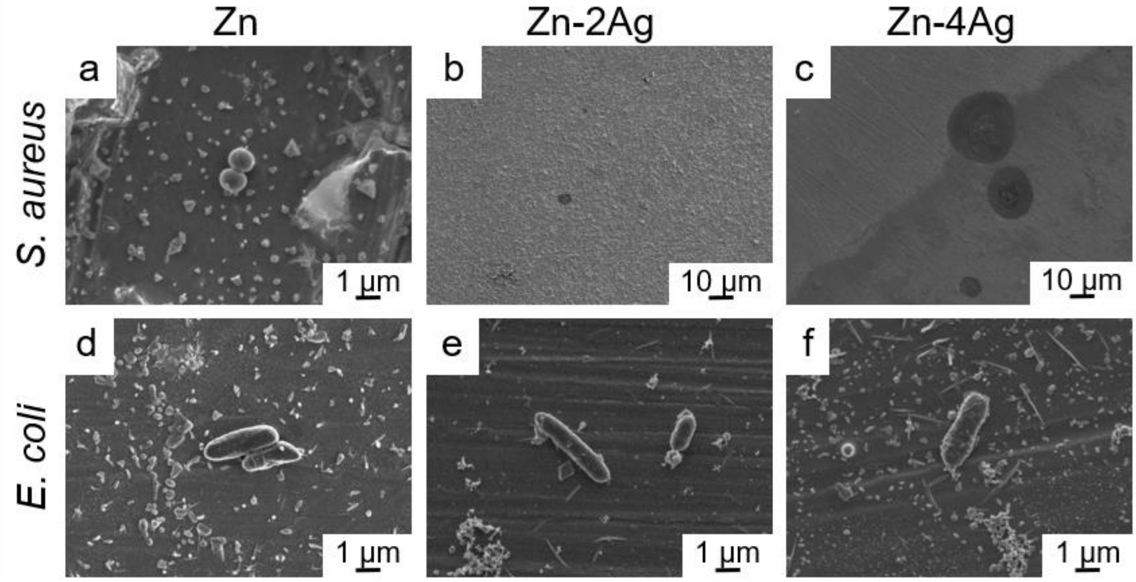

Fig. 10. SEM images of Zn, Zn-2Ag, and Zn-4Ag surfaces after 1 h of incubation with *S. aureus* and *E. coli*. No bacteria could be found for Zn-2Ag and Zn-4Ag cultured with *S. aureus*.

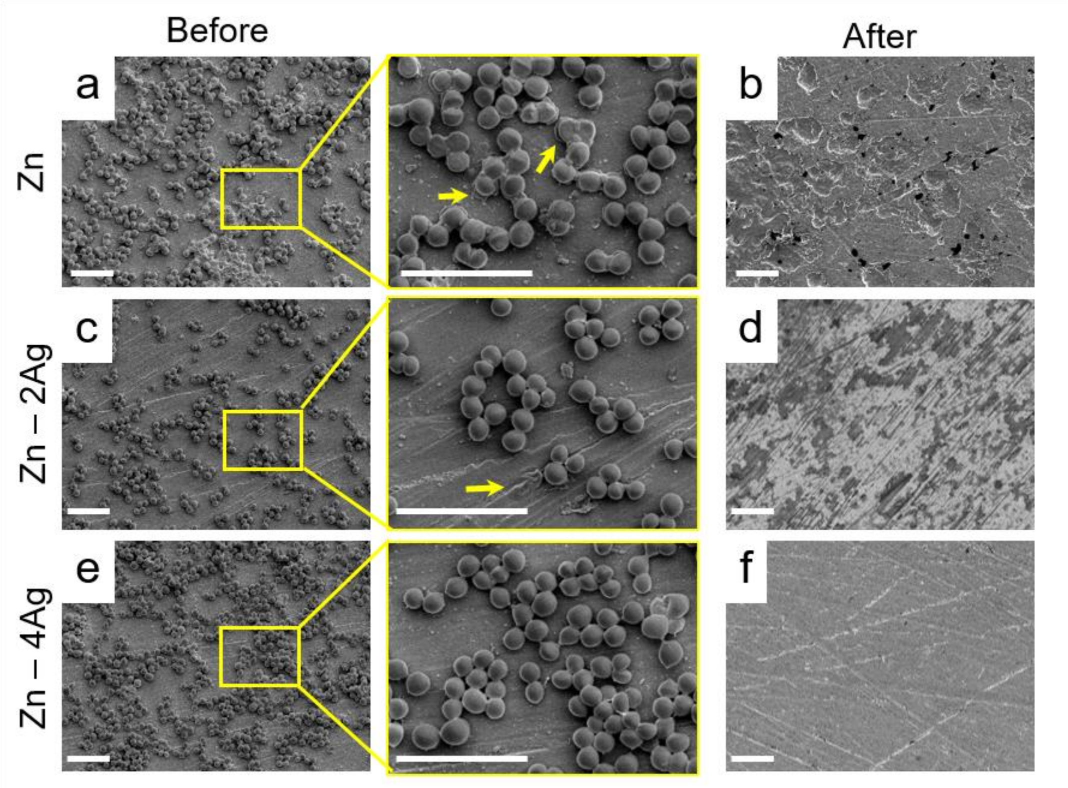

Fig. 11. SEM images of (a, b) Zn, (c, d) Zn-2Ag, and (e, f) Zn-4Ag surfaces after 2 h of incubation with *S. aureus*, before (left) and after (right) the removal of bacteria and corrosion products. Yellow arrows indicate (a) presence of biofilm, and (c) disrupted *S. aureus* morphology. Scale bar: 5 µm.

Fig. 12 shows a noticeable decrease of *S. aureus* adhesion on Zn (**Fig. 12a**) and Zn-2Ag (**Fig. 12c**) and no biofilm was observed after 24 h of bacterial adhesion, following the reduced CFU counted (**Fig. 9a**). The bacteria were surrounded by degradation by-products composed of C, O, P, Cl, and Zn, in accordance to the EDS analysis. On the contrary, more bacteria with disrupted morphologies were observed on the Zn-4Ag sample (**Fig. 12e**). The cracks on the Zn-4Ag surface indicated the degradation of the alloy. After the cleaning of the samples, the Zn exhibited severe bacterial degradation with corrosion pits of 1-4 µm in diameter (**Fig. 12b**). A particularly aggressive degradation was found in the Zn-4Ag sample (**Fig. 12f**), whereas the Zn-2Ag surface was more uniformly degraded (**Fig. 12d**).

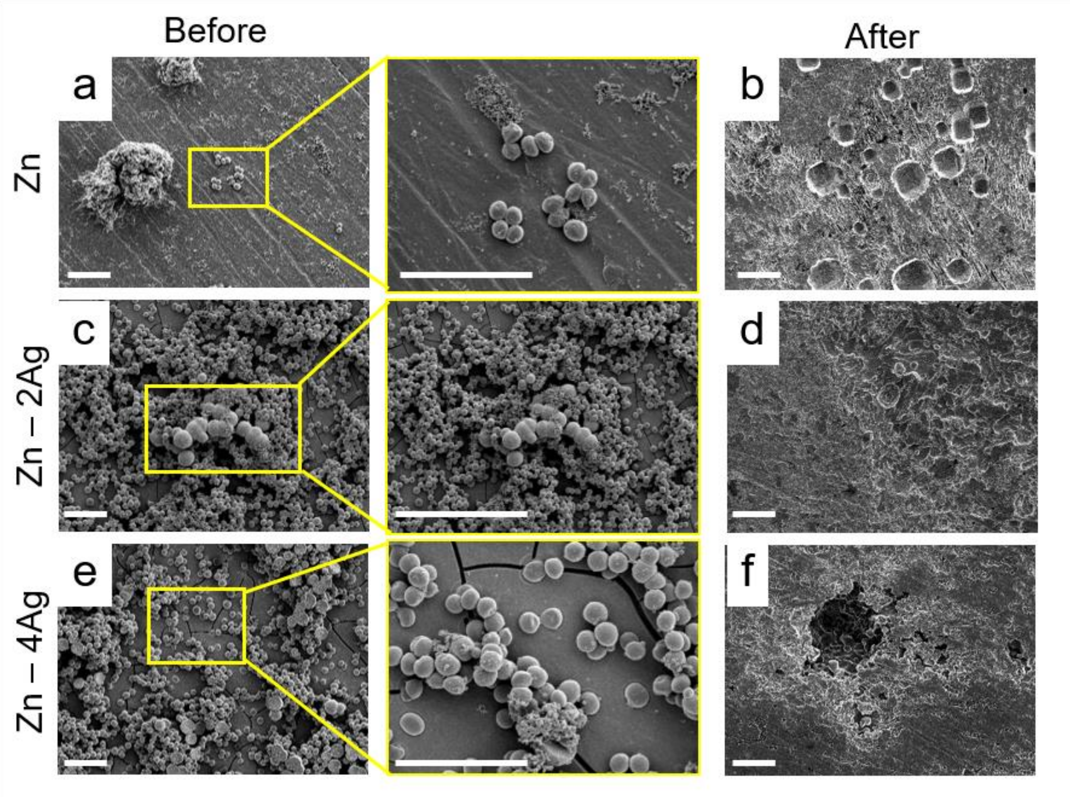

Fig. 12. SEM images of (a, b) Zn, (c, d) Zn-2Ag, and (e, f) Zn-4Ag surfaces after 24 h of incubation with S. aureus, before (left) and after (right) the removal of bacteria and corrosion products. Scale bar: 5 μm.

Fig. 13 and **Fig. 14** show the SEM images of the surfaces cultured after 2 and 24 h with *E. coli*. After 2 h, all the samples presented dispersed *E. coli* bacteria through their surfaces (**Fig. 13a, c, e**), with lysed membranes, indicated with the yellow arrow in **Fig. 13c**. The Zn and Zn-2Ag surfaces presented uniformly degraded surface after the bacterial removal (**Fig. 13b, d**), whereas localized corrosion pits were found for Zn-4Ag alloy (**Fig. 13f**).

After 24 h, the *E. coli* were covered and surrounded by the corrosion by-products (**Fig. 14a, e**). The morphology disruption observed in **Fig. 14c** and **e** indicated bacterial death, in accordance with the quantitative results (**Fig. 9**). Moreover, the surfaces presented some cracks due to the surface degradation (**Fig. 14c, e**). After the corrosion by-products removal, the Zn presented a more homogeneous surface (**Fig. 14b**) than the Zn-Ag alloys (**Fig. 14d, f**). The EDS analysis confirmed the presence of Ag-rich phases in the spherical features of the alloys.

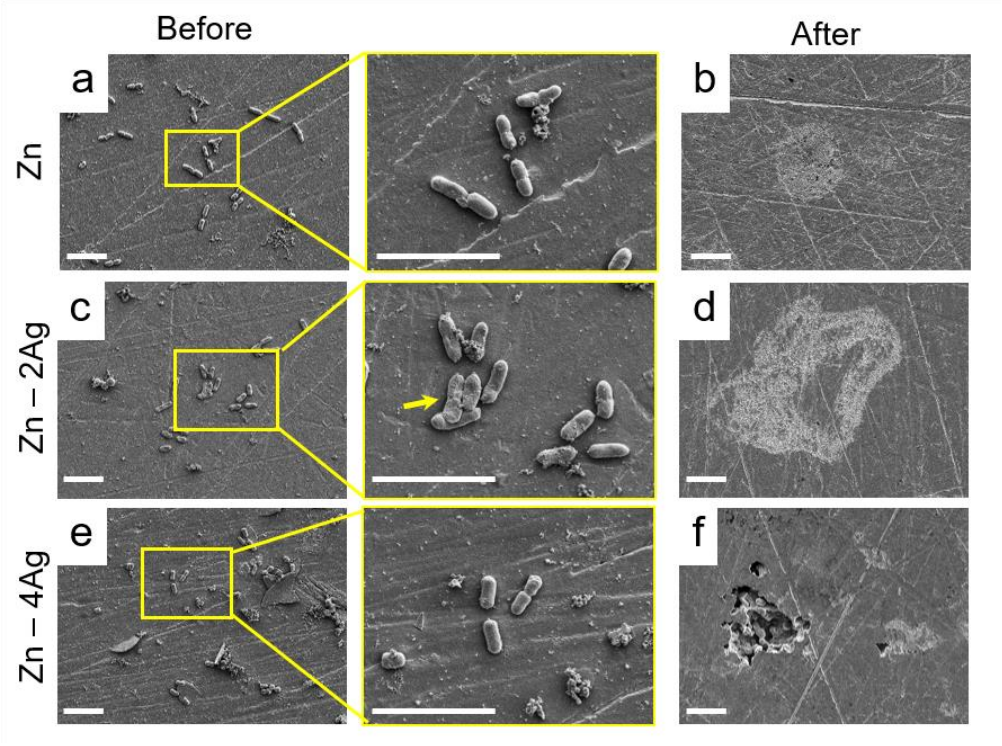

Fig. 13. SEM images of (a, b) Zn, (c, d) Zn-2Ag, and (e, f) Zn-4Ag surfaces after 2 h of incubation with E. coli, before (left) and after (right) the removal of bacteria and corrosion products. Yellow arrow indicates bacterial morphology disruption. Scale bar: 5 μm.

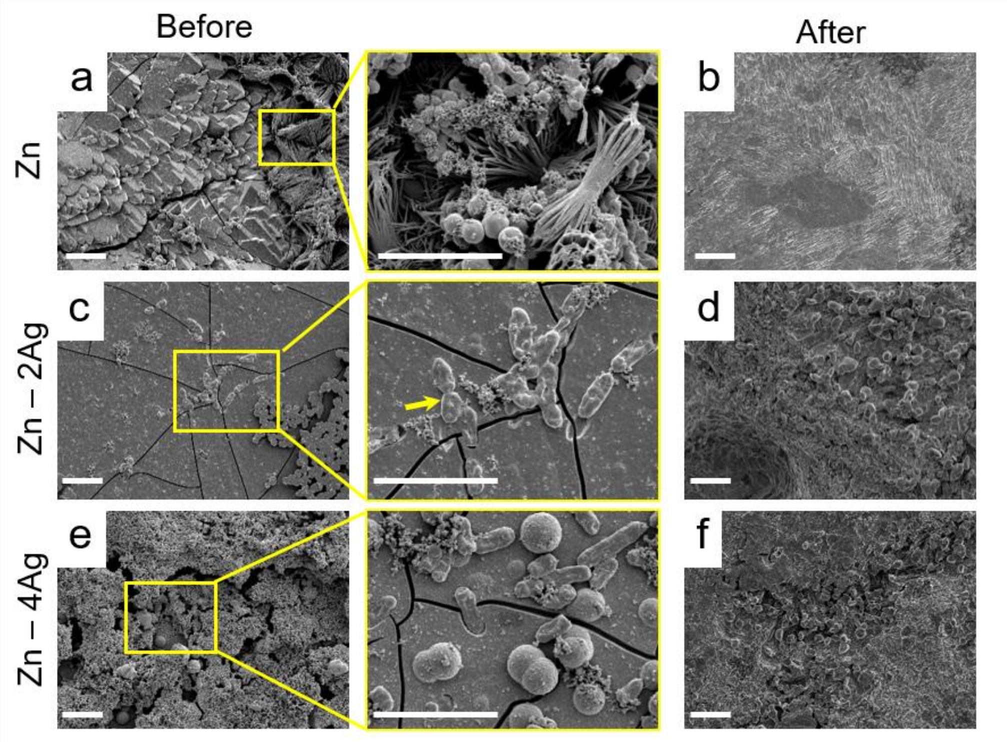

Fig. 14. SEM images of (a, b) Zn, (c, d) Zn-2Ag, and (e, f) Zn-4Ag surfaces after 24 h of incubation with E. coli, before (left) and after (right) the removal of bacteria and corrosion products. Scale bar: 5 μm.

IV. Discussion

An ideal ureteral stent should provide the proper radial strength to the ureter to drain the urine from the kidneys to the bladder, avoid incrustations and stone formation, and prevent bacterial infections [2]. The long-term risks rely on the formation of precipitated deposits onto the stent surface, where bacteria are more easily attached [4]. Moreover, the double J shape of the ureteral stents requires exceptional formability and Zn-Ag materials have been reported to exhibit an excellent elongation at fracture, meanwhile providing higher mechanical strength than polymeric-based ureteral stents [23].

According to Zn-Ag phase diagram, the solubility of Ag in the Zn matrix is 1.67 % at room temperature [23]. Above this Ag concentration, the $AgZn_3$ phase forms. The Ag content in the Zn-2Ag alloy is slightly above the solubility limit, resulting in a lower $AgZn_3$ volume fraction than in the Zn-4Ag alloy, where the Ag content is around 4 wt.%. In this work, increasing UTS and YS values were obtained for Zn-Ag alloys, suggesting that the precipitation of the $AgZn_3$ phase strengthened the Zn by precipitation hardening and grain refinement [23]. Moreover, the high elongation at fracture values obtained for Zn-Ag alloys would provide high formability for stent production. Previous studies on hexagonal-closed packed Zn-based alloys attributed the increase in elongation to the presence of $AgZn_3$ phase [23]. A slight decrease of both UTS and YS from Zn-2Ag to Zn-4Ag alloy was observed. The $AgZn_3$ of Zn-4Ag provided additional $AgZn_3$/Zn interphases for phase boundary sliding leading to a softening effect [47].

The degradation of pure Zn occurs through the grain boundaries and expands to the Zn grains depending on their orientation and size [48]. Therefore, the extensive degradation of Zn was attributed to the degradation of Zn grains (**Fig. 5a**). However, the corrosion performance of Zn changes after the alloying due to the grain refinement and the presence of secondary phases which take part in the degradation stage [49,50]. The microstructural refinement results in a higher concentration of grain boundaries that can release corrosion localization and enhance corrosion resistance [51]. Thus, the lower corrosion rate of Zn-2Ag was related to the grain refinement obtained after alloying [23]. On the other hand, the secondary phases of Zn alloys may act as cathodic regions and form galvanic pairs with the Zn matrix [50], where the larger cathode-to-anode area ratios are related to more powerful localized degradation [52,53]. After removal of the corrosion layer, the Zn-Ag alloys presented a non-degraded $AgZn_3$ phase surrounded by a degraded Zn matrix, confirming the degradation of the alloys by galvanic corrosion mechanisms (**Fig. 5b, c**). The detected Cl was related to the precipitation of AgCl(s) after the combination of released Ag^+ with the Cl^- existing in the media [54]. Furthermore, the larger volume fraction of the $AgZn_3$ phase in the Zn-4Ag alloy formed stronger galvanic pairs with the Zn matrix, leading to greater current density and corrosion rate values (**Table 3**). Homogeneous corrosion of the material is desired for biomedical applications since localized degradation may lead to the cracking of the material and subsequent implant failure. Here, accentuated galvanic corrosion of the Zn-4Ag alloy may have a detrimental effect on the further performance of the implant.

The degradation behaviour of biodegradable metals is dependent on the tested conditions, in which the working media highly influences the degradation of the metal [55–58]. The role of organic compounds from bacterial media onto the metal corrosion remains uncertain. For example, organic molecules as proteins have been reported to deposit onto the metallic surfaces and protect them from further corrosion, as well as Zn^{2+} ion is known to coordinate with different metalloproteins [59], which would accelerate de degradation of the metal. However, the main anodic and cathodic reactions occurring during degradation in inorganic media have been well-described elsewhere [48]. Respect to this, Zn-based materials degrade following an oxidation reaction (Eq. 3) and reducing the oxygen present in the medium (Eq. 4). Therefore, the produced OH^- anions from the cathodic reaction have been related to the increase of pH observed during the degradation of Zn(s) as described in previous studies [60,61].

$$Zn\ (s) \rightarrow Zn^{2+} + 2e^-\ \text{(anodic reaction)} \tag{3}$$

$$2H_2O + O_2\ (g) + 4e^- \rightarrow 4OH^-\ \text{(cathodic reaction)} \tag{4}$$

Afterwards, the produced Zn^{2+} combines with the anions existing in the degrading media forming different Zn-based minerals (oxides, hydroxides, carbonates, phosphates), usually detected in the corrosion layer of the corroded Zn alloys. From the composition of BHI media (**Table 1**), Zn^{2+} would react with the hydrogen carbonate (Eq. 5) and hydrogen phosphate (Eq. 6) anions, as well as with the H_2O molecules (Eq. 7) present in the media.

$$Zn^{2+} + HCO_3^- \rightarrow ZnCO_3\ (s) + H^+ \text{(by-product formation)} \tag{5}$$

$$3Zn^{2+} + 2HPO_4^{2-} \rightarrow Zn_3(PO_4)_2\ (s) + 2H^+\ \text{(by-product formation)} \tag{6}$$

$$Zn^{2+} + H_2O \rightarrow ZnO\ (s) + 2H^+\ \text{(by-product formation)} \tag{7}$$

Eq. 7 and Eq. 8 describe the H^+ cation as a by-product that would influence the pH of the solution by turning it more acidic. Herein, the decreased values of pH measured through the immersion test (**Fig. 6a**) are attributed to the release of H^+ that, in the tested conditions, seems to be more predominant than the produced OH^-. The ureteral stents are prone to encrustations and stone formation, because of the continuous accumulation of salty compounds on the stent [62]. Moreover, the surface irregularities of the stents through the deposition of solid by-products (e.g. $ZnCO_3$(s), $Zn_3(PO_4)_2$(s), ZnO(s)) can favour the bacterial adhesion and further infections [63]. As the precipitation of salts is directly related with the alkalinisation of the pH, an acidification of the local pH nearby the stent would be preferred for the application [62,64]. Regarding possible cytotoxicity effects, the inner epithelial layer of the ureter secretes mucosa to protect cells from the acid urine pH of 5-6 [65]. Thus, the measured pH of around 6 is not expected to induce cytotoxicity.

The drug resistance developed by bacteria complicates the treatment of UTIs and aggravate the consequences [28]. Thus, the antibacterial effect of metallic ions as Zn^{2+} or and Ag^{+} has been widely explored [30,31] Moreover, the degrading surface of bioresorbable metals may prevent the bacterial attachment and avoid further growth and colonization.

After immersion studies, the Zn^{2+} and Ag^{+} release curves followed a similar tendency in which the maximum concentration of the released ion was found after 24 h to then, continuously decrease the values (**Fig. 6b, c**). Biodegradable metals degrade by the continuous formation and breaking of a corrosion layer [55]. Therefore, the decreasing tendency of the release curves was related to the creation of a protective corrosion layer that delayed the metal degradation and inhibit the ion release. The increase in the concentration of Zn^{2+} detected on day 10 suggested the breaking of this corrosion layer and thus, the enhanced ion release. The Zn, C, O, and P elements detected at the corrosion layer of the samples after the immersion were attributed to Zn carbonates, oxides, or phosphates present in the corrosion layer of the Zn-based alloys [55,66]. The breaking of the corrosion layer would dissolve some of these salty deposits releasing the Zn^{2+} ion to the media and participating in the increase of Zn^{2+} detected on day 10 of immersion (**Fig. 6b**). The lower quantity of Ag-rich salts in the corrosion layer was not expected to influence the Ag^{+} release curve. The maximum Zn^{2+} concentration detected was lower than 800 μg/dL for all the samples and then, lower than the MIC against *S. aureus* and *E. coli* (76800 μg/dL) [67]. Likewise, the maximum concentration of Ag^{+} detected was ≈ 0.35 μg/dL, which did not reach the MIC against *S. aureus* (800 μg/dL) or *E. coli* (400 μg/dL) [67]. Therefore, the ionic concentration below the MICs explained the absence of an inhibition zone in the agar diffusion test or the unhampered bacterial growth in the indirect tests (**Fig. 7**).

Nevertheless, larger lag time values when compared to the control were reported for *E. coli* cultured with the Zn and Zn-2Ag extracts (**Table 5**), indicating a lean antibacterial effect against this strain. On the opposite, *S. aureus* exhibited shorter lag times when cultured with pure Zn or Zn-4Ag conditioned media, suggesting that the degradation of the samples stimulated bacterial growth (**Table 4**). Among the tested conditions, Zn-2Ag led to the most desirable bacterial response in the indirect contact test, with delayed *E. coli* growth and no *S. aureus* stimulation. In this regard, *E. coli* has been reported to be more vulnerable to greater Ag^+ and Zn^{2+} concentrations due to the structural differences into their membranes [68,69]. Gram+ bacteria such as *S. aureus* have a thick peptidoglycan wall that helps them to reduce the penetration of toxic metallic cations to their cytoplasm. Besides, the metallic cations exert an antibacterial effect over the correspondent MIC; below this value, the ions may motivate bacterial growth by participating in intracellular metabolic processes [37,70], explaining the lag time values obtained for *S. aureus*. Moreover, the degradation of Zn alloys ensembles a complex combination of reactions, where the formation of by-products and the pH changes may also affect bacterial behaviour and not only as a direct consequence of the Zn^{2+} or Ag^+ release from their degradation.

The antibacterial effect by contact with the surfaces was evaluated with *S. aureus* and *E. coli* adhesion after different adhesion timepoints. The observed increase of the CFU for both strains from 1 h to 2 h was attributed to the longer time the bacteria had to properly adhere to the surfaces (**Fig. 9**).

The initial biofilm was formed onto the pure Zn surface after 2 h of culture with *S. aureus* (Fig. 11a) and disappeared after 24 h (**Fig. 12**), indicating that bacteria could not grow and proliferate and hence, explaining the decreased counted CFU (**Fig. 9a**). Likewise, the CFU of Zn-2Ag and Zn-4Ag was reduced with time. Thus, the degradation of the samples and the percentage of Ag of the studied alloys, might play a fundamental role in bacterial proliferation.

After 24 h, SEM images showed lower *S. aureus* adhesion attached to the Zn-2Ag surface than to pure Zn, indicating that Ag promoted antibacterial activity at longer times by contact and not by ion diffusion (**Fig. 12a, c**). However, SEM images of Zn-4Ag after 24 h of *S. aureus* adhesion showed a relatively high number of adhered bacteria probably due to the obtained rough surface after corrosion (**Fig. 12e**). This was confirmed by SEM images of the surface after cleaning which revealed severe degradation with notable corrosion pits. The tendency of bacteria to attach to rough surfaces and to infiltrate into complex structures has been previously reported [71,72]. Here, the corrosion pits could act as a channel or tunnel in which bacteria could penetrate, leading to undesired bacterial adhesion on the Zn-4Ag. Since no *S. aureus* could be counted (**Fig. 9a**), it seemed that the bacteria were adhered to and then killed, confirming an antibacterial effect by contact. Furthermore, the excellent antibacterial effect of Zn-2Ag at this point may be also related to the homogeneously degraded surface without important surface defects (**Fig. 12d**), in contrast with the corrosion pits observed on the Zn surface (**Fig. 12b**).

Similar mechanisms were observed for Zn-4Ag cultured with *E. coli.* After 2 h, the localized degradation of the sample (**Fig. 13f**) resulted in a higher number of bacteria attached in comparison with the Zn-2Ag (**Fig. 9b**). Therefore, an excessive Ag content in the Zn alloy composition may have undesired effects, since the degradation and the irregularities due to corrosion would be used as anchorage points for bacteria. Finally, a large amount of degradation products formed (**Fig. 12** and **Fig. 14**) were attributed to zinc carbonates, oxides, phosphates, and chlorides were found as degradation by-products [57].

V. Conclusions

This work evaluated Zn-2Ag and Zn-4Ag alloys as potential materials for bioresorbable ureteral stents. The grain refinement and the precipitation of the $AgZn_3$ phase in the alloys enhanced the UTS, YS, and elongation at fracture with respect to pure Zn *via* precipitation hardening; however, the higher volume fraction in Zn-4Ag led to the slight softening of the material. The refined microstructure of the Zn-2Ag compared with the pure Zn increased the corrosion protection, and the powerful galvanic pair between $AgZn_3$ and Zn phases in Zn-4Ag accelerated the degradation. Finally, the antibacterial effect of Zn-Ag alloys was attributed to the contact of bacteria with the Ag-containing surfaces. However, the aggressive degradation of Zn-4Ag led to ineffective antibacterial activity where the bacteria infiltrated the corrosion pits and accumulated onto the degradation products. Overall, the Zn-2Alloy presented enhanced mechanical properties and antibacterial activity against both *S. aureus* and *E. coli*. However, its microstructure refinement or the implementation of protective coatings should be explored to avoid galvanic corrosion for further biomedical applications.

VI. References

[1] K. Zhang, H. Cui, H. Jiang, Y. Hao, R. Long, Q. Ma, H. Zhang, The current status and applications of ureteral stents, 2020.

[2] D. Lange, S. Bidnur, N. Hoag, B.H. Chew, Ureteral stent-associated complications-where we are and where we are going, Nat Rev Urol. 12 (2015) 17–25. https://doi.org/10.1038/nrurol.2014.340.

[3] A.A. Barros, C. Oliveira, E. Lima, A.R.C. Duarte, K. Healy, R.L. Reis, 7.41 Ureteral stents technology: Biodegradable and drug-eluting perspective, in: Comprehensive Biomaterials II, Elsevier, 2017: pp. 793–812. https://doi.org/10.1016/B978-0-12-803581-8.10189-4.

[4] N. Altunal, A. Willke, O. Hamzaoğlu, Ureteral stent infections: a prospective study, Brazilian Journal of Infectious Diseases. 21 (2017) 361–364. https://doi.org/10.1016/j.bjid.2016.12.004.

[5] E.O. Kehinde, V.O. Rotimi, K.A. Al-Awadi, H. Abdul-Halim, F. Boland, A. Al-Hunayan, A. Pazhoor, Factors predisposing to urinary tract infection after J ureteral stent insertion, 2002.

[6] B. Lojanapiwat, Colonization of internal ureteral stent and bacteriuria, World J Urol. 24 (2006) 681–683. https://doi.org/10.1007/s00345-006-0135-6.

[7] K. Hendlin, E. Korman, M. Monga, New metallic ureteral stents: Improved tensile strength and resistance to extrinsic compression, J Endourol. 26 (2012) 271–274. https://doi.org/10.1089/end.2011.0332.

[8] A. Mosayyebi, A. Vijayakumar, Q.Y. Yue, E. Bres-Niewada, C. Manes, D. Carugo, B.K. Somani, Engineering solutions to ureteral stents: Material, coating and design, Cent European J Urol. 70 (2017) 270–274. https://doi.org/10.5173/ceju.2017.1520.

[9] D.W.Y. Toong, J.C.K. Ng, Y. Huang, P.E.H. Wong, H.L. Leo, S.S. Venkatraman, H.Y. Ang, Bioresorbable metals in cardiovascular stents: Material insights and progress, Materialia (Oxf). 12 (2020) 100727. https://doi.org/10.1016/j.mtla.2020.100727.

[10] M. Asgari, R. Hang, C. Wang, Z. Yu, Z. Li, Y. Xiao, Biodegradable metallicwires in dental and orthopedic applications: A review, Metals (Basel). 8 (2018) 1–32. https://doi.org/10.3390/met8040212.

[11] D. Zhao, F. Witte, F. Lu, J. Wang, J. Li, L. Qin, Current status on clinical applications of magnesium-based orthopaedic implants: A review from clinical translational perspective, Biomaterials. 112 (2017) 287–302. https://doi.org/10.1016/j.biomaterials.2016.10.017.

[12] A. Francis, Y. Yang, S. Virtanen, A.R. Boccaccini, Iron and iron-based alloys for temporary cardiovascular applications, J Mater Sci Mater Med. 26 (2015) 1–16. https://doi.org/10.1007/s10856-015-5473-8.

[13] D. Vojtěch, J. Kubásek, J. Čapek, I. Pospíšilová, Magnesium, zinc and iron alloys for medical applications in biodegradable implants, METAL 2014 - 23rd International Conference on Metallurgy and Materials, Conference Proceedings. (2014).

[14] P.C. Banerjee, S. Al-Saadi, L. Choudhary, S.E. Harandi, R. Singh, Magnesium implants: Prospects and challenges, Materials. 12 (2019) 1–21. https://doi.org/10.3390/ma12010136.

[15] D. Vojtěch, J. Kubásek, J. Šerák, P. Novák, Mechanical and corrosion properties of newly developed biodegradable Zn-based alloys for bone fixation, Acta Biomater. 7 (2011) 3515–3522. https://doi.org/10.1016/j.actbio.2011.05.008.

[16] E. Mostaed, M. Sikora-Jasinska, J.W. Drelich, M. Vedani, Zinc-based alloys for degradable vascular stent applications, Acta Biomater. 71 (2018) 1–23. https://doi.org/10.1016/j.actbio.2018.03.005.

[17] P.K. Bowen, J.W. Drelich, J. Goldman, Zinc exhibits ideal physiological corrosion behavior for bioabsorbable stents, Advanced Materials. 25 (2013) 2577–2582. https://doi.org/10.1002/adma.201300226.

[18] H. Yang, B. Jia, Z. Zhang, X. Qu, G. Li, W. Lin, D. Zhu, K. Dai, Y. Zheng, Alloying design of biodegradable zinc as promising bone implants for load-bearing applications, Nat Commun. 11 (2020). https://doi.org/10.1038/s41467-019-14153-7.

[19] J. Venezuela, M.S. Dargusch, The influence of alloying and fabrication techniques on the mechanical properties, biodegradability and biocompatibility of zinc: A comprehensive review, Acta Biomater. 87 (2019) 1–40. https://doi.org/10.1016/j.actbio.2019.01.035.

[20] E. Mostaed, M.S. Ardakani, M. Sikora-Jasinska, J.W. Drelich, Precipitation induced room temperature superplasticity in Zn-Cu alloys, Mater Lett. 244 (2019) 203–206. https://doi.org/10.1016/j.matlet.2019.02.084.

[21] J. Lin, X. Tong, Z. Shi, D. Zhang, L. Zhang, K. Wang, A. Wei, L. Jin, J. Lin, Y. Li, C. Wen, A biodegradable Zn-1Cu-0.1Ti alloy with antibacterial properties for orthopedic applications, Acta Biomater. 106 (2020) 410–427. https://doi.org/10.1016/j.actbio.2020.02.017.

[22] P. Li, C. Schille, E. Schweizer, U.E. Klotz, J. Geis-Gerstorfer, L. Scheideler, F. Rupp, C. Legner, A. Heiss, Mechanical Characteristics, In Vitro Degradation, Cytotoxicity, and Antibacterial Evaluation of Zn-4.0Ag Alloy as a Biodegradable Material, Int J Mol Sci. 19 (2018) 755. https://doi.org/10.3390/ijms19030755.

[23] M. Sikora-Jasinska, E. Mostaed, A. Mostaed, R. Beanland, D. Mantovani, M. Vedani, Fabrication, mechanical properties and in vitro degradation behavior of newly developed Zn-Ag alloys for degradable implant applications, Materials Science and Engineering C. 77 (2017) 1170–1181. https://doi.org/10.1016/j.msec.2017.04.023.

[24] E. Zhang, X. Zhao, J. Hu, R. Wang, S. Fu, G. Qin, Antibacterial metals and alloys for potential biomedical implants, Bioact Mater. 6 (2021) 2569–2612. https://doi.org/10.1016/j.bioactmat.2021.01.030.

[25] E.A. Deitch, A.A. Marino, V. Malakanok, J.A. Albright, Silver nylon cloth: in vitro and in vivo evaluation of antimicrobial activity, J Trauma. 27 (1987).

[26] A.B.G. Lansdown, Silver I: its antibacterial properties and mechanism of action, J Wound Care. 11 (2002).

[27] C. Ning, X. Wang, L. Li, Y. Zhu, M. Li, P. Yu, L. Zhou, Z. Zhou, J. Chen, G. Tan, Y. Zhang, Y. Wang, C. Mao, Concentration Ranges of Antibacterial Cations for Showing

the Highest Antibacterial Efficacy but the Least Cytotoxicity against Mammalian Cells: Implications for a New Antibacterial Mechanism, Chem Res Toxicol. 28 (2015) 1815–1822. https://doi.org/10.1021/acs.chemrestox.5b00258.

[28] B. Foxman, The epidemiology of urinary tract infection, Nat Rev Urol. 7 (2010) 653–660. https://doi.org/10.1038/nrurol.2010.190.

[29] A. Hassoun, P.K. Linden, B. Friedman, Incidence, prevalence, and management of MRSA bacteremia across patient populations-a review of recent developments in MRSA management and treatment, Crit Care. 21 (2017) 211. https://doi.org/10.1186/s13054-017-1801-3.

[30] F.H. El-Batal, A.A. El-Kheshen, A.A. Abd El Aty, G.T. El-Bassyouni, Studies of Bone-Bonding Ability and Antibacterial Properties of Ag+, Cu2+ or Zn2+ ions Doping within Hench’s Bioglass and Glass-Ceramic Derivatives, Silicon. 10 (2018) 1231–1241. https://doi.org/10.1007/s12633-017-9580-7.

[31] J. Cui, R. Yeasmin, Y. Shao, H. Zhang, H. Zhang, J. Zhu, Fabrication of Ag+, Cu2+, and Zn2+ Ternary Ion-Exchanged Zeolite as an Antimicrobial Agent in Powder Coating, Ind Eng Chem Res. 59 (2020) 751–762. https://doi.org/10.1021/acs.iecr.9b05338.

[32] Y.F. Zheng, X.N. Gu, F. Witte, Biodegradable metals, Materials Science and Engineering R. 77 (2014) 1–34. https://doi.org/10.1007/978-1-4614-3942-4_5.

[33] Z. Lin, X. Sun, H. Yang, The Role of Antibacterial Metallic Elements in Simultaneously Improving the Corrosion Resistance and Antibacterial Activity of Magnesium Alloys, Mater Des. 198 (2021). https://doi.org/10.1016/j.matdes.2020.109350.

[34] J.K. Ohler-Ock, M.O. Re, R.C.L. Feneley, Long-term catheterization of the bladder: prevalence and morbidity, Br J Urol. 77 (1996) 347–351.

[35] X. Qu, H. Yang, B. Jia, M. Wang, B. Yue, Y. Zheng, K. Dai, Zinc alloy-based bone internal fixation screw with antibacterial and anti-osteolytic properties, Bioact Mater. 6 (2021) 4607–4624. https://doi.org/10.1016/j.bioactmat.2021.05.023.

[36] X. Qu, H. Yang, B. Jia, Z. Yu, Y. Zheng, K. Dai, Biodegradable Zn–Cu alloys show antibacterial activity against MRSA bone infection by inhibiting pathogen adhesion and biofilm formation, Acta Biomater. 117 (2020) 400–417. https://doi.org/10.1016/j.actbio.2020.09.041.

[37] D. Rutherford, J. Jíra, K. Kolářová, I. Matolínová, J. Mičová, Z. Remeš, B. Rezek, Growth inhibition of gram-positive and gram-negative bacteria by zinc oxide hedgehog particles, Int J Nanomedicine. 16 (2021) 3541–3554. https://doi.org/10.2147/IJN.S300428.

[38] L. Tan, Q. Wang, X. Lin, P. Wan, G. Zhang, Q. Zhang, K. Yang, Loss of mechanical properties in vivo and bone-implant interface strength of AZ31B magnesium alloy screws with Si-containing coating, Acta Biomater. 10 (2014) 2333–2340. https://doi.org/10.1016/j.actbio.2013.12.020.

[39] G. Eddy Jai Poinern, S. Brundavanam, D. Fawcett, Biomedical Magnesium Alloys: A Review of Material Properties, Surface Modifications and Potential as a Biodegradable

Orthopaedic Implant, Am J Biomed Eng. 2 (2013) 218–240. https://doi.org/10.5923/j.ajbe.20120206.02.

[40] ASTM E8, ASTM E8/E8M standard test methods for tension testing of metallic materials, Annual Book of ASTM Standards 4. (2010) 1–27. https://doi.org/10.1520/E0008.

[41] ASTM G5-14. Standard Reference Test Method for Making Potentiodynamic Anodic Polarization Measurements, Annual Book of ASTM Standards. (2014). https://doi.org/10.1520/G0005-14.2.

[42] ASTM G102-89, 2015. Standard Practice for Calculation of Corrosion Rates and Related Information from Electrochemical Measurements, Annual Book of ASTM Standards. (2015). https://doi.org/10.1520/G0102-89R15E01.2.

[43] ASTM G31-72, 2004. Standard Practice for Laboratory Immersion Corrosion Testing of Metals, Annual Book of ASTM Standards. (2004). https://doi.org/10.1520/G0031-72R04.2.

[44] ISO 8407:2009. Corrosion of metals and alloys — Removal of corrosion products from corrosion test specimens, International Organization for Standardization. (2009).

[45] CLSI M07-A9, 2012. Methods for Dilution Antimicrobial Susceptibility Tests for Bacteria That Grow Aerobically, Clinical and Laboratory Standards Institute. (2012).

[46] ASTM D5465-93, 1998. Standard Practice for Determining Microbial Colony Counts from Waters Analyzed by Plating Methods, Annual Book of ASTM Standards. (1998).

[47] E. Mostaed, M. Sikora-Jasinska, M.S. Ardakani, A. Mostaed, I.M. Reaney, J. Goldman, J.W. Drelich, Towards revealing key factors in mechanical instability of bioabsorbable Zn-based alloys for intended vascular stenting, Acta Biomater. 105 (2020) 319–335. https://doi.org/10.1016/j.actbio.2020.01.028.

[48] S. Huang, W. Wu, Y. Su, L. Qiao, Y. Yan, Insight into the corrosion behaviour and degradation mechanism of pure zinc in simulated body fluid, Corros Sci. 178 (2021). https://doi.org/10.1016/j.corsci.2020.109071.

[49] P. jun Wang, L. wei Ma, X. qun Cheng, X. gang Li, Influence of grain refinement on the corrosion behavior of metallic materials: A review, International Journal of Minerals, Metallurgy and Materials. 28 (2021) 1112–1126. https://doi.org/10.1007/s12613-021-2308-0.

[50] C. García-Mintegui, L.C. Córdoba, J. Buxadera-Palomero, A. Marquina, E. Jiménez-Piqué, M.P. Ginebra, J.L. Cortina, M. Pegueroles, Zn-Mg and Zn-Cu alloys for stenting applications: From nanoscale mechanical characterization to in vitro degradation and biocompatibility, Bioact Mater. 6 (2021) 4430–4446. https://doi.org/10.1016/j.bioactmat.2021.04.015.

[51] D. Ahmadkhaniha, A. Järvenpää, M. Jaskari, M.H. Sohi, A. Zarei-Hanzaki, M. Fedel, F. Deflorian, L.P. Karjalainen, Microstructural modification of pure Mg for improving mechanical and biocorrosion properties, J Mech Behav Biomed Mater. 61 (2016) 360–370. https://doi.org/10.1016/j.jmbbm.2016.04.015.

[52] L. Tan, R.A. Dodd, W.C. Crone, Corrosion and wear-corrosion behavior of NiTi modified by plasma source ion implantation, Biomaterials. 24 (2003) 3931–3939. https://doi.org/10.1016/S0142-9612(03)00271-0.

[53] W. Zhou, T. Shen, N.N. Aung, Effect of heat treatment on corrosion behaviour of magnesium alloy AZ91D in simulated body fluid, Corros Sci. 52 (2010) 1035–1041. https://doi.org/10.1016/j.corsci.2009.11.030.

[54] J.H. Jonte, D.S. Martin, The solubility of silver chloride and the formation of complexes in chloride solution, J Am Chem Soc. 74 (1952) 2052–2054.

[55] H. Dong, F. Lin, A.R. Boccaccini, S. Virtanen, Corrosion behavior of biodegradable metals in two different simulated physiological solutions: Comparison of Mg, Zn and Fe, Corros Sci. 182 (2021). https://doi.org/10.1016/j.corsci.2021.109278.

[56] K.B. Törne, Investigation of corrosion properties of metals for degradable implant applications, 2017.

[57] K.B. Törne, Zn – Mg and Zn – Ag degradation mechanism under biologically relevant conditions, Surf Innov. (2017) 1–12.

[58] K. Törne, M. Larsson, A. Norlin, J. Weissenrieder, Degradation of zinc in saline solutions, plasma, and whole blood, J Biomed Mater Res B Appl Biomater. 104 (2016) 1141–1151. https://doi.org/10.1002/jbm.b.33458.

[59] A.I. Anzellotti, N.P. Farrell, Zinc metalloproteins as medicinal targets, Chem Soc Rev. 37 (2008) 1629–1651. https://doi.org/10.1039/b617121b.

[60] J. Kubásek, D. Vojtěch, E. Jablonská, I. Pospíšilová, J. Lipov, T. Ruml, Structure, mechanical characteristics and in vitro degradation, cytotoxicity, genotoxicity and mutagenicity of novel biodegradable Zn–Mg alloys, Materials Science and Engineering: C. 58 (2016) 24–35. https://doi.org/10.1016/j.msec.2015.08.015.

[61] H. Yang, B. Jia, Z. Zhang, X. Qu, G. Li, W. Lin, D. Zhu, K. Dai, Y. Zheng, Alloying design of biodegradable zinc as promising bone implants for load-bearing applications, Nat Commun. 11 (2020). https://doi.org/10.1038/s41467-019-14153-7.

[62] H. Hedelin, C.-G. Bratr, G. Eckerdal, K. Lincoln, Relationship between Urease-producing Bacteria, Urinary p H and Encrustation on Indwelling Urinary Catheters, Br J Urol. 61 (1991) 521–531.

[63] S. Khoddami, B.H. Chew, D. Lange, Problems and solutions of stent biofilm and encrustations : A review of literature, 46 (2020) 11–18. https://doi.org/10.5152/tud.2020.20408.

[64] R.G. Burr, I.M. Nuseibeh, Urinary catheter blockage depends on urine pH, calcium and rate of flow, Spinal Cord. 35 (1997) 521–525.

[65] B. Mo~m, D. Zambra:No, Uhrastructure of Transitional Epithelium of Man, 1968.

[66] M. Wątroba, K. Mech, W. Bednarczyk, J. Kawałko, M. Marciszko-Wiąckowska, M. Marzec, D.E.T. Shepherd, P. Bała, Long-term in vitro corrosion behavior of Zn-3Ag and

Zn-3Ag-0.5Mg alloys considered for biodegradable implant applications, Mater Des. 213 (2022). https://doi.org/10.1016/j.matdes.2021.110289.

[67] W.L. Du, S.S. Niu, Y.L. Xu, Z.R. Xu, C.L. Fan, Antibacterial activity of chitosan tripolyphosphate nanoparticles loaded with various metal ions, Carbohydr Polym. 75 (2009) 385–389. https://doi.org/10.1016/j.carbpol.2008.07.039.

[68] Q.L. Feng, J. Wu, G.Q. Chen, F.Z. Cui, T.N. Kim, J.O. Kim, A mechanistic study of the antibacterial effect of silver ions on Escherichia coli and Staphylococcus aureus, 2000.

[69] G. Yao, J. Lei, W. Zhang, C. Yu, Z. Sun, S. Zheng, S. Komarneni, Antimicrobial activity of X zeolite exchanged with Cu 2+ and Zn 2+ on Escherichia coli and Staphylococcus aureus, Environmental Science and Pollution Research. 26 (2019) 2782–2793. https://doi.org/10.1007/s11356-018-3750-z.

[70] B. Suryawati, Zinc homeostasis mechanism and its role in bacterial virulence capacity, in: AIP Conf Proc, American Institute of Physics Inc., 2018. https://doi.org/10.1063/1.5062819.

[71] J.W. Alexander, J.S. Solomkin, M.J. Edwards, Updated recommendations for control of surgical site infections, Ann Surg. 253 (2011) 1082–1093. https://doi.org/10.1097/SLA.0b013e31821175f8.

[72] A. Faris, L. Khalid, M. Hashim, S. Yaghi, T. Magde, W. Bouresly, Z. Hamdoon, A.T. Uthman, H. Marei, N. Al-Rawi, Characteristics of Suture Materials Used in Oral Surgery: Systematic Review, Int Dent J. 72 (2022) 278–287. https://doi.org/10.1016/j.identj.2022.02.005.

Part II.

Modification of Zn-based alloys

Chapter III.

Implementation of dual-action coatings to control degradation and enhance endothelialisation of Zn alloys

Chapter III. Implementation of dual-action coatings to control degradation and enhance endothelialisation of Zn alloys

Objective

To control degradation and enhance endothelialisation of Zn-0.5Mg and Zn-2Ag alloys by implementing a PCL coating and functionalizing the surfaces with RGD, REDV, and RGD-REDV peptide sequences.

Graphical abstract

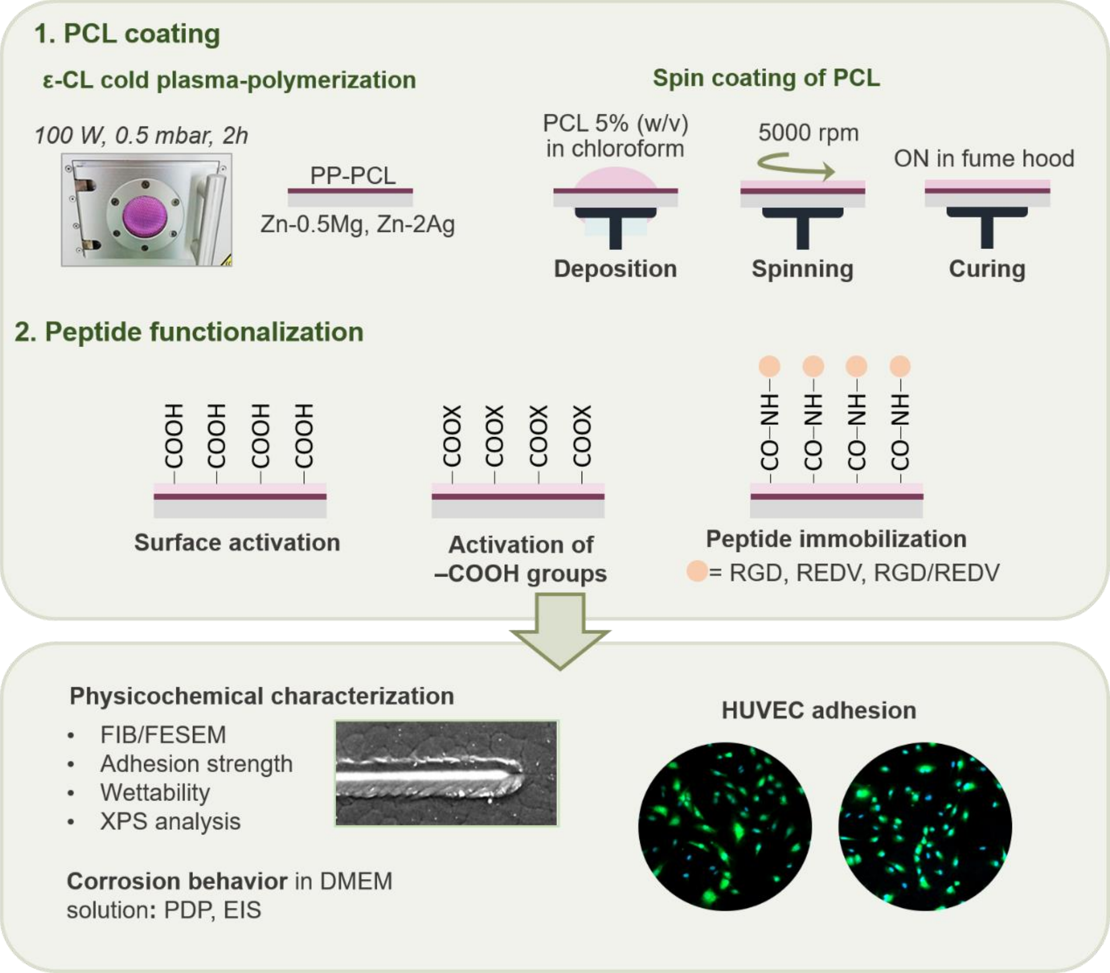

Main results

This chapter presents a well-adhered PCL coating that provides proper corrosion protection and surface stability to ZnMg and ZnAg alloys, allowing peptide immobilization on the surfaces. All the functionalized surfaces presented improved cell adhesion and spreading, where the RGD-REDV platform stands out by exhibiting the highest HUVEC number, demonstrating the synergistic effect of RGD and REDV peptides.

I. Introduction

The insufficient radial strength of Zn recommends alloying it with other elements (e.g., silver (Ag) or Mg) for mechanical reinforcement *via* precipitation hardening [4–6]. Nevertheless, the formation of secondary phases affects corrosion behaviour since the different degradation rates of the Zn matrix and secondary phases lead to the formation of galvanic pairs, breaking the homogeneous corrosion behaviour of Zn [7]. Consequently, this localized corrosion may lead to the cracking of the implant and, thus, undermine the reinforcement effect of the alloying. Moreover, the initial surface degradation leads to surface instability that inhibits endothelial cell adhesion and the subsequent desired endothelialisation [8]. Therefore, implementing protective coatings with pro-endothelialisation peptides could enhance the biological response of biodegradable Zn alloys by delaying surface degradation and thus maintaining surface morphology and stability during the endothelialisation process.

Polymeric coatings, usually based on polylactide (PLA), polyglycolide (PGA), or polycaprolactone (PCL), have been reported to act as a non-toxic corrosion barrier for biodegradable Mg [20–24]. Their interest also relies on their ability to encapsulate and deliver drugs and their capacity to attach bioactive molecules [25]. Indeed, PCL is a well-known biodegradable polymer already used in several biomedical applications, such as soft tissue engineering, drug delivery systems, or wound closure devices [26–28]. PCL has been considered a potential biodegradable coating to reduce Mg corrosion by protecting the underlying metallic surface from the body fluids [22,29]. Its adequate protection ability and the possibility to obtain a thin coating without significant modification of the stent strut thickness are of great interest for cardiovascular applications. Besides, the PCL could reduce platelet adhesion and the associated risk of LST [30,31]. Nevertheless, the lack of cell-specificity adhesion of the PCL coating requires another strategy (i.e., functionalisation) to enhance surface endothelialisation.

Functionalisation of biodegradable polymers has been extensively studied through proteins [32,33], growth factors [34], and peptides [35,36]. Among them, cell adhesion biomolecules such as laminin [37], fibronectin [38], and peptides that originated from them [39–41] are of great interest since they accelerate early adhesive events. The most commonly used peptide is the RGD (Arg-Gly-Asp) sequence, which is identified in fibronectin and other proteins of the extracellular matrix, and has been thoroughly investigated for improving cell adhesion on biomaterials [30,42,43]. Other peptides, such as the REDV (Arg-Glu-Asp-Val) motif, have been used to promote endothelial cell adhesion over platelet adhesion onto inert substrates [44]. However, the optimal peptide configuration and its surface distribution to foster endothelialisation have not been elucidated yet, and no studies have been reported for the direct functionalisation of biodegradable metallic surfaces due to their degradation.

Thus, the present study explores a novel strategy for corrosion control and endothelialisation enhancement. To this end, Zn-Mg and Zn-Ag alloys were coated by PCL and later functionalised with RGD, REDV, and dual peptidic platform combining RGD-REDV sequences. The PCL coating was produced after ε–caprolactone (ε–CL) polymerization and spin-coating. The peptides were synthesized by solid-phase synthesis and immobilized onto the surfaces by 1-ethyl-3-(3-dimethylaminopropyl)carbodiimide and N-hydroxysuccinimide (EDC/NHS) chemistry. The corrosion protection was evaluated by potentiodynaic polarization (PDP) and electrochemical impedance spectroscopy (EIS) tests. Finally, human umbilical vein endothelial cells (HUVEC) adhesion was assessed *in vitro*, revealing improved features with respect to non-functionalised Zn alloy.

II. Materials and Methods

II.1. Sample preparation

II.1.1. ZnMg and ZnAg substrates

Zn-0.5Mg (0.5 wt. % Mg) and Zn-2Ag (2 wt. % Ag) alloys were provided by Goodfellow (UK) in rods of 10 mm diameter. The rods were cut into 2.5 mm thick discs, and abraded with silicon carbide grinding papers (P800, P1200, P2500, and P400 from Neuertek S.A., Spain). Prior to surface treatments, samples were ultrasonically cleaned with absolute ethanol (Sigma Aldrich, USA). For simplification, Zn-0.5Mg and Zn-2Ag alloys were named as ZnMg and ZnAg. All the sample codes used in the paper are included in **Table 1**.

II.1.2. Polycaprolactone (PCL) coating

Biodegradable metals were plasma polymerized before the spin-coating of PCL to overcome the usual low stability of polymeric coatings on metallic surfaces. The plasma polymerization pre-treatment was carried out in two steps. First, surfaces were O_2 plasma activated with constant O_2 flux (O_2 5.0, PRAXAIR, Spain) for 10 min (0.5 mbar, 150 W).

Secondly, a PCL nanolayer was formed by ε–CL polymerization via cold-plasma polymerization using a low-pressure radiofrequency plasma (13.56 Hz) (Standard Femto Plasma System, Diener, Germany). Polymerization was achieved through Ar (Ar 5.0, PRAXAIR, Spain) bubbling into ε–CL monomer in liquid phase for 2 h (0.5 mbar, 100W) [45]. Pre-treated samples exposed to the plasma polymerization process were named as PP-ZnMg and PP-ZnAg (**Table 1**).

Subsequently, PCL (Purasorb PC12, Corbion, Spain) with a molecular weight of 70.000 – 90.000 g/mol was dissolved in chloroform at 5.0 wt. % and stirred by a high-speed mixer at 2000 rpm for 2 minutes. The polymer film was obtained by spin coating (WS-400-6NPP Spin Coater, Laurell Technologies, USA) at 5000 rpm and 4000 rpm/s for 30 s. The spin-coating of the polymer solution was applied twice, with 10 min drying in a fume hood between repetitions. Spin-coated samples were dried in a fume hood for at least 24 h before testing to ensure total chloroform evaporation. Samples subjected to the plasma polymerization pre-treatment and posterior spin coating were coded as SC-ZnMg and SC-ZnAg (**Table 1**).

Table 1. Processes applied to ZnMg and ZnAg alloys. Sample codes used in the paper are indicated. PP: plasma polymerization. SC: spin coating.

Sample	Process	Code
Zn-0.5Mg	None	ZnMg
	PP	PP-ZnMg
	PP + SC	SC-ZnMg
	PP + SC + functionalisation with RGD	SC-ZnMg-RGD
	PP + SC + functionalisation with REDV	SC-ZnMg-REDV
	PP + SC + functionalisation with RGD-REDV	SC-ZnMg-RGD-REDV
Zn-2Ag	None	ZnAg
	PP	PP-ZnAg
	PP + SC	SC-ZnAg
	PP + SC + functionalisation with RGD	SC-ZnAg-RGD
	PP + SC + functionalisation with REDV	SC-ZnAg-REDV
	PP + SC + functionalisation with RGD-REDV	SC-ZnAg-RGD-REDV

II.1.3. Solid-phase peptide synthesis

RGD and REDV peptide sequences and the RGD-REDV platform were synthesized as previously described [46,47]. In brief, Fmoc Rink-amide MBHA resin (200 mg, 0.74 mmol g^{-1}) was used as solid support for solid-phase peptide synthesis following the Fmoc/tBu strategy. Deprotection steps and washings between couplings were carried out with *N*,*N*-dimethylformamide (DMF), and dichloromethane (DCM). Solvents and soluble reagents were removed using a vacuum filtration system. All reactions and treatments were performed at room temperature (RT). Couplings were monitored using the Kaiser test and reverse-phase high-performance liquid chromatography (RP-HPLC) analysis. Before cleavage, the free N-terminus was either acetylated (Ac) or reacted with 5(6)-carboxyfluorescein (CF) to obtain fluorescent analogues for physicochemical characterization assays. Acetylated peptides were purified by semipreparative RP-HPLC running linear gradients from 0 % to 40 % ACN over 40 min. The purified peptides were characterized by analytical RP-HPLC and MALDI-TOF (Matrix Assisted Laser Desorption Ionization - Time of Flight) as follows:

RGD Ac-Arg-Gly-Asp-Ser-PEG-PEG-Lys-Lys-NH_2: RP-HPLC (0 – 40 % ACN over 15 min, t_R = 4.335 min, purity 96.2 %), MALDI-TOF (m/z calcd. for $C_{41}H_{76}N_{14}O_{16}$, 1021.13; found, 1021.58).

CF-RGD CF-Arg-Gly-Asp-Ser-PEG-PEG-Lys-Lys-NH_2: RP-HPLC (5 – 100 % ACN over 8 min, t_R = 6.382 min, purity 86.9 %), MALDI-TOF (m/z calcd for $C_{60}H_{84}N_{14}O_{21}$, 1337.39; found, 1338.65).

REDV Ac-Arg-Glu-Asp-Val-PEG-PEG-Lys-Lys-NH_2: RP-HPLC (5 – 100 % ACN over 8 min, t_R = 5.572 min, purity 90.2 %), MALDI-TOF (m/z calcd for $C_{46}H_{84}N_{14}O_{17}$, 1105.24; found, 1105.64).

CF-REDV CF-Arg-Glu-Asp-Val-PEG-PEG-Lys-Lys-NH_2: RP-HPLC (5 – 100 % ACN over 8 min, t_R = 6.557 min, purity 79.5%), MALDI-TOF (m/z calcd for $C_{65}H_{92}N_{14}O_{22}$, 1421.51; found, 1422.65).

RGD-REDV [(Ac-Arg-Gly-Asp-Ser-PEG-PEG) (Ac-Arg-Glu-Asp-Val-PEG-PEG)]-Lys-ßAla-Lys-Lys-NH_2: RP-HPLC (5 – 95 % ACN over 3 min, t_R = 1.115 min, purity 93.2 %), MALDI-TOF (m/z calcd for $C_{84}H_{150}N_{26}O_{33}$, 2052.24; found, 2052.04).

CF-RGD-REDV [(Ac-Arg-Gly-Asp-Ser-PEG-PEG) (CF-Arg-Glu-Asp-Val-PEG-PEG)]-Lys-ßAla-Lys-Lys-NH_2: RP-HPLC (5 – 100% ACN over 8 min, t_R = 6.390 min, purity 59.5 %), MALDI-TOF (m/z calcd for $C_{103}H_{158}N_{26}O_{38}$, 2368.51; found, 2369.03).

II.1.4. Surface functionalisation of the PCL spin-coated samples with peptides

The functionalisation of the spin-coated samples with the synthesized peptides was carried out in three steps, as described in **Fig. 1.** (i) Surfaces were first activated with O_2

plasma using a low-pressure radiofrequency plasma, as described in Section II.1.2. (ii) The generated carboxylic groups were then activated with 0.1 M 1-ethyl-3-(3-dimethylaminopropyl)carbodiimide (EDC) and 0.2 M *N*-hydroxysuccinimide (NHS), at pH 6.5 for 15 minutes. Samples were subsequently rinsed with Milli-Q water. (iii) RGD and REDV linear peptides and the RGD-REDV platform were dissolved in Milli-Q water at 100 µM and covalently immobilized to the samples by depositing 50 µL of the peptide solution onto the surface for two hours at RT. Finally, biofunctionalised surfaces were cleaned with Milli-Q water and dried with N_2 gas flow (N_2 5.0, PRAXAIR, Spain). Functionalised samples were coded as sample-peptide: SC-ZnMg-RGD, SC-ZnAg-RGD, SC-ZnMg-REDV, SC-ZnAg-REDV, SC-ZnMg-RGD-REDV, and SC-ZnAg-RGD-REDV (**Table 1**).

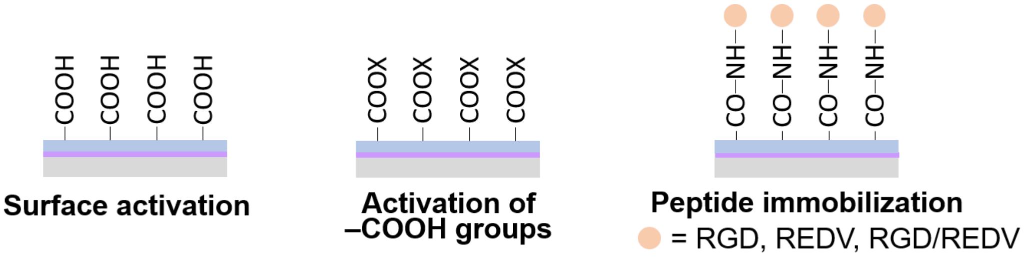

Fig. 1. Surface functionalisation of spin-coated samples with the synthesised peptides: (i) surface activation, (ii) activation of the –COOH functional groups, yielding an active ester –COOX and (iii) immobilization of the peptide sequences by formation of an amide bond between the active esters and the amino-anchoring units of the peptides.

II.2. Physicochemical characterization of PCL-coated and functionalised surfaces

The morphology and thickness of the PCL coatings onto Zn surfaces were observed by dual beam focused ion beam/field emission scanning electron microscope (FIB/FESEM) (Neon40 Crossbeam™, Zeiss, Germany). A platinum (Pt) protective layer was laid down using electron-beam-induced Pt deposition and following ion-beam-induced Pt deposition. Then, a 10 nA ion current was applied to remove the material to a certain depth and lowered to 2 nA to approach the Pt layer. The final polishing step was performed at 500 pA to obtain a flat cross-section face. All measurements were hardware corrected for the sample tilting. Afterward, the thickness coating was measured by SmartTiff software (Zeiss, Germany).

Scratch tests were carried out with an MTS Nanoindenter XP with a Berkovich diamond tip. The scratch length was 500 µm, and the applied load was linearly increased from 0 to 5 mN. After the test, the specimens were visually inspected by SEM.

The surface wettability of non-coated and spin-coated surfaces was evaluated. In addition, activated surfaces were tested to confirm the activation steps required in the PP pre-treatment (Section II.1.2), and in the peptide functionalisation (**Fig. 1,i**). To this end, the sessile drop method was performed using a Contact Angle System OCA15 plus (Dataphysics, Germany). Static Contact Angles (SCA) measurements were performed with a 3 µL ultrapure Milli-Q water drop at RT. SCA was calculated using Laplace-Young fitting with SCA20 software (Dataphysics, Germany).

Surface chemical composition analysis was performed by X-ray photoelectron spectroscopy (XPS) (SPECS Surface Nano Analysis GmbH, SPECS, Germany) using an XR50 Al anode source at 150W (10 kV) and a Phoibos 150MCD-9 detector at a working pressure below 5×10^{-8} mbar. An MCD-9 detector was used as an electron detector with a take-off angle of 90 ° relative to the surfaces. The pass energy was fixed at 20 eV with 0.1 eV steps and 1 eV steps for high resolution and survey spectra, respectively. The relative elemental composition of the Zn 2p, C 1s, O 1s, and N 1s elements were analysed by Casa XPS 2.3.19PR1.0 software (Casa Software Ltd, UK). The deconvolution of the C 1s spectra was performed for the plasma-polymerized and the spin-coated samples. All peaks were referred to C1s at 284.4 eV for calibration. Peptide coverage on the different surfaces was visualized by fluorescence microscopy (Nikon E600, Tokyo, Japan) using the CF-labelled peptides.

II.3. Corrosion evaluation

Electrochemical analysis was performed with a PARSTAT 2273 potentiostat/galvanostat (Princeton Applied Research, USA) in Dulbecco's Modified Eagle Medium (DMEM) solution at 37 ± 1 ºC and pH 7.4 ± 0.1. A three-electrode electrochemical cell with the sample as the working electrode, a saturated calomel electrode (SCE) as the reference electrode, and a Pt electrode as the counter electrode was used.

Potentiodynamic polarization (PDP) scans were performed after 30 minutes of immersion, from -1.4 to -0.6 V, against the open circuit potential (OCP) at a scan rate of 1 mV/s, following ASTM G5-14 [48]. The corrosion current density (i_{corr}) ($\mu A/cm^2$) and the corrosion potential (E_{corr}) (V) were estimated by Tafel extrapolation of the cathodic branch of the obtained polarization curves with Origin 2020 software (OriginLab, USA).

Electrochemical impedance spectroscopy (EIS) measurements were carried out at 6 and 48 h after immersion and recorded over the frequency range of 10^5 to 10^{-2} Hz and at an

AC amplitude of 10 μA.rms. The EIS data were analysed using equivalent circuit modelling (ZSimpWin v3.21 software, Princeton Applied Research).

II.4. Endothelial cell adhesion

Human umbilical vein endothelial cells (C-12203 HUVEC-c pooled, PromoCell GmbH, Germany) were cultured under standard conditions (humidified atmosphere, 5 % CO_2 (v/v), 37 ± 1 ºC) in endothelial cell growth media ready-to-use (C-22010, Promocell, Germany) in Nunc tissue culture flasks (Thermo Fisher Scientific, US) and passaged when reached 80 – 90 % confluence. Cells were isolated on culture flasks by two minutes of 1 mL-trypsinization (Trypsin/EDTA, Sigma-Aldrich, US) at standard conditions and resuspended in cell growth medium and 10 % FBS (v/v) for trypsin neutralization. Cells were used for experiments in passages 7-9. Cell number and spreading of adhered cells were analysed to determine the efficiency of the surface biofunctionalisation. To this end, HUVEC in culture were isolated, stained with Green CMFDS C7025 CellTracker^{TM} (Thermo Fisher Scientific, US) for 20 minutes, and passaged. Next, HUVECs were seeded at a density of 15.000 cells per disk. After 6 h of incubation at 37 ºC, samples were rinsed twice with the medium to remove the non-adherent cells. Adhered cells were then fixed for 30 minutes with 4% (w/v) paraformaldehyde (PFA, Sigma Aldrich, USA) and rinsed with DMEM solution (3 x 5 minutes). Samples were permeabilized with 500 μL/disk of 0.05% (w/v) triton X-100 in distilled water for 15 minutes and were washed with distilled water (3 x 5 minutes). Disks were mounted on microscope slides with Mounting Medium with DAPI ab104139 (Abcam, UK) and observed by fluorescence microscopy (Nikon E600, Tokyo, Japan). The number and spreading of attached cells were assessed using ImageJ software (National Institutes of Health, MD).

II.5. Statistical analysis

The experimental data collected in this study were reported as mean ± standard deviation (SD). Unless previously specified, all the characterization was performed with $n = 3$ samples for each specimen. The statistical analysis was performed using Minitab Statistical software (Minitab Inc., USA). A Shapiro-Wilk normality test determined if the data set followed a normal distribution. Equality of variance test (ANOVA) or a non-parametric test (Kruskal-Wallis test) determined the statistically significant differences in normally or non-normally distributed data, respectively (p-value < 0.05 for all tests).

III. Results

III.1. Physicochemical characterization of PCL coating

III.1.1. PCL coating thickness

Fig. 2 shows the FIB/FESEM images of the plasma-polymerized and the spin-coated samples after cross-section to evaluate the thickness of the PCL coating. The plasma-polymerized samples exhibited a PCL nanolayer (**Fig. 2a,d**) with a thickness lower than 25 nm (**Fig. 2b, e**). As expected, a thicker and homogeneous coating was obtained after the PCL spin-coating, with values of 781 ± 45 nm thickness for SC-ZnMg (**Fig. 2c**) and 691 ± 23 nm for SC-ZnAg (**Fig. 2f**).

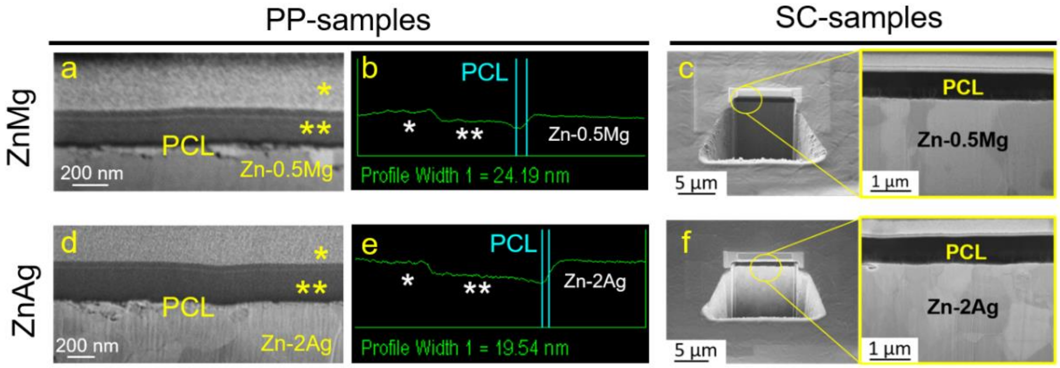

Fig. 2. Thickness evaluation of the PCL coatings by FIB/FESEM: (a, b) PP-ZnMg, (c) SC-ZnMg, (d, e) PP-ZnAg, and (f) SC-ZnAg. * = ion-beam Pt deposition. ** = electron-beam Pt deposition.

III.1.2. Adhesion strength of the PCL coating

A scratch test was performed to determine the adherence of the PCL coating to the studied Zn alloys. **Fig. 3** shows the scratches after the assay onto the spin-coated series. No PCL delamination or detachment was detected for any surface, indicating that PCL firmly adhered to the metallic surfaces.

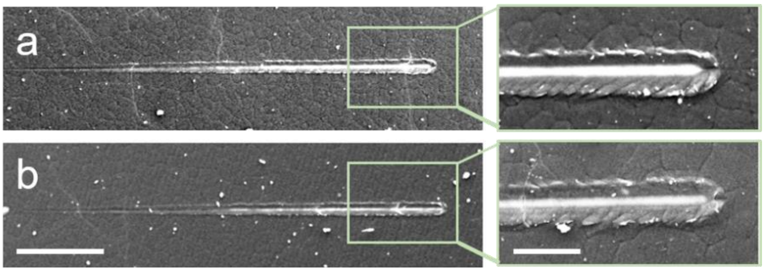

Fig. 3. Results of the scratch test: Qualitative SEM images of the scratch area produced onto (a) SC-ZnMg and (b) SC-ZnAg alloy. Right images provide a higher magnification of the analysed samples (green squares) Scale bar (left): 100 µm. Scale bar (right): 10 µm.

III.1.3. Wettability

The wettability of the different studied surfaces was studied through SCA measurements. The SCA values of the untreated alloys were 88.4 ± 3.9° for ZnMg, and 83.3 ± 1.5° for ZnAg. The activation in the plasma polymerization process was verified by SCA values <1° for the activated Zn-Mg and Zn-Ag alloys, manifesting an extensive increase in the available oxygens on the surfaces. After PCL spin coating, the SCA of SC-ZnMg and SC-ZnAg samples were 88.3 ± 1.1° and 89.5 ± 2.1°, respectively. Finally, a significant increase of wettability was detected on the spin-coated surfaces after O_2 plasma activation, with 58.0 ± 2.1° value for the activated SC-ZnMg alloy and 57.6 ± 1.7° for the activated SC-ZnAg alloy.

III.1.4. XPS analysis

The atomic ratios of the most significant elements (Zn, C, N, O) on the investigated surfaces are shown in **Table 2**. XPS analysis revealed the presence of Zn, C, and O on all surfaces. Plain ZnMg and ZnAg samples presented a substantial percentage of oxygen attributed to the natural passivation layer of the metals. Carbon was also detected on the non-coated surfaces, probably due to atmospheric contamination of the samples. PP-ZnMg and PP-ZnAg showed a decrease in the Zn 2p atomic ratio along with an increase of both C 1s and O 1s, confirming the shielding of the Zn alloys due to the presence of the PCL layer. The significant reduction of the Zn 2p signal (<0.2 %) after the spin coating, together with the increasing atomic ratio of C 1s up to ≈ 80 % process, confirmed the presence of a much thicker PCL coating in SC-ZnMg and SC-ZnAg samples. Furthermore, all peptide-functionalised series presented N 1s on their surfaces, corresponding to the amide bonds and side chains of the immobilized peptide sequences. Of note, nitrogen was not detected for the other conditions.

To further characterize the coating process of plasma-polymerized and spin-coated series, high-resolution C 1s XPS spectra were studied (**Fig. 4a-d**). The C 1s XPS peak of the plasma-polymerized samples (**Fig. 4a, b**) was deconvoluted into four peaks attributed to C-C/C-H (C1), C-OH/C-O (C2), C=O (C3), and O=C-O (C4) [49,50]. Only three peaks were detected in the case of SC-ZnMg and SC-ZnAg, corresponding to C1, C2, and C4. Moreover, the atomic concentration of assigned carbons included in **Fig. 4e** confirmed the presence of the PCL layer.

Table 2. Percentage atomic ratios (%) of the more significant elements of the different surfaces. N.D.: non-detected.

Surface	Zn 2p	C 1s	O 1s	N 1s
ZnMg	49.09 ± 4.36	8.52 ± 1.11	42.40 ± 3.25	N.D.
ZnAg	55.61 ± 5.51	9.49 ± 2.62	34.91 ± 2.89	N.D.
PP-ZnMg	13.25 ± 0.54	29.66 ± 4.36	57.10 ± 3.82	N.D.
PP-ZnAg	16.99 ± 1.55	18.90 ± 8.49	64.10 ± 6.94	N.D.
SC-ZnMg	0.04 ± 0.01	83.72 ± 0.03	16.25 ± 0.04	N.D.
SC-ZnAg	0.04 ± 0.03	83.44 ± 0.21	16.52 ± 0.18	N.D.
SC-ZnMg-RGD	0.16 ± 0.05	81.96 ± 1.22	16.98 ± 0.93	0.91 ± 0.34
SC-ZnAg-RGD	0.14 ± 0.03	82.69 ± 1.65	15.78 ± 1.39	1.40 ± 0.43
SC-ZnMg-REDV	0.12 ± 0.04	82.65 ± 1.85	15.80 ± 1.58	1.45 ± 0.31
SC-ZnAg-REDV	0.19 ± 0.02	82.07 ± 0.95	16.52 ± 0.30	1.24 ± 0.67
SC-ZnMg-RGD-REDV	0.53 ± 0.10	79.79 ± 2.45	18.50 ± 2.20	1.19 ± 0.35
SC-ZnAg-RGD-REDV	0.84 ± 0.07	77.20 ± 2.21	19.89 ± 2.26	2.07 ± 0.02

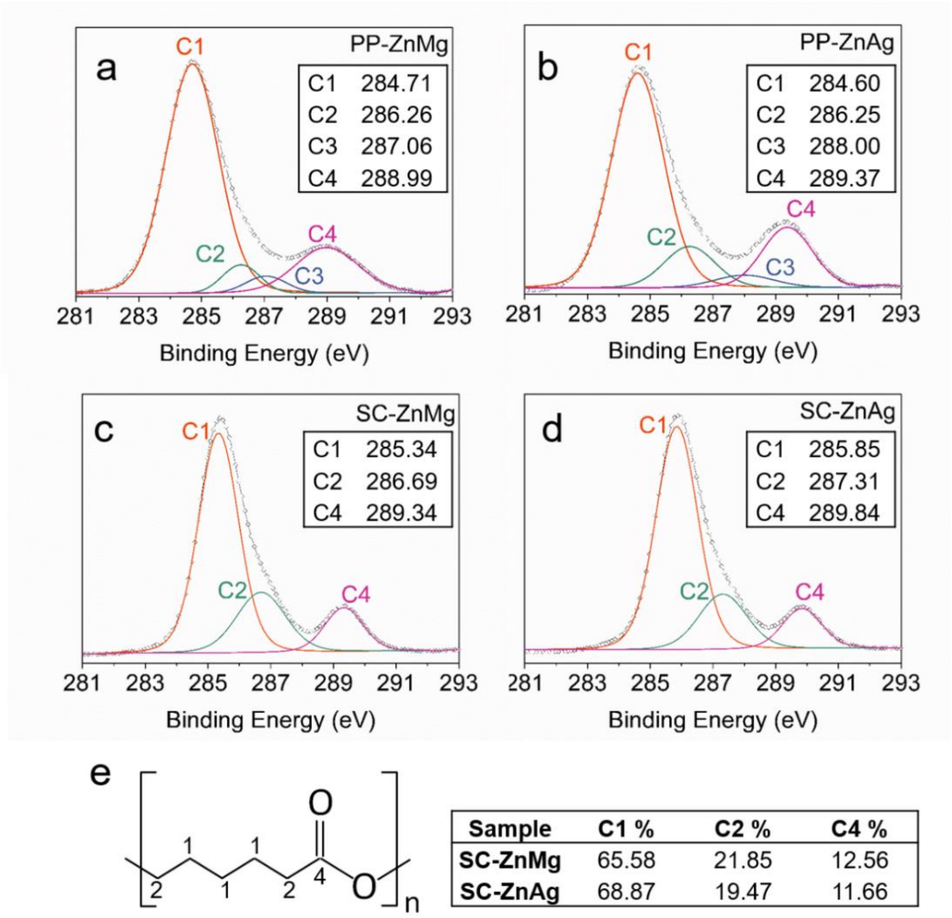

Sample	C1 %	C2 %	C4 %
SC-ZnMg	65.58	21.85	12.56
SC-ZnAg	68.87	19.47	11.66

Fig. 4. High-resolution C 1s XPS spectra of the surfaces after plasma polymerization: (a) PP-ZnMg, and (b) PP-ZnAg; and surfaces after spin-coating: (c) SC-ZnMg, and (d) SC-ZnAg. (e) PCL chemical formula and quantitative analysis of C 1s XPS spectra of spin-coated samples.

III.1.5. Surface characterization of RGD, REDV, and RGD-REDV biofunctionalised surfaces

The fluorescent images of the surfaces functionalised with the CF-labelled peptides are shown in **Fig. 5.** The results confirmed the XPS data and demonstrated the successful immobilization of the peptides over the surfaces. As expected, no fluorescent signal was detected for the SC-ZnMg and the SC-ZnAg samples.

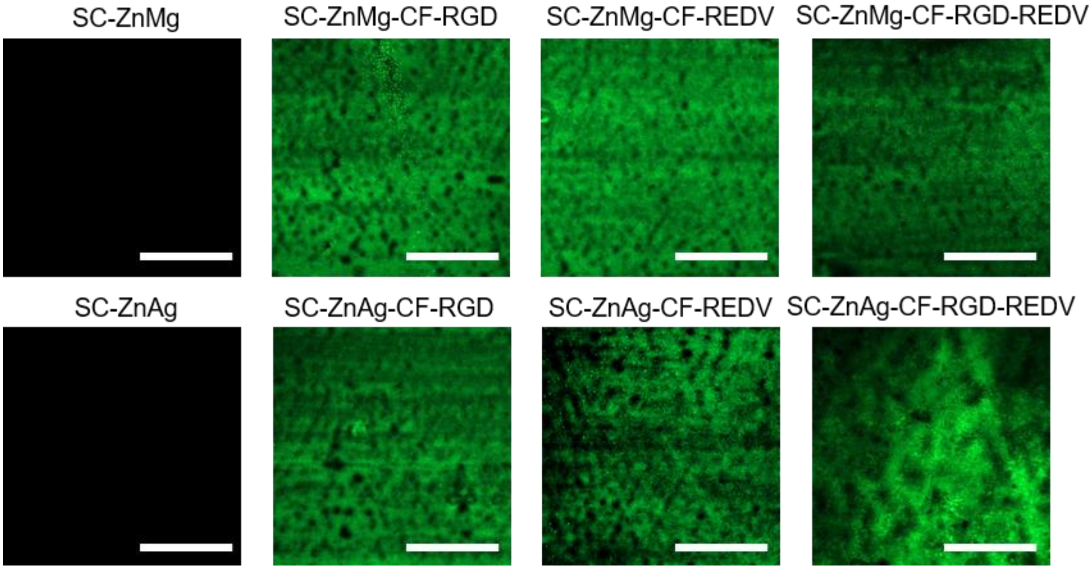

Fig. 5. Fluorescent images of functionalised samples with synthesised CF-labelled peptides and the non-functionalised controls. Scale bar: 500 μm.

III.2. Corrosion evaluation

III.2.1. Potentiodynamic polarization test

Fig. 6 shows the potentiodynamic curves obtained from the PDP test, and the calculated corrosion parameters are listed in **Table 3.** As presented in **Fig. 6,** no relevant corrosion protection was observed by plasma-polymerized samples compared to the untreated surfaces for both of the studied alloys. On the contrary, for both SC-ZnMg and SC-ZnAg samples, the implementation of the PCL coating implied a noticeable displacement of the potentiodynamic curves to minor current density values. The current density decreased from 18.75 ± 6.10 μA/cm^2 for ZnMg down to 0.21 ± 0.09 μA/cm^2 for SC-ZnMg; and from 18.20 ± 0.08 μA/cm^2 for ZnAg down to 0.24 ± 0.05 μA/cm^2 for SC-ZnAg. Moreover, the PCL coating shifted the E values in the positive direction, indicating that the coating delayed the corrosion of the alloys.

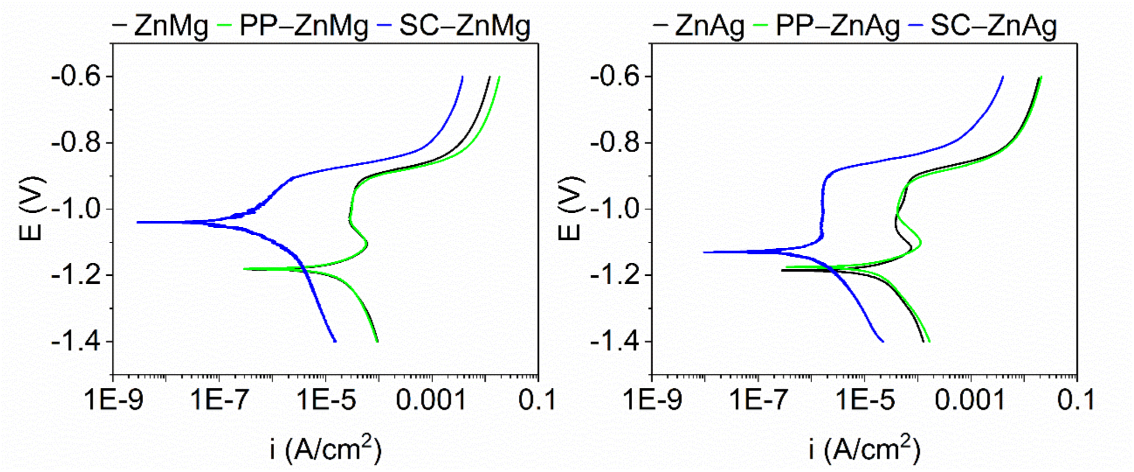

Fig. 6. Potentiodynamic curves obtained from the PDP test of ZnMg, PP-ZnMg, and SC-ZnMg series (left) and ZnAg, PP-ZnAg, and SC-ZnAg series (right). Similar curves were obtained for bare alloys and PP surface series, indicating no difference in corrosion behaviour for these conditions.

Table 3. Corrosion parameters (E (V), i (µA/cm^2)) calculated from PDP test of bare and coated ZnMg and ZnAg alloys.

Zn-Mg system			
Sample	**ZnMg**	**PP-ZnMg**	**SC-ZnMg**
E (V) **i (µA/cm^2)**	-1.171 ± 0.016 18.75 ± 6.10	-1.170 ± 0.018 13.18 ± 5.44	-1.128 ± 0.011 0.21 ± 0.09
Zn-Ag system			
Sample	**ZnAg**	**PP-ZnAg**	**SC-ZnAg**
E (V) **i (µA/cm^2)**	-1.202 ± 0.030 18.20 ± 0.08	-1.193 ± 0.002 12.43 ± 1.97	-1.125 ± 0.011 0.24 ± 0.05

III.2.2. Electrochemical Impedance Spectroscopy

Fig. 7 shows the most representative Nyquist and Bode plots and the equivalent circuits (EC) used for the fitting. Constant-phase elements (CPE) are typically introduced in experimental EIS measurements substituting conventional capacitors to provide an adequate fitting of the experimental systems [51,52]. The plots obtained for ZnMg and ZnAg through the immersion time were fitted to the EC models depicted in **Fig. 7e.i-ii.** The EC presented in **Fig. 7e.i** models a porous corrosion layer used to describe the irregular corrosion layer formed in bare metals when immersed into a solution [53]. The EC components are the following: the resistance of the solution (R_S); the capacitance of the corrosion film (CPE_{CF}); the solution resistance inside the pores (R_P); the capacitance of the metal-solution interface at the pores (CPE_P); and the charge-transfer resistance

(R_{CT}). The EC shown in **Fig. 7e,ii** includes the so-called Warburg impedance (W), a particular CPE usually used to describe mechanisms regulated by diffusion [54].

After 6 h of immersion in DMEM solution, the Nyquist plots of ZnMg (**Fig. 7a**) and ZnAg (**Fig. 7c**) exhibited one capacitive loop and a linear region, revealing the presence of a layer and diffusion mechanisms (data fitted in **Fig. 7e,ii**). Here, the layer responds to the known passivation layer formed onto metallic surfaces when entering into contact with the surrounding media [7,54], and the W element represents the diffusion of metallic ions through the solution due to the initial corrosion of the sample. Corrosion behaviour changed after 48 h of immersion, with the EIS plots better fitted to **Fig. 7e,i**, where any diffusion mechanism took place. The absolute impedance (|Z|) values of ZnAg were 7.9 kΩ·cm^2 at 6 h and 16.6 kΩ·cm^2 at 48 h for ZnAg, higher than |Z| for ZnMg, with 5.5 kΩ·cm^2 and 12.4 kΩ·cm^2 at 6 h and 48 h, respectively.

Fig. 7a, c includes the Nyquist plots of SC-ZnMg and SC-ZnAg, respectively. For every time point, both samples exhibited two capacitive loops indicating the presence of a double layer. After 48 h of immersion, the Nyquist plots fitted to the EC depicted in **Fig. 7e,iii.** This EC describes the presence of a double layer which includes the outer layer resistance (R_{OL}) and capacitance (CPE_{OL}); and the inner layer resistance (R_{IL}) and capacitance (CPE_{IL}). In our case, the outer layer corresponds to the PCL coating, and the inner layer refers to the underneath metallic surface. SC-ZnMg presented higher |Z| than SC-ZnAg (56.4 kΩ·cm^2 and 23.7 kΩ·cm^2, respectively). Some diffusion mechanisms were observed for spin-coated samples after 6 h of immersion, possibly due to the adsorption of species in solution onto the polymeric surface. The |Z| of both SC-ZnMg and SC-ZnAg at 6 h was around 30 kΩ·cm^2.

The Bode plots depicted in **Fig. 7b, d** clearly show the increasing |Z| of the spin-coated samples compared with the uncoated alloys: from around 15 kΩ·cm^2 for both alloys to almost 60 kΩ·cm^2 for ZnMg and 30 kΩ·cm^2 for ZnAg, confirming that the PCL coating provides corrosion protection to the samples.

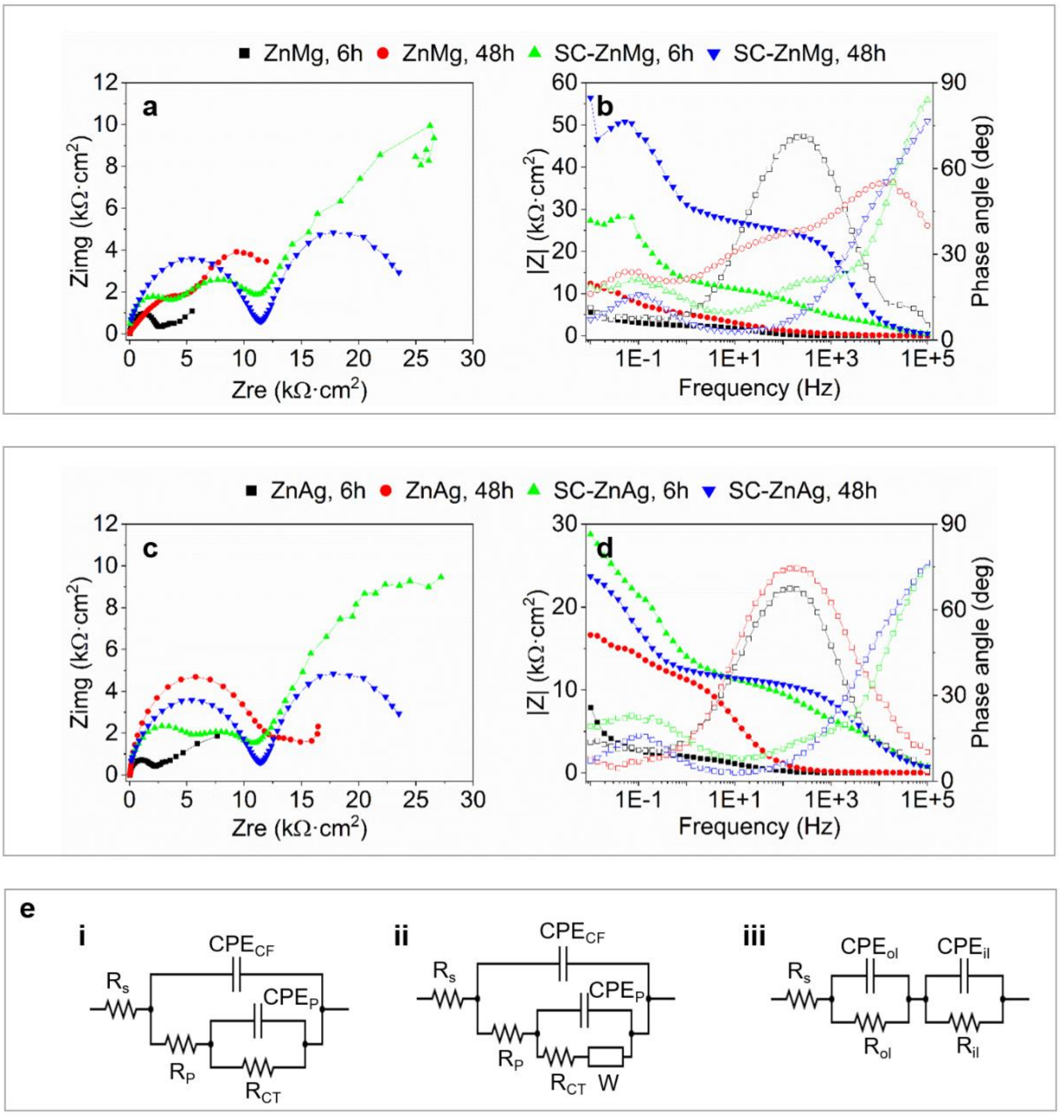

Fig. 7. EIS evaluation of the bare and the spin-coated alloys after 6 and 48 h immersion in DMEM solution. (a) Nyquist and (b) Bode plots for the ZnMg and SC-ZnMg samples; and (c) Nyquist and (d) Bode plots for the ZnAg and SC-ZnAg samples. (e) Equivalent circuits used for the fitting: (i) Porous corrosion layer. (ii) Porous corrosion layer with diffusion mechanisms. (iii) Double layer. In Bode plots (b, d), filled symbols are the absolute impedance, and empty symbols indicate the phase angle.

III.3. In vitro biocompatibility

The microscopy fluorescent images of the adhered HUVEC onto the studied surfaces after 6 h, together with the quantification of cell number and area are presented in **Fig. 8** and **Fig. 9**, respectively.

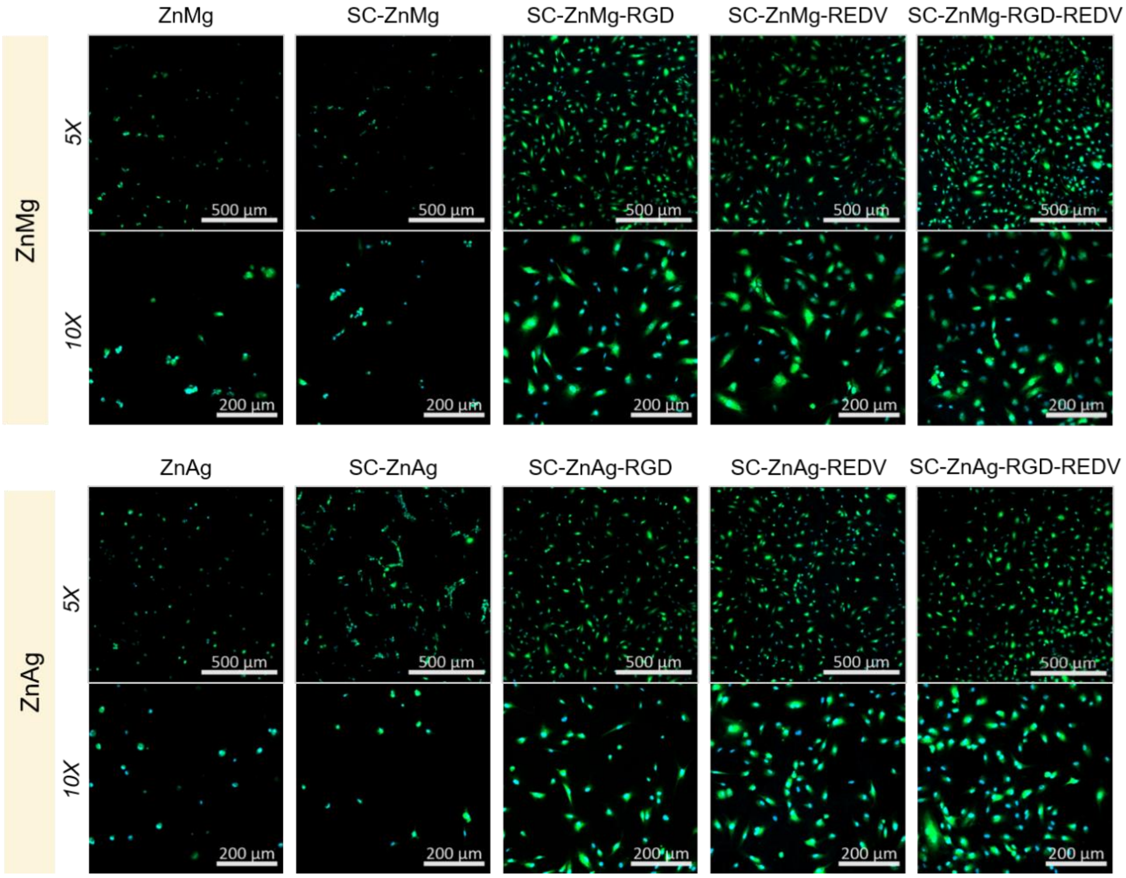

Fig. 8. Fluorescence images of adhered HUVEC on ZnMg and ZnAg modified surfaces after 6 h. Cells were previously stained with CellTracker Green before cell seeding. Cell nuclei were stained with DAPI (blue) before observation. Yellow arrows indicate the initial formation of tubular-like structures.

ZnMg, ZnAg, and spin-coated surfaces exhibited rounded-shape cells with no statistical differences regarding cell number (**Fig. 9a**) or spreading (**Fig. 9b**) between them. In contrast, the biofunctionalised surfaces significantly enhanced HUVEC adhesion and spreading.

Of note, functionalised surfaces improved HUVEC adhesion with a fold change >5 compared with SC-ZnMg and SC-ZnAg surfaces (**Fig. 9a)**. In particular, SC-ZnMg-RGD-REDV and SC-ZnAg-RGD-REDV presented the highest number of adhered cells, indicating a higher effect for the RGD-REDV system compared to the presentation of the single peptides. On the other hand, cell area showed no significant differences between the samples functionalised with RGD, REDV, or RGD-REDV peptides, with, nonetheless, an average of 4-fold change increase compared with the spin-coated series (**Fig. 9b**).

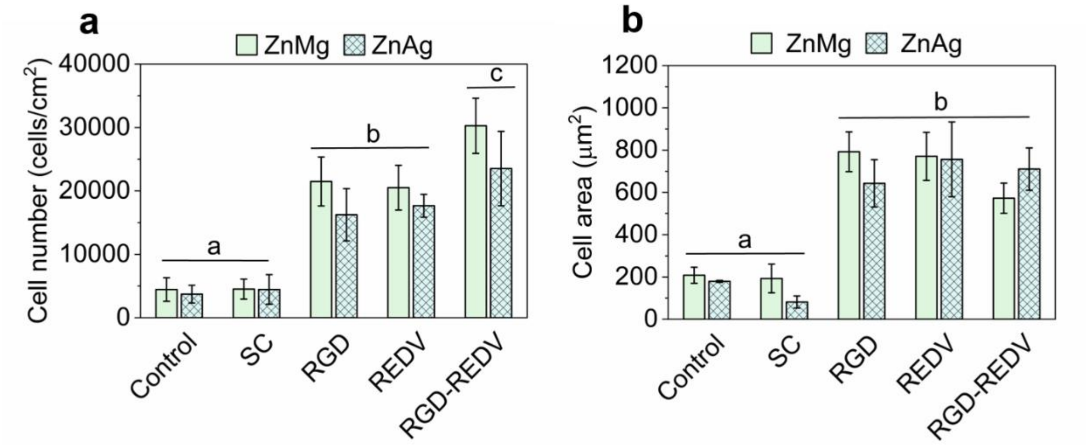

Fig. 9. Quantitative parameters of HUVEC adhesion on ZnMg and ZnAg modified surfaces after 6 h: (a) cell number and (b) cell area. Bars designated with different letters (a, b, c) denote statistically significant differences ($p<0.05$) between groups.

IV. Discussion

Among the existing biodegradable metals, Zn-based alloys present an adequate degradation rate, between 0.02 – 0.05 mm/year under physiological conditions, to be used for cardiovascular stents [4]. However, several studies underline the local toxicity of Zn as a consequence of the initial surface degradation of the material [8,55]. Besides, its surface degradation hinders cell adhesion, delaying the biointegration of the stent [7]. Therefore, different surface treatments have been applied to manage the initial degradation of Zn alloys [15,56,57]. PCL coatings have been previously implemented as a corrosion barrier to biodegradable Mg alloy surfaces [20] while providing a tuneable surface for drug loading or functionalisation with other molecules [25]. Nevertheless, the different nature between polymers and Mg generally leads to weak interfacial adhesion that might result in coating delamination [58,59]. To overcome this limitation, direct polymerization onto the metallic substrate has been reported to improve the interfacial adhesion of biodegradable polymer coatings on metal surfaces [60]. In this regard, wettability measurements on the activated alloys verified the extensive surface-oxygen bond formation in the PP pre-treatment, providing the required bonding sites to the PCL nanolayer.

In this work, an 800 nm homogeneous PCL coating was obtained for both SC-ZnMg and SC-ZnAg samples after a three-step process: (1) O_2 plasma surface activation; (2) ε-CL plasma polymerization; and (3) PCL spin-coating. PP pre-treatment provides a PCL nanocoating adhered to the metallic surfaces [45]. After polymerization, the polymeric surfaces are adequate for the spin coating of a thicker PCL layer. The detected C 1s in bare samples may be related to some contamination of the metallic surfaces. High-resolution C 1s XPS spectra of the spin-coated samples in **Fig. 4c,d** showed the C1, C2, and C4 peaks corresponding to PCL [49]. Moreover, **Fig. 4e** showed that their relative concentrations followed the descending order C1, C2, and C4, in line with the PCL chemical formula, verifying the presence of the PCL layer on both alloys. The C3 peak found on PP-ZnMg and PP-ZnAg corresponds to the recombination or oxidation of the resulting fragments of ε-CL from the ring opening during the plasma-polymerization process (**Fig. 4a,b)** [50]. Since the analysis depth for the XPS instrument is around 10 nm, the Zn 2p detection in the PP series suggested that the thickness of the plasma-polymerized PCL was below 10 nm. Thicker coatings are reported to enhance corrosion protection but may be detrimental to the adhesion strength, leading to possible delamination of the coating and thus compromising the device's reliability [22,61]. In this respect, the SC-ZnMg and SC-ZnAg samples showed no delamination or detachment of the PCL coating after the scratching test (**Fig. 3**), indicating an adequate interfacial bonding strength.

As demonstrated by the PDP and EIS tests, the coating prevents the Zn alloys from corrosion. The PDP tests pointed out a remarkable current density decrease for the spin-coated samples compared with the uncoated Zn alloys, along with more positive values of corrosion potential (**Table 3**), thus supporting the enhancement in the corrosion protection of SC-ZnMg and SC-ZnAg alloys. Moreover, a dynamic corrosion layer was observed from EIS measurements for plain ZnMg and ZnAg, evidencing the degradation of the alloys by the already-known mechanisms of a forming and breaking corrosion layer at metallic surfaces [7]. Nyquist spectra proved no porosity for the PCL coating, in line with the morphology observed by FIB/FESEM images (**Fig. 2**). Moreover, Bode plots showed that the spin-coated samples presented higher values of |Z| over uncoated alloys, confirming that the PCL coating provides higher corrosion resistance to the samples, in agreement with the PDP results.

PCL has been reported to inhibit cell adhesion [31], being a potential candidate for cardiovascular applications by reducing platelet attachment and hence the risk of thrombotic events. However, the unspecific inhibition of cell adhesion also reduces endothelialisation. Ideally, the damaged endothelium after stent implantation must be recovered for the proper biointegration of the cardiovascular stent [62,63]. Thus, stent surface endothelialisation should be accelerated. In this regard, the functionalisation with RGD peptide has been demonstrated to promote cell adhesion onto different inert substrates [64,65]. On the other hand, REDV has been reported to selectively promote HUVEC adhesion over smooth muscle cells (SMCs) and platelets [66]. Peptides have been successfully immobilized onto polymers [67,68], ceramics [69,70], hydrogels [71], or inert metallic surfaces such as Ti [72] or CoCr [43,73]. Nevertheless, degrading surfaces of bioresorbable metals require first surface stabilization before functionalisation, as previously reported [74–76].

In the present study, linear peptide sequences RGD and REDV, along with the peptidic platform RGD-REDV and the CF-labelled CF-RGD, CF-REDV, and CF-RGD-REDV, analogues have been synthetized and successfully immobilized on SC-ZnMg and SC-ZnAg surfaces. To this end, the peptides were designed to incorporate two lysine (Lys) residues at the C-terminus, which act as anchoring units to covalently bind to the activated carboxylic groups of PCL via the free primary amines of the side chains. Moreover, the peptides incorporated short polyethylene glycol (PEG) units as spacers, to provide an adequate accessibility of the active sequences, a prerequisite for achieving optimal HUVEC adhesion [44]. Before functionalisation, an activation step with O_2-plasma was carried out on the spin-coated surfaces to generate free carboxylic acid by ester hydrolysis of the PCL (**Fig. 1**). The differences in wettability confirmed the activation of the surfaces. The initial SCA of the spin-coated samples was around 90 º, in line with the values of spin-coated PCL films among these thickness ranges [24]. The increased surface hydrophilicity after activation (SCA ≈ 60 º) was related to the creation of available COOH groups, which increase wettability. It should be noted that the activated COOH group's lifetime is brief, and thus wettability values are not intrinsic to the surface and change with time. Afterward, the peptide immobilization was corroborated by the N 1s signal observed in the XPS analysis (**Table 2**) and the homogenous distribution of the CF-analogues visualized by fluorescent microscopy (**Fig. 5**).

In vitro HUVEC adhesion studies in **Fig. 8** show poor HUVEC adhesion onto the bare ZnMg and ZnAg samples, which could be attributed to the initial surface degradation [8]. Bioresorbable metallic surfaces form a passivation layer when entering into contact with an aqueous solution owing to surface degradation and the formation of new compounds with the aqueous species from the surroundings [53,77]. This exchange of species and the chemical and physical variations on the surface do not allow the cells to attach effectively

[8]. Moreover, the lack of bioactive signals on the surfaces are expect to preclude stable cell adhesion. Likewise, the presence of a few rounded-shaped cells on SC-ZnMg and SC-ZnAg indicates that the surfaces fail to support substantial HUVEC adhesion, as expected due to the presence of the PCL coating [30,31]. On the contrary, HUVECs were attached on the functionalised surfaces as observed by fluorescent microscopy, covering the entire surface (**Fig. 5**). Moreover, a noteworthy increase in HUVEC adhesion and spreading was observed after the functionalisation with RGD, REDV, and RGD-REDV cell-adhesive peptides (**Fig. 9**). Interestingly, the surfaces functionalised with the RGD-REDV platform showed a substantial increase in the number of adherent cells compared to the presentation of the single peptides (RGD or REDV) (Figure 9a). This observation may be attributed to a synergistic effect between the RGD peptide, which is non-specific and recognizes several integrin subtypes [78], and the REDV sequence, which has been reported to specifically bind to $\alpha_4\beta_1$, an integrin expressed by ECs [66], thus promoting an overall increased HUVEC adhesion. Overall, the in vitro cellular studies demonstrate that the functionalisation of PCL-coated Zn-based alloys functionalisation with cell-adhesive peptides (especially when combining RGD with REDV) represents an effective strategy to enhance HUVECs adhesion.

V. Conclusions

In this work, we explored the possibility of increasing ECs' adhesion on ZnMg and ZnAg alloys by combining PCL coating and biofunctionalisation techniques. A homogeneous PCL coating was effectively implemented onto the biodegradable ZnMg and ZnAg alloys *via* a two-step process, including plasma polymerization and spin coating, with a suitable interfacial adhesion and no apparent delamination or detachment. The PDP and the EIS tests confirmed improved corrosion resistance for both SC-ZnMg, and SC-ZnAg samples, attributed to the presence of the PCL coating. The linear peptide sequences RGD, REDV, and the peptidic platform RGD-REDV were successfully synthetized *via* solid-phase peptide synthesis and covalently immobilized onto the SC-ZnMg, and SC-ZnAg samples, as the PCL coating preserves the degradation of the samples and allows their conjugation with bioactive molecules under aqueous environments. The HUVEC adhesion was enhanced after the peptide biofunctionalisation, reaching a statistically higher number of adhered cells and better spreading. Among the peptide sequences, the RGD-REDV platform presented the highest HUVEC adhesion in terms of cell numbers, pointing to a synergistic effect by combining both RGD and REDV sequences. Therefore, the proposed new dual-strategy holds great potential to overcome the clinical limitations of current stents by enhancing surface endothelialisation and corrosion protection of different Zn-based alloys.

VI. References

[1] J.G. Wall, H. Podbielska, M. Wawrzyńska, Functionalised Cardiovascular Stents, 2017. https://doi.org/10.1016/c2014-0-04186-x.

[2] Y.F. Zheng, X.N. Gu, F. Witte, Biodegradable metals, Materials Science and Engineering R. 77 (2014) 1–34. https://doi.org/10.1007/978-1-4614-3942-4_5.

[3] P. Ramadugu, K. Latha Alikatte, A Review on Biodegradable and Bioabsorbable Stents for Coronary Artery Disease, J Bioequivalence Bioavailab. 08 (2016) 64–67. https://doi.org/10.4172/jbb.1000269.

[4] G.K. Levy, J. Goldman, E. Aghion, The prospects of zinc as a structural material for biodegradable implants—a review paper, Metals (Basel). 7 (2017) 1–18. https://doi.org/10.3390/met7100402.

[5] E. Mostaed, M. Sikora-Jasinska, J.W. Drelich, M. Vedani, Zinc-based alloys for degradable vascular stent applications, Acta Biomater. 71 (2018) 1–23. https://doi.org/10.1016/j.actbio.2018.03.005.

[6] G. Li, H. Yang, Y. Zheng, X.H. Chen, J.A. Yang, D. Zhu, L. Ruan, K. Takashima, Challenges in the use of zinc and its alloys as biodegradable metals: Perspective from biomechanical compatibility, Acta Biomater. 97 (2019) 23–45. https://doi.org/10.1016/j.actbio.2019.07.038.

[7] C. García-Mintegui, L.C. Córdoba, J. Buxadera-Palomero, A. Marquina, E. Jiménez-Piqué, M.P. Ginebra, J.L. Cortina, M. Pegueroles, Zn-Mg and Zn-Cu alloys for stenting applications: From nanoscale mechanical characterization to in vitro degradation and biocompatibility, Bioact Mater. 6 (2021) 4430–4446. https://doi.org/10.1016/j.bioactmat.2021.04.015.

[8] G. Katarivas Levy, A. Kafri, Y. Ventura, A. Leon, R. Vago, J. Goldman, E. Aghion, Surface stabilization treatment enhances initial cell viability and adhesion for biodegradable zinc alloys, Mater Lett. 248 (2019) 130–133. https://doi.org/10.1016/j.matlet.2019.04.006.

[9] A. Zaffora, F. di Franco, D. Virtù, F. Carfì Pavia, G. Ghersi, S. Virtanen, M. Santamaria, Tuning of the Mg Alloy AZ31 Anodizing Process for Biodegradable Implants, ACS Appl Mater Interfaces. 13 (2021) 12866–12876. https://doi.org/10.1021/acsami.0c22933.

[10] H. Dong, J. Zhou, S. Virtanen, Fabrication of ZnO nanotube layer on Zn and evaluation of corrosion behavior and bioactivity in view of biodegradable applications, Appl Surf Sci. 494 (2019) 259–265. https://doi.org/10.1016/j.apsusc.2019.07.165.

[11] A.I. Alateyah, T.A. Aljohani, M.O. Alawad, S. Elkatatny, W.H. El-Garaihy, Improving the corrosion behavior of biodegradable am60 alloy through plasma

electrolytic oxidation, Metals (Basel). 11 (2021). https://doi.org/10.3390/met11060953.

[12] A. Fattah-alhosseini, K. Babaei, M. Molaei, Plasma electrolytic oxidation (PEO) treatment of zinc and its alloys: A review, Surfaces and Interfaces. 18 (2020). https://doi.org/10.1016/j.surfin.2020.100441.

[13] R.G. Hu, S. Zhang, J.F. Bu, C.J. Lin, G.L. Song, Recent progress in corrosion protection of magnesium alloys by organic coatings, Prog Org Coat. 73 (2012) 129–141. https://doi.org/10.1016/j.porgcoat.2011.10.011.

[14] A. Carangelo, A. Acquesta, T. Monetta, In-vitro corrosion of AZ31 magnesium alloys by using a polydopamine coating, Bioact Mater. 4 (2019) 71–78. https://doi.org/10.1016/j.bioactmat.2018.12.005.

[15] A.J. Drelich, P.K. Bowen, L. LaLonde, J. Goldman, J.W. Drelich, Importance of oxide film in endovascular biodegradable zinc stents, Surf Innov. 4 (2016) 133–140. https://doi.org/10.1680/jsuin.16.00014.

[16] S.R. Yeomans, Galvanized Steel in Concrete: An Overview, 2004.

[17] N. Wint, J. Leung, J.H. Sullivan, D.J. Penney, Y. Gao, The galvanic corrosion of welded ultra-high strength steels used for automotive applications, Corros Sci. 136 (2018) 366–373. https://doi.org/10.1016/j.corsci.2018.03.025.

[18] M. Pantoja, J. Abenojar, M.A. Martínez, F. Velasco, Silane pretreatment of electrogalvanized steels: Effect on adhesive properties, Int J Adhes Adhes. 65 (2016) 54–62. https://doi.org/10.1016/j.ijadhadh.2015.11.006.

[19] Z. Gao, D. Zhang, X. Li, S. Jiang, Q. Zhang, Current status, opportunities and challenges in chemical conversion coatings for zinc, Colloids Surf A Physicochem Eng Asp. 546 (2018) 221–236. https://doi.org/10.1016/j.colsurfa.2018.03.018.

[20] L.Y. Li, L.Y. Cui, R.C. Zeng, S.Q. Li, X.B. Chen, Y. Zheng, M.B. Kannan, Advances in functionalized polymer coatings on biodegradable magnesium alloys – A review, Acta Biomater. 79 (2018) 23–36. https://doi.org/10.1016/j.actbio.2018.08.030.

[21] L. Xu, A. Yamamoto, Characteristics and cytocompatibility of biodegradable polymer film on magnesium by spin coating, Colloids Surf B Biointerfaces. 93 (2012) 67–74. https://doi.org/10.1016/j.colsurfb.2011.12.009.

[22] J. Degner, F. Singer, L. Cordero, A.R. Boccaccini, S. Virtanen, Electrochemical investigations of magnesium in DMEM with biodegradable polycaprolactone coating as corrosion barrier, Appl Surf Sci. 282 (2013) 264–270. https://doi.org/10.1016/j.apsusc.2013.05.115.

[23] Y.K. Kim, K.B. Lee, S.Y. Kim, Y.S. Jang, J.H. Kim, M.H. Lee, Improvement of osteogenesis by a uniform PCL coating on a magnesium screw for biodegradable applications, Sci Rep. 8 (2018) 1–11. https://doi.org/10.1038/s41598-018-31359-9.

[24] W. Jiang, Q. Tian, T. Vuong, M. Shashaty, C. Gopez, T. Sanders, H. Liu, Comparison Study on Four Biodegradable Polymer Coatings for Controlling Magnesium Degradation and Human Endothelial Cell Adhesion and Spreading,

ACS Biomater Sci Eng. 3 (2017) 936–950. https://doi.org/10.1021/acsbiomaterials.7b00215.

[25] A. Saberi, H.R. Bakhsheshi-Rad, S. Abazari, A.F. Ismail, S. Sharif, S. Ramakrishna, M. Daroonparvar, F. Berto, A comprehensive review on surface modifications of biodegradable magnesium-based implant alloy: Polymer coatings opportunities and challenges, Coatings. 11 (2021). https://doi.org/10.3390/coatings11070747.

[26] E. Malikmammadov, T.E. Tanir, A. Kiziltay, V. Hasirci, N. Hasirci, PCL and PCL-based materials in biomedical applications, J Biomater Sci Polym Ed. 29 (2018) 863–893. https://doi.org/10.1080/09205063.2017.1394711.

[27] B. Dhandayuthapani, Y. Yoshida, T. Maekawa, D.S. Kumar, Polymeric scaffolds in tissue engineering application: A review, Int J Polym Sci. 2011 (2011). https://doi.org/10.1155/2011/290602.

[28] R. Song, M. Murphy, C. Li, K. Ting, C. Soo, Z. Zheng, Current development of biodegradable polymeric materials for biomedical applications, Drug Des Devel Ther. 12 (2018) 3117–3145. https://doi.org/10.2147/DDDT.S165440.

[29] B.M. Wilke, L. Zhang, Electrochemical Investigations of Polycaprolactone-Coated AZ31 Mg Alloy in Earle's Balance Salt Solution and Conventional Simulated Body Fluid, Jom. 68 (2016) 1701–1710. https://doi.org/10.1007/s11837-016-1869-2.

[30] T.W. Chung, M.G. Yang, D.Z. Liu, W.P. Chen, C.I. Pan, S.S. Wang, Enhancing growth human endothelial cells on Arg-Gly-Asp (RGD) embedded poly (ε-caprolactone) (PCL) surface with nanometer scale of surface disturbance, J Biomed Mater Res A. 72 (2005) 213–219. https://doi.org/10.1002/jbm.a.30225.

[31] H. Cui, P.J. Sinko, The role of crystallinity on differential attachment/proliferation of osteoblasts and fibroblasts on poly (caprolactone-co-glycolide) polymeric surfaces, Front Mater Sci. 6 (2012) 47–59. https://doi.org/10.1007/s11706-012-0154-8.

[32] X. Liu, J.M. Holzwarth, P.X. Ma, Functionalized Synthetic Biodegradable Polymer Scaffolds for Tissue Engineering, Macromol Biosci. 12 (2012) 911–919. https://doi.org/10.1002/mabi.201100466.

[33] Q. Shi, X. Chen, T. Lu, X. Jing, The immobilization of proteins on biodegradable polymer fibers via click chemistry, Biomaterials. 29 (2008) 1118–1126. https://doi.org/10.1016/j.biomaterials.2007.11.008.

[34] G. Sun, Y.I. Shen, S. Kusuma, K. Fox-Talbot, C.J. Steenbergen, S. Gerecht, Functional neovascularization of biodegradable dextran hydrogels with multiple angiogenic growth factors, Biomaterials. 32 (2011) 95–106. https://doi.org/10.1016/j.biomaterials.2010.08.091.

[35] F. Raza, H. Zafar, Y. Zhu, Y. Ren, A. Ullah, A.U. Khan, X. He, H. Han, M. Aquib, K.O. Boakye-Yiadom, L. Ge, A review on recent advances in stabilizing peptides/proteins upon fabrication in hydrogels from biodegradable polymers, Pharmaceutics. 10 (2018). https://doi.org/10.3390/pharmaceutics10010016.

[36] L. Oliver-Cervelló, H. Martin-Gómez, C. Mas-Moruno, New trends in the development of multifunctional peptides to functionalize biomaterials, Journal of Peptide Science. 28 (2022). https://doi.org/10.1002/psc.3335.

[37] E.M. Yazlovitskaya, O.M. Viquez, T. Tu, A. de Arcangelis, E. Georges-Labouesse, A. Sonnenberg, A. Pozzi, R. Zent, The laminin binding α3 and α6 integrins cooperate to promote epithelial cell adhesion and growth, Matrix Biology. 77 (2019) 101–116. https://doi.org/10.1016/j.matbio.2018.08.010.

[38] K. Ishihara, K. Mitera, Y. Inoue, K. Fukazawa, Effects of molecular interactions at various polymer brush surfaces on fibronectin adsorption induced cell adhesion, Colloids Surf B Biointerfaces. 194 (2020). https://doi.org/10.1016/j.colsurfb.2020.111205.

[39] G. Bullock, J. Atkinson, P. Gentile, P. Hatton, C. Miller, Osteogenic peptides and attachment methods determine tissue regeneration in modified bone graft substitutes, J Funct Biomater. 12 (2021). https://doi.org/10.3390/jfb12020022.

[40] R.M. Epand, H.J. Vogel, Diversity of antimicrobial peptides and their mechanisms of action, Biochim Biophys Acta Biomembr. 1462 (1999) 11–28. https://doi.org/10.1016/S0005-2736(99)00198-4.

[41] A.A. Khalili, M.R. Ahmad, A Review of cell adhesion studies for biomedical and biological applications, Int J Mol Sci. 16 (2015) 18149–18184. https://doi.org/10.3390/ijms160818149.

[42] C. Mas-Moruno, R. Fraioli, F. Albericio, J.M. Manero, F.J. Gil, Novel peptide-based platform for the dual presentation of biologically active peptide motifs on biomaterials, ACS Appl Mater Interfaces. 6 (2014) 6525–6536. https://doi.org/10.1021/am5001213.

[43] M. Castellanos, Functionalized CoCr surfaces with adhesive molecules to improve endothelialization, (2017).

[44] M.I. Castellanos, C. Mas-Moruno, A. Grau, X. Serra-Picamal, X. Trepat, F. Albericio, M. Joner, F.J. Gil, M.P. Ginebra, J.M. Manero, M. Pegueroles, Functionalization of CoCr surfaces with cell adhesive peptides to promote HUVECs adhesion and proliferation, Appl Surf Sci. 393 (2017) 82–92. https://doi.org/10.1016/j.apsusc.2016.09.107.

[45] J. Buxadera-Palomero, C. Canal, S. Torrent-Camarero, B. Garrido, F. Javier Gil, D. Rodríguez, Antifouling coatings for dental implants: Polyethylene glycol-like coatings on titanium by plasma polymerization, Biointerphases. 10 (2015) 029505. https://doi.org/10.1116/1.4913376.

[46] C. Mas-Moruno, R. Fraioli, F. Albericio, J.M. Manero, F.J. Gil, Novel peptide-based platform for the dual presentation of biologically active peptide motifs on biomaterials, ACS Appl Mater Interfaces. 6 (2014) 6525–6536. https://doi.org/10.1021/am5001213.

[47] M. Hoyos-Nogués, F. Velasco, M.-P. Ginebra, M. Manero, F.J. Gil, C. Mas-Moruno, Regenerating bone via multifunctional coatings: The blending of cell integration and bacterial inhibition properties on the surface of biomaterials, 2017. http://pubs.acs.org.

[48] ASTM G5-14. Standard Reference Test Method for Making Potentiodynamic Anodic Polarization Measurements, Annual Book of ASTM Standards. (2014). https://doi.org/10.1520/G0005-14.2.

[49] P. Louette, F. Bodino, J.-J. Pireaux, Poly(caprolactone) (PCL) XPS Reference Core Level and Energy Loss Spectra, Surface Science Spectra. 12 (2005) 154–158. https://doi.org/10.1116/11.20051107.

[50] S. Bhatt, J. Pulpytel, M. Mirshahi, F. Arefi-Khonsari, Nano thick poly(ε-caprolactone)-poly(ethylene glycol) coatings developed by catalyst-free plasma assisted copolymerization process for biomedical applications, RSC Adv. 2 (2012) 9114–9123. https://doi.org/10.1039/c2ra21211k.

[51] M.R. Shoar Abouzari, F. Berkemeier, G. Schmitz, D. Wilmer, On the physical interpretation of constant phase elements, Solid State Ion. 180 (2009) 922–927. https://doi.org/10.1016/j.ssi.2009.04.002.

[52] A. Lasia, Electrochemical Impedance Spectroscopy EIS, and Corrosion, 2011.

[53] K. Törne, M. Larsson, A. Norlin, J. Weissenrieder, Degradation of zinc in saline solutions, plasma, and whole blood, J Biomed Mater Res B Appl Biomater. 104 (2016) 1141–1151. https://doi.org/10.1002/jbm.b.33458.

[54] M.B. Kannan, C. Moore, S. Saptarshi, S. Somasundaram, M. Rahuma, A.L. Lopata, Biocompatibility and biodegradation studies of a commercial zinc alloy for temporary mini-implant applications, Sci Rep. 7 (2017) 1–11. https://doi.org/10.1038/s41598-017-15873-w.

[55] E.R. Shearier, P.K. Bowen, W. He, A.J. Drelich, J.W. Drelich, J. Goldman, F. Zhao, In Vitro Cytotoxicity, Adhesion, and Proliferation of Human Vascular Cells Exposed to Zinc, ACS Biomater Sci Eng. 2 (2016) 634–642. https://doi.org/10.1021/acsbiomaterials.6b00035.

[56] W. Yuan, D. Xia, S. Wu, Y. Zheng, Z. Guan, J. v. Rau, A review on current research status of the surface modification of Zn-based biodegradable metals, Bioact Mater. 7 (2022) 192–216. https://doi.org/10.1016/j.bioactmat.2021.05.018.

[57] H. Dong, J. Zhou, S. Virtanen, Fabrication of ZnO nanotube layer on Zn and evaluation of corrosion behavior and bioactivity in view of biodegradable applications, Appl Surf Sci. 494 (2019) 259–265. https://doi.org/10.1016/j.apsusc.2019.07.165.

[58] C. Chen, J. Tan, W. Wu, L. Petrini, L. Zhang, Y. Shi, E. Cattarinuzzi, J. Pei, H. Huang, W. Ding, G. Yuan, F. Migliavacca, Modeling and Experimental Studies of Coating Delamination of Biodegradable Magnesium Alloy Cardiovascular Stents, ACS Biomater Sci Eng. 4 (2018) 3864–3873. https://doi.org/10.1021/acsbiomaterials.8b00700.

[59] C.G. Hopkins, P.E. McHugh, J.P. McGarry, Computational investigation of the delamination of polymer coatings during stent deployment, Ann Biomed Eng. 38 (2010) 2263–2273. https://doi.org/10.1007/s10439-010-9972-y.

[60] J. Choi, S.B. Cho, B.S. Lee, Y.K. Joung, K. Park, D.K. Han, Improvement of interfacial adhesion of biodegradable polymers coated on metal surface by

nanocoupling, Langmuir. 27 (2011) 14232–14239. https://doi.org/10.1021/la2030318.

[61] L. Xu, A. Yamamoto, Characteristics and cytocompatibility of biodegradable polymer film on magnesium by spin coating, Colloids Surf B Biointerfaces. 93 (2012) 67–74. https://doi.org/10.1016/j.colsurfb.2011.12.009.

[62] D.W.Y. Toong, J.C.K. Ng, Y. Huang, P.E.H. Wong, H.L. Leo, S.S. Venkatraman, H.Y. Ang, Bioresorbable metals in cardiovascular stents: Material insights and progress, Materialia (Oxf). 12 (2020) 100727. https://doi.org/10.1016/j.mtla.2020.100727.

[63] D.W.Y. Toong, J.C.K. Ng, Y. Huang, P.E.H. Wong, H.L. Leo, S.S. Venkatraman, H.Y. Ang, Bioresorbable metals in cardiovascular stents: Material insights and progress, Materialia (Oxf). 12 (2020). https://doi.org/10.1016/j.mtla.2020.100727.

[64] C.A. Hoesli, A. Garnier, P.M. Juneau, P. Chevallier, C. Duchesne, G. Laroche, A fluorophore-tagged RGD peptide to control endothelial cell adhesion to micropatterned surfaces, Biomaterials. 35 (2014) 879–890. https://doi.org/10.1016/j.biomaterials.2013.09.076.

[65] S. Vanslambrouck, P. Chevallier, A.A. Guay-Bégin, G. Laroche, Effect of linking arm hydrophilic/hydrophobic nature, length and end-group on the conformation and the RGD accessibility of surface-immobilized fibronectin, Materials Science and Engineering C. 107 (2020) 110335. https://doi.org/10.1016/j.msec.2019.110335.

[66] W. Wang, L. Guo, Y. Yu, Z. Chen, R. Zhou, Z. Yuan, Peptide REDV-modified polysaccharide hydrogel with endothelial cell selectivity for the promotion of angiogenesis, J Biomed Mater Res A. 103 (2015) 1703–1712. https://doi.org/10.1002/jbm.a.35306.

[67] H. Martin-Gómez, L. Oliver-Cervelló, I. Sánchez-Campillo, V. Marchán, M.P. Ginebra, C. Mas-Moruno, A versatile click chemistry-based approach for functionalizing biomaterials of diverse nature with bioactive peptides, Chemical Communications. 57 (2021) 982–985. https://doi.org/10.1039/d0cc07463b.

[68] M. Gutiérrez-Sánchez, V.A. Escobar-Barrios, A. Pozos-Guillén, D.M. Escobar-García, RGD-functionalization of PLA/starch scaffolds obtained by electrospinning and evaluated in vitro for potential bone regeneration, Materials Science and Engineering C. 96 (2019) 798–806. https://doi.org/10.1016/j.msec.2018.12.003.

[69] C. Damia, D. Marchat, C. Lemoine, N. Douard, V. Chaleix, V. Sol, N. Larochette, D. Logeart-Avramoglou, J. Brie, E. Champion, Functionalization of phosphocalcic bioceramics for bone repair applications, Materials Science and Engineering C. 95 (2019) 343–354. https://doi.org/10.1016/j.msec.2018.01.008.

[70] M. Schnabelrauch, M. Dubs, A.R. Kautz, J. Weisser, C. Bergemann, H. Rebl, J. Schmidt, C. Witt, T. Oberbach, D. Imhof, J.B. Nebe, Biofunctionalization of ceramic implant surfaces to improve their bone ingrowth behavior, in: Materials Science Forum, Trans Tech Publications Ltd, 2018: pp. 2483–2488. https://doi.org/10.4028/www.scientific.net/MSF.941.2483.

[71] E. Mauri, A. Sacchetti, N. Vicario, L. Peruzzotti-Jametti, F. Rossi, S. Pluchino, Evaluation of RGD functionalization in hybrid hydrogels as 3D neural stem cell culture systems, Biomater Sci. 6 (2018) 501–510. https://doi.org/10.1039/c7bm01056g.

[72] J. Guillem-Marti, M. Gelabert, A. Heras-Parets, M. Pegueroles, M.P. Ginebra, J.M. Manero, RGD Mutation of the Heparin Binding II Fragment of Fibronectin for Guiding Mesenchymal Stem Cell Behavior on Titanium Surfaces, ACS Appl Mater Interfaces. 11 (2019) 3666–3678. https://doi.org/10.1021/acsami.8b17138.

[73] M.I. Castellanos, C. Mas-Moruno, A. Grau, X. Serra-Picamal, X. Trepat, F. Albericio, M. Joner, F.J. Gil, M.P. Ginebra, J.M. Manero, M. Pegueroles, Functionalization of CoCr surfaces with cell adhesive peptides to promote HUVECs adhesion and proliferation, Appl Surf Sci. 393 (2017) 82–92. https://doi.org/10.1016/j.apsusc.2016.09.107.

[74] J. Tian, S. Shen, C. Zhou, X. Dang, Y. Jiao, L. Li, S. Ding, H. Li, Investigation of the antimicrobial activity and biocompatibility of magnesium alloy coated with HA and antimicrobial peptide, J Mater Sci Mater Med. 26 (2015). https://doi.org/10.1007/s10856-015-5389-3.

[75] L. Chen, J. Li, S. Wang, S. Zhu, C. Zhu, B. Zheng, G. Yang, S. Guan, Surface modification of the biodegradable cardiovascular stent material Mg-Zn-Y-Nd alloy via conjugating REDV peptide for better endothelialization, J Mater Res. 33 (2018) 4123–4133. https://doi.org/10.1557/jmr.2018.410.

[76] Y. Wu, L. Chang, J. Li, L. Wang, S. Guan, Conjugating heparin, Arg–Glu–Asp–Val peptide, and anti-CD34 to the silanic Mg–Zn–Y–Nd alloy for better endothelialization, J Biomater Appl. 35 (2020) 158–168. https://doi.org/10.1177/0885328220926655.

[77] K. Törne, A. Örnberg, J. Weissenrieder, Influence of strain on the corrosion of magnesium alloys and zinc in physiological environments, Acta Biomater. 48 (2017) 541–550. https://doi.org/10.1016/j.actbio.2016.10.030.

[78] G. Peng, D. Yao, Y. Niu, H. Liu, Y. Fab, Surface modification of multiple bioactive peptides to improve endothelialization of vascular grafts, (n.d.).

Chapter IV.

Influence of ECAP process on mechanical, corrosion and bacterial properties of Zn-2Ag alloy

Results submitted for publication in Materials & Design (21/09/2022), and currently under revision

Chapter IV. Influence of ECAP process on mechanical, corrosion and bacterial properties of Zn-2Ag alloy

Objective

To evaluate the concurrent combined effect of grain refinement and Ag alloying on biodegradation and bacterial activity of Zn-2Ag (2 wt.%) alloy after severe plastic deformation.

Graphical abstract

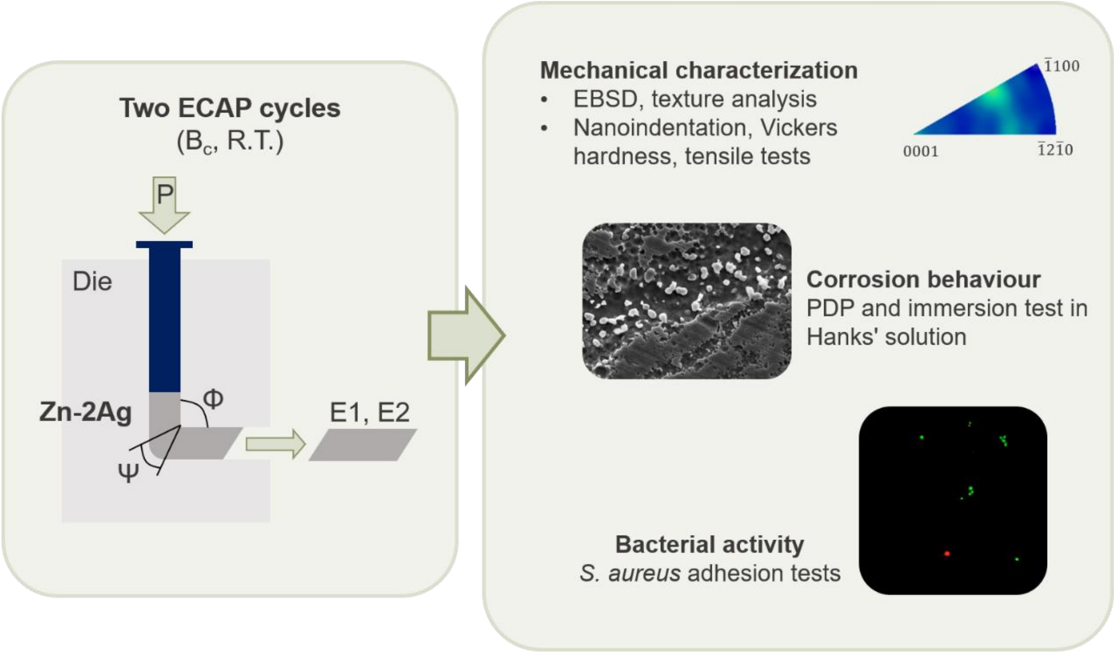

Main results

This chapter presents ECAP as a potential processing route for wire manufacturing for wound closure applications. After ECAP, the E2 sample exhibited a UFG structure with randomly distributed grain orientation and lower texture. Mechanical isotropy was confirmed at the nano and microscale, along with reduced UTS and YS. Moreover, the more homogeneous degradation and Ag distribution in the Zn matrix after ECAP provided exceptional antibacterial activity against *S. aureus* bacteria.

I. Introduction

Wound closure devices such as sutures and staples are designed to approximate the edges of the injury tissue until its healing. The device should promote rapid closure by applying proper tension to prevent infections, but excessive stress could lead to ischemia or tissue necrosis. The fundamental material requirements for sutures gather good knot tensile strength and security, proper ductility, and biocompatibility [1]. In the last decades, bioresorbable materials have attracted so much attention since they eliminate the need for second surgeries for removal and reduce the associated long-term risks [2].

Few studies have been focused on Zn-based materials for wound-closure applications up to date [3]. Guo *et al*. [4] developed Zn wires of 3- and 0.3-mm diameters with good *in vitro* biocompatibility and knot feasibility, where the best mechanical performance was related to the most refined microstructure. So far, achieving adequate mechanical performance, corrosion behaviour, and biological response of Zn-based alloys remains an open challenge. Mechanical anisotropy has been reported as one of the causes of implant failure since the stress is not well-distributed along with the material after its implantation [2]. In this regard, the mechanical properties of Zn are closely related to its texture [5]. Another crucial factor for maintaining implant stability is its uniform degradation. Localized corrosion could accumulate local stress and lead to the breaking of the implant. Severe plastic deformation (SPD) is widely used to produce bulk ultrafine-grained (UFG) materials by introducing extremely large strain during the deformation process. Among them, equal channel angular pressing (ECAP) is an effective procedure to prepare UFG metals with excellent mechanical and corrosion properties[6,7] and to improve the biocompatibility of Mg alloys [8]. Concerning ECAP processing of Zn alloys, different studies have been performed. The obtained mechanical toughening in Zn-Mg or Zn-Mn alloys has been attributed to grain refinement of the Zn-alloy matrix, alongside the secondary phases' fragmentation and distribution [9]. However, mechanical strengthening is not obtained for every Zn-based conjugation. For instance, the ultimate tensile strength (UTS) and yield strength (YS) of Zn-Cu alloys dramatically decreased after ECAP, whereas superplastic behaviour was observed [10]. Nonetheless, the ECAP effect on the bacterial response of Zn alloys has not yet been studied.

Surgical site infections (SSIs) are surgical-related infections related to wound closure interventions that appear within 30 days after implantation (or one year in the case of implants) [11]. Different factors affect the risk of bacterial incidences, such as the geometry of the implant or its composition. For instance, multifilament and braided sutures are more prone to infection because of the increased attachment of the bacteria within the structure [12]. Therefore, suture materials are loaded with antibiotics such as triclosan [13] or gentamicin [14]. However, the development of antibacterial resistance forces researchers to find alternatives to avoid SSI. *Staphylococcus aureus (S. aureus)* is present in most SSIs and bloodstream infections. The bacterial resistance development and the lack of equally effective alternatives complicate methicillin-resistant *S. aureus* (MRSA) treatment [15]. Antibacterial agents such as silver (Ag) nanoparticles have been included in the polymeric structures hindering possible infections [16]. Besides, the incorporation of metallic ions such as silver (Ag^+), copper (Cu^{2+}), and zinc (Zn^{2+}), or the correspondent oxides (AgO(s), CuO(s), ZnO(s)) to conventional titanium have been demonstrated to provide antibacterial properties to the implants [17].

This work aims to provide more insights into the mechanical effects of grain refinement in Zn-based alloys and evaluate its impact on bacterial performance. To this end, a Zn-2Ag (2 wt.% Ag) alloy was processed and investigated to evaluate the reachable strengthening induced by grain refining by ECAP and the concurrent combined effect of grain refinement and Ag alloying on biodegradation and antibacterial activity.

II. Materials and Methods

II.1. Materials and ECAP processing

Zn-2Ag (2 wt.% Ag) metallic bar was provided by GoodFellow (UK). The as-received condition of the bars was extruded and cold rolled. Billets with 10 mm of diameter and 100 mm of length were machined from the starting material. The ECAP die was composed of two cylindrical channels intersecting at an angle of 90º with an outer arc of curvature of 20°. This geometry provides an equivalent plastic strain of 1,05 for each pass according to the Iwahashi equation [18]. Samples were pressed at room temperature with a speed of 5 mm/min using molybdenum disulphide (MoS_2) as a lubricant. Zn-2Ag billets were subjected to up to two ECAP cycles by rotating the sample along its longitudinal axis by 90º before the second pass (route B_C, according to the established designation given in the literature [19]). Samples subjected to one and two ECAP cycles were named E1, and E2, respectively. Pressed bars were cut into 2.5 mm disks and ground following standard metallographic procedures.

II.2. Microstructure characterization

The microstructure of the as-received Zn-2Ag and pressed samples after ECAP cycles were observed. To this end, the specimens were cut in the transversal and longitudinal direction, parallel to the direction of ECAP extrusion. The transversal and longitudinal sections were then abraded with silicon carbide grinding papers (grit size P800, P1200, and P2500, and polished using 6 and 3-μm diamond suspension. Fine polishing was achieved using 0.05 μm alumina suspension (Buehler, EEUU). The samples were etched by a solution consisting of 0.5 g of oxalic acid, 2.5 mL of acetic acid, and 25 mL of absolute ethanol (Sigma-Aldrich, USA).

Field-emission gun scanning electron microscopy (FEG-SEM) (Carl Zeiss AG - EVO® 50 Series, Zeiss, Germany) equipped with an X-ray energy-dispersive spectrometry (EDS) detector (Oxford Instruments, Aztec Energy, UK) was used for microstructural characterization. ImageJ software (National Institutes of Health, MD) was used to determine the area and the distribution of the secondary phases on transversal and longitudinal sections of the samples.

The composition of the samples was studied by X-ray diffractometry (XRD, D8 ADVANCE Twin, Bruker, USA), with Cu K_α operating at 40 kV and 100 mA and scanning from 20º to 90 º. The scan rate was 2º min^{-1}, and the step size was 0.02º.

II.3. Electron Backscattered Diffraction (EBSD) analysis

The microstructural evolution of the samples was studied by Electron Backscattered Diffraction (EBSD) technique (C Nano, Oxford Instruments, UK) interfaced with the FEG-SEM. The scan area selected was 200 μm x 270 μm with 0.15 μm of step size for all the conditions for good statistical representation. All the data were processed with CHANNEL 5 software (Oxford Instruments, UK). The grains were defined as a set of a minimum 10 points with a mutual misorientation < 10º. Before EBSD analysis, the surfaces were prepared by standard mechanical procedures until final polishing with 0.05 μm alumina suspension.

II.4. High-speed nanoindentation mapping

Nanoindentations were performed by a KLA iMicro nanoindenter (KLA, USA) using a diamond Berkovich tip with its area function determined against fused silica standard. Each indent performed one complete indentation cycle per second. Matrixes of 100 x 100 indentations were carried out to a maximum constant load of 1 mN with 2 μm spacing between the indents. In total, 10^4 indentation cycles were performed to map the processed samples for obtaining reliable correlations at the micrometre length and for subsequent statistical analysis. Results were analysed by InView software (KLA, USA). Before nanoindentation studies, the samples were ground up to 2500 grit and polished with alumina suspension down to 0.05 μm.

II.5. Mechanical characterization

Mechanical properties were evaluated by Vickers micro-hardness and tensile tests before and after the ECAP process. Microhardness measurements were performed on the transversal and longitudinal direction of the samples with an indenter load of 100 g and dwelling time of 10 s using a Vickers microhardness tester (Durascan G5, Emcotest). According to the obtained results, the Zn-2Ag and the E2 condition were selected for the following characterization. Tensile dog-bone samples (20 mm gage length, 4 mm diameter, and 8 mm fillet radius) were machined along the ECAP direction. Tensile tests were carried out following ASTM E8/E8M [20] with an electromechanical testing frame (MTS Alliance RT/100, MTS system, USA) at room temperature and a strain rate of 1 mm/min. The tensile tests were replicated using three samples per each condition.

II.6. Corrosion characterization

The corrosion behaviour of the samples was studied by potentiodynamic polarization (PDP) tests and static immersion tests at 37 ± 1 ºC and pH 7.4 ± 0.1 in Hanks' solution containing 0.4 g/L of KCl, 0.06 g/L of KH_2PO_4, 8 g/L of NaCl, 0.045 g/L of Na_2HPO_4, 0.35 g/L of $NaHCO_3$, and 0.19 g/L of $CaCl_2$.

PDP analysis was performed using a PARSTAT 2273 potentiostat (Princeton Applied Research, USA), where a three-electrode setup with a Pt electrode as a counter electrode, and a saturated calomel electrode (SCE) as a reference electrode was used. The open circuit potential (OCP) was first measured until its stabilization. The potential window selected for PDP was from -1.4 to -0.6 V potential against the OCP at a scan rate of 0.16 mV/s, according to ASTM G5-14 [21]. The corrosion rate (CR) was calculated from the Tafel extrapolation using PowerSuit software (Princeton Applied Research, USA), following ASTM G102-89 [22].

A static immersion test was performed following ASTM G31-72 [23]. Samples were weighed and then immersed for 10 days in 20 mL of Hanks' solution at 37 ± 1 ºC. The whole solution was renewed every 24 h to avoid a drift in the pH. The redox potential (E) and the pH were monitored with a Hanna HI 5521 multiparameter (Hanna Instruments, Italy). The Pourbaix diagrams of Zn and Ag in Hanks' solution were calculated by HSC 5.1 Software. The released Zn^{2+} and Ag^{+} at 1, 3, 7, and 10 days after immersion were analysed by high-resolution inductively coupled plasma mass spectrometry (HR-ICP-MS) (ELEMENT XR, Thermo Fisher). For this purpose, aliquots of the solution were collected and filtered with a 0.2 μm filter and later diluted with 1% HNO_3(v/v). The CR was determined from mass loss measurements for corroded samples cleaned in a solution of 200 g/L CrO_3(s) at 70±1 ºC, according to ISO 8407 [24]. Surface morphology of the samples before and after the removal of the corrosion products was observed by SEM equipped with X-ray energy dispersive spectrometry (EDS) (JSM-7001F, JEOL, Japan).

II.7. Bacterial adhesion

S. aureus (CCUG 15915, Culture Collection University of Göteborg (CCUG), Göteborg, Sweden) was selected to evaluate the antibacterial properties of the samples. Bacteria in frozen stock were aerobically cultured at 37 ± 1 ºC in a brain heart infusion (BHI, Scharlab, Spain) overnight. Bacteria concentration was adjusted to a final optical density of 0.2 at 600 nm, equivalent to 10^8 colony-forming units (CFU) per millilitre.

Two additional conditions were introduced as controls for the adhesion test: Ti and pure Zn discs were prepared following the metallographic procedure described in section II.1. Samples were inoculated with 20 μL of bacteria suspension for 3 h. Subsequently, samples were rinsed in phosphate buffer solution (PBS) to remove the non-adhered bacteria.

The LIVE/DEAD™ *Bac*Light™ bacterial viability kit (Thermo Fisher, USA) was used to observe the attached alive bacteria (fluorescent green) and dead bacteria (fluorescent red). The staining was prepared by diluting the component SYTO 9 and propidium iodide (1.67 mM) in PBS to a final concentration of 3 μm/mL. For the live/dead staining, adhered bacteria were fixed with 500 μL of 2.5% glutaraldehyde in PBS at 5 ±1 ◦C for 30 minutes and incubated in the staining for 15 minutes. Afterwards, bacteria were observed by fluorescence microscopy (Nikon E600, Tokyo, Japan). For the attached bacteria quantification, samples were introduced in PBS and ultrasonically cleaned for 1 minute. The resulting detached bacteria were incubated in agar plates overnight, and the CFUs were counted.

II.8. Statistical analysis

The results of this work were reported as the mean values ± standard deviation (SD). Unless previously specified, three replicates (n = 3) were done in the experiments. For statistical analysis, a first normality test (Shapiro-Wilk test) was performed to evaluate the normal distribution of the data. Later, an equality of variances test (ANOVA) or a non-parametric test (Kruskal-Wallis test) were performed when data were normally or non-normally distributed, respectively. Minitab Statistical Software (Minitab Inc., USA) was used for the statistical analysis.

III. Results

III.1. Microstructure characterization

Fig. 1 shows the SEM micrographs of Zn-2Ag, E1, and E2. The microstructure of all the samples was composed of two phases: Zn and $AgZn_3$. According to EDS and XRD results in **Fig. 2** and the Zn-Ag phase diagram [25], the darker area corresponds to the Zn matrix and the brighter one to the secondary $AgZn_3$ phase. The microstructure of Zn-2Ag presented a homogeneous $AgZn_3$ phase distribution with a certain degree of alignment to the extrusion direction (**Fig. 1a, d**). Image analysis confirmed similar distribution of the $AgZn_3$ phase through the Zn matrix for E1 and E2 samples, with $AgZn_3$ particles with areas ranging from 0.05 to 2.5 µm^2 and no evidence of fragmentation of the secondary phases.

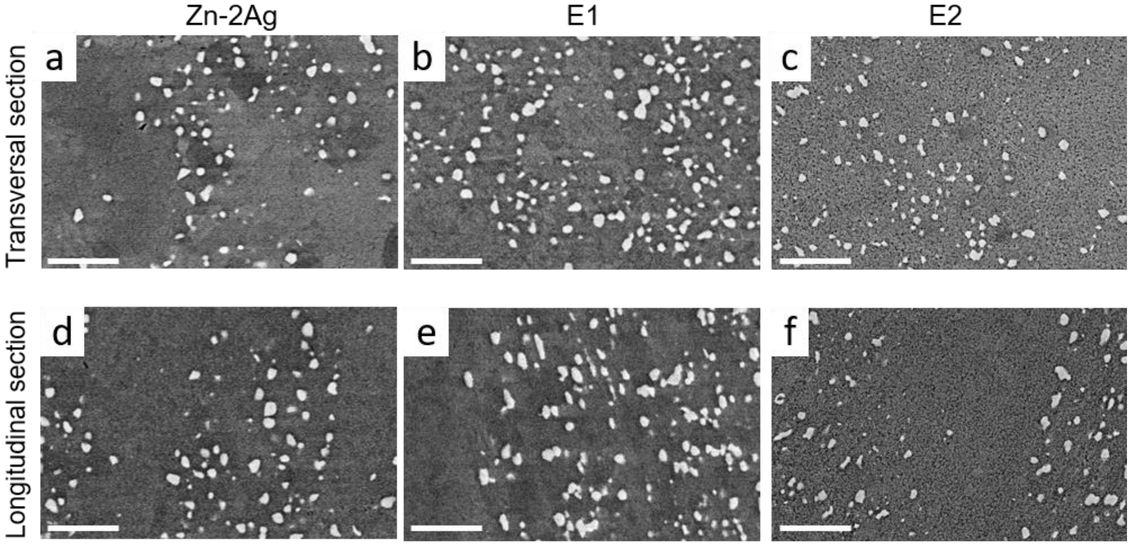

Fig. 1. Microstructure of the transversal sections (top) and longitudinal sections (bottom) of Zn-2Ag (a, d), E1 (b, e), and E2 (c, f). The darker area corresponds to the Zn matrix, and the brighter one to the $AgZn_3$ phase. Scale bar: 10 µm.

a

	Lattice parameters				
Phase	a (nm)	b (nm)	c (nm)	Pearson symbol	Space group
Zn	2.6649	2.6649	4.9470	hP2	$P6_3/mmc$
$AgZn_3$	2.8227	2.8227	4.4274	hP2	$P6_3/mmc$

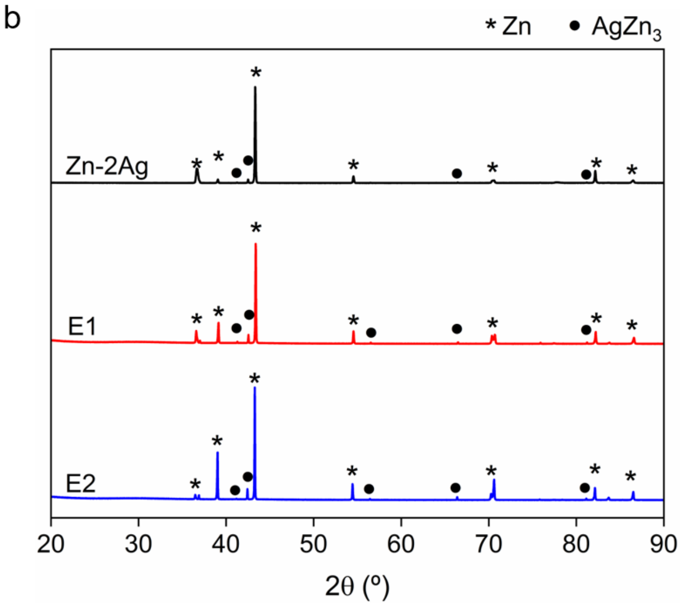

Fig. 2. XRD results: (a) crystallographic data of Zn and $AgZn_3$ phases. (b) XRD spectra of Zn-2Ag, E1, and E2 samples.

III.2. EBSD analysis

Fig. 3 shows the transversal and longitudinal EBSD inverse pole figure (IPF) maps of the samples, and the data analysis of the grain size is included in **Fig. 4**. EBSD-IPF maps evidenced the grain refinement and the homogeneous grain size distribution in both directions after ECAP. **Fig. 3d** presents the longitudinal section of the original Zn-2Ag alloy, showing preferential grain orientation due to the extrusion process. However, the oriented and elongated Zn grains of Zn-2Ag alloy became homogenous and non-oriented after ECAP processing (**Fig. 3e, f**).

The box plot representations in **Fig. 4a, b** showed wider data dispersion for Zn-2Ag alloy and the most homogeneous grain size distribution for E2. Moreover, the UFG structure was obtained for E1 and E2, reaching grain size values below 1 μm^2 in the latter case (**Fig. 4c**). The statistical analysis corroborated significant grain refinement after each ECAP pass.

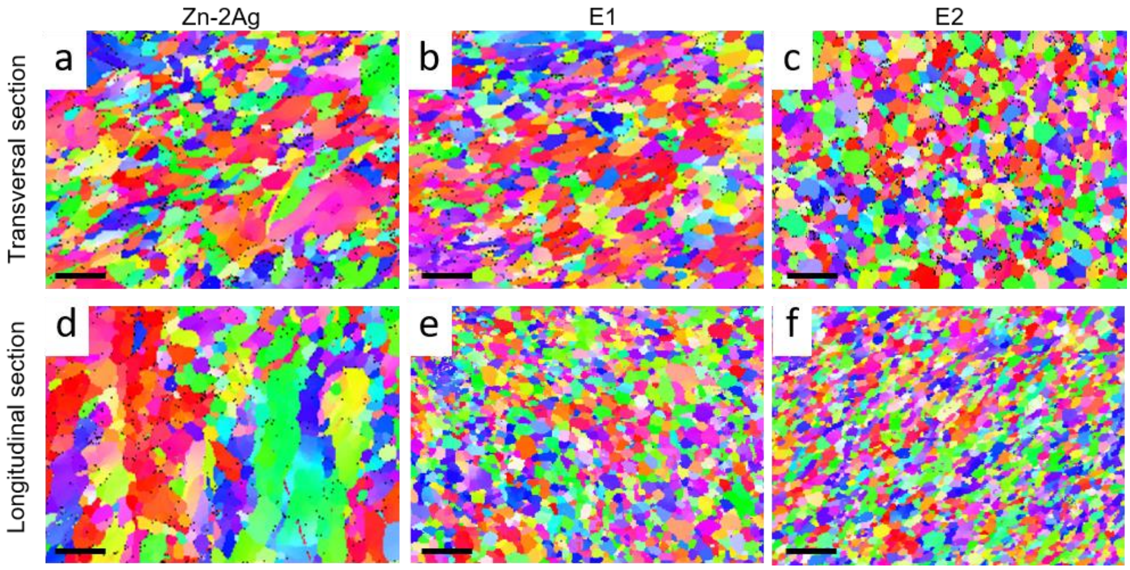

Fig. 3. EBSD-IPF map of the transversal section (top) and longitudinal section (bottom) of ZnAg at the different stages: as-received (a, d), after the first ECAP cycle (b, e), and after the second ECAP cycle (c, f). Scale bar: 5 μm.

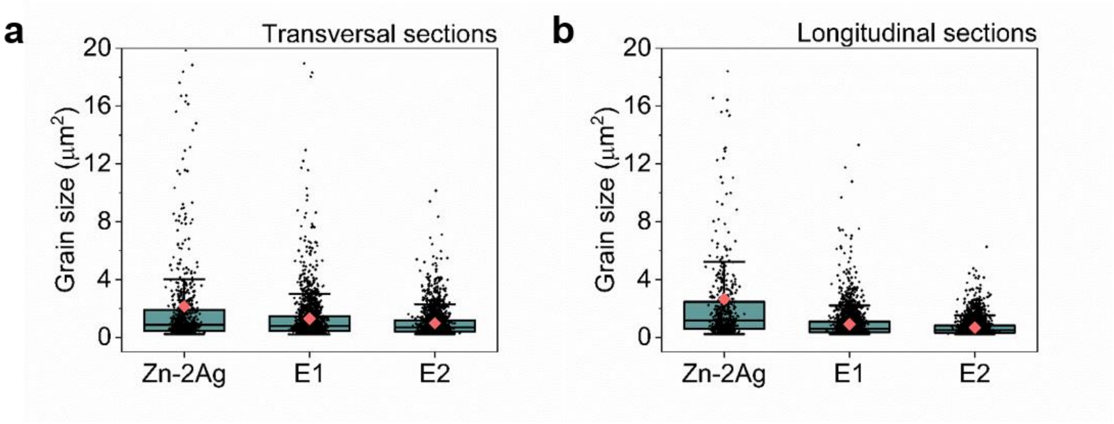

c

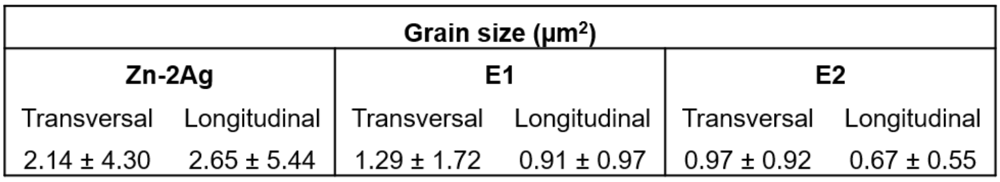

Grain size (μm^2)					
Zn-2Ag		**E1**		**E2**	
Transversal	Longitudinal	Transversal	Longitudinal	Transversal	Longitudinal
2.14 ± 4.30	2.65 ± 5.44	1.29 ± 1.72	0.91 ± 0.97	0.97 ± 0.92	0.67 ± 0.55

Fig. 4. Box plot of the grain size of the as-received and ECAP samples at the (a) transversal and (b) longitudinal sections; and (c) the calculated grain size values using CHANNEL 5 software.

Fig. 5 shows the IPF of the analysed samples. The weak texture in the transversal direction remained substantially similar after the ECAP process (**Fig. 5a-c**). However, the ECAP deformation caused noticeable changes in the longitudinal direction (**Fig. 5d-f**). From the IPF of the longitudinal section of the Zn-2Ag alloy, it is evident that the most of the grains were preferentially oriented to the [0001] pole in the extruded bar and scattered to the other directions with the ECAP cycles, developing a more random texture.

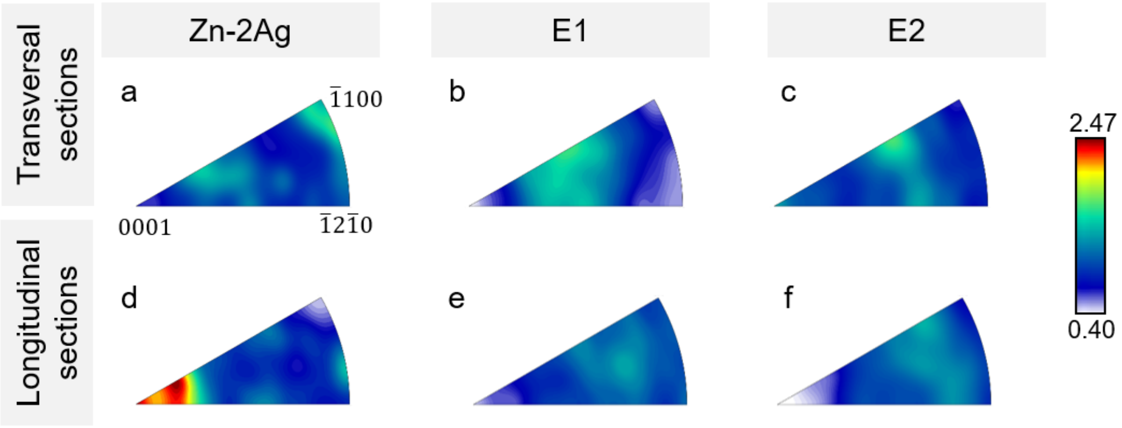

Fig. 5. IPF images of the transversal and longitudinal sections of Zn-2Ag, E1, and E2 samples.

III.3. High-speed nanoindentation mapping

The nanohardness and the elastic modulus maps obtained after high-speed nanoindentation tests are shown in **Fig. 6** and **Fig. 7**, respectively, and quantified in **Table 2**. The Zn grains could be perfectly distinguished from the transversal section maps of Zn-2Ag (**Fig. 6a**, **Fig. 7a**), indicating that nanohardness and elastic modulus highly depend on grain orientation [26,27]. The hardness isotropy increased on the transversal section after ECAP (**Fig. 6 b, c**), together with significantly lower average nanohardness values indicating the softening of the material (**Table 1**). A similar homogeneity trend could be observed from elastic modulus maps of E1 and E2 transversal section analysis (**Fig. 7 b, c**).

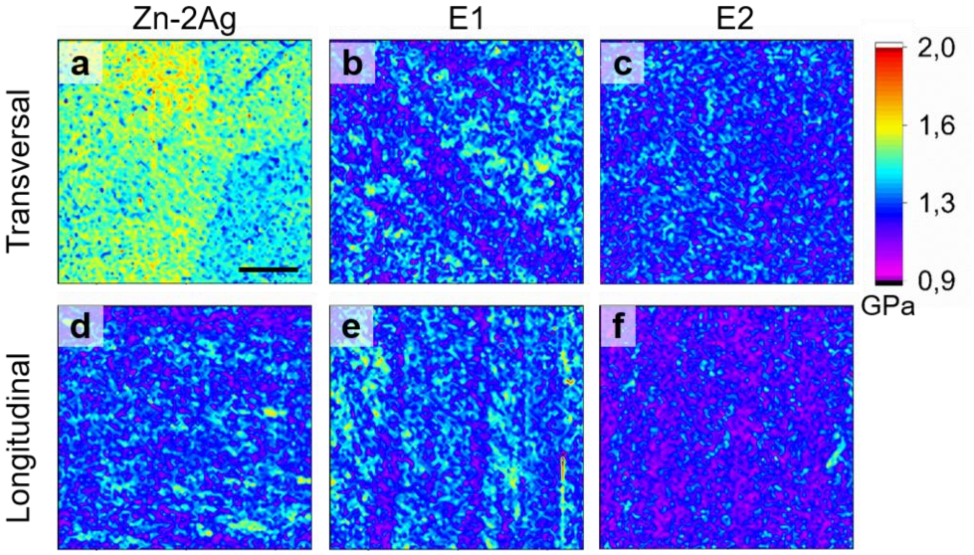

Fig. 6. Hardness nanoindentation maps of Zn-2Ag (a, d), E1 (b, e), and E2 (c, f) at the transversal (top) and longitudinal (bottom) sections. Scale bar: 50 µm.

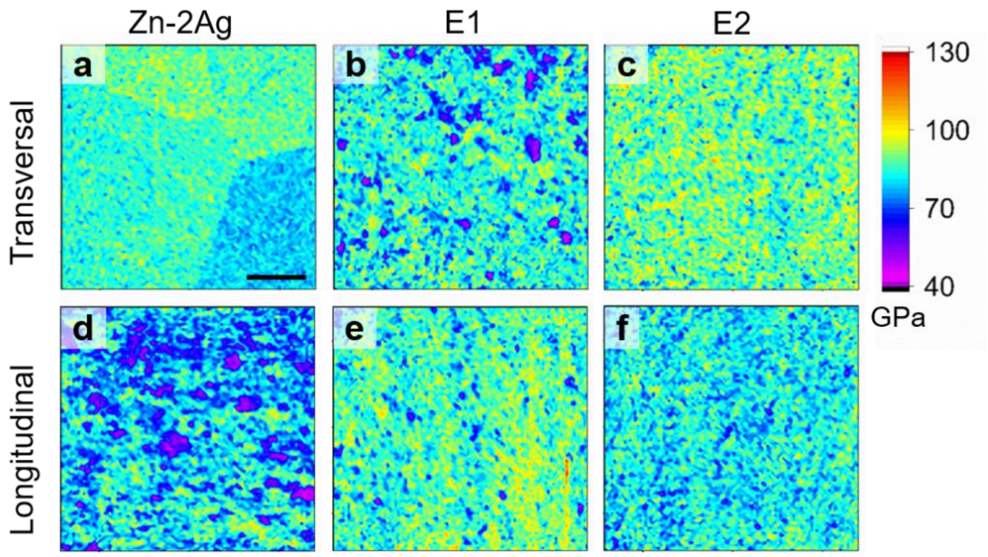

Fig. 7. Elastic modulus nanoindentation maps of Zn-2Ag (a, d), E1 (b, e), and E2 (c, f) at the transversal (top) and longitudinal (bottom) sections. Scale bar: 50 μm.

Table 1. Elastic modulus (E) and nanohardness (H) calculated parameters from nanoindentation maps of the transversal and longitudinal section of Zn-2Ag, E1, and E2. TD = transversal direction. LD = longitudinal direction.

	Zn-2Ag		**E1**		**E2**	
Direction	TD	LD	TD	LD	TD	LD
E (GPa)	84.9 ± 6.7	77.3 ± 12.0	82.1 ± 10.8	86.2 ± 9.8	88.2 ± 9.8	81.8 ± 9.5
H (GPa)	1.47 ± 0.13	1.25 ± 0.13	1.26 ± 0.14	1.28 ± 0.14	1.24 ± 0.13	1.18 ± 0.12

III.4. Mechanical characterization

The evaluation of the mechanical behaviour was performed through microhardness measurements and tensile tests. The hardness values and tensile curves collected are summarized in **Fig. 8.** The Zn-2Ag alloy microhardness showed a clear drop for both directions after the second ECAP cycle (**Fig. 8a**). For this reason, the subsequent tensile characterization was focused on the E2 condition only. The tensile tests (**Fig. 8b**) showed a notable decrease in the ultimate tensile strength (UTS) and yield strength (YS) after two ECAP cycles. Both tested materials featured a very limited work hardening ability in the plastic regime but extensive ductility, reaching values of fracture elongation (A %) above 200 % for E2. **Fig. 8** includes representative fractographs of the samples after the tensile test. The fracture morphology of the Zn-2Ag mainly showed dimples with a diameter in the range of 2 – 20 μm (**Fig. 8c**), whereas the dimple size decreased below 2 μm for the E2 sample (**Fig. 8d**), in line with the observed microstructure structure refinement.

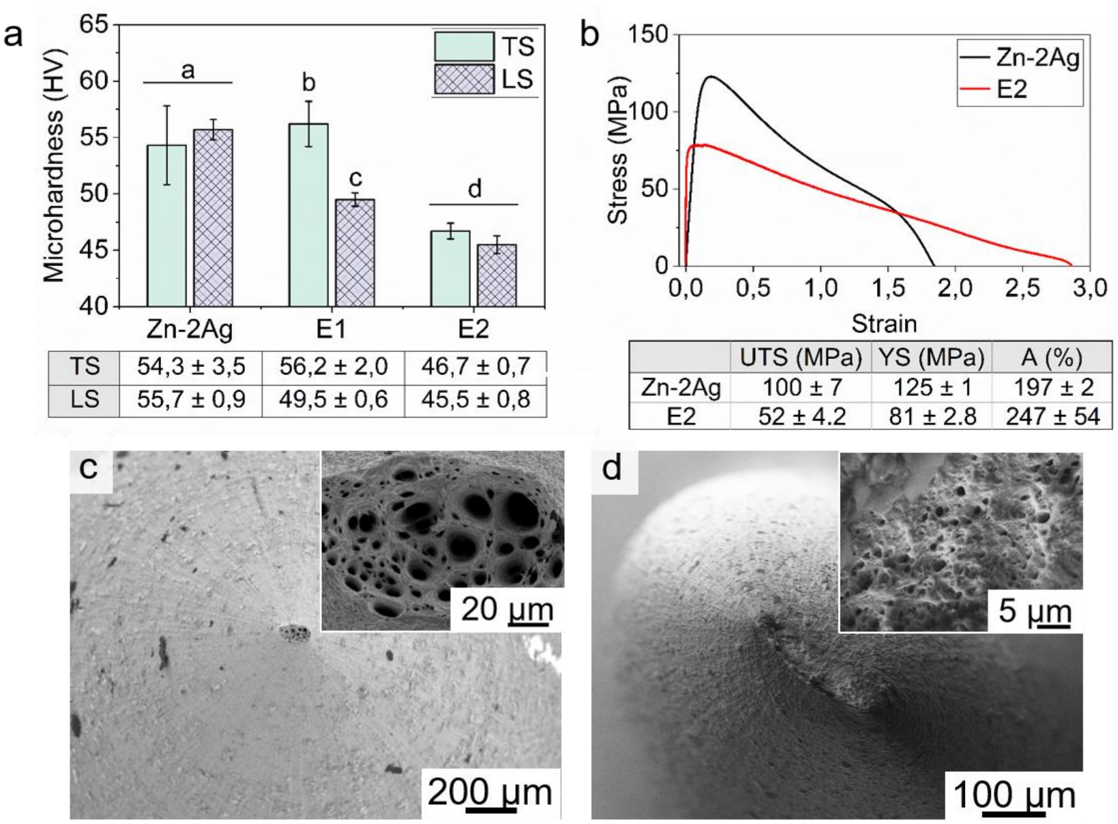

Fig. 8. (a) Vickers micro-hardness results of Zn-2Ag, E1, and E2 samples. [a,b,c,d] symbols join groups with non-statistically significant differences. (b) Tensile curves and calculated tensile properties of the Zn-2Ag and E2 samples. SEM fractographic images of (c) Zn-2Ag, and (d) E2 samples.

III.5. Corrosion characterization

The corrosion parameters calculated from PDP and immersion tests in Hanks' solution are listed in **Table 2**. No significant differences were observed between Zn-2Ag and E2 samples for any parameter (**Table 2**). The values obtained are in accordance with previous corrosion studies on Zn-Ag alloys [28].

Table 2. Corrosion parameters obtained from PDP and static immersion test in Hanks' solution: corrosion potential (E), current density (i), CR (PDP), and CR (mass loss).

	E (V)	i (μA/cm^2)	CR, PDP (mm/yr)	CR, mass loss (mm/yr)
Zn-2Ag	-1.176 ± 0.018	2.26 ± 0.13	0.034 ± 0.002	0.099 ± 0.032
E2	-1.193 ± 0.008	1.98 ± 0.43	0.029 ± 0.006	0.090 ± 0.046

Although the corrosion parameters presented no statistical differences, the ion release of the samples differed. As shown in **Fig. 9a**, the release of Zn^{2+} was higher for E2 in comparison with Zn-2Ag, with a total final concentration of 20.66 ± 0.24 μg/dL and 13.69 ± 0.21 μg/dL, respectively. On the other hand, the Ag^+ release presented the opposite relation, with lower total concentration for E2 (0.11 ± 0.01 μg/dL) than for Zn-2Ag (0.92 ± 0.02 μg/dL) (**Fig. 9b**). **Table 3** shows the Zn^{2+} and Ag^{+} concentrations measured by ICP-MS on days 1, 2, 3, 7, and 10 of immersion and their relation in %. **Fig. 9c, d** show the pH and the E evolution through the immersion test in Hank's solution, respectively. As expected, the pH increased with respect to the initial value of 7.4, confirming the release of corrosion products from the alloys. The obtained values of E were between -40 and -80 mV. The calculated Pourbaix diagrams of Zn and Ag in Hanks' are depicted **in Fig. 9 e, f**. Applying the obtained values of pH and E in the Pourbaix diagrams, the most stable Zn solid phases are $ZnCO_3$(s) and ZnO (s), while the most stable Ag solid phases are Ag(s), and AgCl (s).

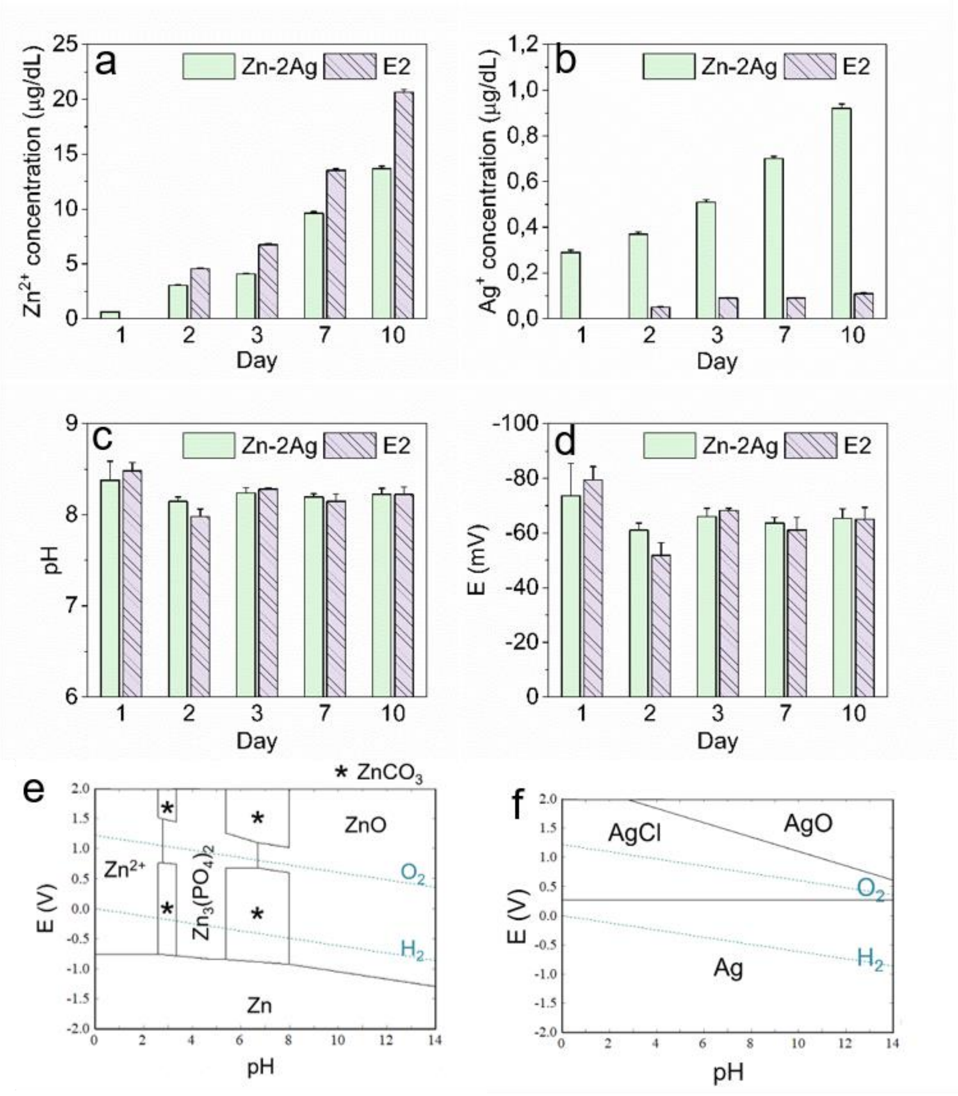

Fig. 9. Accumulative (a) Zn^{2+} and (b) Ag^{+} ion release of the samples measured by ICP-MS after 1, 2, 3, 7, and 10 days of immersion. Evolution of (c) pH and (d) E with the immersion time. Pourbaix diagrams of (e) Zn and (f) Ag in Hanks' solution at tested conditions obtained by HSC 5.1 Software.

Table 3. ICP-MS results of released Zn^{2+} and Ag^{+} at days 1, 2, 3, 7, and 10 of immersion in Hanks' solution at 37 ± 1 ºC. Limit of detection (LOD): Zn^{2+} = 0.01 µg/dL; Ag^{+} = 0.001 µg/dL.

	Zn-2Ag		**E2**	
Day	Zn^{2+} (µg/dL)	Ag^{+} (µg/dL)	Zn^{2+} (µg/dL)	Ag^{+} (µg/dL)
1	12.26 ± 0.03 (81%)	2.93 ± 0.05 (19 %)	<LOD	<LOD
2	24.37 ± 0.30 (97 %)	0.75 ± 0.02 (3 %)	45.46 ± 0.58 (99 %)	0.55 ± 0.02 (1 %)
3	10.22 ± 0.40 (88 %)	1.46 ± 0.04 (12 %)	21.88 ± 0.74 (98 %)	0.52 ± 0.01 (2 %)
7	13.81 ± 0.20 (97 %)	0.47 ± 0.01 (3 %)	16.97 ± 0.08 (100 %)	<LOD
10	13.66 ± 0.16 (95 %)	0.74 ± 0.02 (5 %)	23.78 ± 0.24 (99 %)	0.19 ± 0.01 (1 %)

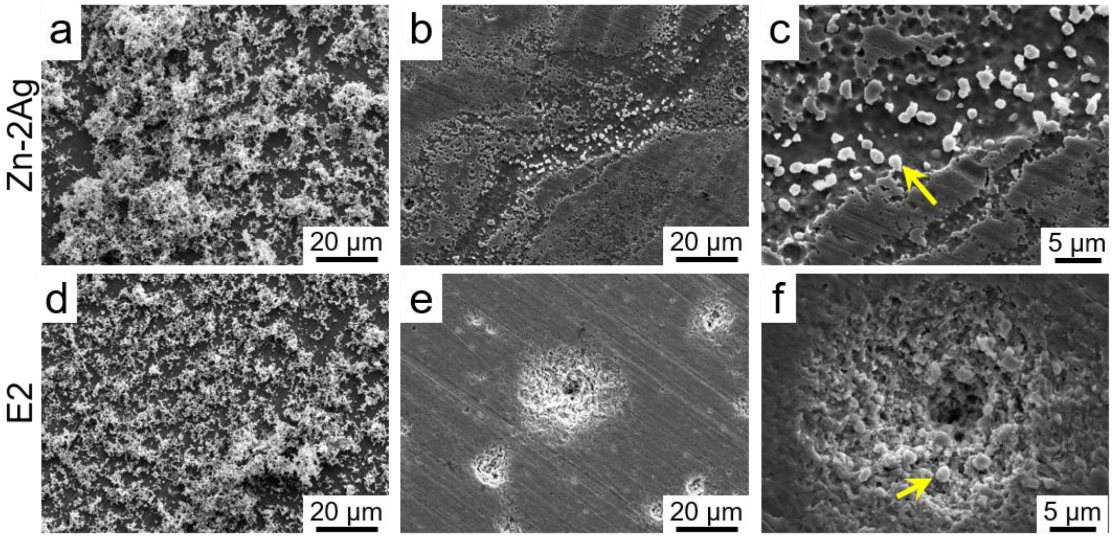

Fig. 10. SEM images of the Zn-2Ag and E2 sample surfaces after 10 days of immersion in Hanks' solution: before (a, d) and after (b-c, e-f) the removal of the corrosion products. Yellow arrows indicate the non-degraded $AgZn_3$ phase.

Fig. 10 shows the SEM images of the surfaces of Zn-2Ag and E2 with the corrosion products after the immersion test. The corrosion layer formed on both studied surfaces was homogeneous, as shown in **Fig. 10 a, d.** The elemental analysis performed by EDS detected Zn, Ca, C, O, P, and Cl, from the precipitation of calcium phosphate minerals, Zn-carbonates, phosphates, oxides, and Ag-chloride as predicted by the Pourbaix diagrams [25,29]. Besides, EDS mapping indicated the presence of Zn and Ag at the underlying metallic surface. SEM images of the corroded surfaces after the corrosion layer removal showed similar corrosion features for Zn-2Ag (**Fig. 10 b, c**) and E2 (**Fig. 10 e, f**), with the most stable $AgZn_3$ phase surrounded by the anodic degradation of the Zn matrix.

III.6. Bacterial response

The bacterial response was evaluated after 3 h of culture with *S. Aureus* on inert c.p. Ti and Zn as controls and on the investigated Zn-2Ag, and E2 samples. **Fig. 11a-d** shows the confocal images obtained after the live-dead assay. Ti surface was thoroughly covered by bacteria (**Fig. 11a**), exceeding the maximum limit for CFU quantification at the tested conditions. On the other hand, the reduced bacteria attachment to Zn-based surfaces (**Fig. 11b-d**) indicated a noticeable antibacterial activity compared with Ti. In addition, the antibacterial performance of Zn-2Ag significantly reduced the bacterial attachment, from (2.4 ± 1.1) x10^7 CFU/mm^2 of the Zn surface (**Fig. 11b**) to (7.8 ± 5.8) x10^6 CFU/mm^2 of the Zn-2Ag alloy. Surprisingly, the ECAP deformation accentuated the antibacterial effect (**Fig. 11d**), with a noticeable CFU reduction down to (7.6 ± 5.9) x10^5 CFU/mm^2.

Fig. 11e-h includes the optical images of the metallic surfaces after the bacterial adhesion test and subsequent cleaning with ethanol and ultrasounds. The Ti surface remained intact, according to its inert nature (**Fig. 11e**). In contrast, degradation signs could be observed in the Zn-based samples (**Fig. 11f-h**). Pure Zn and E2 samples showed distributed degradation pits, whereas the Zn-2Ag presented a heterogeneously degraded surface with a pronounced degradation compared to the studied series.

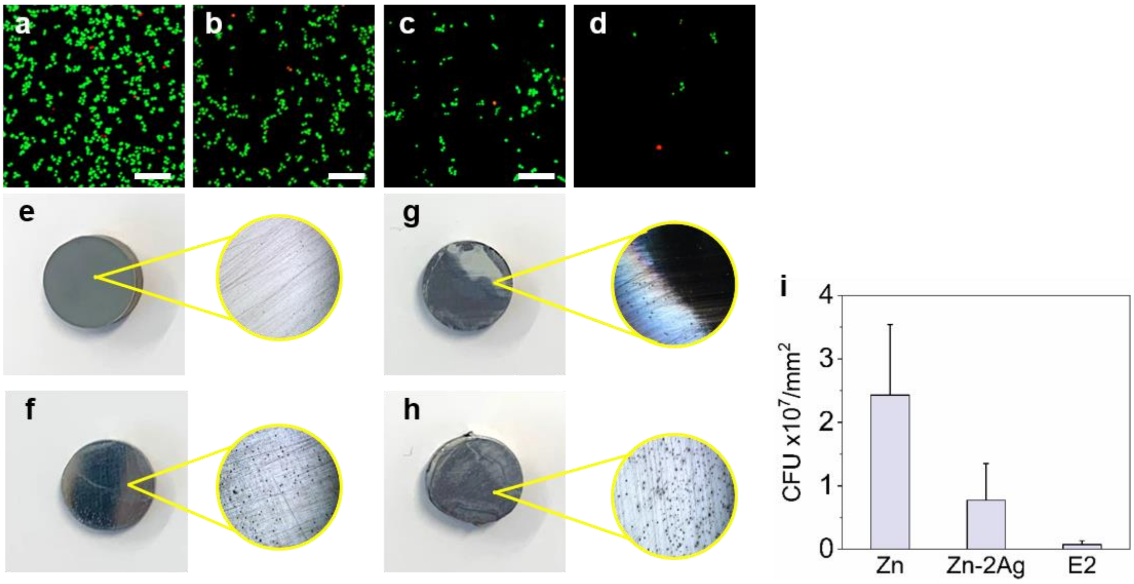

Fig. 11. Bacterial adhesion tests of the studied surfaces cultured with *S. Aureus* after 3 h of incubation. Live-dead staining of *S. Aureus* incubated onto (a) Ti, (b) Zn, (c) Zn-2Ag, and (d) E2. Scale bar: 50 μm. Images of the surfaces after the adhesion test and subsequent cleaning: (e) Ti, (f) Zn, (g) Zn-2Ag, and (h) E2. (i) Quantification of attached bacteria to the surfaces. Ti is not included since it exceeded the maximum CFU for quantification.

IV. Discussion

Biodegradable metals emerged to overcome the drawbacks of conventional implants, including inflammation, long-term consequences, or second surgeries for their removal [30,31]. Among them, Zn stands out due to its biocompatibility and degradation rate [32]. However, its insufficient mechanical properties force it to alloy Zn with other elements, strengthening the material *via* solid solution, grain refining, and precipitation hardening, but inevitably altering the degradation mechanisms and affecting the biological behaviour of the alloys [33]. Thus, extensive research is focused on modifying the secondary phases' distribution to obtain a homogeneous microstructure [34,35]. In this regard, mechanical isotropy directly affects mechanical performance, enhancing the safety of the implants and increasing implantation tolerance [36–38]. Several studies have been performed to control anisotropy or to fabricate isotropic structures [39,40]. In this work, two ECAP cycles have been successfully applied to a Zn-2Ag alloy to obtain a homogeneous UFG structure. The excellent starting formability of the material allowed two ECAP passes to be performed at room temperature avoiding any failure [41], hence providing an additional degree of freedom for the control of the final microstructure. The as-received Zn-2Ag alloy developed UFG microstructure with randomly distributed grain orientation after the ECAP process. Homogeneous nanohardness (**Fig. 6**) and elastic modulus (**Fig. 7**) were reported for both E1 and E2 samples. The direct influence of the secondary phases in the final mechanical performance in binary Zn-based alloys has been previously reported [33]. Here, the average results of both elastic modulus and hardness are calculated without considering the presence of two phases since the equipment was not sensible enough to distinguish between the Zn matrix and the small areas occupied by the $AgZn_3$ phase. The mechanical properties of hexagonal-closed pack (hcp) alloys have been reported to be closely related to the texture [42]. However, despite the homogeneous texture observed in E1 and E2, Vickers-hardness measurements evidenced the isotropic response only for E2 (**Fig. 8a**), suggesting that the grain size and crystal orientation may be fundamental in the mechanical behaviour of the samples. As previously reported by Bednarczyk *et al.* [5], the ECAP process is almost ineffective in strengthening hcp materials but induces a dramatic change in grain size and orientation. Indeed, as-received extruded rods exhibited a sharp texture. The low crystal symmetry in hcp structures results in the activation of only one slip system per grain, diminishing the possibility of dislocations slip within the grains and thus increasing material strength [43]. After ECAP, the crystal refinement and orientation redistribution result in lower texture, hence easier slip of dislocations which better accommodates the macroscopic deformation resulting in lower YS, UTS, and exceptional fracture elongation (**Fig. 8**) [44,45]. Nonetheless, the obtained values of YS and UTS are still superior to those of actual bioresorbable polymeric sutures [46]. This superior mechanical strength would avoid complex multi-braid structures and related bacterial infection risks. Moreover, the obtained high elongation at fracture is supposed to provide good formability, good handling, and knot security [47].

Microstructural refinement has been widely reported to improve corrosion protection by reducing localized corrosion [8,48]. This is due to the refinement and homogeneous distribution of the secondary phases, which minimizes its cathodic capacity, and hence the possible galvanic pairs lose their effectiveness [7,8]. On the other side, grain refinement could accelerate corrosion by the increased Gibb’s free energy related to grain boundaries surface, whose concentration is higher in UFG structures [49]. These two effects might also compensate for each other, leaving the corrosion rate of the SPD alloy substantially unchanged. In our degradation studies in Hanks' solution, Zn-2Ag and E2 samples exhibited similar corrosion parameters (**Table 2**), but the ICP-MS measurements provided some differences regarding the ionic release of metallic species (**Table 3**). The Zn^{2+} release detected for both samples is in the physiological range (2 – 15 μM) [50], with a final total concentration of 3.1 μM and 2.1 μM for E2 and Zn-2Ag, respectively. Interestingly, the Ag^+ release seemed to be hindered after the ECAP process. Since no observable changes were noticed regarding the area of the $AgZn_3$ phase, this hindering may be attributed to the grain refinement. According to the Zn-Ag phase diagram, the solid solubility of Ag in the Zn matrix is around 1.67 wt.% at room temperature [51], and above this concentration, the $AgZn_3$ precipitates. As observed in the immersion test, the $AgZn_3$ phase is non-degradable (**Fig. 10**); thus, the detected released Ag^+ would be related to the Ag dissolved into the Zn matrix. The Zn-2Ag exhibited a burst release on the first day and fluctuating Ag^+ concentrations ranging from 3 to 12 % of the total measured ion release in the following days. (**Table 3**). However, E2 presented a more homogeneous release of 1 – 2 % of Ag^+ through the experiment, suggesting a better Ag distribution along the surface after ECAP. In this manner, the percentage of released Zn^{2+} in the E2 increased to 98 – 99 %. The excessive administration of silver may have genotoxic effects, but further studies would be needed to assess its carcinogenic potential [52,53].

Lately, Guillory *et al.* [54] observed a positive *in vivo* performance of Zn-based wires with 4 wt.% of Ag implanted into female Sprague Dawley rats for 6 months. Thus, the amount of delivered Ag^+ of the Zn-2Ag series should not have a cytotoxic effect. Finally, the degradation time for actual biomaterials used for wound closure is 4 – 6 weeks, for PLA/PGA 75/25 and PGA, or more than 1.5-5 years, for PLA [55]. Assuming a constant corrosion rate of 0.090 mm/year (**Table 2**), a typical USP 5-0 suture (Ø 100 μm) [56] would degrade at an intermediate time of 6 months after implantation.

Bacterial infection is a worldwide concern due to the medical resistance developed by bacterial strains such as *S. aureus*, which is the most common strain in the skin, soft tissue, bone, joints, and device-associated infections [15]. Lately, the investigation focused on new antibacterial approaches for biomaterials has attracted global interest. The use of copper or silver as antibacterial agents has been investigated for different biomaterials [16]. Ti is a common biomaterial used for wound suture applications; however, Ti requires to be treated to avoid possible bacterial infections [17]. A possible strategy includes the introduction of ZnO onto Ti-based materials due to its well-known antibacterial effect properties [57–59]. Therefore, the reduced number of bacteria attached to Zn-based surfaces (**Fig. 11**) may be related to the presence of a ZnO in its natural passivation layer. As expected, the presence of Ag in the Zn-Ag alloys reduced the bacterial attachment. The minimum inhibitory concentration (MIC) reported of colloidal silver is 1.39 mg/dL [60], and the reported MIC for silver nanoparticles 0.62.5 mg/dL [61]. Both values are much superior to the total Ag^+ detected at the immersion test; thus, the decreased bacterial adhesion of Zn-Ag alloys was not related to Ag^+ diffusion mechanisms but to the Ag presence on the metallic surfaces and its antibacterial effect by contact. Surprisingly, the antibacterial activity was considerably enhanced after ECAP processing. Previous reports have shown lower bacterial adhesion to polymeric and thus softer surfaces [62], but the opposite trend in polymeric materials has also been published [63]. Nonetheless, most studies refer to polymeric surfaces that intrinsically offer mesh-like structures in which other factors, such as porosity, may affect bacterial adhesion [62]. Thus, surface hardness and bacterial adhesion relationship would require further investigation. Regarding this, the supposition of a better Ag distribution after ECAP would contribute to the excellent antibacterial effect observed in the E2 sample.

Another important observation was the different aspect of the degraded Zn-2Ag and E2 sample surfaces after the bacterial adhesion test (**Fig. 11**), in contrast to the similar corroded surface after corrosion tests in Hanks' solution. In previous studies, the changing degradation behaviour of Zn surfaces depending on the immersion media has been studied [64,65]. Furthermore, an extensive characterization of Zn and Zn-4Ag in different corrosive media has been performed by Sikora-Janinska *et al.* [66], in which organic species were reported to form a passivation layer and protect the surfaces from further corrosion. Biodegradable implants may avoid bacterial infection by providing a non-stable surface for bacterial adhesion[67]. However, the accumulation of bacteria onto the degraded and rougher surfaces of Zn-based alloys has been previously reported [33]. In connection with our bacterial test, the more degraded surface of Zn-2Ag may limit the antibacterial effect, whereas the uniform surface degradation of E2 provided a smoother surface to which bacteria hardly attached, contributing to the enhancement of the antibacterial activity.

V. Conclusions

In this work, Zn-2Ag was successfully subjected to ECAP at room temperature. The microstructure of the samples consisted of a Zn matrix and a secondary $AgZn_3$ phase. EBSD results confirmed the generation of UFG structures after ECAP with randomly distributed texture and similar size and distribution of second phases for E1 and E2 samples. Nanoindentation maps suggested isotropic mechanical properties of the ECAP-processed samples. However, Vickers measurements only confirmed the isotropy for E2, demonstrating the influence of the grain refinement on the nano- and micro-mechanical performance of the material. Lower UTS and YS with higher elongation have been reported after ECAP, following previous studies on hcp materials. Similar corrosion rates were observed for Zn-2Ag and E2 in Hanks' solution, with a released concentration of Zn^{2+} among the physiological range of 2 – 15 mM. The more homogeneous Ag^+ release of the E2 sample was attributed to the better Ag distribution along the Zn matrix after the ECAP process. The released Ag^+ was below the MIC for *S. Aureus;* thus, the antibacterial effect was attributed to the bacterial contact with the Ag-containing surfaces. Moreover, the better Ag distribution in E2 and its uniformly degraded surface after the bacterial adhesion test would contribute to the excellent antibacterial performance of the sample. In summary, the ECAP process provided mechanical isotropy, good formability, and exceptional antibacterial activity to biodegradable Zn-2Ag, being a potential processing route candidate for the manufacturing of wires for wound closure applications.

VI. References

[1] J.J.D. Venezuela, S. Johnston, M.S. Dargusch, The Prospects for Biodegradable Zinc in Wound Closure Applications, Adv Healthc Mater. 8 (2019) 1–15. https://doi.org/10.1002/adhm.201900408.

[2] C. Li, C. Guo, V. Fitzpatrick, A. Ibrahim, M.J. Zwierstra, P. Hanna, A. Lechtig, A. Nazarian, S.J. Lin, D.L. Kaplan, Design of biodegradable, implantable devices towards clinical translation, Nat Rev Mater. 5 (2020) 61–81. https://doi.org/10.1038/s41578-019-0150-z.

[3] N. Yang, J. Venezuela, S. Almathami, M. Dargusch, Zinc-nutrient element based alloys for absorbable wound closure devices fabrication: Current status, challenges, and future prospects, Biomaterials. 280 (2022). https://doi.org/10.1016/j.biomaterials.2021.121301.

[4] H. Guo, R.H. Cao, Y.F. Zheng, J. Bai, F. Xue, C.L. Chu, Diameter-dependent in vitro performance of biodegradable pure zinc wires for suture application, J Mater Sci Technol. 35 (2019) 1662–1670. https://doi.org/10.1016/j.jmst.2019.03.006.

[5] W. Bednarczyk, M. Wątroba, J. Kawałko, P. Bała, Can zinc alloys be strengthened by grain refinement? A critical evaluation of the processing of low-alloyed binary zinc alloys using ECAP, Materials Science and Engineering A. 748 (2019) 357–366. https://doi.org/10.1016/j.msea.2019.01.117.

[6] D.N. Awang Sh'Ri, Z.S. Zahari, A. Yamamoto, Effect of ecap die angle on mechanical properties and biocompatibility of ss316l, Metals (Basel). 11 (2021). https://doi.org/10.3390/met11101513.

[7] J.X. Chen, X.Y. Zhu, L.L. Tan, K. Yang, X.P. Su, Effects of ECAP Extrusion on the Microstructure, Mechanical Properties and Biodegradability of Mg–2Zn–xGd–0.5Zr Alloys, Acta Metallurgica Sinica (English Letters). 34 (2021) 205–216. https://doi.org/10.1007/s40195-020-01136-7.

[8] S. v. Dobatkin, E.A. Lukyanova, N.S. Martynenko, N.Y. Anisimova, M. v. Kiselevskiy, M. v. Gorshenkov, N.Y. Yurchenko, G.I. Raab, V.S. Yusupov, N. Birbilis, G.A. Salishchev, Y.Z. Estrin, Strength, corrosion resistance, and biocompatibility of ultrafine-grained Mg alloys after different modes of severe plastic deformation, in: IOP Conf Ser Mater Sci Eng, Institute of Physics Publishing, 2017. https://doi.org/10.1088/1757-899X/194/1/012004.

[9] X. Zhuo, Y. Wu, J. Ju, H. Liu, J. Jiang, Z. Hu, J. Bai, F. Xue, Recent progress of novel biodegradable zinc alloys: from the perspective of strengthening and toughening, Journal of Materials Research and Technology. 17 (2022) 244–269. https://doi.org/10.1016/j.jmrt.2022.01.004.

[10] W. Bednarczyk, J. Kawałko, M. Wątroba, P. Bała, Achieving room temperature superplasticity in the Zn-0.5Cu alloy processed via equal channel angular pressing, Materials Science and Engineering A. 723 (2018) 126–133. https://doi.org/10.1016/j.msea.2018.03.052.

[11] F. Gottrup, A. Melling, D.A. Hollander, An overview of surgical site infections: aetiology, incidence and risk factors; An overview of surgical site infections: aetiology, incidence and risk factors, n.d.

[12] J.W. Alexander, J.S. Solomkin, M.J. Edwards, Updated recommendations for control of surgical site infections, Ann Surg. 253 (2011) 1082–1093. https://doi.org/10.1097/SLA.0b013e31821175f8.

[13] I. Ahmed, A.J. Boulton, S. Rizvi, W. Carlos, E. Dickenson, N.A. Smith, M. Reed, The use of triclosan-coated sutures to prevent surgical site infections: A systematic review and meta-analysis of the literature, BMJ Open. 9 (2019). https://doi.org/10.1136/bmjopen-2019-029727.

[14] D.J. Hess, M.J. Henry-Stanley, C.L. Wells, Gentamicin promotes staphylococcus aureus biofilms on silk suture, Journal of Surgical Research. 170 (2011) 302–308. https://doi.org/10.1016/j.jss.2011.06.011.

[15] A. Hassoun, P.K. Linden, B. Friedman, Incidence, prevalence, and management of MRSA bacteremia across patient populations-a review of recent developments in MRSA management and treatment, Crit Care. 21 (2017) 211. https://doi.org/10.1186/s13054-017-1801-3.

[16] T. Baygar, N. Sarac, A. Ugur, I.R. Karaca, Antimicrobial characteristics and biocompatibility of the surgical sutures coated with biosynthesized silver nanoparticles, Bioorg Chem. 86 (2019) 254–258. https://doi.org/10.1016/j.bioorg.2018.12.034.

[17] S. Ferraris, S. Spriano, Antibacterial titanium surfaces for medical implants, Materials Science and Engineering C. 61 (2016) 965–978. https://doi.org/10.1016/j.msec.2015.12.062.

[18] Y. Iwahashi, J. Wang, Z. Horita, M. Nemoto, T.G. Langdon, Principle of Equal-Channel Angular Pressing for the processing of ultra-fine grained materials, Scr Mater. 35 (1996) 143–146. https://doi.org/10.1002/art.21843.

[19] V.M. Segal, Equal channel angular extrusion: From macromechanics to structure formation, Materials Science and Engineering A. 271 (1999) 322–333. https://doi.org/10.1016/s0921-5093(99)00248-8.

[20] ASTM E8, ASTM E8/E8M standard test methods for tension testing of metallic materials, Annual Book of ASTM Standards 4. (2010) 1–27. https://doi.org/10.1520/E0008.

[21] ASTM G5-14. Standard Reference Test Method for Making Potentiodynamic Anodic Polarization Measurements, Annual Book of ASTM Standards. (2014). https://doi.org/10.1520/G0005-14.2.

[22] ASTM G102-89, 2015. Standard Practice for Calculation of Corrosion Rates and Related Information from Electrochemical Measurements, Annual Book of ASTM Standards. (2015). https://doi.org/10.1520/G0102-89R15E01.2.

[23] ASTM G31-72, 2004. Standard Practice for Laboratory Immersion Corrosion Testing of Metals, Annual Book of ASTM Standards. (2004). https://doi.org/10.1520/G0031-72R04.2.

[24] ISO 8407:2009. Corrosion of metals and alloys — Removal of corrosion products from corrosion test specimens, International Organization for Standardization. (2009).

[25] M. Sikora-Jasinska, E. Mostaed, A. Mostaed, R. Beanland, D. Mantovani, M. Vedani, Fabrication, mechanical properties and in vitro degradation behavior of newly developed Zn-Ag alloys for degradable implant applications, Materials Science and Engineering C. 77 (2017) 1170–1181. https://doi.org/10.1016/j.msec.2017.04.023.

[26] P. Tang, J. Feng, Z. Wan, X. Huang, S. Yang, L. Lu, X. Zhong, Influence of grain orientation on hardness anisotropy and dislocation behavior of AlN ceramic in nanoindentation, Ceram Int. 47 (2021) 20298–20309. https://doi.org/10.1016/j.ceramint.2021.04.038.

[27] C.Y. Hu, X.L. Wan, Y.J. Zhang, X.T. Deng, Z.D. Wang, R.D.K. Misra, The synergistic effect of grain boundary and grain orientation on micro-mechanical properties of austenitic stainless steel, J Mech Behav Biomed Mater. 118 (2021). https://doi.org/10.1016/j.jmbbm.2021.104473.

[28] G.K. Levy, J. Goldman, E. Aghion, The prospects of zinc as a structural material for biodegradable implants—a review paper, Metals (Basel). 7 (2017) 1–18. https://doi.org/10.3390/met7100402.

[29] K.B. Törne, Zn – Mg and Zn – Ag degradation mechanism under biologically relevant conditions, Surf Innov. (2017) 1–12.

[30] Y.F. Zheng, X.N. Gu, F. Witte, Biodegradable metals, Materials Science and Engineering R. 77 (2014) 1–34. https://doi.org/10.1007/978-1-4614-3942-4_5.

[31] H. Li, Y. Zheng, L. Qin, Progress of biodegradable metals, Progress in Natural Science: Materials International. 24 (2014) 414–422. https://doi.org/10.1016/j.pnsc.2014.08.014.

[32] H.S. Han, S. Loffredo, I. Jun, J. Edwards, Y.C. Kim, H.K. Seok, F. Witte, D. Mantovani, S. Glyn-Jones, Current status and outlook on the clinical translation of biodegradable metals, Materials Today. 23 (2019) 57–71. https://doi.org/10.1016/j.mattod.2018.05.018.

[33] C. García-Mintegui, L.C. Córdoba, J. Buxadera-Palomero, A. Marquina, E. Jiménez-Piqué, M.P. Ginebra, J.L. Cortina, M. Pegueroles, Zn-Mg and Zn-Cu alloys for stenting applications: From nanoscale mechanical characterization to in vitro degradation and biocompatibility, Bioact Mater. 6 (2021) 4430–4446. https://doi.org/10.1016/j.bioactmat.2021.04.015.

[34] D.W.Y. Toong, J.C.K. Ng, Y. Huang, P.E.H. Wong, H.L. Leo, S.S. Venkatraman, H.Y. Ang, Bioresorbable metals in cardiovascular stents: Material insights and progress, Materialia (Oxf). 12 (2020) 100727. https://doi.org/10.1016/j.mtla.2020.100727.

[35] S. Prithivirajan, S. Narendranath, V. Desai, Analysing the combined effect of crystallographic orientation and grain refinement on mechanical properties and corrosion behaviour of ECAPed ZE41 Mg alloy, Journal of Magnesium and Alloys. 8 (2020) 1128–1143. https://doi.org/10.1016/j.jma.2020.08.015.

[36] X. Yan, Q. Li, S. Yin, Z. Chen, R. Jenkins, C. Chen, J. Wang, W. Ma, R. Bolot, R. Lupoi, Z. Ren, H. Liao, M. Liu, Mechanical and in vitro study of an isotropic Ti6Al4V lattice structure fabricated using selective laser melting, J Alloys Compd. 782 (2019) 209–223. https://doi.org/10.1016/j.jallcom.2018.12.220.

[37] L. Wang, J. Kang, C. Sun, D. Li, Y. Cao, Z. Jin, Mapping porous microstructures to yield desired mechanical properties for application in 3D printed bone scaffolds and orthopaedic implants, Mater Des. 133 (2017) 62–68. https://doi.org/10.1016/j.matdes.2017.07.021.

[38] R. Hedayati, M. Sadighi, M. Mohammadi-Aghdam, A.A. Zadpoor, Analytical relationships for the mechanical properties of additively manufactured porous biomaterials based on octahedral unit cells, Appl Math Model. 46 (2017) 408–422. https://doi.org/10.1016/j.apm.2017.01.076.

[39] L. Wang, J. Kang, C. Sun, D. Li, Y. Cao, Z. Jin, Mapping porous microstructures to yield desired mechanical properties for application in 3D printed bone scaffolds and orthopaedic implants, Mater Des. 133 (2017) 62–68. https://doi.org/10.1016/j.matdes.2017.07.021.

[40] J. Feng, B. Liu, Z. Lin, J. Fu, Isotropic octet-truss lattice structure design and anisotropy control strategies for implant application, Mater Des. 203 (2021). https://doi.org/10.1016/j.matdes.2021.109595.

[41] S. Liu, D. Kent, H. Zhan, N. Doan, M. Dargusch, G. Wang, Dynamic recrystallization of pure zinc during high strain-rate compression at ambient temperature, Materials Science and Engineering A. 784 (2020) 139325. https://doi.org/10.1016/j.msea.2020.139325.

[42] S.Ya. Betsofen, I.A. Grushin, M.I. Gordeeva, K.A. Speranskii, Inverse Pole Figures and the Anisotropy of the Properties of HCP Alloys, Russian Metallurgy (Metally). 2022 (2022) 355–362. https://doi.org/10.1134/S0036029522040048.

[43] T. Matsunaga, T. Kameyama, K. Takahashi, E. Sato, Constitutive relation for ambient-temperature creep in hexagonal close-packed metals, Mater Trans. 50 (2009) 2858–2864. https://doi.org/10.2320/matertrans.M2009223.

[44] E. Mostaed, M. Hashempour, A. Fabrizi, D. Dellasega, M. Bestetti, F. Bonollo, M. Vedani, Microstructure, texture evolution, mechanical properties and corrosion behavior of ECAP processed ZK60 magnesium alloy for biodegradable applications, J Mech Behav Biomed Mater. 37 (2014) 307–322. https://doi.org/10.1016/j.jmbbm.2014.05.024.

[45] E. Mostaed, A. Fabrizi, D. Dellasega, F. Bonollo, M. Vedani, Microstructure, mechanical behavior and low temperature superplasticity of ECAP processed ZM21 Mg alloy, J Alloys Compd. 638 (2015) 267–276. https://doi.org/10.1016/j.jallcom.2015.03.029.

[46] B. Joseph, A. George, S. Gopi, N. Kalarikkal, S. Thomas, Polymer sutures for simultaneous wound healing and drug delivery – A review, Int J Pharm. 524 (2017) 454–466. https://doi.org/10.1016/j.ijpharm.2017.03.041.

[47] M. Asgari, R. Hang, C. Wang, Z. Yu, Z. Li, Y. Xiao, Biodegradable metallicwires in dental and orthopedic applications: A review, Metals (Basel). 8 (2018) 1–32. https://doi.org/10.3390/met8040212.

[48] P. jun Wang, L. wei Ma, X. qun Cheng, X. gang Li, Influence of grain refinement on the corrosion behavior of metallic materials: A review, International Journal of Minerals, Metallurgy and Materials. 28 (2021) 1112–1126. https://doi.org/10.1007/s12613-021-2308-0.

[49] M.W. Vaughan, A.I. Karayan, A. Srivastava, B. Mansoor, J.M. Seitz, R. Eifler, I. Karaman, H. Castaneda, H.J. Maier, The effects of severe plastic deformation on the mechanical and corrosion characteristics of a bioresorbable Mg-ZKQX6000 alloy, Materials Science and Engineering C. 115 (2020). https://doi.org/10.1016/j.msec.2020.111130.

[50] K.L. Chang, T.C. Hung, B.S. Hsieh, Y.H. Chen, T.F. Chen, H.L. Cheng, Zinc at pharmacologic concentrations affects cytokine expression and induces apoptosis of human peripheral blood mononuclear cells, Nutrition. 22 (2006) 465–474. https://doi.org/10.1016/j.nut.2005.11.009.

[51] E. Mostaed, M. Sikora-Jasinska, J.W. Drelich, M. Vedani, Zinc-based alloys for degradable vascular stent applications, Acta Biomater. 71 (2018) 1–23. https://doi.org/10.1016/j.actbio.2018.03.005.

[52] N. Hadrup, A.K. Sharma, K. Loeschner, Toxicity of silver ions, metallic silver, and silver nanoparticle materials after in vivo dermal and mucosal surface exposure: A review, Regulatory Toxicology and Pharmacology. 98 (2018) 257–267. https://doi.org/10.1016/j.yrtph.2018.08.007.

[53] A.B.G. Lansdown, A pharmacological and toxicological profile of silver as an antimicrobial agent in medical devices, Adv Pharmacol Sci. 2010 (2010). https://doi.org/10.1155/2010/910686.

[54] R.J. Guillory, E. Mostaed, A.A. Oliver, L.M. Morath, E.J. Earley, K.L. Flom, T.M. Kolesar, A. Mostaed, H.D. Summers, M.P. Kwesiga, J.W. Drelich, K.D. Carlson, D. Dragomir-Daescu, J. Goldman, Improved biocompatibility of Zn–Ag-based stent materials by microstructure refinement, Acta Biomater. (2022). https://doi.org/10.1016/j.actbio.2022.03.047.

[55] P. Gentile, V. Chiono, I. Carmagnola, P. v. Hatton, An overview of poly(lactic-co-glycolic) Acid (PLGA)-based biomaterials for bone tissue engineering, Int J Mol Sci. 15 (2014) 3640–3659. https://doi.org/10.3390/ijms15033640.

[56] D. L. Dunn, Wound Closure Manual, 2005.

[57] T. Sun, H. Hao, W. ting Hao, S. min Yi, X. peng Li, J. rong Li, Preparation and antibacterial properties of titanium-doped ZnO from different zinc salts, Nanoscale Res Lett. 9 (2014) 1–11. https://doi.org/10.1186/1556-276X-9-98.

[58] M. Roknian, A. Fattah-alhosseini, S.O. Gashti, M.K. Keshavarz, Study of the effect of ZnO nanoparticles addition to PEO coatings on pure titanium substrate: Microstructural analysis, antibacterial effect and corrosion behavior of coatings in Ringer’s physiological solution, J Alloys Compd. 740 (2018) 330–345. https://doi.org/10.1016/j.jallcom.2017.12.366.

[59] B. Abebe, E.A. Zereffa, A. Tadesse, H.C.A. Murthy, A Review on Enhancing the Antibacterial Activity of ZnO: Mechanisms and Microscopic Investigation, Nanoscale Res Lett. 15 (2020). https://doi.org/10.1186/s11671-020-03418-6.

[60] E.M. Petrus, S. Tinakumari, L.C. Chai, A. Ubong, N. Chai, R. Son, A study on the minimum inhibitory concentration and minimum bactericidal concentration of Nano Colloidal Silver on food-borne pathogens, 2011.

[61] P. Parvekar, J. Palaskar, S. Metgud, R. Maria, S. Dutta, The minimum inhibitory concentration (MIC) and minimum bactericidal concentration (MBC) of silver nanoparticles against Staphylococcus aureus , Biomater Investig Dent. 7 (2020) 105–109. https://doi.org/10.1080/26415275.2020.1796674.

[62] Y. Cheng, G. Feng, C.I. Moraru, Micro-and nanotopography sensitive bacterial attachment mechanisms: A review, Front Microbiol. 10 (2019). https://doi.org/10.3389/fmicb.2019.00191.

[63] Y. Wang, A. Guan, I. Isayeva, K. Vorvolakos, S. Das, Z. Li, K.S. Phillips, Interactions of Staphylococcus aureus with ultrasoft hydrogel biomaterials, Biomaterials. 95 (2016) 74–85. https://doi.org/10.1016/j.biomaterials.2016.04.005.

[64] K. Törne, M. Larsson, A. Norlin, J. Weissenrieder, Degradation of zinc in saline solutions, plasma, and whole blood, J Biomed Mater Res B Appl Biomater. 104 (2016) 1141–1151. https://doi.org/10.1002/jbm.b.33458.

[65] K. Beaussant Törne, A. Örnberg, J. Weissenrieder, Characterization of the protective layer formed on zinc in whole blood, Electrochim Acta. 258 (2017) 1476–1483. https://doi.org/10.1016/j.electacta.2017.12.018.

[66] M. Sikora-Jasinska, J. Goldman, E. Mostaed, J.W. Drelich, Albumins inhibit the corrosion of absorbable Zn alloys at initial stages of degradation, Surf Innov. 8 (2020) 234–249. https://doi.org/10.1680/jsuin.19.00063.

[67] A.A. Barros, C. Oliveira, E. Lima, A.R.C. Duarte, K. Healy, R.L. Reis, 7.41 Ureteral stents technology: Biodegradable and drug-eluting perspective, in: Comprehensive Biomaterials II, Elsevier, 2017: pp. 793–812. https://doi.org/10.1016/B978-0-12-803581-8.10189-4.

Concluding remarks

Conclusions

Bioresorbable implants arose to overcome some limitations of conventional inert implants, such as second surgeries for implant removal, long-term complications like late-stent thrombosis, or their use in paediatric populations where the implant does not grow with the patient. However, the intertwined effects of biodegradation, mechanical properties, and biological response on these materials comprise a challenge to unravel through the surface and structural modifications.

This PhD Thesis aimed to provide more knowledge on Zn-Mg, Zn-Cu, and Zn-Ag alloys, their corrosion behaviour, and their biological response as potential materials for bioresorbable metallic implants for different biomedical applications.

The results displayed and analysed in the previous chapters, summarized and highlighted in the following conclusions, expanded our comprehension of the field that could lead to a more rationalized selection, modification, and design of bioresorbable metallics materials for biomedical applications.

- *Zn-Mg and Zn-Cu alloys for cardiovascular applications*

The effect of precipitated secondary phases, Zn+Mg_2Zn_{11} or ε–$CuZn_5$, into the Zn matrix of Zn-Mg and Zn-Cu alloys was relevant in mechanical, corrosion, and biological behaviour. The nanoindentation studies confirmed the direct relation of the secondary phases and their volume fraction on the mechanical reinforcement of Zn. Zn-Mg and Zn-Cu systems showed better mechanical properties for the lower volume fraction of the secondary phase: Zn-1Mg showed a lower fracture elongation compared to Zn-0.5Mg, and Zn-5Cu did not provide significant improvement in UTS or YS compared to Zn-3Cu. Corrosion studies showed similar degradation behaviour for Zn and Zn-0.5Mg alloy, while Zn-1Mg exhibited a thicker corrosion layer. Moreover, the galvanic corrosion in Zn-Cu alloys was more pronounced for the Zn-5Cu alloy. Therefore, a higher secondary phase volume fraction led to more robust galvanic pairs favouring galvanic corrosion mechanisms in contrast to the homogeneous degradation of unalloyed Zn. Bacterial studies suggested that bacteria preferentially attached to the corrosion products, increasing the risk of further infections. Furthermore, the *in vitro* assays indicated cytotoxicity and the impossibility of HAoECs adhering to the degrading surfaces. Finally, the high ε-$CuZn_5$ volume fraction of Zn-Cu alloys led to severe galvanic corrosion, seriously affecting degradation behaviour and biocompatibility. Generally, the results suggested that it would be more appropriate to use low-alloyed Zn and the imperative to find a compromise between mechanical reinforcement and galvanic corrosion.

- *Zn-Ag alloys with antibacterial properties*

The effect of the secondary $AgZn_3$ phase on the mechanical properties, degradation behaviour, and bacterial activity of Zn-Ag alloys was corroborated. The precipitation of the $AgZn_3$ phase enhanced the UTS, YS, and elongation at fracture compared with pure Zn. However, the higher $AgZn_3$ volume fraction in Zn-4Ag led to a slight softening of the alloy. Regarding corrosion, Zn-2Ag presented a more homogeneous degradation behaviour than Zn-4Ag, attributed to the lower $AgZn_3$ volume fraction. The bacterial activity of the Zn-Ag alloys was related to the Ag content and the degradation behaviour. In this regard, the Ag-alloyed materials showed a lower adherence of bacteria compared to pure Zn, demonstrating the antibacterial activity of Ag. Moreover, the degrading surfaces avoided biofilm formation and subsequent bacterial infection risks. However, the galvanic degradation mechanisms observed in Zn-4Ag harmed the antibacterial effect, where bacteria could penetrate through the corrosion pits. In conclusion, lower alloyed Zn offered better mechanical reinforcement, more homogeneous degradation, and higher antibacterial activity.

- *Zn-Mg and Zn-Ag surface modification for degradation control and endothelialisation enhancement*

Based on previous conclusions, Zn–0.5Mg and Zn–2Ag were selected as alloys with a lower volume fraction of secondary phases with better mechanical and biological properties to improve their performance for cardiovascular stents. To that end, a dual coating was implemented on the surfaces. First, a well-adhered PCL coating avoided early degradation and provided surface stability. Then, the PCL layer was successfully functionalized with synthetised RGD, REDV, and RGD-REDV platform. HUVECs could satisfactorily attach to every functionalized surface, where the RGD-REDV platform showed increased cell number. Thus, this dual-capacity coating showed promising results for the re-endothelialisation of Zn alloys.

- *Zn-Ag severe plastic deformation for degradation control and enhanced antibacterial properties*

Zn–2Ag was successfully submitted to two cycles of ECAP processing, obtaining a UFG microstructure where the $AgZn_3$ secondary phase was not observably affected and maintained the same distribution. The mechanical analysis reported high dependence of the mechanical properties on the texture and grain size, showing anisotropy with the grain orientation. After two ECAP cycles, the alloy presented isotropic nano- and micro-mechanical properties. Moreover, the study confirmed the antibacterial mechanism against *S. aureus* of the samples by contact and not by diffusion mechanisms. The exceptional antibacterial activity after ECAP suggested that the antibacterial effect was due to the homogeneous distributed Ag into the Zn matrix and the more uniform surface degradation.

Zn–based materials exhibit interesting degradation properties as bioresorbable implants. This PhD Thesis contributed to the fundamental knowledge of the field, where the analysis of Mg, Cu, and Ag as alloying elements for Zn provided some clues into the proper chemical composition for the intended biomedical applications. The different alloying element content is crucial for mechanical and degradation behaviour. Furthermore, considering a protective coating layer to control early degradation might be mandatory for Zn–based materials. Finally, severe plastic deformation techniques are strongly indicated to homogenize the degradation of Zn alloys.

Future perspectives

From the results of this PhD Thesis, the following specific recommendations are proposed for further investigation:

1. To investigate other Zn-xCu alloys formulations with x < 3 wt.%, expecting mechanical improvement compared with pure Zn and less aggressive localized corrosion than the reported for the studied Zn-Cu alloys. Alternatively, Zn-3Cu alloy could be subjected to ECAP to homogenize its degradation.
2. To transfer the understanding of the PCL coating process to investigate other coating techniques, e.g., dip coating, that can be used for complex implant geometries as is the case of cardiovascular stents.
3. To perform proliferation cell assays on the functionalised surfaces to elucidate the effectiveness of peptides on the HUVEC proliferation after the adhesion.
4. To evaluate the biological response of Zn-2Ag after ECAP *via* cytotoxicity tests.

Other important aspects of Zn-based alloys must be carefully considered regarding their use as bioresorbable implants:

- *Mechanical stability of Zn-based implants*

The melting temperature of Zn is T_m = 419 ºC, and its service temperature (0.45 T_m) is equivalent to 38 ºC. Implantable devices are sterilized, packaged, and then stored at R.T, where strain softening, natural aging, or static recrystallization (SRX) can occur. Fan *et al.* [1] related these phenomena to the atomic diffusion in the Zn lattice and recommended alloying with Cu or Ag as lattice stabilizers due to the high energy activation they require to diffuse. Huang *et al.* [2] recently reported an extensive review suggesting that strain softening would be directly related to non-uniform elongation and suggested that Ag, Cu, or Mn would avoid strain sensitivity events. On the other hand, the DRX occurring in the ECAP deformation reduces the stored energy in the material and might avoid uncontrolled SRX. Therefore, Zn-2Ag would still be a potential material for bioresorbable implants with adequate mechanical stability, and the ECAP process would be recommended as a post-processing route for Zn-based materials. However, further studies to confirm this hypothesis must be performed.

- *Manufacturing routes of Zn-based alloys*

The low working temperatures of Zn also carry economic benefits due to the low energy cost of conventional casting and processing. However, current techniques for cardiovascular stent manufacturing consist of metallic tube extrusion and laser cutting. Consequently, the low melting point of Zn may lead to vapor Zn emissions throughout the laser process or larger areas of heat-affected zones [3,4]. In recent years, novel additive manufacturing techniques have attracted interest since they allow the production of affordable personalised medical devices. Nevertheless, some fundamental issues should be addressed, such as undesired Zn evaporation during laser powder bed fusion or sintering complications due to the stable oxide layer surrounding Zn particles [5–8].

References

[1] S. Fan, R. Yue, S. Li, G. Yuan, Z. Jin, First-principles calculations of diffusion activation energies for designing anti-self-aging biodegradable zinc alloys, J Mater Res. 36 (2021) 1475–1486. https://doi.org/10.1557/s43578-021-00177-7.

[2] H. Huang, G. Li, Q. Jia, D. Bian, S. Guan, O. Kulyasova, R.Z. Valiev, J. v. Rau, Y. Zheng, Recent advances on the mechanical behavior of zinc based biodegradable metals focusing on the strain softening phenomenon, Acta Biomater. (2022). https://doi.org/10.1016/j.actbio.2022.08.041.

[3] E. Mostaed, M. Sikora-Jasinska, A. Mostaed, S. Loffredo, A.G. Demir, B. Previtali, D. Mantovani, R. Beanland, M. Vedani, Novel Zn-based alloys for biodegradable stent applications: Design, development and in vitro degradation, J Mech Behav Biomed Mater. 60 (2016) 581–602. https://doi.org/10.1016/j.jmbbm.2016.03.018.

[4] D.W.Y. Toong, J.C.K. Ng, Y. Huang, P.E.H. Wong, H.L. Leo, S.S. Venkatraman, H.Y. Ang, Bioresorbable metals in cardiovascular stents: Material insights and progress, Materialia (Oxf). 12 (2020) 100727. https://doi.org/10.1016/j.mtla.2020.100727.

[5] Y. Qin, J. Liu, Y. Chen, P. Wen, Y. Zheng, Y. Tian, M. Voshage, J.H. Schleifenbaum, Influence of laser energy input and shielding gas flow on evaporation fume during laser powder bed fusion of zn metal, Materials. 14 (2021). https://doi.org/10.3390/ma14102677.

[6] A.G. Demir, L. Monguzzi, B. Previtali, Selective laser melting of pure Zn with high density for biodegradable implant manufacturing, Addit Manuf. 15 (2017) 20–28. https://doi.org/10.1016/j.addma.2017.03.004.

[7] Y. Qin, P. Wen, M. Voshage, Y. Chen, P.G. Schückler, L. Jauer, D. Xia, H. Guo, Y. Zheng, J.H. Schleifenbaum, Additive manufacturing of biodegradable Zn-xWE43 porous scaffolds: Formation quality, microstructure and mechanical properties, Mater Des. 181 (2019). https://doi.org/10.1016/j.matdes.2019.107937.

[8] Y. Qin, P. Wen, H. Guo, D. Xia, Y. Zheng, L. Jauer, R. Poprawe, M. Voshage, J.H. Schleifenbaum, Additive manufacturing of biodegradable metals: Current research status and future perspectives, Acta Biomater. 98 (2019) 3–22. https://doi.org/10.1016/j.actbio.2019.04.046.

Outcomes of the Thesis

The main outcomes of the PhD are summarizing in the form of different activity indicators:

Publications

- **García-Mintegui, C**., Córdoba, L., Buxadera-Palomero, J., Marquina, A., Jimenez-Pique, E., Ginebra, M.P., Cortina, J., Pegueroles, M. *Zn-Mg and Zn-Cu alloys for stenting applications: From nanoscale mechanical characterization to in vitro degradation and biocompatibility.* Bioactive Materials, 6(12). 4430 – 4446 (2021). Open access. Impact Factor: 16.874 (JCR). Ranking: 2/89, Q1 (Engineering, Biomedical). ISSN: 2452-199X

- **García-Mintegui, C**., Goncharov, I. S., Ortiz-Membrado L., Jiménez-Piqué E., Ginebra M.P., Vedani M., Cortina J., Pegueroles M. *Influence of ECAP process on mechanical, corrosion and bacterial properties of Zn-2Ag alloy for wound closure devices.* (submitted to Materials & Design)

- **García-Mintegui, C**., Chausse, V., Labay, C., Mas-Moruno, C., Ginebra, M.P., Cortina, J., Pegueroles, M. *Functionalization of PCL-coated Zn-Mg and Zn-Ag alloys for cardiovascular applications.* (under preparation).

- **García-Mintegui, C.**, Dorrego G., Buxadera-Palomero, J., Cortina, J., Pegueroles, M. *Characterization of Zn-Ag alloys for bioresorbable ureteral stents.* (under preparation).

Conference contributions

- Córdoba, L.C., **García-Mintegui, C**., Pegueroles, M. *3S-printed Zn-Mg bioabsorbable stents: a new paradigm in personalized coronary artery disease treatment.* 11TH Biometal. 25th – 30th August 2019, Alicante (Spain) – Oral presentation.

- **García-Mintegui, C**., Buxadera-Palomero, J., Cortina, J., Pegueroles, M. *Electrochemical characterization and biocompatibility of Zn-based alloys for cardiovascular applications.* XLII Congreso de la Sociedad Ibérica de Biomecánica y Biomateriales. 15th – 16th November 2019, Madrid (Spain) – Oral presentation.
- **García-Mintegui, C.**, Córdoba, L.C., Jiménez-Piqué, E., Cortina, J., Pegueroles, M. *Corrosion and nanoscale mechanical evaluation of Zn-Mg and Zn-Cu alloys.* Updates in Bioabsorbable Metals 2020. 24th – 25th August 2020, Virtual – Oral presentation.
- **García-Mintegui, C.** *Biodegradable Zn-based materials for biomedical applications.* MMAMT-Modern materials and advanced manufacturing technology. 21st – 23rd September 2021, St. Petersburg (Russia) – Oral presentation.

- **García-Mintegui, C.,** Chausse, V., Labay, C., Mas-Moruno, C., Cortina, J., Pegueroles, M. *Inorganic and organic surface modification strategies to control degradation and enhance cell adhesion on biodegradable Zn-based alloys.* 13TH Biometal. 23rd – 26th August 2021, Virtual – Oral presentation.
- **García-Mintegui, C.**, Chausse, V., Labay, C., Mas-Moruno, C., Cortina, J., Pegueroles, M. *Functionalization of biodegradable Zn based alloys with poly(ε-caprolactone) and bioactive peptides to control degradation and enhance endothelialisation.* 31st Annual Conference of the European Society for Biomaterials (ESB 2021). 5th – 9th September 2021, Virtual – Oral presentation.
- **García-Mintegui, C.**, Goncharov, I., Vedani, M., Cortina, J., Pegueroles, M. *Biodegradable metallic zinc alloys for biomedical applications.* 11th EEIGM International Conference on Advanced Materials Research. 16th – 17th June 2022, Barcelona (Spain) – Poster presentation.
- **García-Mintegui, C.**, Goncharov, I., Ortiz-Membrado, L., Jiménez-Piqué, E., Vedani, M., Cortina, J., Pegueroles, M. *ECAP processing influence on the mechanical properties and the bacterial activity of Zn-2Ag alloys.* 14TH Biometal. 24th – 29th August 2019, Alicant (Spain) – Oral presentation.
- **García-Mintegui, C.**, Dorrego, G., Buxadera-Palomero, J., Cortina, J., Pegueroles, M. *Antibacterial Activity and Biodegradation of Zn-Ag Alloys for Biomedical Applications.* 32nd Annual Conference of the European Society for Biomaterials (ESB 2022). 4th – 8th September 2022, Bordeaux (France) – Poster presentation.

Research stays

Research on the fabrication of zinc-based stents by equal channel angular pressing (ECAP) and binder jetting. 15th September – 17th December 2021, Department of Mechanical Engineering of the Politecnico di Milano (Milan, Italy). Supervisor: Maurizio Vedani.

The PhD was developed under the financial support of:

Scholarships

- Pre-doctoral grant (Contracte predoctoral Centre de Recerca en Ciència I Enginyeria Multiescala) – Barcelona Research Center in Multiscale Science and Engineering, Universitat Politécnica de Catalunya, September 2018 – April 2019.
- Pre-doctoral grant (FI-AGAUR 2019) – Agència de Gestió d'Ajuts Universitaris i de Recerca (AGAUR), Generalitat de Catalunya, April 2019 – August 2022.
- 4th year-pre-doctoral grant – Becas Santander/UPC, September 2022 – January 2023.

Research Funding

The presented thesis was funded and part of the investigation of a MINECO/FEDER granted project: ‘Dual-action biomaterials coatings for bacterial infections and tissue integration (DUALITY)’ (RTI2018-098075-B-C21). IPs: Marta Pegueroles and José María Manero. Period: 01/01/2019-31/06/2022. Total funding: 177.000 €